ADAPTIVE RAYTRACING-BASED SUPPRESSION OF SEVERE WATER-BOTTOM MULTIPLES IN MARINE SEISMIC DATA

SIMON R.M. O'BRIEN

INFORMATION TO USERS

This manuscript has been reproduced from the microfilm master. UMI films the text directly from the original or copy submitted. Thus, some thesis and dissertation copies are in typewriter face, while others may be from any type of computer printer.

The quality of this reproduction is dependent upon the quality of the copy submitted. Broken or indistinct print, colored or poor quality illustrations and photographs, print bleedthrough, substandard margins, and improper alignment can adversely affect reproduction.

In the unlikely event that the author did not send UMI a complete manuscript and there are missing pages, these will be noted. Also, if unauthorized copyright material had to be removed, a note will indicate the deletion.

Oversize materials (e.g., maps, drawings, charts) are reproduced by sectioning the original, beginning at the upper left-hand corner and continuing from left to right in equal sections with small overlaps.

Photographs included in the original manuscript have been reproduced xerographically in this copy. Higher quality 6" x 9" black and white photographic prints are available for any photographs or illustrations appearing in this copy for an additional charge. Contact UMI directly to order.

Bell & Howell Information and Learning
300 North Zeeb Road, Ann Arbor, MI 48106-1346 USA

UMI®
800-521-0600

Memorial
University of Newfoundland

This is to authorize the Dean of Graduate Studies to deposit two copies of my thesis/report entitled

ADAPTIVE RAYTRACING-BASED SUPPRESSION OF SEVERE WATER-BOTTOM MULTIPLES IN MARINE SEISMIC DATA

in the University Library, on the following conditions. I understand that I may choose only ONE of the Options here listed, and may not afterwards apply for any additional restriction. I further understand that the University will not grant any restriction on the publication of thesis/report abstracts.

(After reading the explanatory notes at the foot of this form, delete TWO of (a), (b) and (c), whichever are inapplicable.)

The conditions of deposit are:

(a) that two copies are to be made available to users at the discretion of their custodians.

OR

(b) that access to, and quotation from, this thesis/report is to be granted only with my written permission for a period of one year from the date on which the thesis/report, after the approval of the award of a degree, is entrusted to the care of the University, namely, OCTOBER 1998, after which time the two copies are to be made available to users at the discretion of their custodians.

OR

(c) that access to, and quotation from, this thesis/report is to be granted only with my written permission for a period of _____ years from the date on which the thesis/report, after approval for the award of a degree, is entrusted to the care of the University; namely, _____, 19 ____; after which time two copies are to be made available to users at the discretion of their custodians.

Date 6 MAY, 1997

Signed _____

_____
Dean of Graduate Studies

Witnessed by _____

NOTES

1. *Restriction (b) will be granted on application, without reason given.*

   However, applications for restriction (c) must be accompanied with a detailed explanation, indicating why the restriction is thought to be necessary and justifying the length of time requested. Restrictions required on the grounds that the thesis is being prepared for publication, or that patents are awaited, will not be permitted to exceed **three** *years.*

   Restriction (c) can be permitted only by a Committee entrusted by the university with the task of examining such applications, and will be granted only in exceptional circumstances.

2. *Thesis writers are reminded that, if they have been engaged in contractual research, they may have already agreed to restrict access to their thesis until the terms of the contract have been fulfilled.*

ADAPTIVE RAYTRACING-BASED SUPPRESSION OF SEVERE WATER-BOTTOM MULTIPLES IN MARINE SEISMIC DATA

by

Simon R. M. O'Brien

A thesis submitted to the
School of Graduate Studies
in partial fulfillment of the
requirements for the degree of
Doctor of Philosophy

Department of Earth Sciences
Memorial University of Newfoundland

May, 1997

St. John's Newfoundland

ABSTRACT

Marine seismic data is generally acquired by towing source and receiver arrays through the water, periodically generating an acoustic pulse and recording the echoes reflected back from the sub-sea layering. Since both the water surface and the sea-floor are good reflectors, much of the source energy reverberates between the two. When the sea-floor is very hard, this 'multiple' energy is recorded at the receivers for some time after the shot instant and can completely mask all of the energy produced by 'primary' reflections from sub-seafloor boundaries. As we are only interested in imaging the primaries, effective multiple attenuation is extremely important to the processing of marine seismic data. While traditional multiple attenuation techniques often produce good results, they all have limited success dealing with extreme sea-floor conditions such as those which are often experienced off the coast of Newfoundland. This thesis develops a new technique which is better able to handle these conditions and makes a comparison with existing techniques.

The attenuation technique, called Raymult, is based on an adaptive prediction-subtraction approach in which raytracing is used to guide the multiple prediction. The near-trace gather is automatically picked and the picks subsequently migrated to generate a water-bottom model. By raytracing each

shot gather, an estimate is generated for the phase, amplitude and arrival time of the multiples on each trace. These estimates are then adjusted until they accurately match the data. Finally, the multiples are subtracted from the gather. The water and sea-floor velocities are the only required input parameters. However, since the routine is able to adapt the raytracing results to fit the data, the accuracy of these parameters is not essential. As a byproduct of the multiple suppression, wavelet estimates are produced for each multiple order.

Raymult is successfully applied to both synthetic and real data examples, and proves very effective in dealing with substantial sea-floor topography as well as the phase and amplitude problems which are typical of data collected over hard sea-floors. There is only minor distortion of the remaining energy in the gathers, so other multiple attenuation techniques, e.g. predictive deconvolution or radon filtering, can be applied subsequently, providing even greater attenuation of the multiples.

TABLE OF CONTENTS

LIST OF FIGURES

ACKNOWLEDGMENTS

This research was supported by a graduate research award from Amoco Canada, an Offshore Career Development Award and an NSERC Research Grant to Dr. J. Hall. Processing was performed using programs incorporated into Seismic Unix, a system developed by the Centre for Wave Phenomena at the Colorado School of Mines. Thank you to Hunt Oil and Pan Canadian for allowing me to use some of their data.

I would like to thank my supervisor, Dr. J. Hall, for his patience and encouragement. I would also like to thank Dr. C. Hurich, Dr. L. Lines and Dr. J. Wright for their generous words of advice; Tony Kocurko for keeping the computers going and solving numerous technical problems; and Dr. A. Calvert for some very useful comments. Finally and most importantly, I would like to thank my family, Pam, Katie and Mark, for their support and for allowing me to disappear from time to time, so that I could get this thing done.

1. INTRODUCTION

1.1 Marine Seismic Data

Seismic imaging of sub-seabed geological structure is usually performed using a ship which tows a source array and one or more streamers containing receivers (Figure 1.1). As the ship proceeds along a traverse, the source emits a powerful acoustic signal which travels through the water layer into the Earth. Whenever the propagating wavefield encounters a boundary between regions with different elastic properties, part of the energy is reflected back towards the surface, where it can be recorded by the receivers, while the remaining energy passes through. The receiver signals, as a function of time, therefore contain information about successive subsurface boundaries and, with repeated shot recordings at regular intervals, the data can be processed to give a continuous profile of the subsurface structure.

Figure 1.2 shows an ideal shot gather, which contains all of the data recorded by the receivers for up to 2 seconds following a single firing of the source. The first arrivals to be recorded are due to the direct wave, which travels straight through the water from source to receiver. On the traces closest to the shot (the 'near' traces), the sea-bottom reflection is recorded next, but farther away from the shot, refracted events arrive earlier. Primary reflections then arrive from

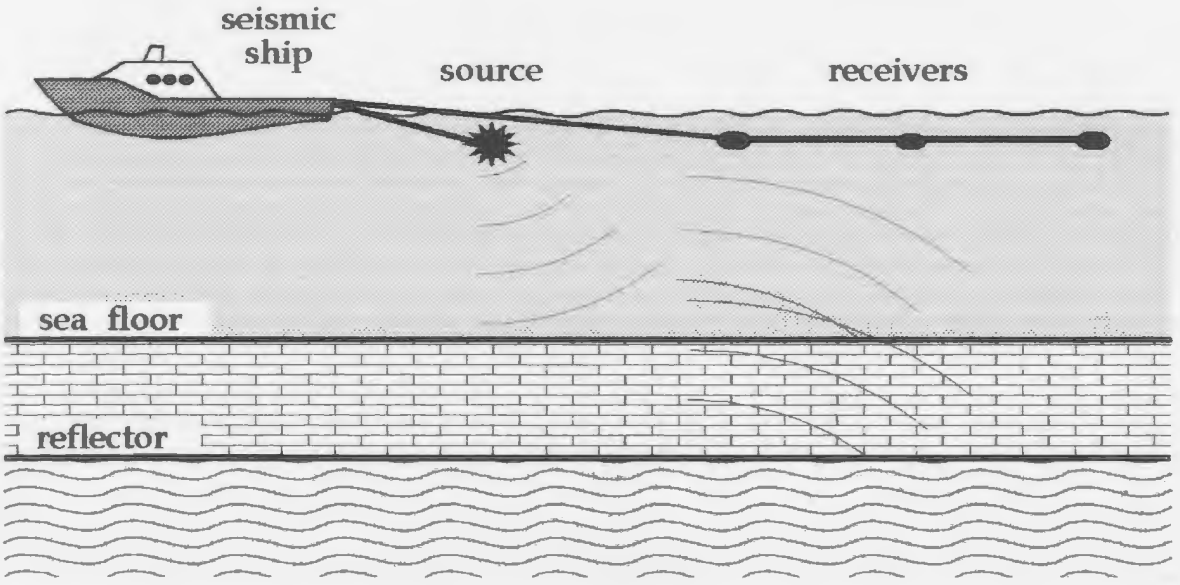

Figure 1.1 Schematic illustration of a simple marine seismic experiment

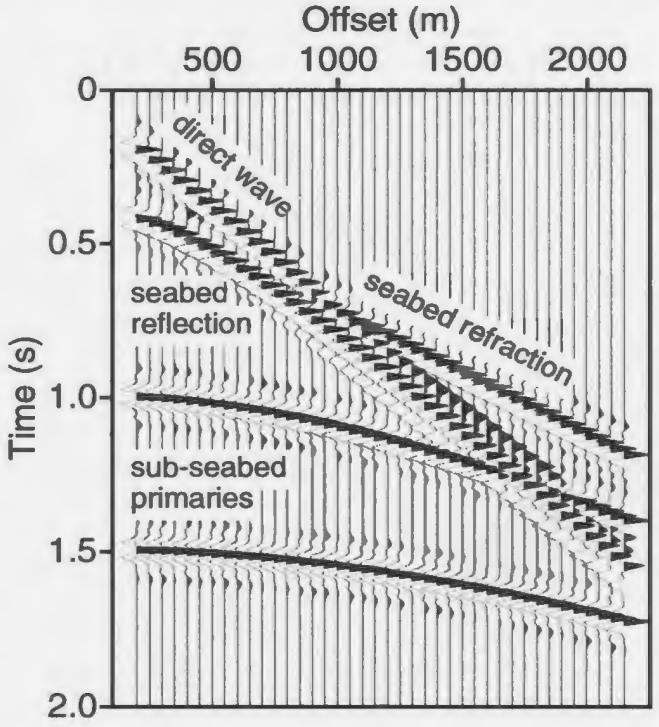

Figure 1.2 Ideal shot gather, the result of a noise free experiment over several horizontal layers. An automatic gain has been applied to reduce the amplitude variations between the various events.

each boundary in the subsurface in turn, with their amplitudes dependent on the magnitude of the contrast in acoustic properties across the boundary.

Unfortunately, the data which are recorded in the field are rarely so clear. The traces always contain some degree of random noise due to a variety of external sources, ranging from waves breaking to sharks biting the cable. In addition, there is often a considerable amount of coherent noise, ambient and/or shot related, the most important of which is caused by the reverberation of seismic energy within the water layer (see Figure 1.3). This thesis includes a review of current techniques for reducing the effects of such reverberations and reports a new method, which is especially useful when the seabed structure is complex.

1.2 Water-bottom Multiples

The amount of seismic energy reflected at an interface is related to the density and velocity contrast between the materials on either side of the boundary. The 'reflection coefficient', which is the ratio between the incident energy and the reflected energy, increases as the contrast increases (see Section 2.1). Since water and air have very large velocity and density contrasts, the sea-surface is almost a perfect reflector, with a downward reflection coefficient close to -1. The negative value is due to the fact that velocity decreases upwards

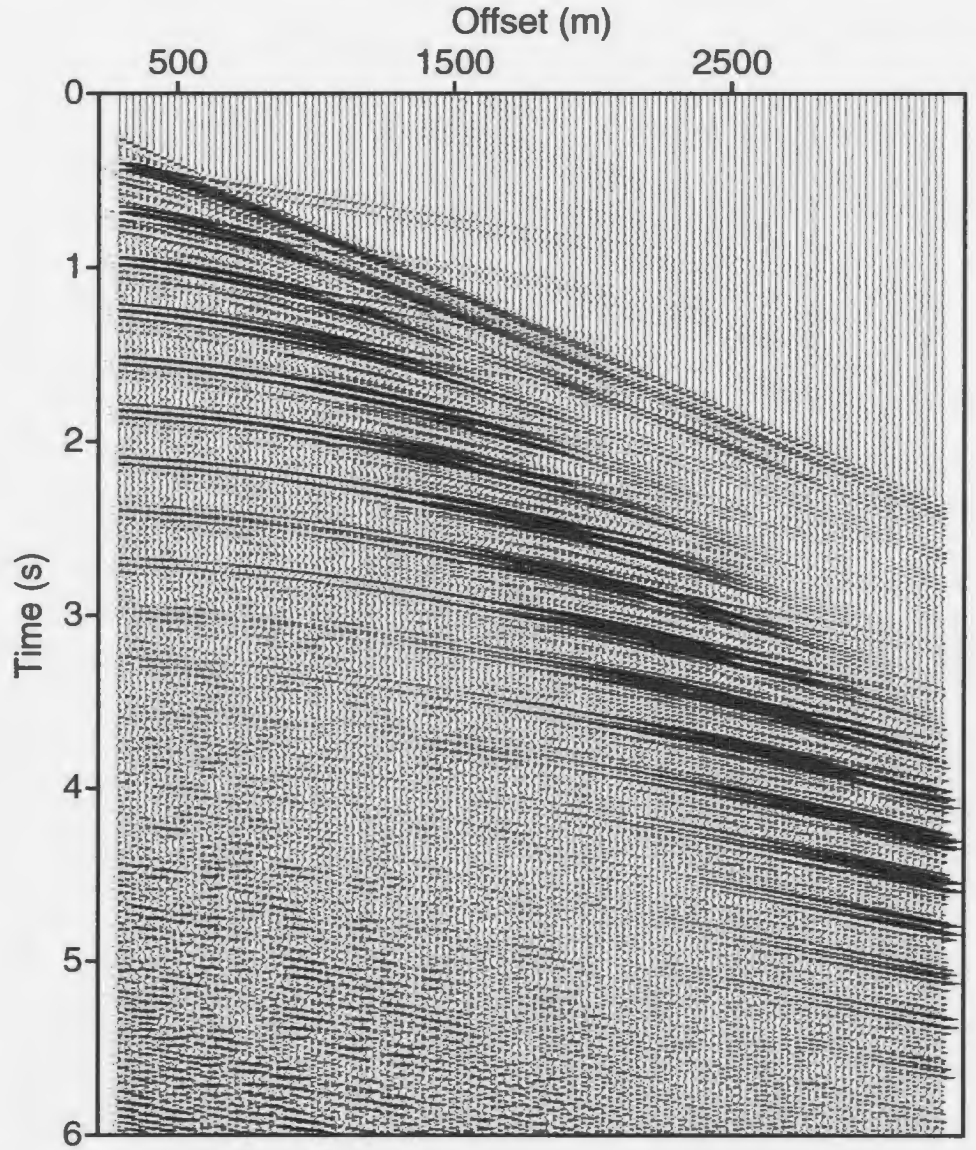

Figure 1.4. Shot gather from a deep seismic dataset collected off the northwest coast of Newfoundland in 1984 by the AGC. At least 15 orders of multiples are clearly visible.

extent. However, the sea-floor conditions on the continental shelf around Newfoundland are such that the water-bottom multiples are extremely severe. The water depth varies between about one hundred and three hundred metres and the sea-floor is very hard. This means that the multiples are of very high amplitude and that they can maintain amplitudes comparable to the primaries for several seconds. The northeast coast has very little sediment cover, so that in addition to having 'loud' multiples, there are very few high amplitude primaries. Many of the shot gathers in the 1984 deep seismic reflection data have at least 12-15 orders of multiples clearly visible (see Figure 1.4), causing multiple energy to completely obscure the first six seconds of data (Keen et al., 1986). This made the upper crustal part of the section totally uninterpretable, and emphasized the need for effective multiple attenuation.

1.3 Multiple Suppression

Multiples were first described as a potential problem in the seismological literature in 1948, when a number of papers in *Geophysics* showed that multiples could be clearly seen in a number of different data sets from the Sacramento Valley (e.g. Ellsworth, 1948; Sloat, 1948). Sloat noted at the time that they could easily be mistaken for primary arrivals and, as a result, could make interpretation very difficult.

Considerable work was done in the early 1950's to model the amplitude and

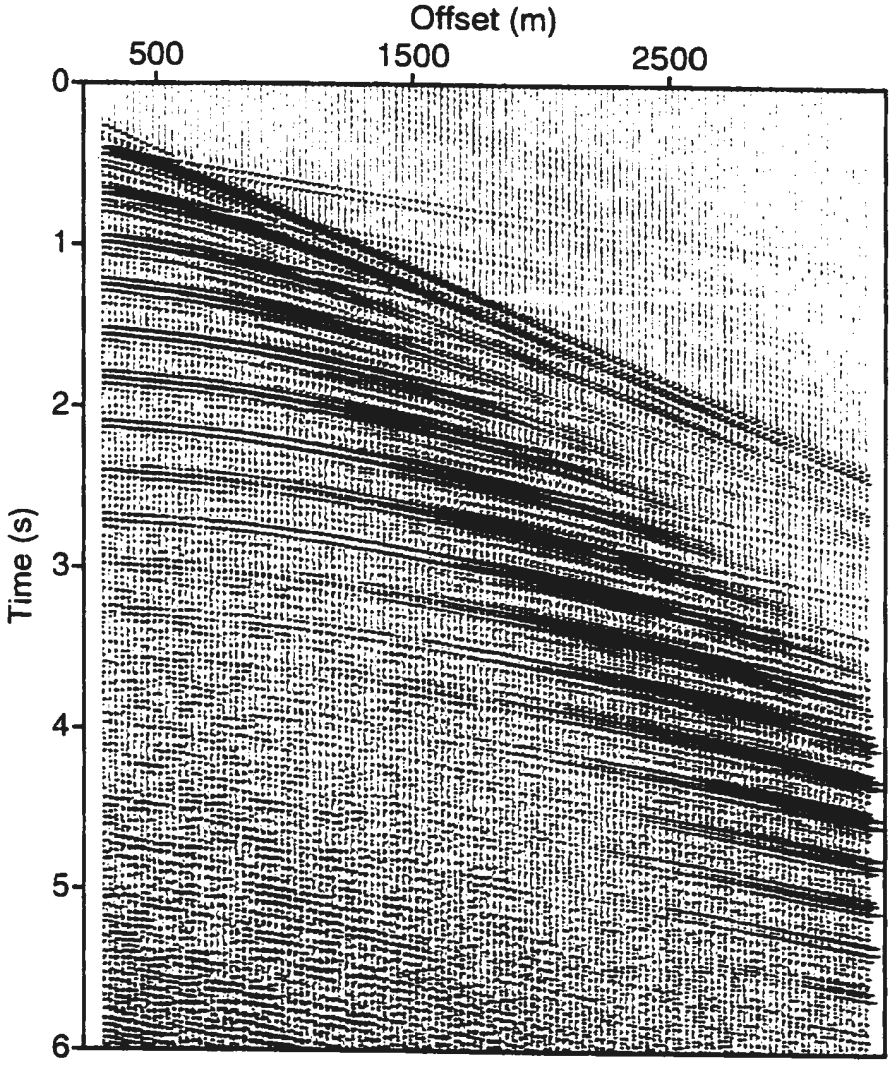

Figure 1.4. Shot gather from a deep seismic dataset collected off the northwest coast of Newfoundland in 1984 by the AGC. At least 15 orders of multiples are clearly visible.

phase characteristics of the multiple events (e.g. Press and Ewing, 1950: Officer, 1951: Burg et al., 1951), to find some way of distinguishing the multiples from the primaries. Backus (1959) was the first to look at the problem from a linear filtering point of view. He showed that the periodic nature of sea-floor multiples can be used to predict which part of the recorded trace is multiple and which part is primary. 'Inverse filtering' can then be used to remove the multiples from the trace. This method is now generally referred to as 'predictive deconvolution' and will be discussed in greater detail in Section 3.2.

A second important attenuation method was developed in the early 1960's, as a result of the development of multi-channel data processing. Because of the velocity difference between the Earth sampled by primary reflections and that sampled by the multiples, there is a difference in the change of arrival time with source-receiver offset (move-out) between a primary and a multiple with the same vertical incidence travel-time. Discrimination on the basis of differential move-out was used in common depth point (CDP) stacking to improve the primary-to-multiple amplitude ratio substantially (Mayne, 1962). Then Schneider et al. (1965) showed that 'optimal stacking', in which carefully chosen filters are applied to each pre-stack trace, can provide an even greater improvement.

Over the past several decades, a number of additional processing techniques

have been developed for multiple attenuation. However, most are based on either the move-out difference between multiples and primaries or on the predictability of the multiples. The degree of success of these methods generally depends on how well the Earth (and thus the recorded data set) agrees with the assumptions which are made about it.

Very recently, advances in seismic acquisition have introduced a number of new possibilities for multiple suppression. Dual-sensor cables, which contain both hydrophones and ocean bottom geophones, provide pressure and velocity information which can be summed to attenuate multiple energy (Dragoset and Barr, 1994; Paffenholz and Barr, 1995). However, the scale factors that must be applied to the data sets are not always easily calculated, which can result in fairly poor attenuation, particularly when the sea-floor reflection coefficient is high. Vertical cables make it easier to separate upgoing and downgoing components of the wavefield, which potentially could produce a way of filtering out the downgoing multiples (Moldoveanu et al., 1993). Burying vertical cables in the seafloor sediments can provide even better attenuation (Moldoveanu et al., 1994), but both of these approaches are only useful in shallow, soft water-bottom situations. Since the original focus of this research was to provide better multiple attenuation on data that we had already acquired, I have concentrated exclusively on developing a new processing approach rather than looking at

acquisition techniques.

1.4 Research Approach

Current multiple suppression techniques tend to be least effective when the sea-bottom is very hard or when there is considerable sea-bottom structure. The only way to deal properly with this problem is to actually incorporate a model of the sea-floor into the suppression technique. This involves a 'prediction-subtraction' approach, in which the multiples are first predicted using the sea bottom information and then subtracted from the data set. The approach which I have taken is to use the receiver data (traces) closest to each shot to develop a model of the sea-floor, and then to use raytracing to predict the arrival times, amplitudes and phases of the multiples for each shot gather. These parameters are then compared to the actual data and a wavelet is estimated. The parameters are then adjusted until the wavelet estimate is best able to reproduce the actual multiple arrivals. The wavelet is then convolved with the new set of multiple parameters and the results are subtracted from the data. Because this approach is able to adjust to the phase and amplitude variations arising from complex reflection coefficients (see Section 2.1), it is even able to handle post-critical multiples. Since it allows the initial assumptions to be adapted to best fit the data, it will always improve the primary-multiple energy ratio.

2. WATER-BOTTOM MULTIPLES

2.1 Seismic Reflection Theory

The most common marine seismic source is an array of airguns. This produces large bubbles of compressed air, whose expansion and subsequent collapse create a pulse of acoustic energy which propagates according to the wave equation:

$$\nabla^2 P - \frac{1}{v^2}\frac{d^2 P}{dt^2} = 0 \tag{2.1}$$

where P is pressure, v is the propagation velocity and t is the time. The pressures are then recorded by a number of evenly spaced receiver groups, themselves short arrays of hydrophones, the outputs from which are summed to give a single trace.

When the acoustic wavefront comes in contact with a boundary, it is divided into reflected and refracted components to ensure continuity of normal stress and displacement across the boundary. The reflection and refraction angles are governed by Snell's law:

$$\frac{\sin\theta_1}{v_1} = \frac{\sin\theta_2}{v_2} \tag{2.2}$$

with the reflection angle being equal to the incident angle (see Figure 2.1). When

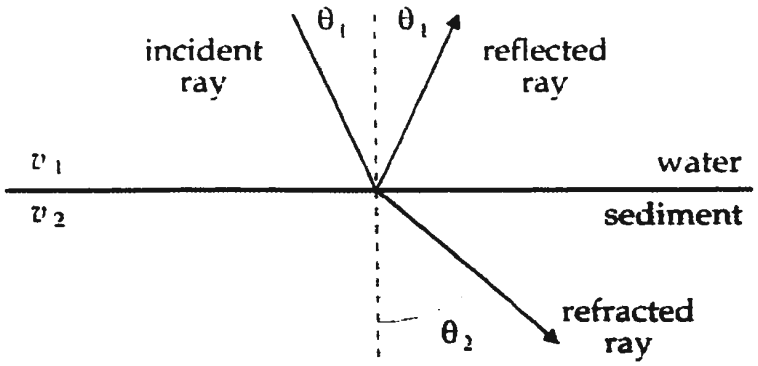

Figure 2.1. Illustration of the reflection and refraction angles used in Equation 2.2.

v_2 is greater than v_1, there is an incident angle for which the refracted angle is 90°. This is called the 'critical' angle. All components of the wavefield which propagate with incident angles greater than the critical are completely reflected.

The relative amplitudes of the reflected and refracted parts are dependent on the change in impedance, the product of velocity and density, across the boundary. At normal incidence, the amplitude ratios are:

$$\frac{A_1}{A_0} = \frac{\rho_2 v_2 - \rho_1 v_1}{\rho_2 v_2 + \rho_1 v_1} = \frac{Z_2 - Z_1}{Z_2 + Z_1}$$
$$\frac{A_2}{A_0} = \frac{2\rho_1 v_1}{\rho_2 v_2 + \rho_1 v_1} = \frac{2Z_1}{Z_2 + Z_1} \qquad (2.3)$$

where A_0 is the incident amplitude, A_1 and A_2 are the reflected and refracted amplitudes; ρ_i are the densities and v_i are the acoustic velocities.

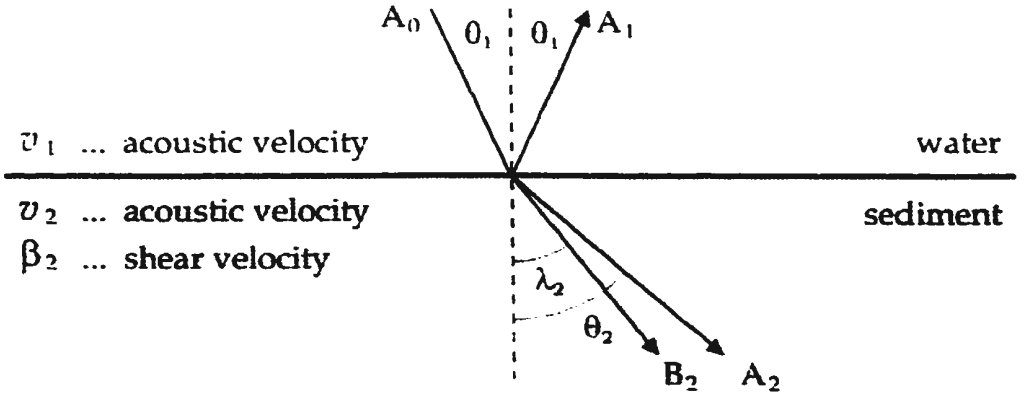

Figure 2.2. Illustration of the reflection and refraction angles used in Equation 2.4. The acoustic impedance, Z, is the product of v_i and ρ_i the shear impedance, W, is the product of β and ρ.

This becomes somewhat more complicated when the angle of incidence (the angle between the propagation direction and the boundary normal) is non-zero, since some of the acoustic energy (P-wave) is then converted into shear energy (S-wave). The equations relating the compressional (*A*) and shear (*B*) amplitudes (see Figure 2.2) of the different components are the Zoeppritz' Equations:

$$\begin{aligned} A_1 \cos\theta_1 + A_2 \cos\theta_2 + B_2 \sin\lambda_2 &= A_0 \cos\theta_1 \\ -A_2 \frac{\beta_2}{v_2} \sin 2\theta_2 + B_2 \cos 2\lambda_2 &= 0 \\ A_1 Z_1 - A_2 Z_2 \cos 2\lambda_2 - B_2 W_2 \sin 2\lambda_2 &= -A_0 Z_1 \end{aligned} \qquad (2.4)$$

The reflection coefficient is then the ratio A_1/A_0. Since the water layer cannot transmit shear waves, the reflected shear wave component is zero and hence has been omitted. Figure 2.3 shows how the reflection coefficient varies with angle of incidence for a simple seafloor model, with a water velocity of 1500 ms^{-1},

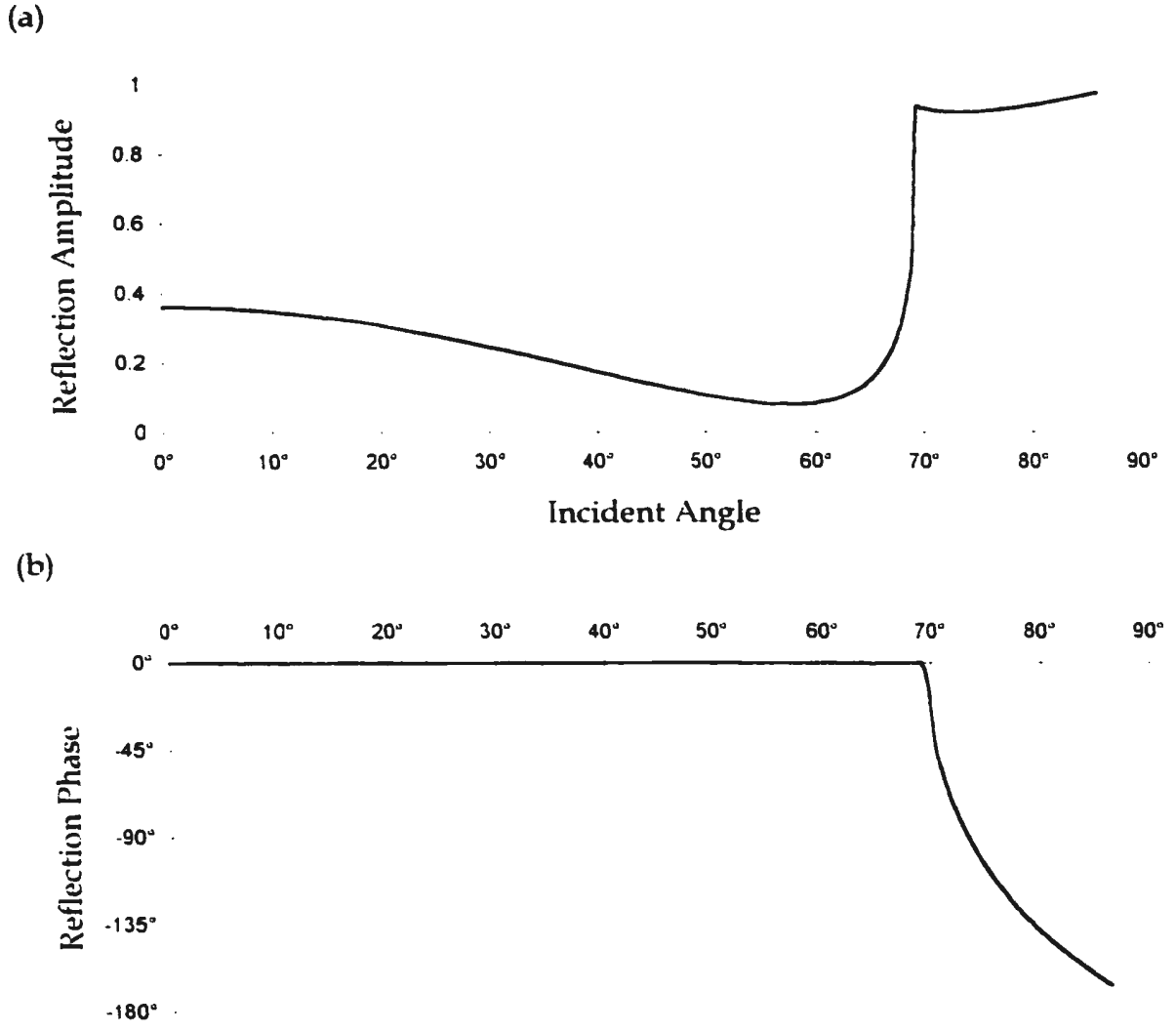

Figure 2.3. Amplitude=A_1/A_0 (a) and phase (b) vs. offset curves for a simple seafloor model. The seafloor has a velocity of 1600 ms^{-1} and a density of 2000 kgm^{-3}, while the water has a velocity of 1500 ms^{-1} and a density of 1000 kgm^{-3}

the seafloor velocities of 1600 ms^{-1} (P-wave) and 1200 ms^{-1} (S-wave), water density of 1000 kgm^{-3} and seafloor density of 2000 kgm^{-3}. Near normal incidence, reflected amplitude decreases as angle increases but reaches a minimum just

before the critical angle, and then quickly increases to an amplitude near unity at the critical angle itself.

Amplitude is not the only thing that varies with offset. Post-critical reflections also have considerable phase variation (see Figure 2.3b). Since most seismic processing techniques assume that the wavelet remains constant in both frequency content and phase, the rapid change in the phase of the reflections after the critical angle makes data processing very difficult. As a result, post-critical data are generally muted and excluded from the processing.

2.2 Seismic Events

The vast majority of coherent energy in marine shot gathers occurs as one of three different types of event: direct, refracted or reflected (see Figure 2.4). The earliest arrival at short offset is the direct arrival, which is the result of wave energy travelling directly from the source to the receivers. As a result, its offset vs. time (x-t) plot is a straight line through the origin, with a slope (dx/dt) equal to the water velocity. It contains no information about the sub-seafloor. However, if sufficient offsets are available, it can be very useful for the assessment of shot-based static corrections (hereafter referred to as statics) and the water velocity, as will be described in Chapter 6. It can also be used to estimate the shape of the source wavelet. However, the fact that both the source and receiver are generally comprised of horizontal arrays means that the

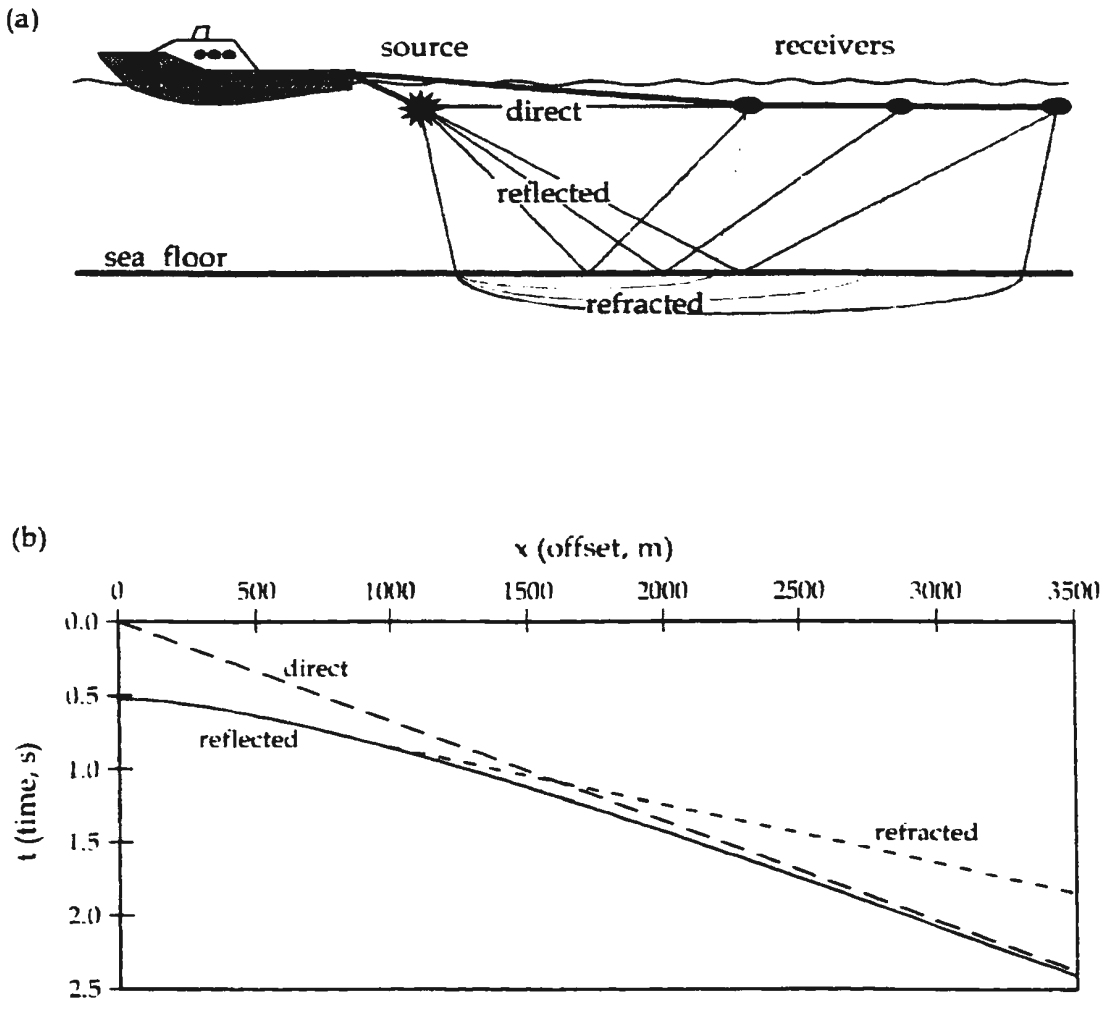

Figure 2.4. Illustration of direct, reflected and refracted seismic events: (a)

recorded wavefield is directionally dependent and that the near-vertical component, which produces most of the reflected energy, is not the same as the near-horizontal component, which produces the direct arrivals. Because of the spherical spreading of the wavefield, the amplitudes decrease linearly with the

distance from the source.

Refracted arrivals are those in which the wavefield passes through the seafloor and is refracted so that it is turned back towards the surface without reflecting. A special case, called a head wave, occurs when the wavefield is refracted at the critical angle and then travels along the boundary itself. When the layers are planar, these events have linear x-t relationships, with slopes equal to the velocity of the layer in which they turned. They do not pass through the origin. They can be very useful in assessing layer velocities, but since the velocity determination is based primarily on travel in the horizontal direction, refraction velocities often differ somewhat from the near-vertical velocities constraining reflections. When the layers have lateral thickness variations, the x-t relationships become more complex, and velocity estimates require modelling and are more subject to errors. If only geometric spreading is taken into account, refraction amplitudes theoretically should decay linearly with offset. However, since they are affected by absorption, especially at wide offset, and lateral impedance variations, the amplitude decay is generally somewhat more rapid.

In a model consisting of a single horizontal layer, reflected events have a hyperbolic x-t relationship which is given by the equation:

$$t(x) = \frac{\sqrt{x^2 + 4d^2}}{v} \tag{2.5}$$

where t is the two-way travel time, x is the source-receiver offset, d is the thickness of the layer and v is the velocity. When the reflector is dipping, the x-t relationship is altered slightly:

$$t(x) = \frac{\sqrt{x^2 + 4d^2 - 4dx\sin\theta}}{v} \qquad (2.6)$$

where θ is the dip angle and d is the normal distance from the reflector to the shot. Although this is still a hyperbola, it is not symmetrical about the shot position (x=0). As many of the basic seismic processing techniques (e.g., semblance-based velocity analysis, CMP stacking) assume that the reflectors are horizontal, the moveout difference caused by dipping reflectors can produce significant processing problems.

Spherical spreading causes reflection amplitudes to decrease linearly with distance from the source, but reflected events are also subject to the reflection coefficients described above. As a result, they often have fairly complex amplitude vs. offset curves. Figure 2.5 shows how the reflection amplitudes might vary with offset for examples of a 'soft' and a 'hard' sea-bottom. The water depth is 200 m. The 'soft' model uses the same parameters as Figure 2.3, while the hard model uses a seafloor velocity of 3000 ms^{-1} and a density of 2500 kgm^{-3}. The soft sea-bottom example is simply a superposition of Figure 2.3 on the geometric spreading curve. The hard sea-bottom example, however, is

(a)

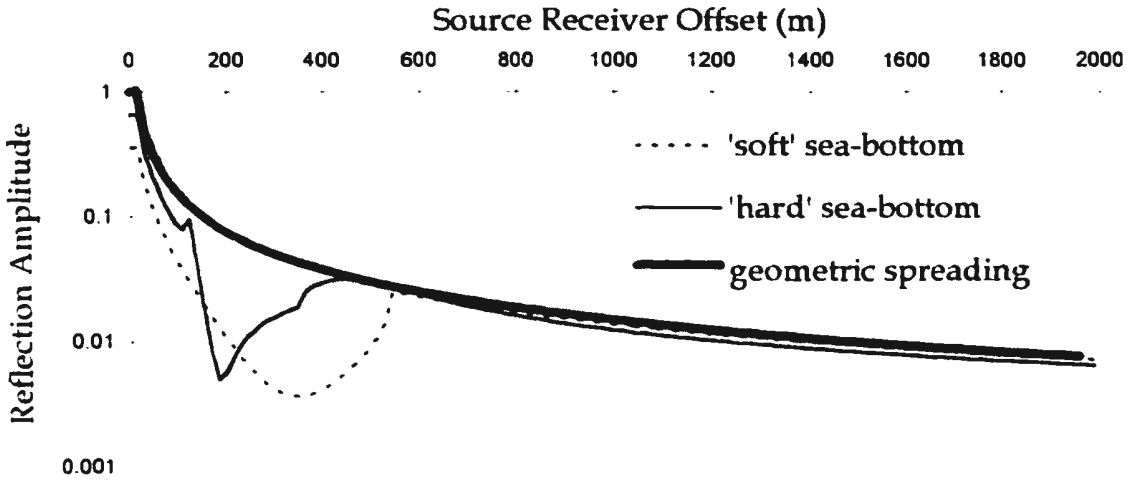

(b)

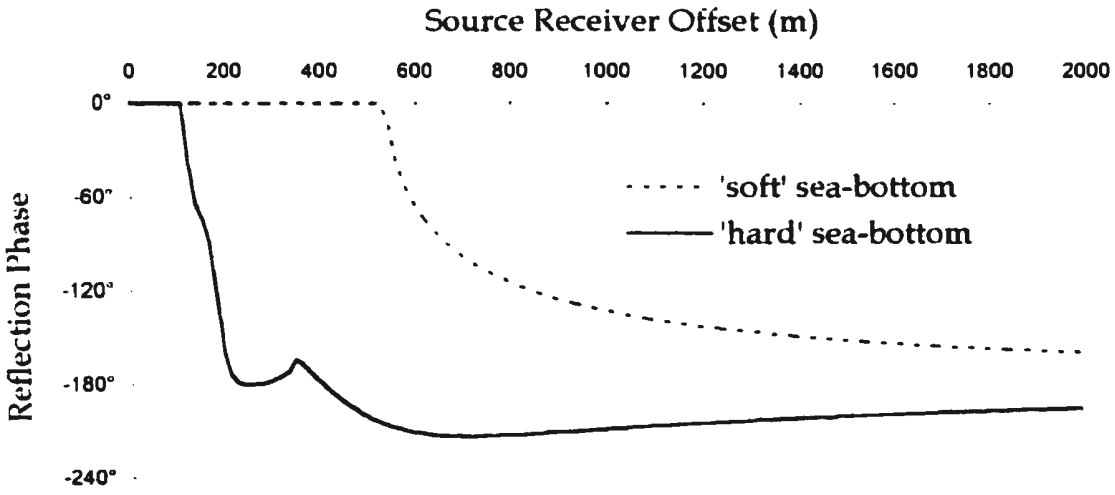

Figure 2.5. Amplitude (a) and phase (b) vs. offset curves for hard and soft sea-floor models. The hard example uses a seafloor velocity of 3000 ms^{-1} and a density of 2500 kgm^{-3}, while the soft example uses a seafloor velocity of 1600 ms^{-1} and a density of 2000 kgm^{-3}. The water velocity for both is 1500 ms^{-1} and the water density is 1000 kgm^{-3}.

somewhat more complicated. Because the shear velocity of the seafloor is greater than the water velocity, there are two critical angles; one P-wave and one S-wave. This is represented on the amplitude curve by two peaks, one near 200 m offset and the other near 500 m.

2.3 Multiple Reflections

Sea-bottom multiples may be considered to be primary reflections from virtual reflectors beneath the sea floor, as shown in Figure 2.6. As a result, they have all the characteristics of simple primaries. The x-t relationship for the n^{th} order multiple from a horizontal reflector is given by:

$$t(x) = \frac{\sqrt{x^2 + 4(n+1)^2 d^2}}{v} \tag{2.7}$$

Clearly, when n=0, this reduces to the equation for primary moveout (Eq. 2.5). Figure 2.6 also illustrates the fact that the multiple images for a dipping reflector have progressively steeper dips. The moveout can therefore be inferred from Equation 2.6:

$$t(x) = \frac{\sqrt{x^2 + 4h^2 - 4hx\sin(n+1)\theta}}{v} \tag{2.8}$$

where h is the perpendicular distance from the source to the imaged reflector. This distance can be calculated by observing that all of the imaged reflectors

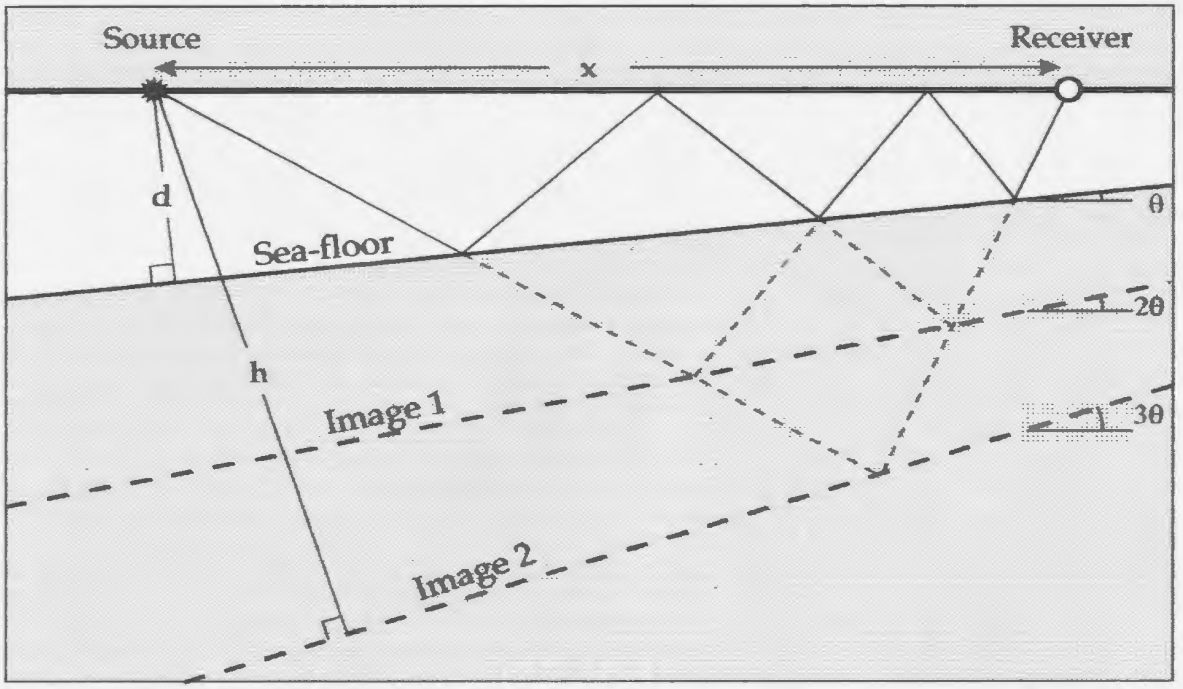

Figure 2.6. Ray-diagram showing a second order sea-floor multiple and its sub-sea-floor images.

have the same intercept with the horizontal (see Figure 2.7):

$$h = d\frac{\sin(n+1)\theta}{\sin\theta} \tag{2.9}$$

This indicates that topography of the seafloor is more exaggerated by each successive order of sea-bottom multiple. This causes the time intervals between different order multiples to vary significantly, and consequently greatly reduces the effectiveness of most attenuation techniques.

Since the reflection coefficient of the ocean surface is approximately -1, the zero-offset reflection coefficient for the n^{th} order multiple is simply:

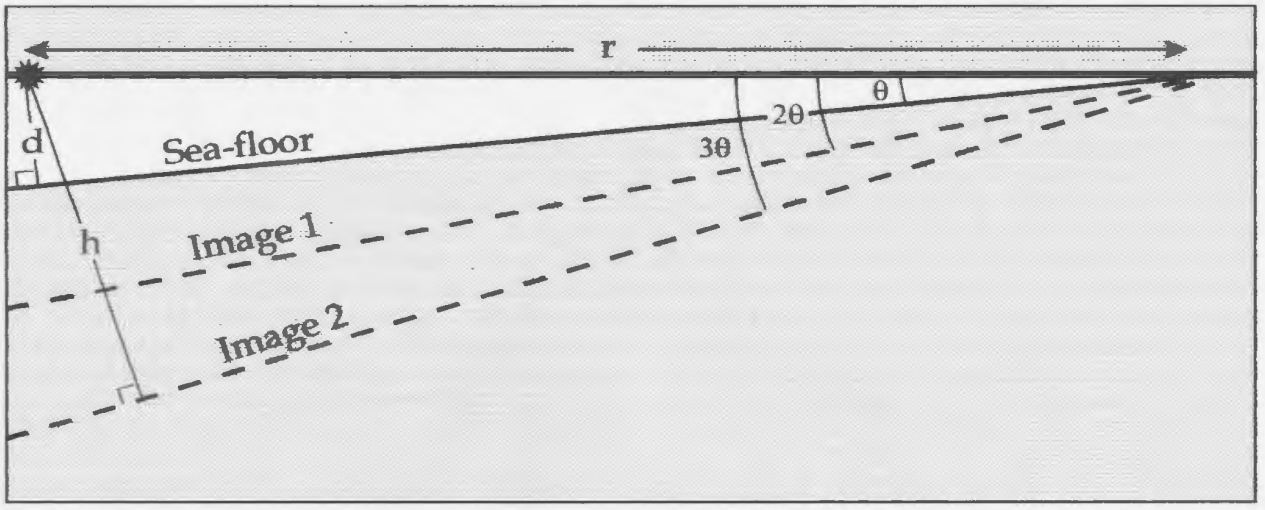

Figure 2.7. Illustration of the image geometry for multiples from a dipping sea-floor, showing the relationship between *d* and *h*.

$$R_n = -(-R_0)^{n+1} \tag{2.10}$$

However, when offset is taken into account, the amplitude relationships are considerably more complicated. The amplitude vs. offset curves for 4 orders of multiples corresponding to the soft model of Figure 2.5 are shown in Figure 2.8. It is quite clear that the geometric relationship of the multiple amplitudes is only valid at very small offsets, even for a soft, flat ocean-bottom. In areas where the seafloor is hard and rough, the amplitudes become very unpredictable, potentially with numerous critical arrivals on each event.

In addition to simple sea-bottom multiples, reverberation within the water layer of energy reflected by deeper primary reflectors produces pegleg multiples (see Figure 2.9a). In hard seafloor conditions, every primary reflector will have a

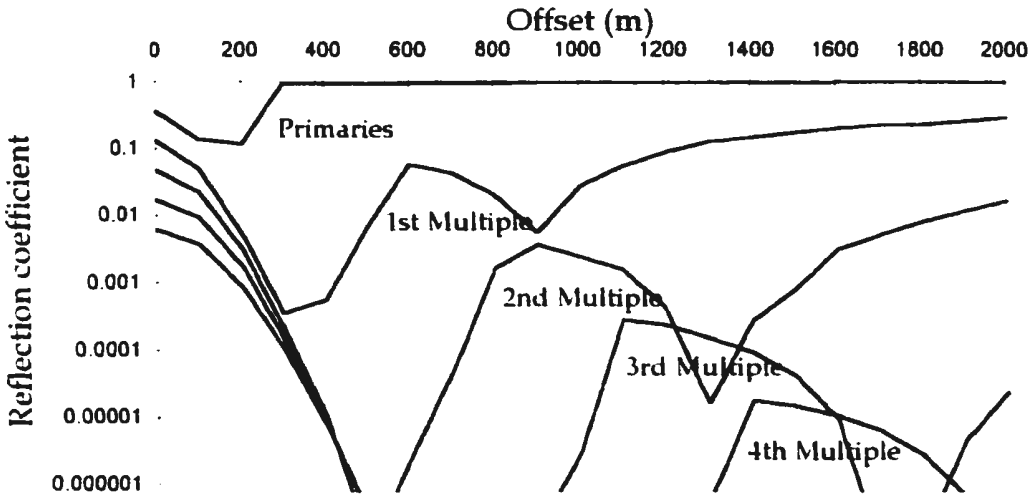

Figure 2.8. Amplitude vs. offset for four orders of water bottom multiples. The sea-floor velocity was 1600 ms^{-1} with a density of 2000 kgm^{-3}.

series of pegleg multiples trailing after it. The moveout for the first pegleg is close to the primary velocity, but each subsequent pegleg has a velocity which gets progressively closer to the water velocity (see Figure 2.9b). Since the water layer reverberations can occur before and after the primary reflection in any sequence, pegleg arrival times can be very difficult to predict. In addition, since several different ray paths can contribute to the same pegleg order, amplitudes and phases are virtually impossible to predict, even under relatively soft, flat sea-floor conditions. While peglegs are often very difficult to remove, they can usually be readily identified by the trend in their moveout velocities.

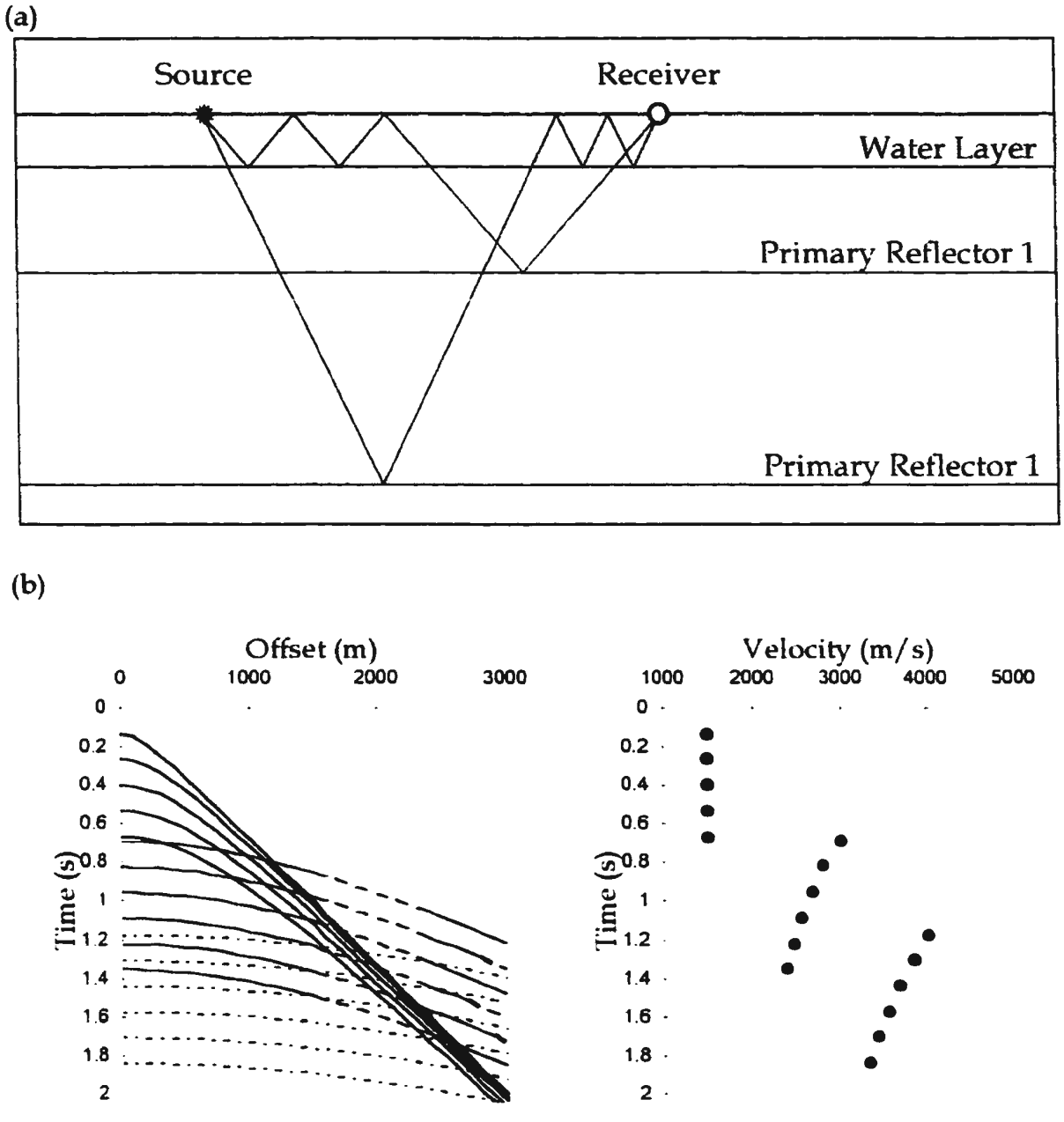

Figure 2.9. Illustration of pegleg multiples. a) shows possible ray paths for second order peglegs for two reflectors. Note that there are actually three different ray paths for second order peglegs, since the reverberations can occur either before or after the deeper reflection. b) shows the arrival times and velocity spectra for the primaries and five pegleg arrivals from each reflector.

2.4 Sea-Bottom Considerations

There are four important factors which determine the nature of sea-bottom multiples:

- the velocity and density of the seafloor rocks
- the water depth
- the topography of the sea-bottom
- the degree of sediment cover

The first factor, which may be referred to as the hardness of the seafloor, controls how the multiple energy decays -- the harder the seafloor, the greater the number of multiples which have amplitudes comparable to the primaries. Water depth does not actually affect the amplitude of the multiples, but it does determine the time between the different multiple orders. Very shallow water conditions will produce multiples in which the wavelet of one order will overlap with the wavelet of the next. As a result, primaries may be completely obscured. On the other hand, the multiples arrive very quickly, so the actual time required for the multiple energy to decay is small. In very deep water, although the energy decay time is much greater, there may be considerable separation between the wavelets of different orders of multiple. Primaries may actually be seen in the gaps between the multiples. The most difficult conditions for

multiples are therefore mid-range depths (100-300 m) which produce multiples which have small separations between orders but also long duration.

Sea-bottom topography was mentioned above. Essentially, rough sea-floors produce multiples with arrival times, amplitudes and phases which are very difficult to predict. Multiple attenuation then requires routines which are capable of adapting to these data irregularities.

Soft-sediment cover can produce an even more serious problem. It is possible for the water-sediment and sediment-rock interfaces to have comparable reflection coefficients. In this case, there are pegleg multiples produced in the soft-sediment layer which effectively extend the length of the wavelet, so that even the multiples from fairly deep water have wavelet overlap. Figure 2.10 shows a shot gather from off the NE coast of Newfoundland with a very serious soft-sediment problem. The interactions of the multiples and the peglegs completely dominate the entire gather. Since the extended wavelet is due to this interaction, it is time and offset dependent, and as a result it is virtually impossible to design an effective shaping filter. At present, there is no way to attenuate this type of multiple.

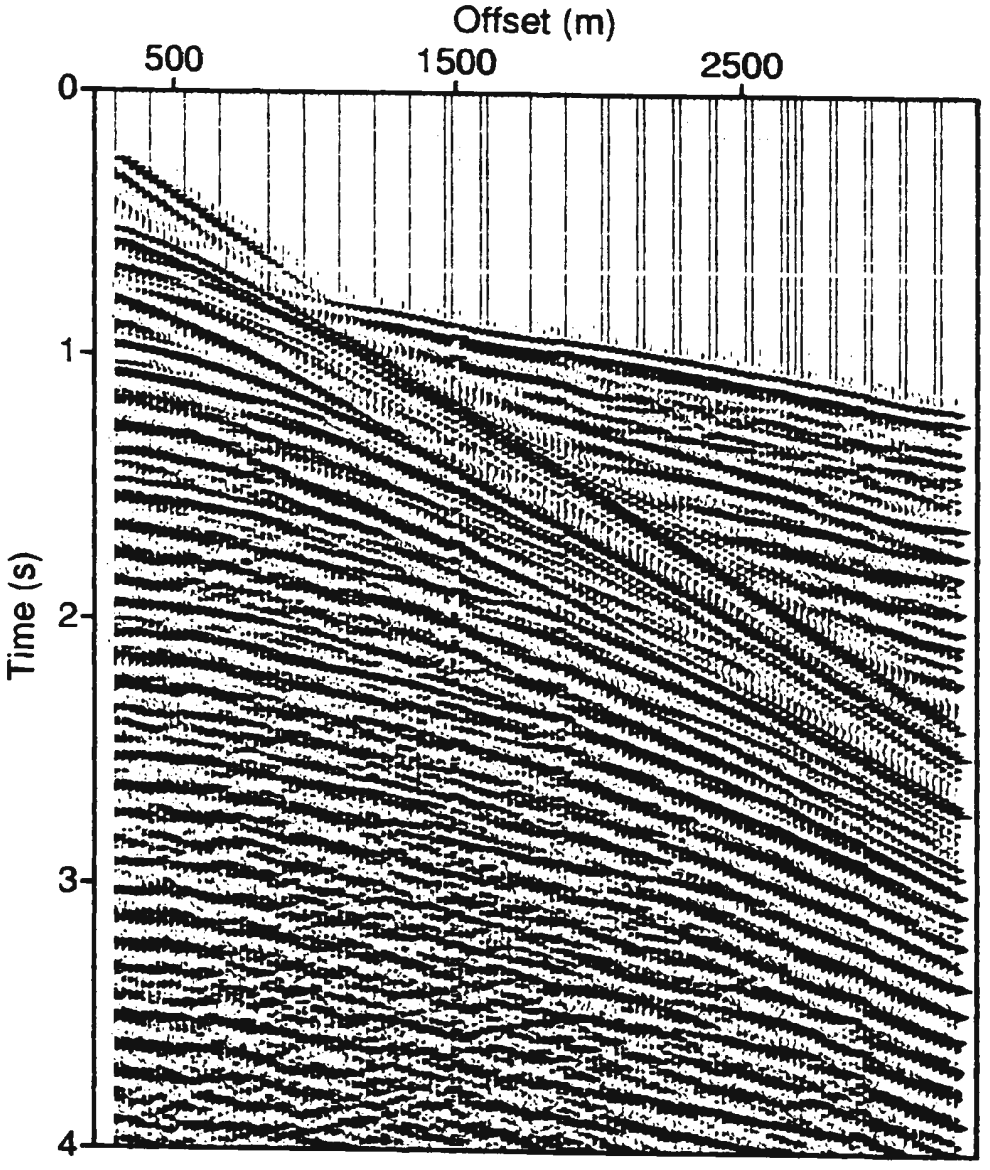

Figure 2.10. Shot gather from 1984 dataset collected off the northeast coast of Newfoundland. Soft sediment cover on the sea-floor produces a water-bottom multiple which is complicated by several peglegs from within the sediments. Refraction arrivals indicate a sediment velocity of 1700 ms^{-1} and a sub-sediment velocity in excess of 5000 ms^{-1}.

3. REVIEW OF CURRENT METHODS

3.1 CMP Stacking

Common mid-point stacking (also sometimes called CDP -- common depth point stacking) is a noise attenuation technique which is applied to virtually all seismic data. It is based on the idea that typical seismic acquisition leads to multiple source-receiver pairs which sample the same 'point' of each reflector (Mayne, 1962). The traces are sorted into 'gathers' according to this source-receiver midpoint (see Figure 3.1). The times are then corrected to account for the different source-receiver offsets using the normal moveout (NMO) equation:

$$t_n = \sqrt{t_o^2 - \frac{x^2}{v^2}} \tag{3.1}$$

where t_n is the NMO corrected time, t_o is the original time, x is the shot-receiver distance and v is the NMO velocity of the reflector. If the correct NMO velocity is chosen, the primary arrivals should line up, as shown in Figure 3.1b. Summing all the traces at a constant time then serves to increase the amplitude of the real arrivals, relative to the random noise. In theory, the improvement in the signal to random noise amplitude ratio should be equal to the square root of the number of traces which are stacked. In practice, however, the improvement is somewhat less, due to trace to trace inconsistencies in the wavelet, misalignment of the events and coherency of the noise.

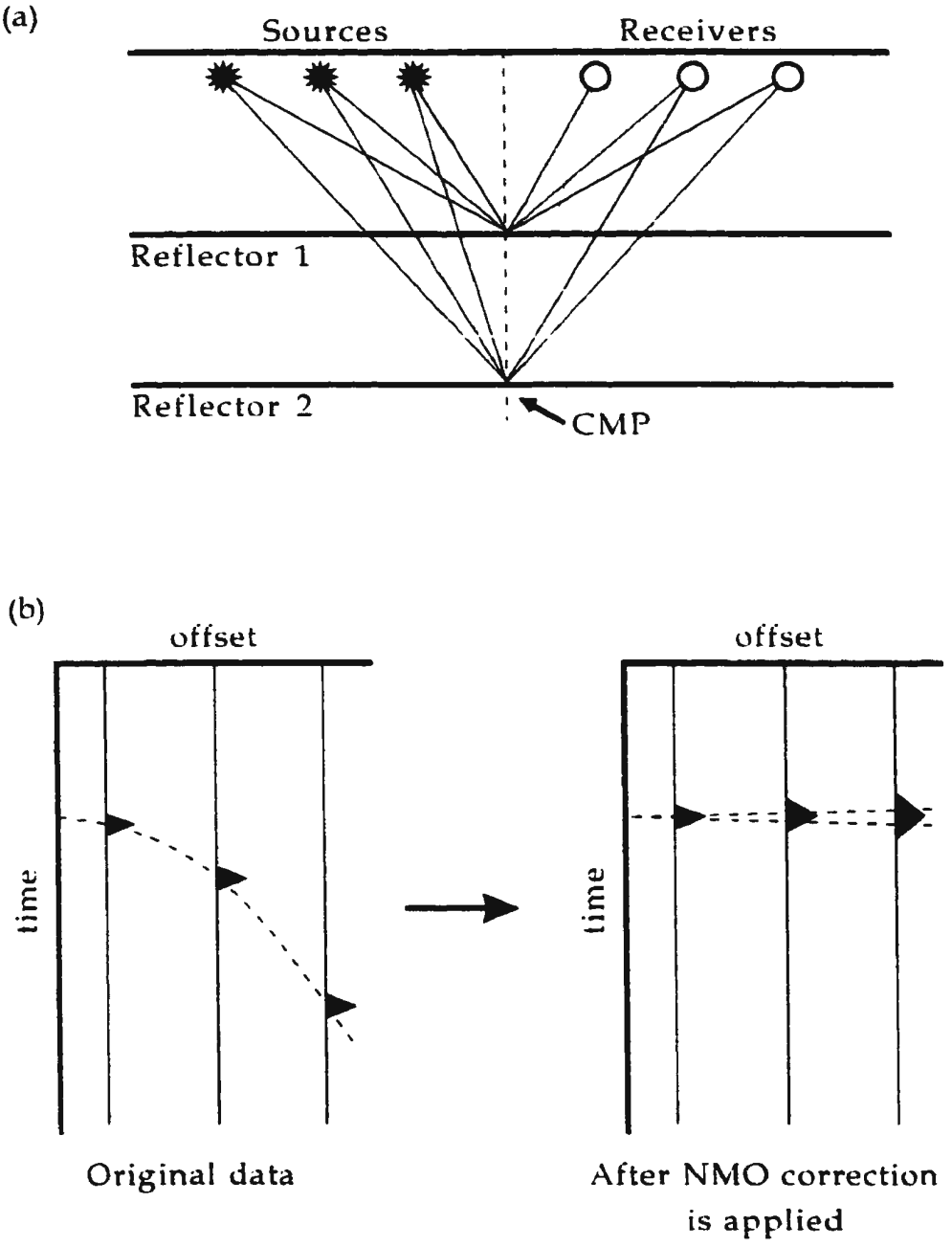

Figure 3.1. Illustration of basic stacking principles. (a) shows how all the traces in a CMP gather sample the same point on each reflector (for flat reflectors). (b) shows how the application of an NMO correction should align the primary arrivals, and how the wavelet is stretched on the far traces.

In marine data, the sources and receivers behave very consistently along a profile, so there tends to be very little variation in the source-receiver wavelet response on the original traces. However, the process of applying NMO, in preparation for stacking, causes the wavelet to change quite significantly from trace to trace, particularly in the first second of data. When the correct NMO velocity is applied to zero phase data (see Figure 3.2a), stacking produces near-optimal improvement in the signal to noise ratio regardless of the stretch, although the resulting stacked wavelet clearly has a lower frequency content than the original. Minimum and mixed phased wavelets, on the other hand, are seriously affected by NMO stretch (see Figure 3.2b). Stacking traces which have a stretch greater than 150% provides very little improvement in the signal to noise ratio, while degrading the spectral bandwidth. As a result, data which require an NMO stretch greater than 150% are typically muted.

The stack is much more seriously affected by the misalignment of the primary events. This is generally caused by a poor choice of stacking velocities, although statics problems and non-flat reflectors can also play an important part. Figure 3.3 shows the stacking response corresponding to a range of timing errors for a 24 fold stack at four different frequencies. The timing errors are defined to be zero at the source, increasing linearly to a maximum at trace 24. Frequency is clearly a major factor, with high frequencies having a much lower response than

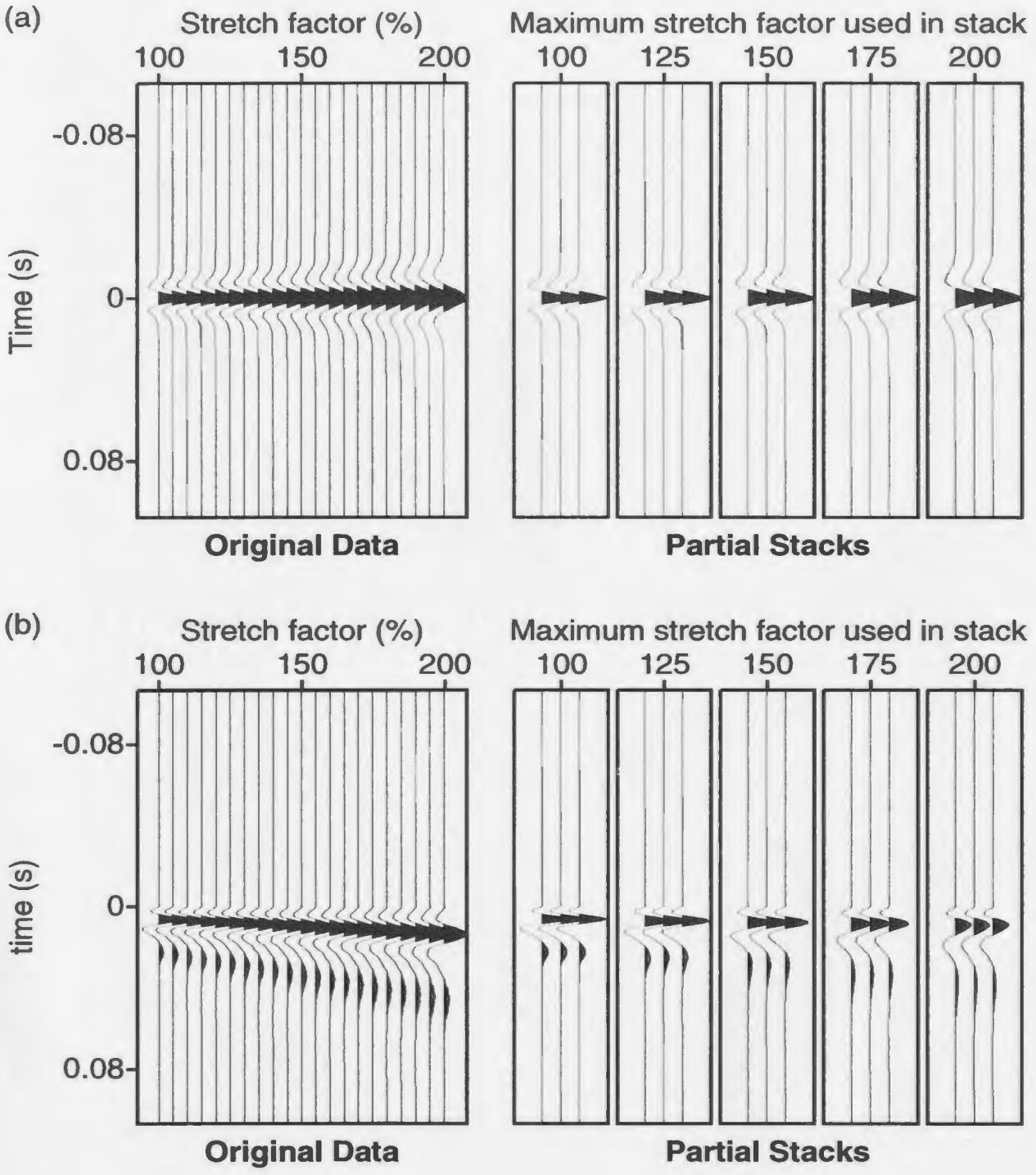

Figure 3.2. Illustration of the effects of NMO stretch on the stack for a zero phase wavelet (a) and a mixed phase wavelet (b).

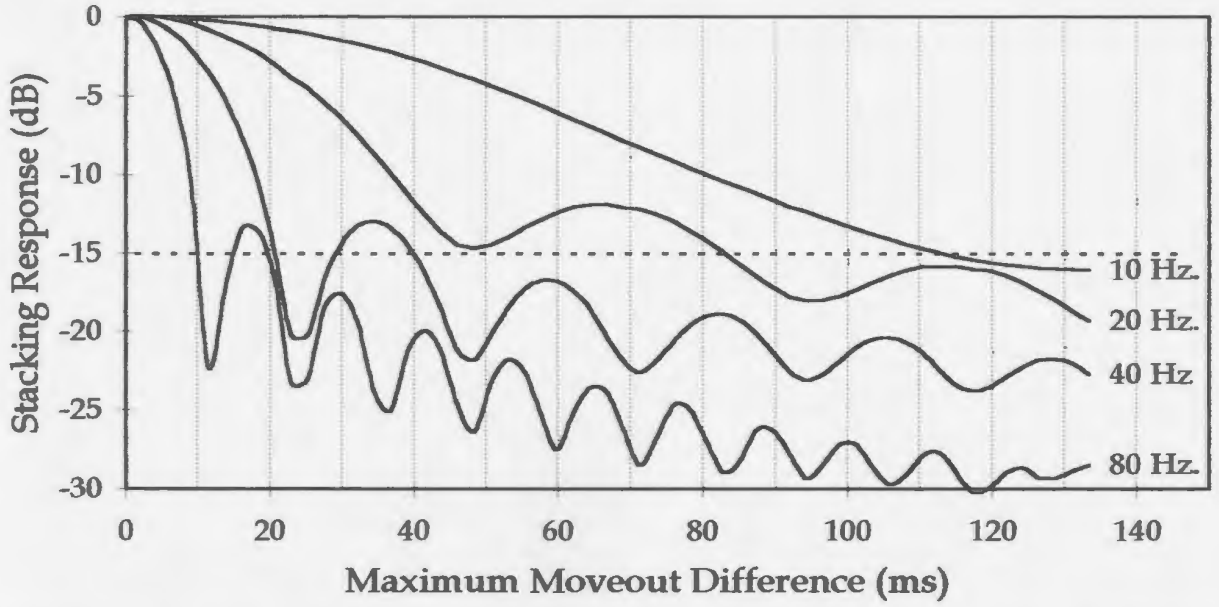

Figure 3.3. The stacking response which corresponds to a range of timing errors for a 24 fold stack at four different frequencies. For comparison, the dashed line shows the optimal attenuation of random noise. The moveout differences were linear with no error at zero offset.

low frequencies. At 10 ms, the 80 Hz response has dropped below the noise response, effectively eliminating the benefits of stacking. At the same time shift, the 40 Hz component has been reduced by 2.5 dB, implying a 25% reduction in the signal to noise ratio, which is equivalent to a fold reduction of almost 50%. The 10 and 20 Hz components, on the other hand, are virtually unaffected by a 10 ms moveout difference.

Figure 3.4 shows the moveout differences associated with velocity errors for two different events. If we assume that the stack uses a full 3000 m spread of receivers, the 2500 ms^{-1} event produces a moveout difference of 10 ms when the velocity error is roughly 25 ms^{-1}, while the 1500 ms^{-1} event produces the 10 ms

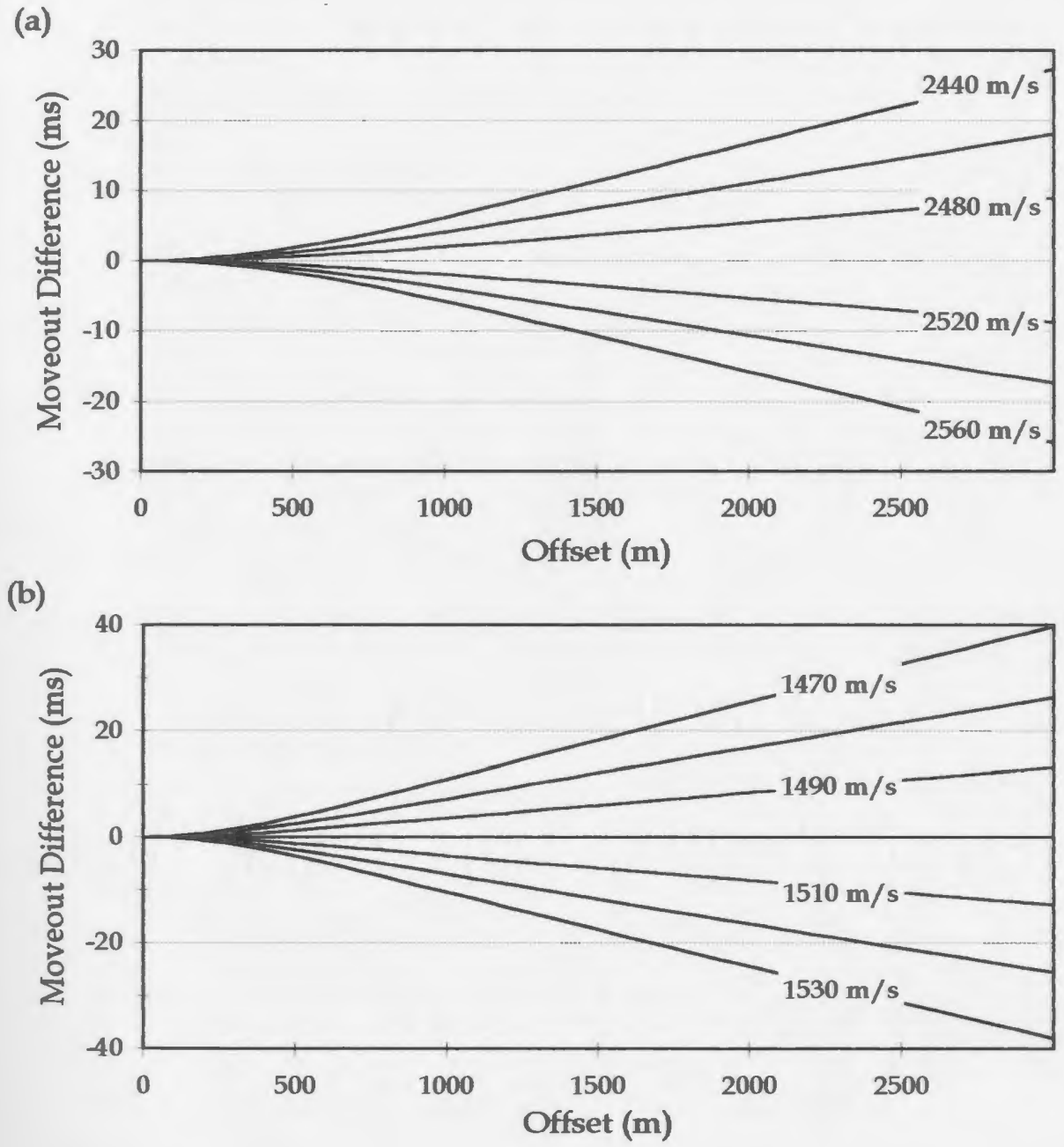

Figure 3.4. The errors in the NMO correction which are introduced by velocity errors for an event at 0.5 seconds with a real velocity of (a) 2500 ms^{-1} and (b) 1500 ms^{-1}.

misfit when the velocity error is only 8 ms^{-1}. This emphasizes the need for accurate velocities, especially for low velocity reflectors. It also illustrates the

fact that events such as sea-bottom multiples, which have velocities that are significantly different from the primary velocities, will not stack constructively.

Figure 3.5 shows the effect of applying NMO velocities to a shot gather. The primaries are aligned perfectly, while the multiples are under-corrected. Clearly, as the primary velocities increase, so does the moveout difference and hence the stack becomes more effective at attenuating the multiples. Unfortunately, due to the hyperbolic nature of reflections, all velocities have very little moveout near the source. As a result, the moveout difference on the near traces is usually insufficient to attenuate high amplitude multiples. Figure 3.6 (a) shows the effect of excluding the first four traces, with offsets up to 400 m, on the stacking response of a 1500 ms^{-1} multiple for a range of primary velocities. The straight stack gives a maximum attenuation of about 15 to 20 dB. The effect of the near trace mute is somewhat irregular, but it does generally give some improvement over the straight stack, potentially up to an additional 15 dB, although it is heavily dependent on the frequency content of the wavelet.

Offset dependent weighting before the stack can give similar results (Tsai, 1985). By emphasizing the far offsets, the stack is more affected by the part of the data which has the greatest moveout differences. Figure 3.6 (b) shows the amplitude response of a linear weighting scheme which ranges from 1 at the near offset to 2 at the far offset. This technique is somewhat more consistent

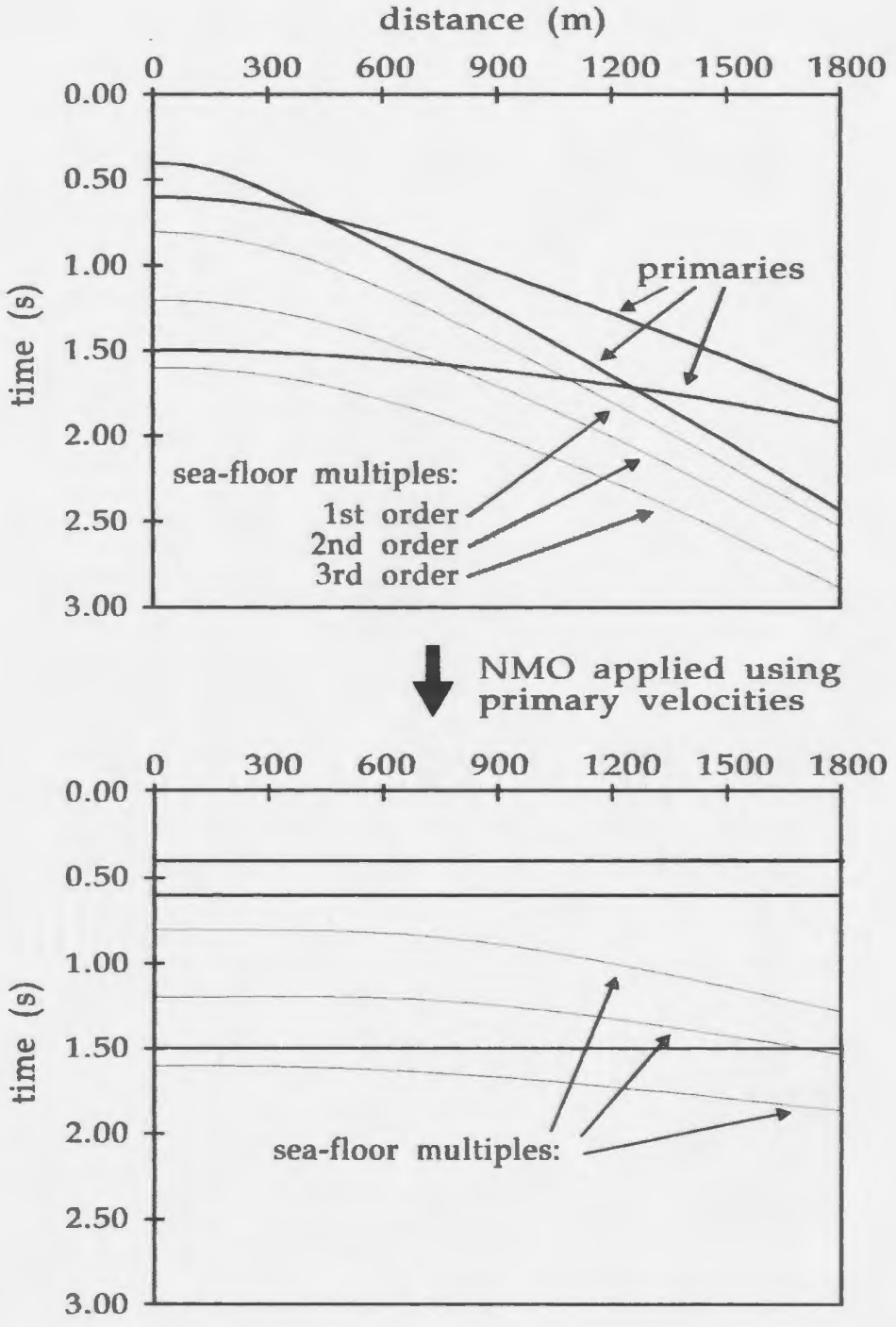

Figure 3.5. The effect of NMO application on primaries and sea-floor multiples (the problems associated with NMO stretch have been ignored). After NMO, the primaries are horizontal, and will therefore stack constructively, while the multiples have residual moveout and will be attenuated.

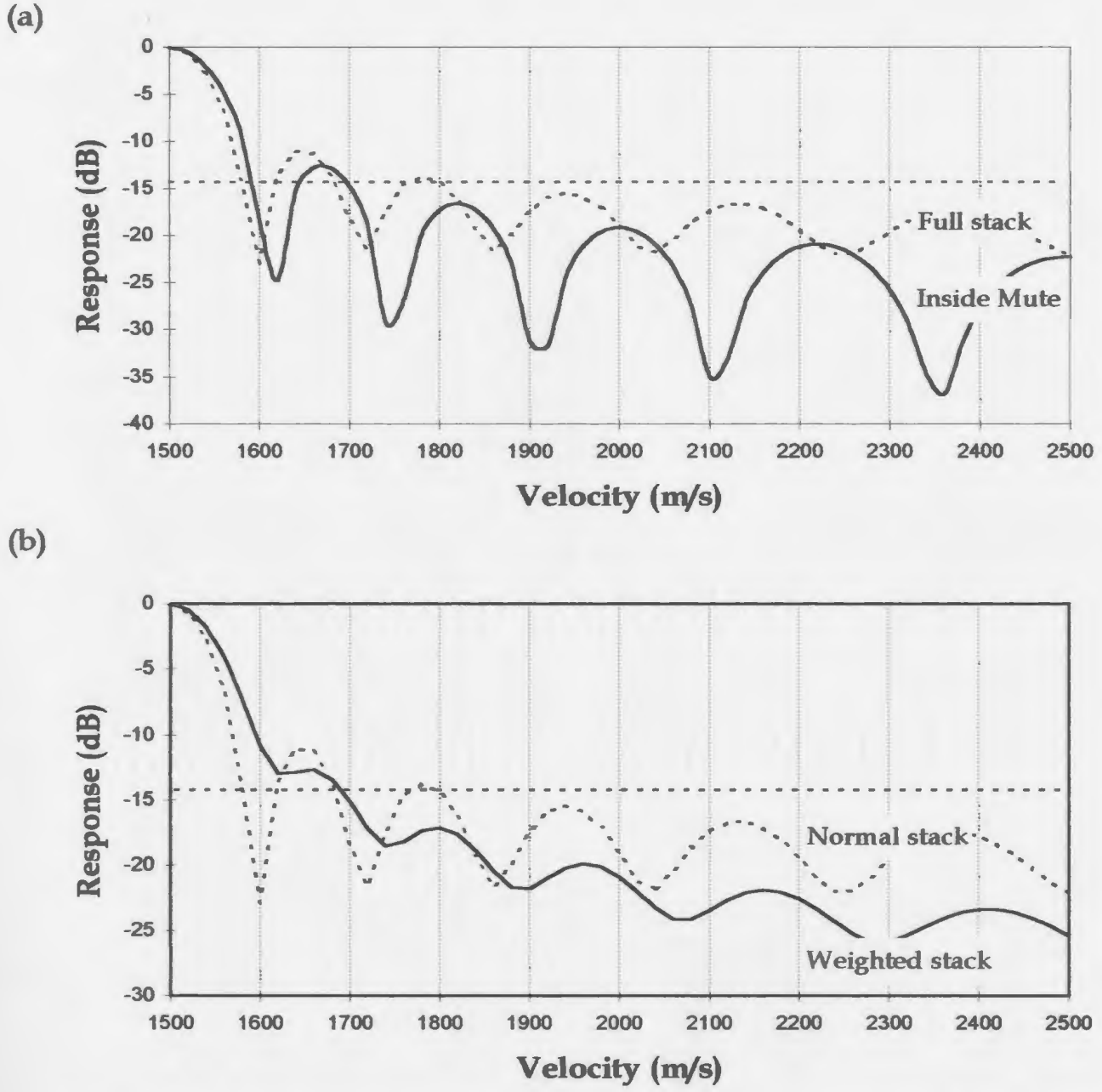

Figure 3.6. Stacking response as a function of velocity for a 1500 ms^{-1} event at 0.5 seconds. a) compares the full 24-fold stack to a stack in which the 4 traces nearest the shot were muted, while b) compares the normal full stack to a weighted stack which uses linear weighting factors, 1 on the near trace and 2 on the far trace.

than an inside mute, giving an attenuation improvement of about 5 dB over the normal stack, provided the primary velocities are greater than 1750 ms^{-1}. A related approach is the use of multi-channel filters, which determine pre-stack weighting functions based on an estimate of the multiple moveout (e.g. Schneider et al., 1965; Buttkus, 1979). These essentially attenuate the multiples by simply scaling down the parts of the data which lie along the multiple trajectories. The performance is clearly dependent on how well the multiples stay within the estimated multiple windows. In addition, depending on the width of the windows used in assessing the weighting function, it can cause serious attenuation of the primaries.

Although stacking is very effective at reducing the amplitude of the sea-bottom multiples, the multiple amplitudes can be so high that 20 dB attenuation is not sufficient. The critical angle of the seafloor reflections is often low enough that several orders of multiples have post-critical arrivals. As a result, some of the multiple arrivals can have amplitudes which are several orders of magnitude greater than the primaries. The moveout difference is usually sufficient that these arrivals do not stack constructively, but instead smear the energy across a much wider time window. The net effect is a broad patch of coherent noise on the post-stack traces that completely mask any primary energy (see Figure 3.7).

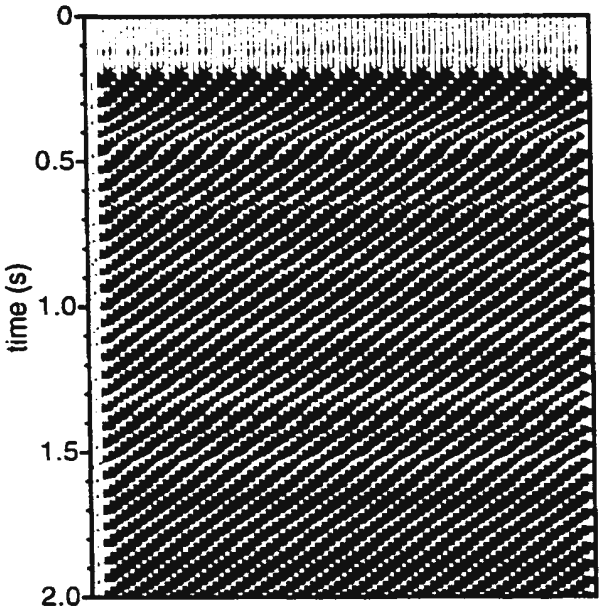

Figure 3.7. The result of stacking high amplitude multiples. The steeply-dipping, coherent noise is caused by the poor attenuation of near-critical sea-floor multiples.

Unfortunately, the only solution is to mute the part of the data which contains post-critical multiples.

In order to compare the effectiveness of some of the attenuation routines, a synthetic data set (see Figure 3.9) was constructed using the velocity and density model shown in Figure 3.8. The sea-bottom multiples and the associated peglegs dominate the pre-stack gather, making it very difficult to pick out the actual primaries. The synthetic gather was then stacked using the optimal stacking velocities and a linear top mute which went from 0.15 seconds on the near trace to 1.3 seconds on the far trace. The stacked trace was then repeated to give the appearance of a stacked section, as shown in Figure 3.10. For comparison, a

depth (m)	velocity (ms^{-1})	density (kgm^{-3})
50	1500	1000
300	1750	2000
400	1900	2200
550	2000	2300
600	2100	2300
700	2300	2400
825	2400	2400
1050	2600	2500
1150	2800	2500
	3000	2600

Figure 3.8. velocity and density model used to generate synthetics for multiple attenuation testing.

primaries-only stack was also performed, and that is presented beside the full stack. The stacked traces show a considerable improvement in the primary-to-multiple amplitude ratio, with the primaries now clearly visible. However, there are also quite a number of multiple events which have comparable amplitudes. Apparently, stacking alone does not provide sufficient attenuation to produce a good interpretable section.

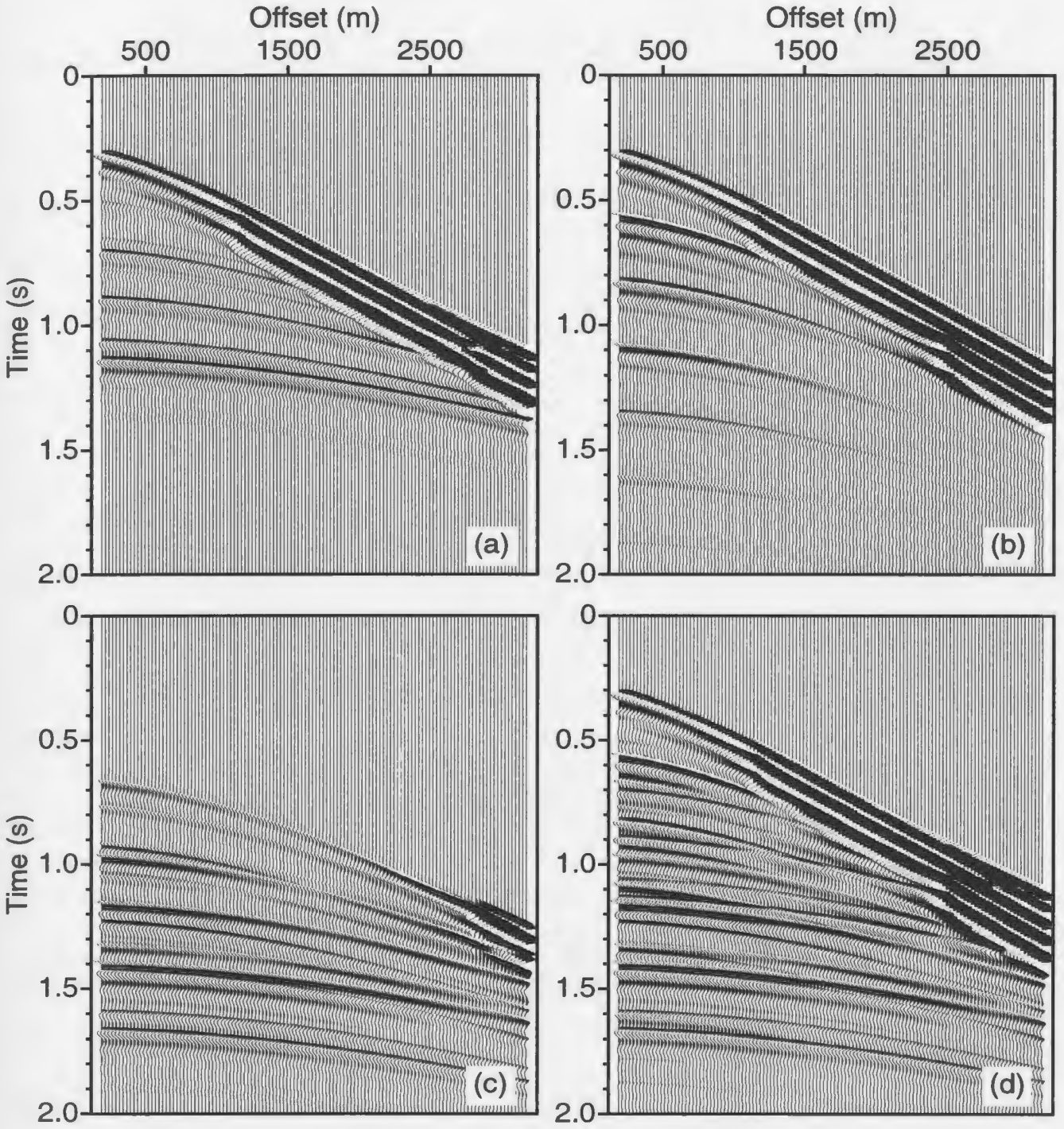

Figure 3.9. Synthetic shot gather generated by raytracing, using the model in Figure 3.8. a) shows the primary arrivals, b) shows the sea-floor multiples, c) shows the interbed peglegs, and d) shows the full shot gather.

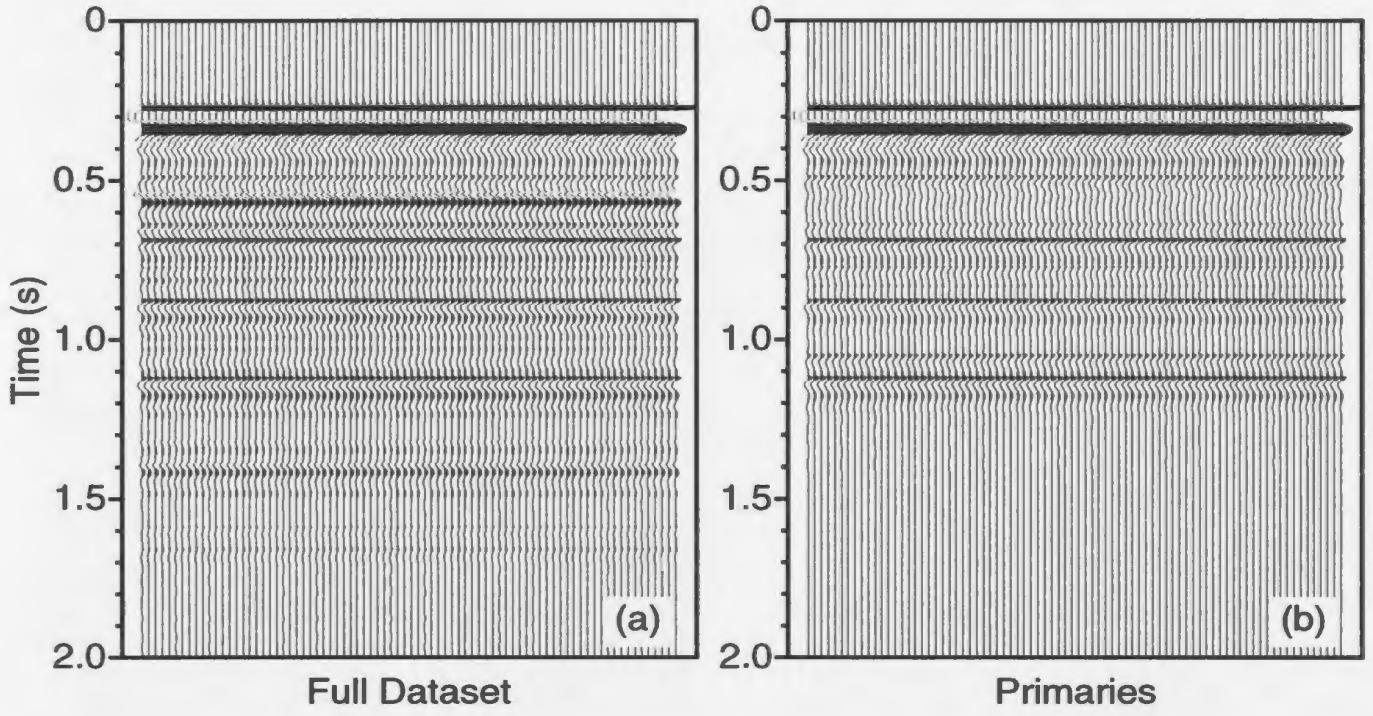

Figure 3.10. The results of stacking the synthetics in Figure 3.9. a) shows the stack using the full gather, while b) shows a stack of only the primary events.

3.2 Inverse Filtering (Predictive Deconvolution)

A convolutional model of seismic data suggests that a seismic trace is the result of the convolution of a source wavelet with a spike sequence representing the primary and multiple reflection coefficients:

$$d(t) = [p(t) + m(t)] * w(t) + n(t) \tag{3.4}$$

where $d(t)$ is the data, $p(t)$ is the primary reflectivity, $m(t)$ is the multiple reflectivity, $w(t)$ is the wavelet and $n(t)$ is random noise (see Figure 3.11). The model assumes that the wavelet is stationary (has the same frequency content throughout - no dispersion). The objective of seismic processing is therefore to remove the effects of the wavelet, the multiples and the noise, in order to produce an estimate of the primary reflectivity.

Deconvolution is a signal-shaping procedure which uses a knowledge of the source wavelet to design a filter which changes the wavelet into a more desired form (typically a spike). In practice, knowledge of the source wavelet may be absolute (i.e. when a wavelet has actually been extracted from the data using synthetic seismograms) or may simply be a statistical estimate based on the autocorrelation of the trace. Deconvolution can be used to convert the wavelet into a spike (spiking decon), any arbitrary wavelet (wavelet shaping) or to a time delayed form of the same wavelet (predictive decon). It is this last type which

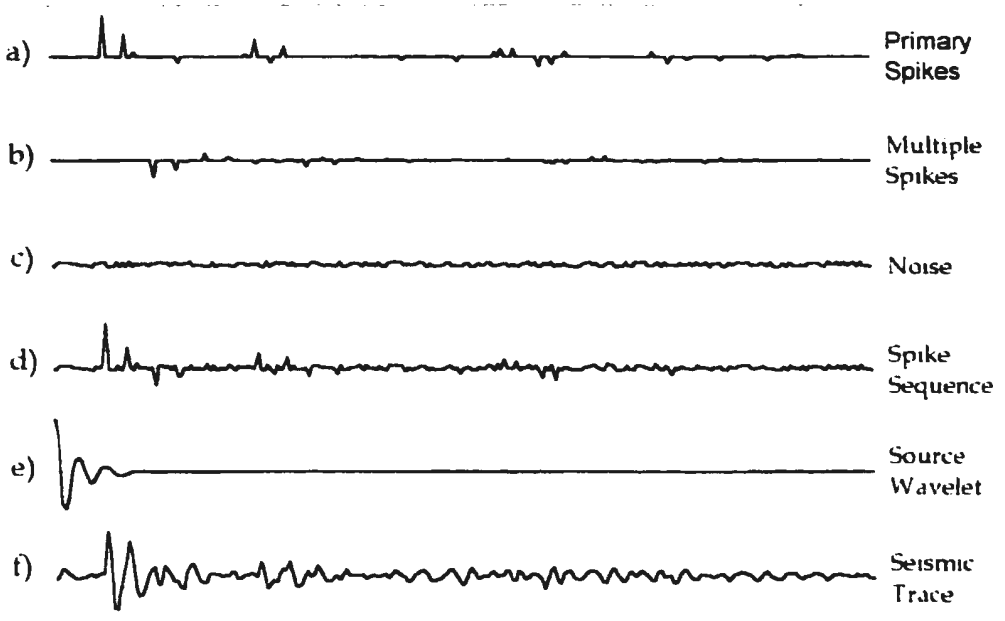

Figure 3.11. The convolutional model of a seismic trace. The trace (f) is produced by convolving a stationary wavelet (e) with a spike sequence (d) made up of primaries (a), multiples (b) and random noise (c).

can be used for multiple attenuation.

It is relatively easy to construct a filter which simply advances a time series forward in time by one multiple period. Robinson and Treitel (1980) show that the 'prediction filter' can be formulated as an optimum filter, which minimizes the least squares error between the observed and predicted data, by solving the set of equations:

$$\begin{bmatrix} r_0 & r_1 & r_2 & \cdots & r_{n-1} \\ r_1 & r_0 & r_1 & \cdots & r_{n-2} \\ r_2 & r_1 & r_0 & \cdots & r_{n-3} \\ \vdots & \vdots & \vdots & \ddots & \vdots \\ r_{n-1} & r_{n-2} & r_{n-3} & \cdots & r_0 \end{bmatrix} \begin{bmatrix} a_0 \\ a_1 \\ a_2 \\ \vdots \\ a_{n-1} \end{bmatrix} = \begin{bmatrix} r_a \\ r_{a+1} \\ r_{a+2} \\ \vdots \\ r_{a+n-1} \end{bmatrix} \tag{3.5}$$

where r_i is the ith lag of the autocorrelation of the data, a_i is the ith element of the prediction filter, n is the length of the filter and α is the desired delay, generally called the prediction lag. If the multiple period is constant, the multiple component of the data can be estimated by convolving the filter with the data and applying the desired delay time. The multiple attenuated data can then be determined by subtracting the multiples from the original data. This can all be done at the time by applying a modified filter, called the 'prediction error filter':

$$pef = \{1, \underbrace{0,0,\ldots 0}_{\alpha-1}, -a_n, -a_1, -a_2, \ldots\} \tag{3.6}$$

If we assume that the multiples are regularly spaced and that the reflection coefficient, R, is constant, then $r_{\alpha-1} = -R \cdot r_0$. Equation 3.5 then implies that the prediction filter is simply a spike with amplitude -R, and as a result, the prediction error filter is a basic feedback filter:

$$pef = \{1, \underbrace{0,0,\ldots 0}_{\alpha-1}, R, 0, 0, 0, \ldots\} \tag{3.7}$$

Provided all of the assumptions about the data (stationary wavelet, constant reflection coefficient, constant multiple period) are met, predictive deconvolution should be able to remove all of the multiples. However, the choices of prediction lag and operator length are critical.

Figure 3.12 shows the attenuation of multiples by predictive deconvolution using a range of prediction lags and operator lengths. The maximum attenuation

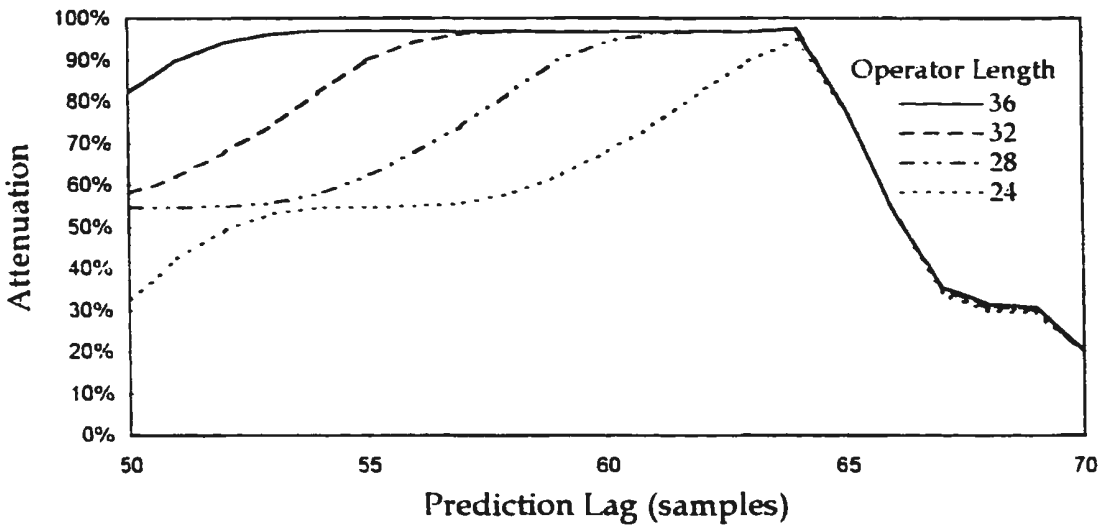

Figure 3.12. The multiple attenuation of predictive deconvolution as a function of operator length and prediction lag. The multiple interval was 64 samples and the wavelet length was 24 samples.

occurs when the prediction lag is equal to the multiple period, regardless of the operator length. This is because, at that lag, the prediction filter is very close to being a spike at zero time, so the operator length essentially just dictates the number of zeroes to pad onto the end of the filter. When the prediction lag is greater than the multiple period, the spike for the prediction filter should be at a negative time, which is obviously not possible. As a result, the filter does not do a good job predicting the multiples, and the attenuation is poor. When the prediction lag is less than the multiple period, the prediction filter simply becomes a time delayed spike, so attenuation is not seriously affected. However,

in order to get a good estimate of the spike amplitude and delay, the effective operator length (that part of the operator which is beyond the spike) has to be long enough to incorporate most of the wavelet energy. As a result the attenuation decays much more quickly with lag error when the operator length is short than when it is long.

In the presence of high amplitude primaries and random noise, the prediction filter may have difficulty determining which part of the trace is multiple and which is not. As a result, the prediction error filter may not produce very good attenuation of the multiples and may actually cause some attenuation of the primaries (see Figure 3.13). A similar problem arises when the multiple period is shorter than the length of the wavelet. The inversion then has trouble distinguishing between energy from one multiple order and another, again causing distortion of the prediction filter. In general, however, this performance limitation is minor compared to problems associated with the basic assumptions predictive deconvolution makes about the multiples.

If it is invalid, the assumption that the reflection coefficient is constant will obviously cause a significant reduction in performance. Figure 3.14 shows the effect of attempting predictive deconvolution when the amplitudes have not been properly corrected for geometric spreading. The least squares procedure finds the optimal filter for the data, but it is biased towards the highest

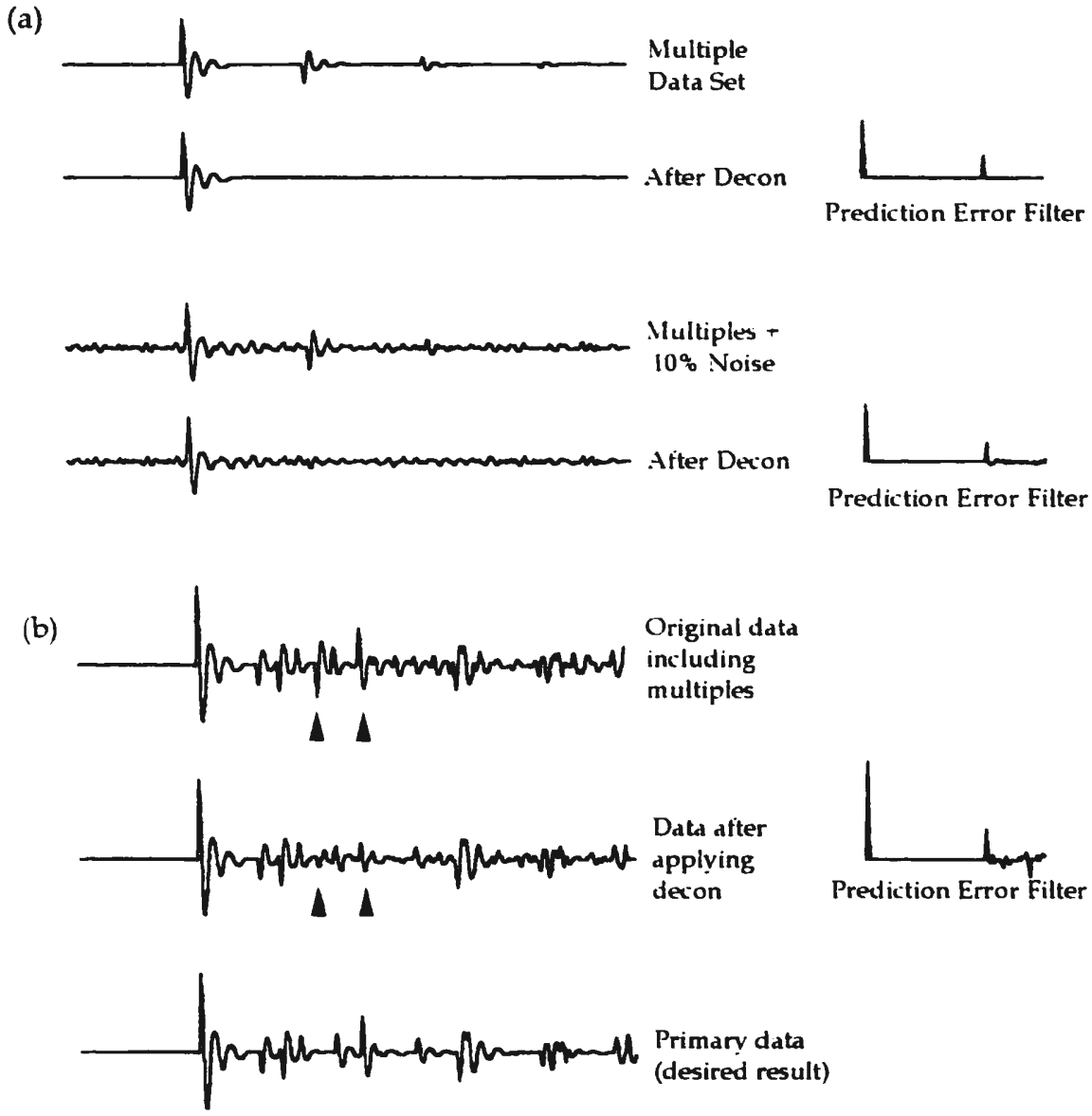

Figure 3.13. The effect of random noise (a) and significant primary energy (b) on filter design and multiple attenuation for predictive decon. The desired prediction filter is shown at the top in (a). The arrows in (b) point to attenuated events, both multiple and primary.

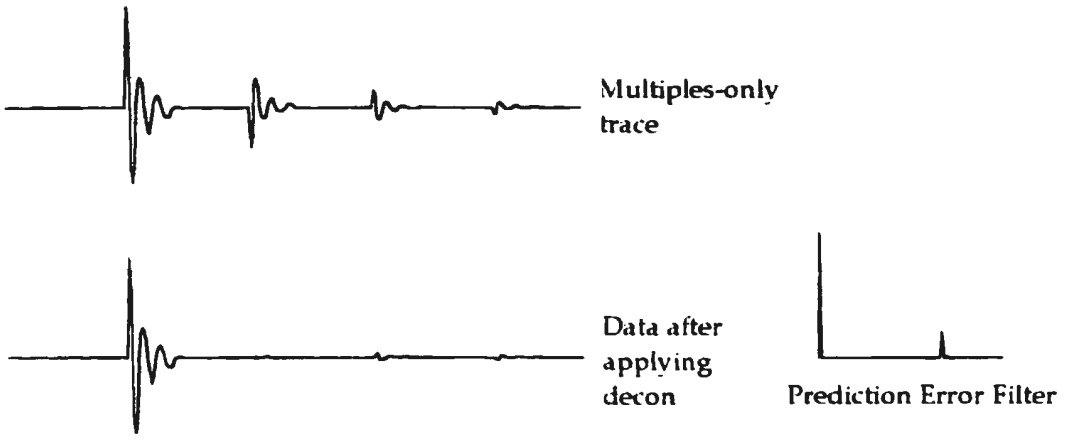

Figure 3.14. The effect of a poor choice of geometric spreading corrections on predictive decon. The prediction filter was designed primarily on the relationship between the primary and the first multiple, so the attenuation is much better for the first multiple than the second and third.

amplitudes, and as a result it is dominated by consideration of the first multiple. As a result, the first multiple is attenuated extremely well, but the filter does an increasingly poorer job on successive multiple orders, as the amplitudes vary farther and farther from the predicted geometric series.

Section 2.3 showed that the geometric-ratio relationship between reflection coefficients for different order multiples only occurs at small source-receiver offsets, even when the seafloor is perfectly flat. Figure 3.15 shows that the amplitude variations between consecutive multiple orders can easily cause a reduction in the attenuation of 25% or more, even on the near trace. With increasing offset, considerable variations in the multiple period as well as severe

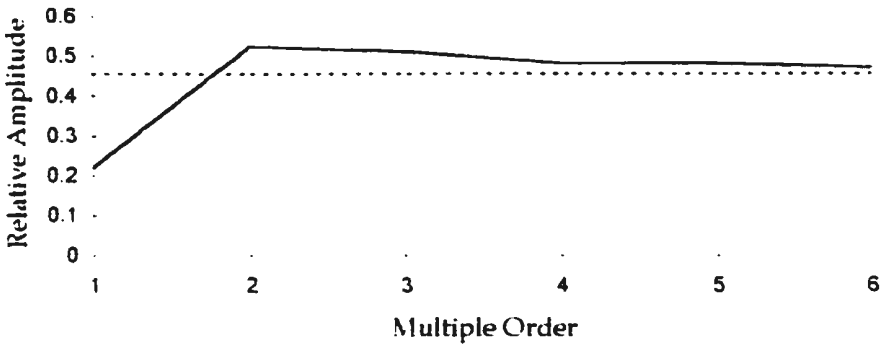

Figure 3.15. The amplitude relationship between consecutive orders of multiples at an offset of 200 m for a water depth of 50 m. Water velocity was 1500 ms^{-1}, while sea-floor velocity was 2000 ms^{-1}. Sea-floor density was 2000 kgm^{-3}. The dashed line shows the constant relationship at zero offset.

amplitude and phase problems greatly reduce the effectiveness of deconvolution. In addition, seafloor topography can make the timing, amplitudes and phases of the multiples even more unpredictable, completely eliminating the effectiveness of predictive deconvolution in pre-stack gathers.

If the multiple period is relatively long, it is sometimes sufficient simply to divide the data up into a number of windows and apply different inverse filters to each window (Clarke, 1968). By only including two or three multiple orders in each window, the prediction filter has a better chance of modelling the changing multiple period. However the shorter design window can cause the inversion to have difficulty distinguishing between primaries and multiples, so there may be some attenuation of primary energy. An alternative is adaptive deconvolution,

in which the deconvolution operator adjusts automatically to the period as it moves down the trace (Griffiths et al., 1977). By calculating a new operator for each point on the trace, both times and amplitudes can be quite well modelled. Although this is somewhat of an improvement over windowed decon, it still has problems with primary attenuation.

In addition to trying to make deconvolution better fit the data, there have been a number of attempts to find a data transform which will cause the data to better conform to the assumptions made by predictive decon. The most basic of these is a simple NMO. Under horizontal seafloor conditions. normal moveout at the water velocity causes the multiples to be perfectly aligned (see Figure 3.16), with a constant multiple period. Following the decon, the moveout is simply removed and reapplied at the primary velocities before stacking. Figure 3.17 shows the effects of applying NMO deconvolution to a synthetic shot gather. It does an excellent job on the near traces, where the amplitudes and phases fit the basic deconvolution assumptions. However, at farther offsets it is not very successful. The NMO stretch causes problems with the stationary wavelet assumption, and as a result, severely stretched arrivals have to be muted. This produces a zone below the mute on which the deconvolution has no effect. In addition, due to differences in their moveout velocities, the pegleg periods are not the same as the simple sea-bottom multiples. This means that predictive

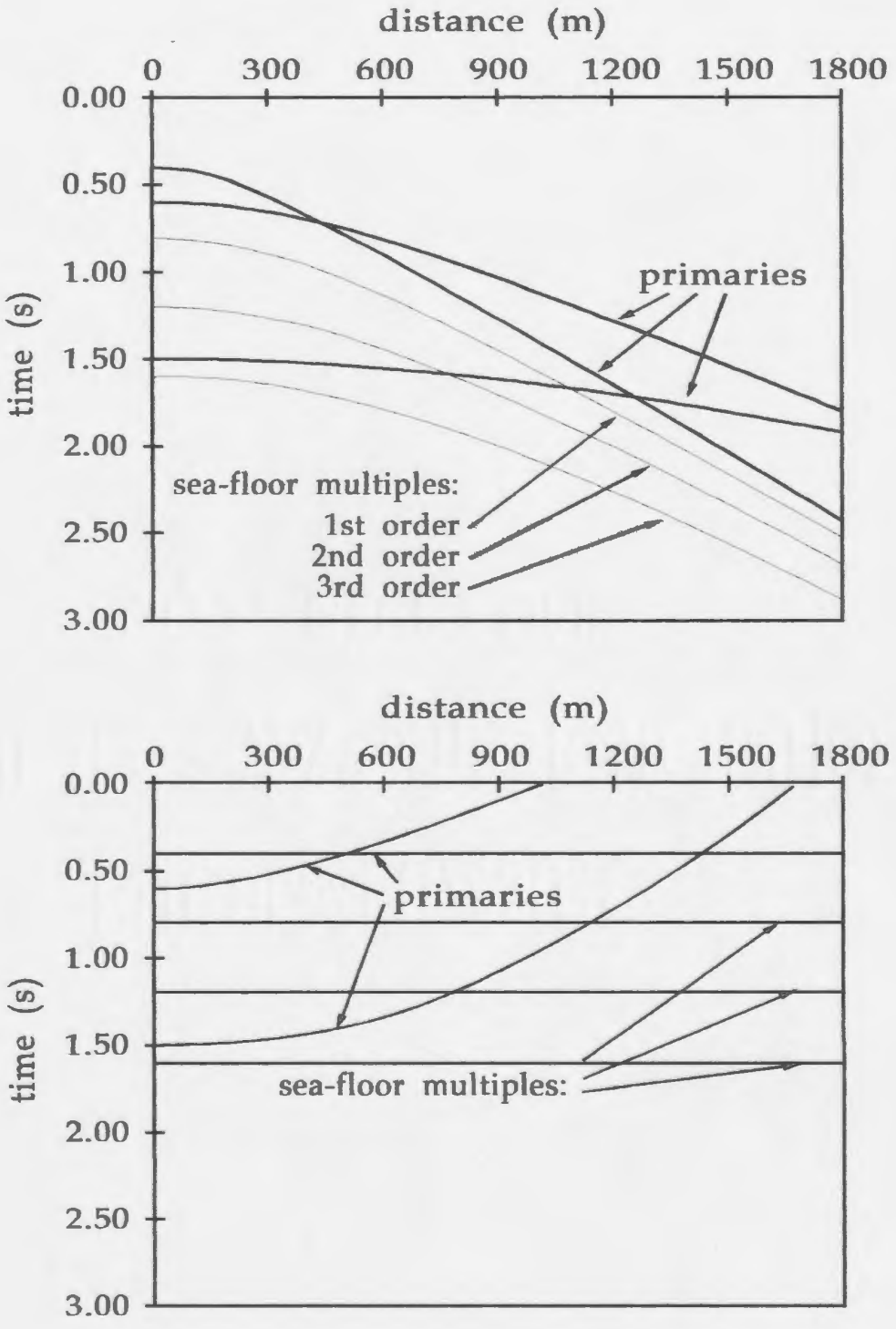

Figure 3.16. The application of NMO using the water velocity. Primaries are over-corrected, but the multiple interval is constant.

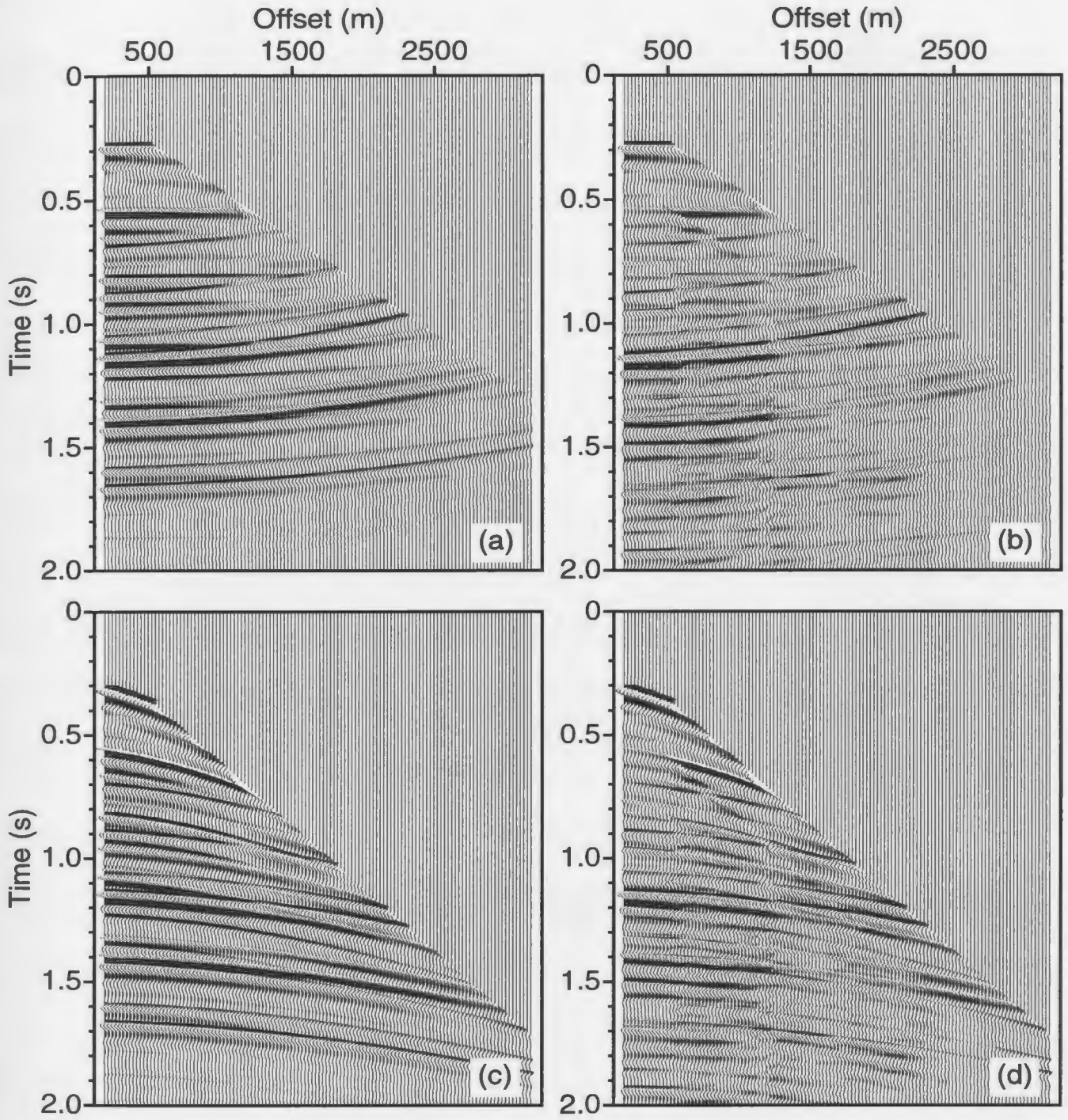

Figure 3.17. NMO decon. (a) shows the gather after NMO has been applied using the water velocity; (b) shows the NMO corrected gather after deconvolution has been applied; (c) shows the original gather; (d) shows the deconvolved gather after the NMO was removed.

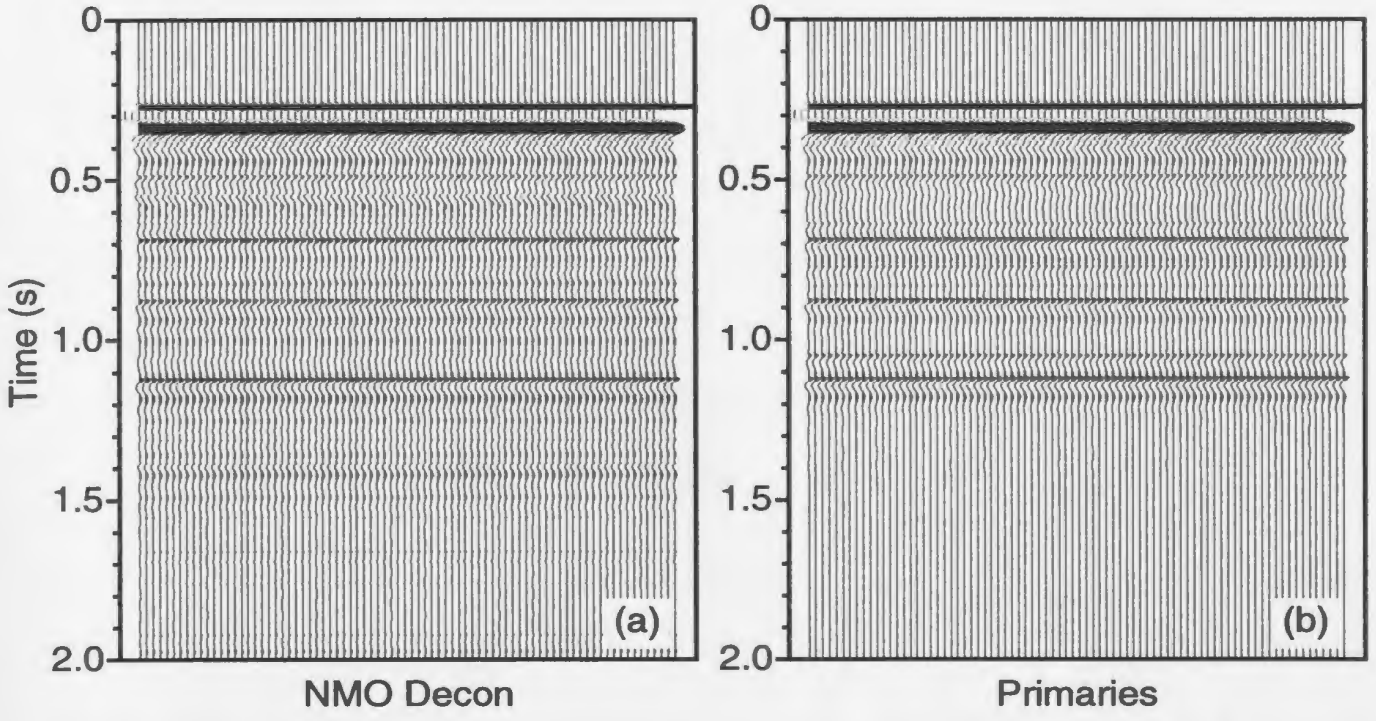

Figure 3.18. NMO deconvolution stack. (a) shows the stack of 3.17 (d), while (b) shows a primaries-only stack. The attenuation of the first multiple (at roughly 0.6 s on Figure 3.10) is very good.

deconvolution on these events is ineffective, and in fact actually causes the addition of noise. However, since stacking already does quite a good job of multiple attenuation at the far offsets, the near offset improvements made by deconvolution do translate into improvements in the stack (see Figure 3.18).

Treitel et al. (1982) showed that predictive deconvolution would be better applied in 'τ-p' space, which is defined by the mapping:

$$\tau = t - p\,x \tag{3.8}$$

where τ is the transformed time, t is the initial time, and x is the shot-receiver

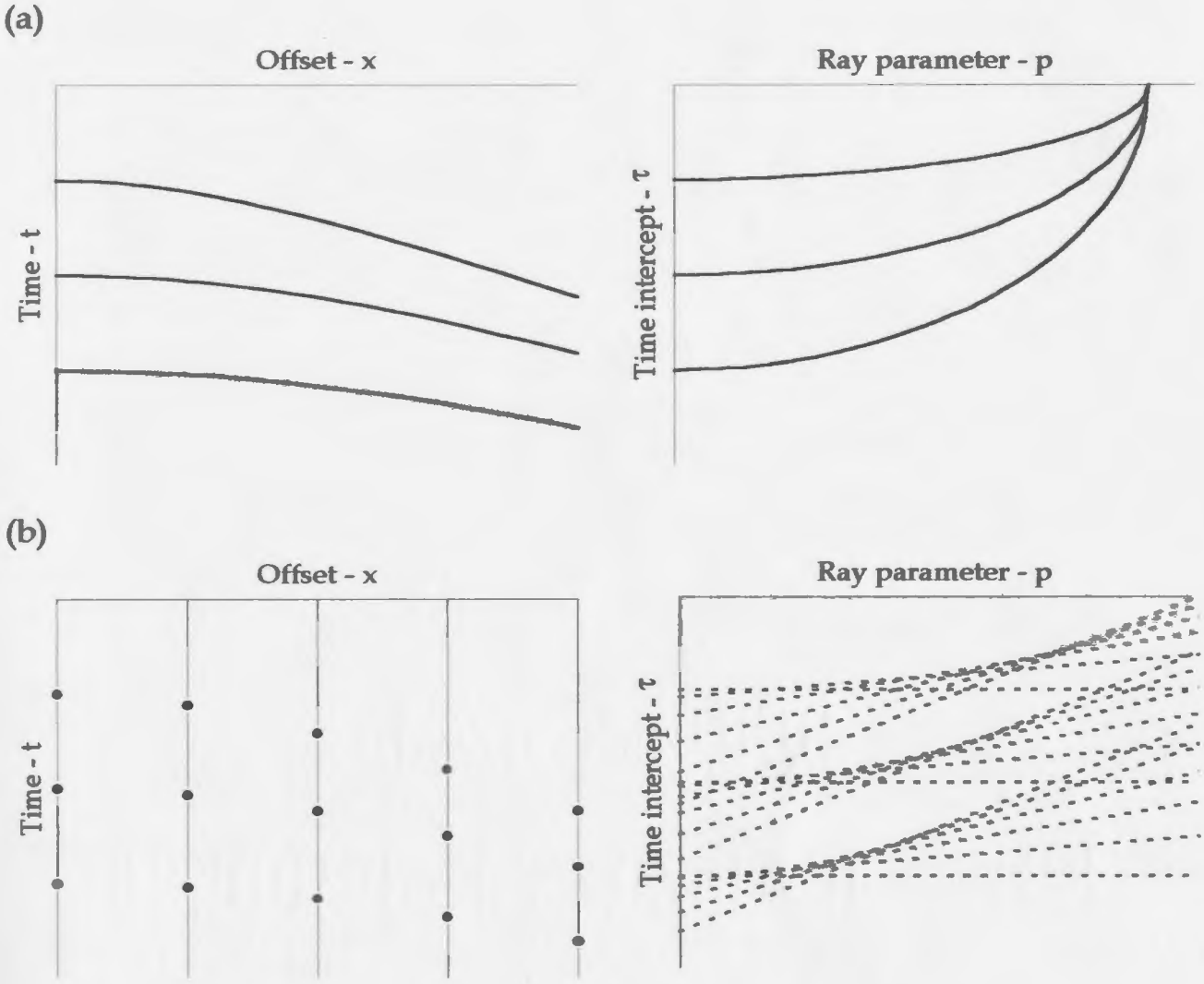

Figure 3.19. The τ-p transform of a shot or CMP gather. a) shows the continuous transform, with the hyperbolic events transforming into ellipses; b) shows the discrete transform, with individual samples transforming into lines.

distance. The 'ray parameter', p, is approximately equivalent to 'slowness', the inverse of velocity. The τ-p transform, often referred to as a 'slant stack', is performed by summing along lines of constant p:

$$v(p,\tau) = \int_{-\infty}^{\infty} u(x, \tau + px)dx \tag{3.9}$$

Treitel et al. (1982) demonstrated that, when the sea-floor is flat, the reflection hyperbolae for the multiples map into ellipses with common p intercepts (see Figure 3.19a). As result, the multiple arrival times on each trace are perfectly periodic. In theory, therefore, τ-p should be the ideal place to perform predictive decon.

Unfortunately, however, predictive deconvolution in τ-p space generally is not very effective, due primarily to the limitations of discrete seismic data. Although continuous hyperbolae are transformed into continuous ellipses, the transform of a discretely sampled hyperbola is much more complicated (see Figure 3.19b). Since each point in x-t space is transformed into a line in τ-p space, the hyperbola is actually transformed into a series of lines. The appearance of an ellipse is only produced as a result of the constructive interference of these lines. While the ellipses themselves are perfectly periodic, the associated lines are not. Predictive deconvolution may do a good job attenuating the multiple energy along the ellipses, but it will not attenuate the lines. This is particularly true at low p values, since the lack of near traces makes it impossible for the transform to properly model the bottom of the ellipse (see Figure 3.20). In addition, there is often a considerable amount of linear noise in the forward τ-p transform caused by localized amplitude peaks, particularly those near the critical offsets.

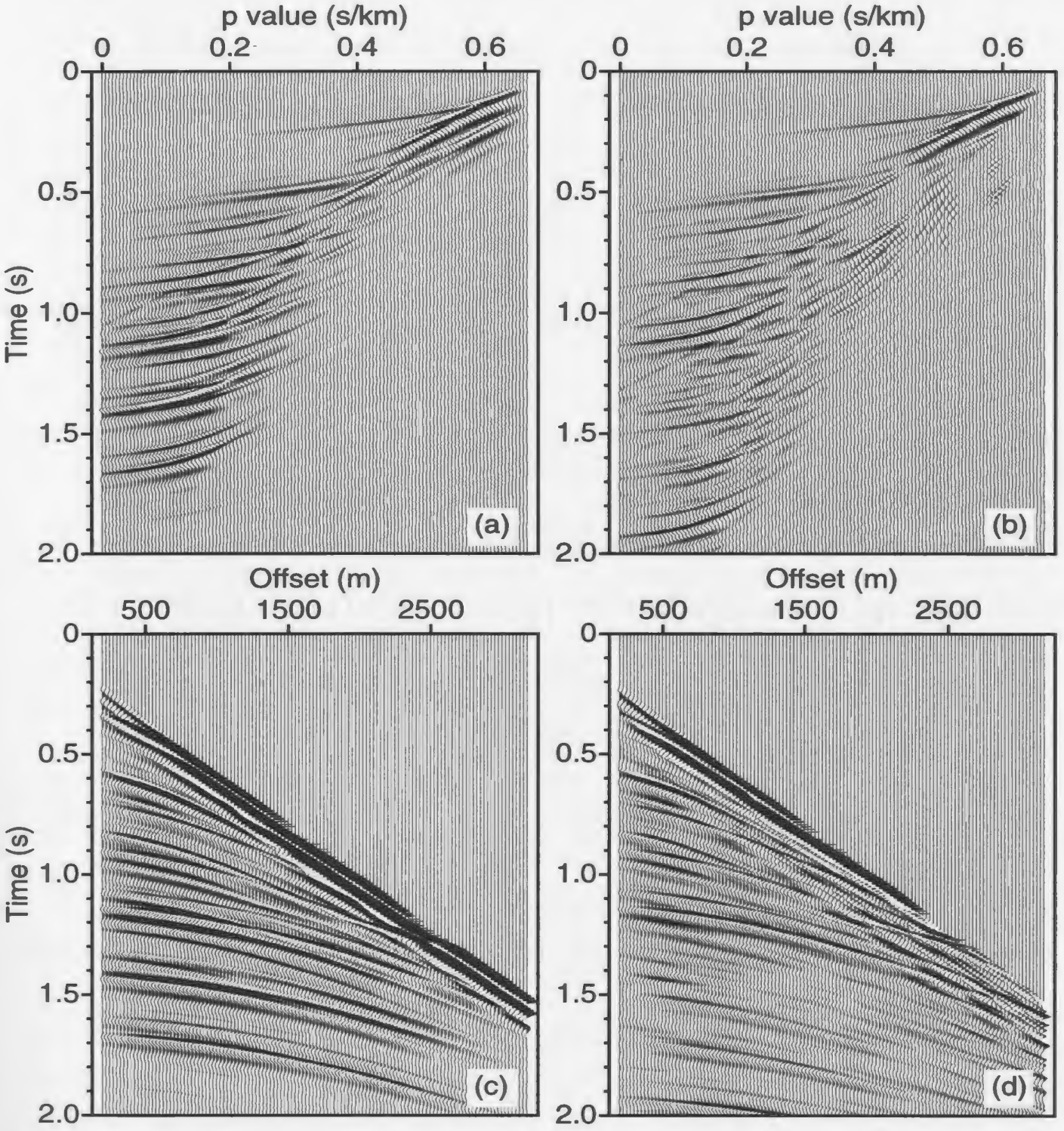

Figure 3.20. τ-p decon. (a) shows the τ-p transform of the gather; (b) shows the τ-p transform after predictive deconvolution has been applied; (c) shows the original gather; (d) shows the restored gather after τ-p decon.

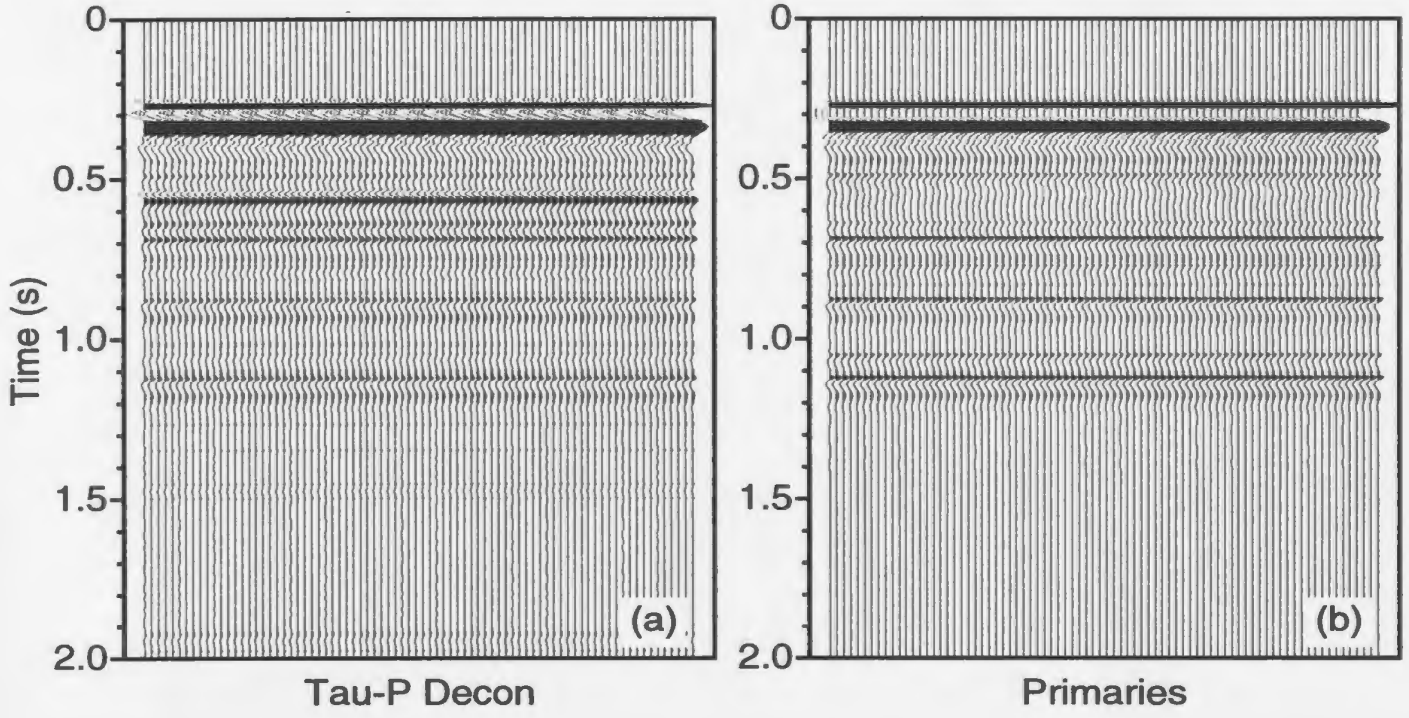

Figure 3.21. *τ-p* deconvolution stack. (a) shows the stack of 3.20 (d), while (b) shows a primaries-only stack. Overall, except for the first multiple, the multiple attenuation is very good, but there is some amplitude distortion.

Since predictive deconvolution assumes that this energy also has multiples, the deconvolution process can actually add quite a lot of noise energy to the data. As a result the stacked results are generally quite disappointing (see Figure 3.21).

In 1980, Taner showed that multiples are also periodic along traces which radiate out from the origin (see Figure 3.22). He pointed out that, for a flat sea-floor, all of the multiple arrivals on each 'radial trace' have the same angle of incidence. As a result, this transform has the added advantage that the reflection coefficient is constant for all orders of multiples on each trace. This means that both the amplitude and phase relationships are consistent and that

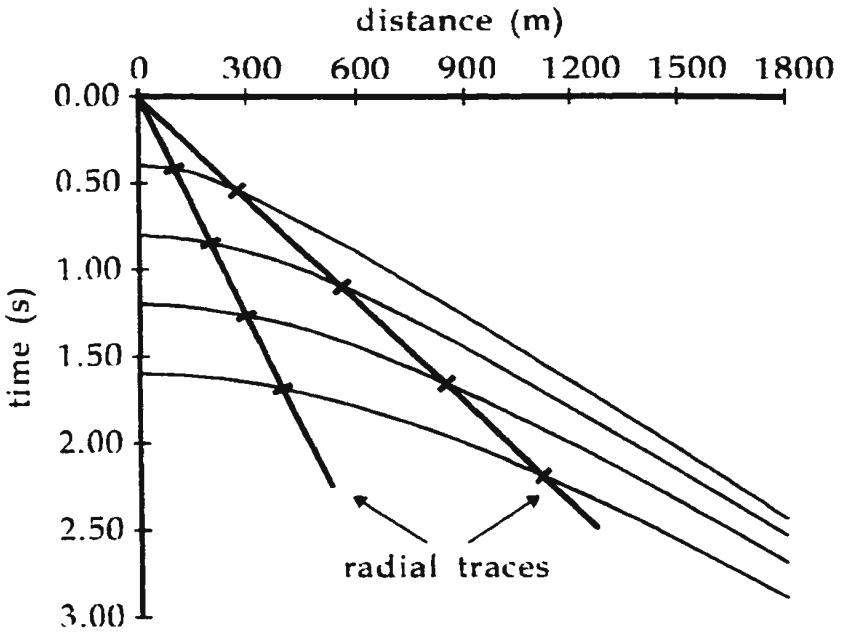

Figure 3.22. The radial trace transform. The re-sampling of a CMP gather into radial traces causes the multiples to have a constant interval on each trace.

deconvolution should be successful even in the post-critical parts of the data (see Figure 3.23).

Unfortunately, this technique also has a number of problems. The spacing of the radial traces inevitably causes over sampling of the top portion of the data and under sampling of the bottom. This can produce major aliasing problems and a loss of information from the deeper parts of the data. In addition, the lack of a zero offset trace means that the near-vertical radial traces have start times greater than the arrival times of the first few multiples. Since predictive

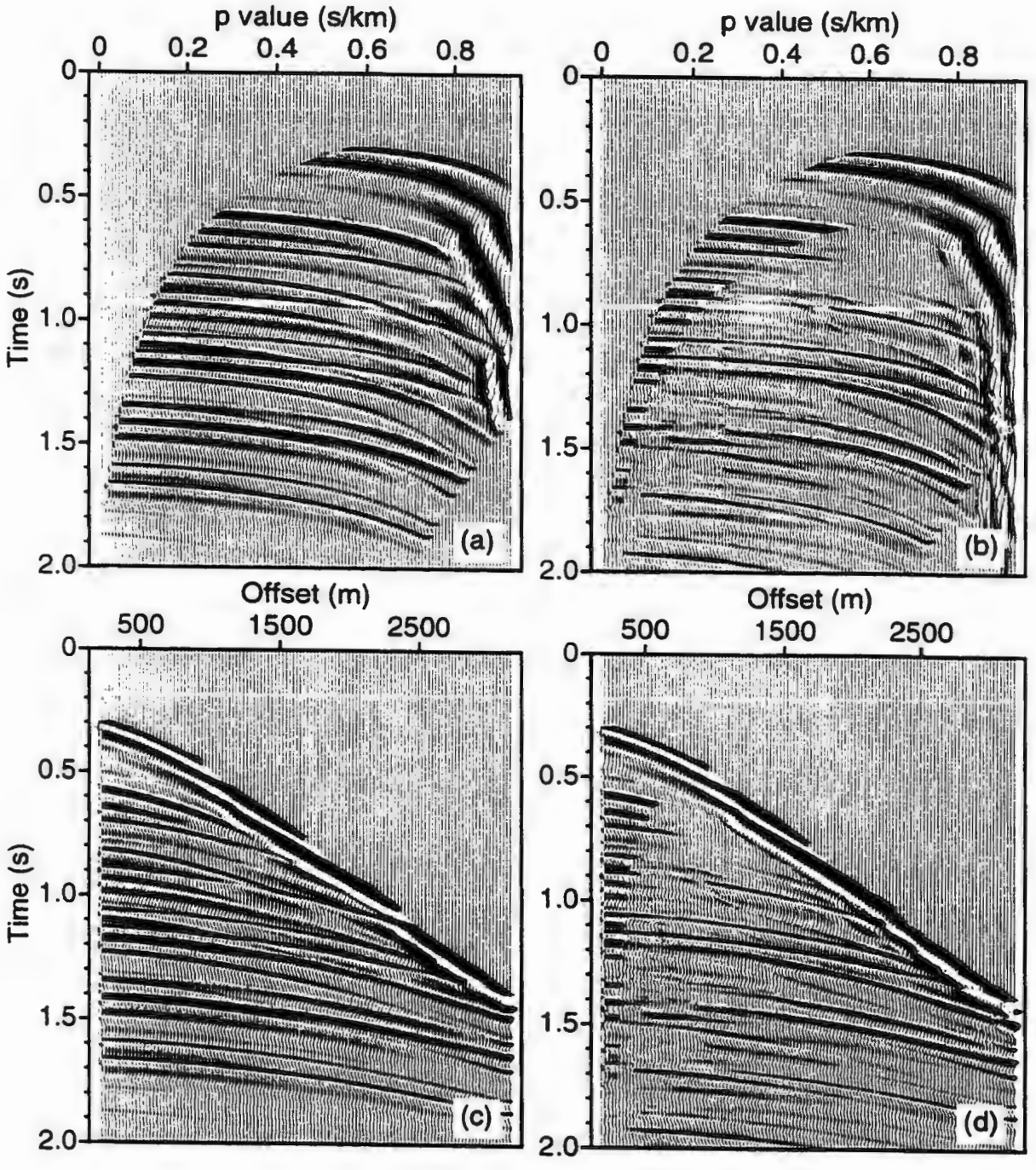

Figure 3.23. Radial trace decon. (a) shows the gather re-sampled into radial traces; (b) shows the radial traces after deconvolution has been applied; (c) shows the restored original gather; (d) shows the restored gather after radial trace decon.

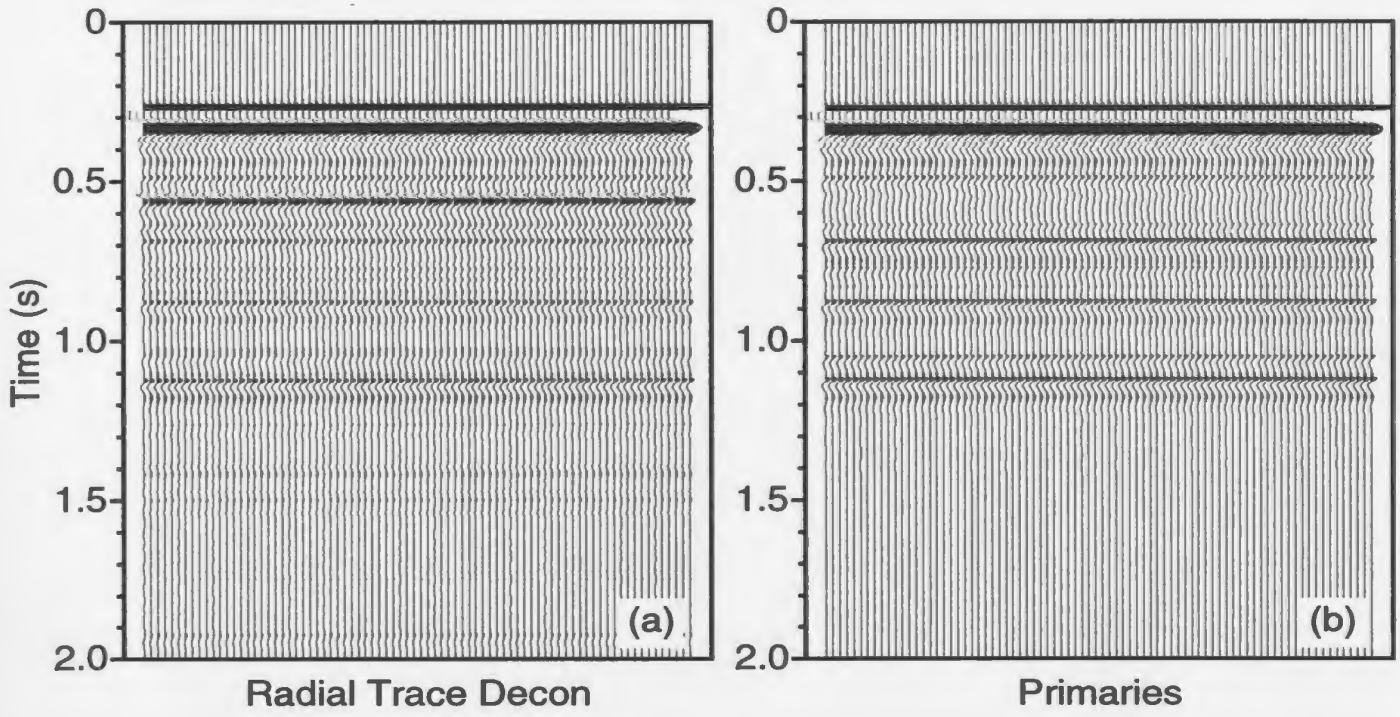

Figure 3.24. Radial trace deconvolution stack. (a) shows the stack of 3.23 (d), while (b) shows primaries-only stack. The prestack improvements at far offsets have not translated into improvements in the stack.

deconvolution requires a previous event in order to work, it cannot attenuate the first few orders of near trace multiples. Once again, the post-stack traces show very little improvement over the basic stack (see Figure 3.24).

All of the deconvolution techniques have a major problem dealing with sea-floor structure, because of both timing and amplitude problems. Since none of the data transforms mentioned above can actually adapt to data irregularities and force the data to become periodic, deconvolution is rarely useful in rough sea-floor conditions.

3.3 Velocity Filtering

Fourier theory shows that any wavefield can be represented as an infinite summation of 'plane-waves', which are both spatially and temporally monochromatic. By applying Fourier transforms to both time and space axes, a gather can be transformed into frequency-wavenumber (*f-k*) space:

$$P(k,\omega) = \int_{0}^{\infty} \int_{-\infty}^{\infty} p(x,t) e^{-i(\omega t - kx)} dt dx \qquad (3.9)$$

where $P(k,\omega)$ is the transformed data set, $p(x,t)$ is the initial data, ω is the radial frequency ($=2\pi f$) and k is the spatial wavenumber. Because it maps events on the basis of their dip in *x-t* space, this transform can be used for velocity filtering.

Normal moveout is first applied to the data set using a velocity between the primary velocities and the water velocity. This causes over-moveout of the primaries and under-moveout of the multiples. The multiples maintain their positive dips while the primaries obtain negative dips (see Figure 3.25). Since these will map into different quadrants in *f-k* space (see Figure 3.26), multiple elimination is simply a matter of muting the quadrant which contains the multiples (Yilmaz, 1987). Although this method can be quite effective, it requires well sampled data since aliasing can be a major problem. In addition, *f-k* filters can introduce considerable noise if they are not applied carefully.

The major limitation with *f-k* attenuation is that it is based on the difference in

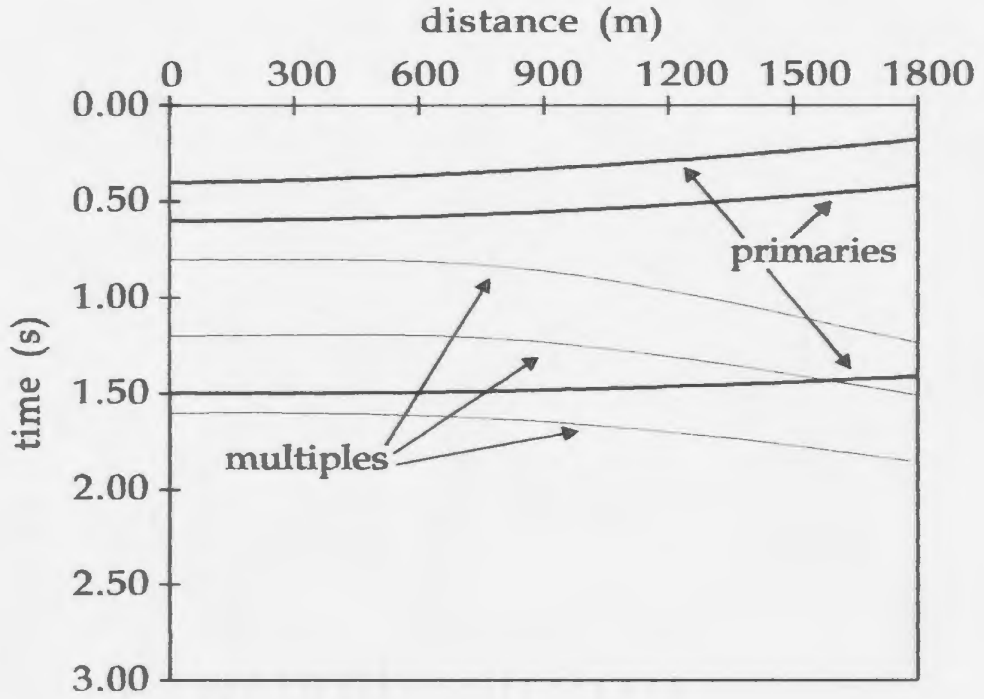

Figure 3.25. NMO application for FK multiple attenuation. The velocity function is chosen to be mid way between the primary velocities and the multiples. As a result, multiple maintain a positive dip while primaries obtain negative dips.

moveout between multiples and primaries. As a result, it tends to work well at far offsets (provided the events are not aliased) where the moveout difference is significant, but not at near offsets, where there is very little difference in moveout (Figure 3.27). This can make the pre-stack gathers look much better, but the stacked traces generally show very little improvement (see Figure 3.28). This is because the actual stacking process works on the same principle of moveout discrimination, so that many of the gains produced by the *f-k* attenuation would have been produced by the stack anyway.

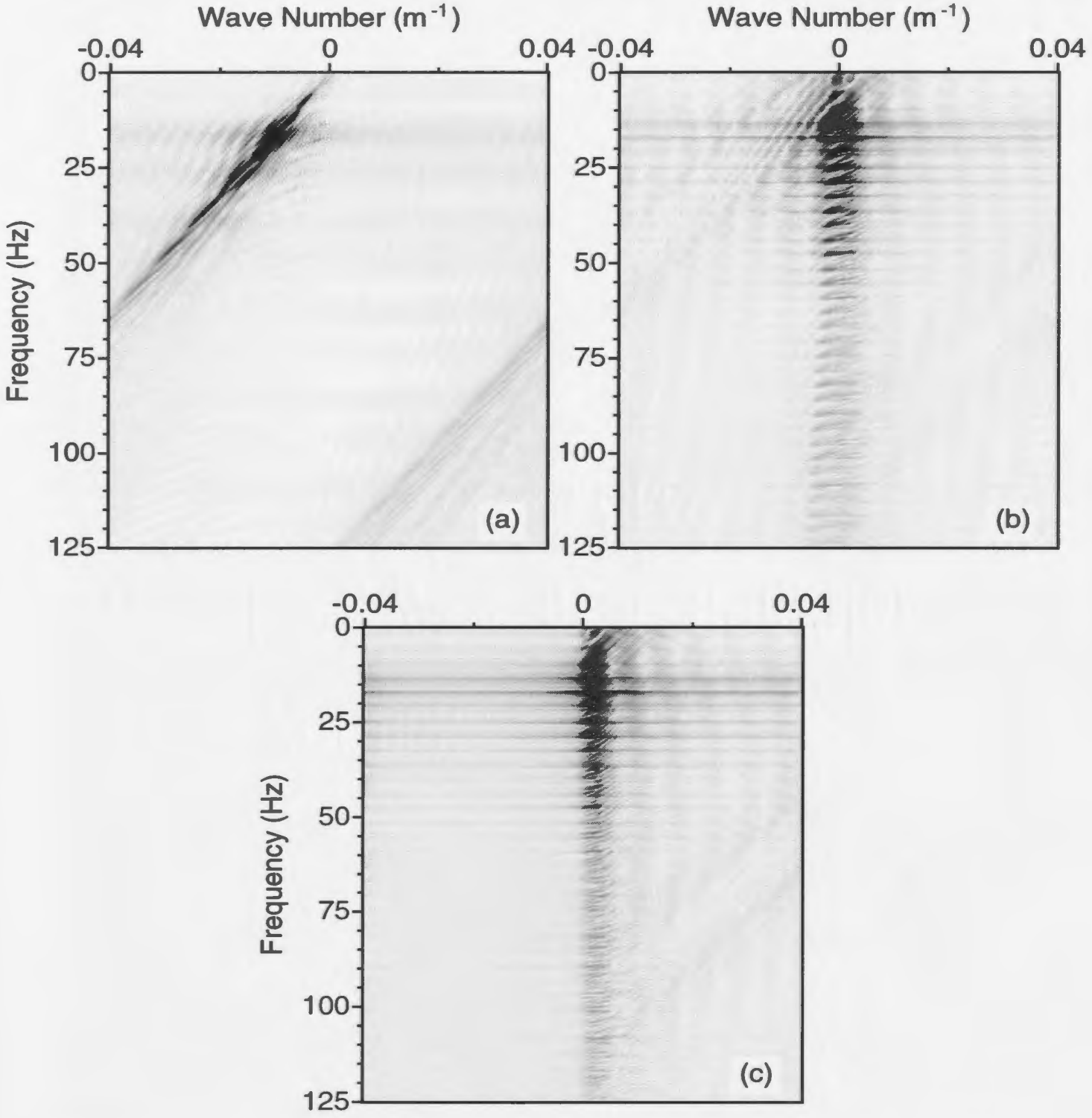

Figure 3.26. FK multiple attenuation. (a) shows the FK transform of the original gather; (b) shows the transform of the gather after NMO has been applied using an intermediate velocity function; (c) shows the transform after muting the negative wavenumbers in order to attenuate the multiples.

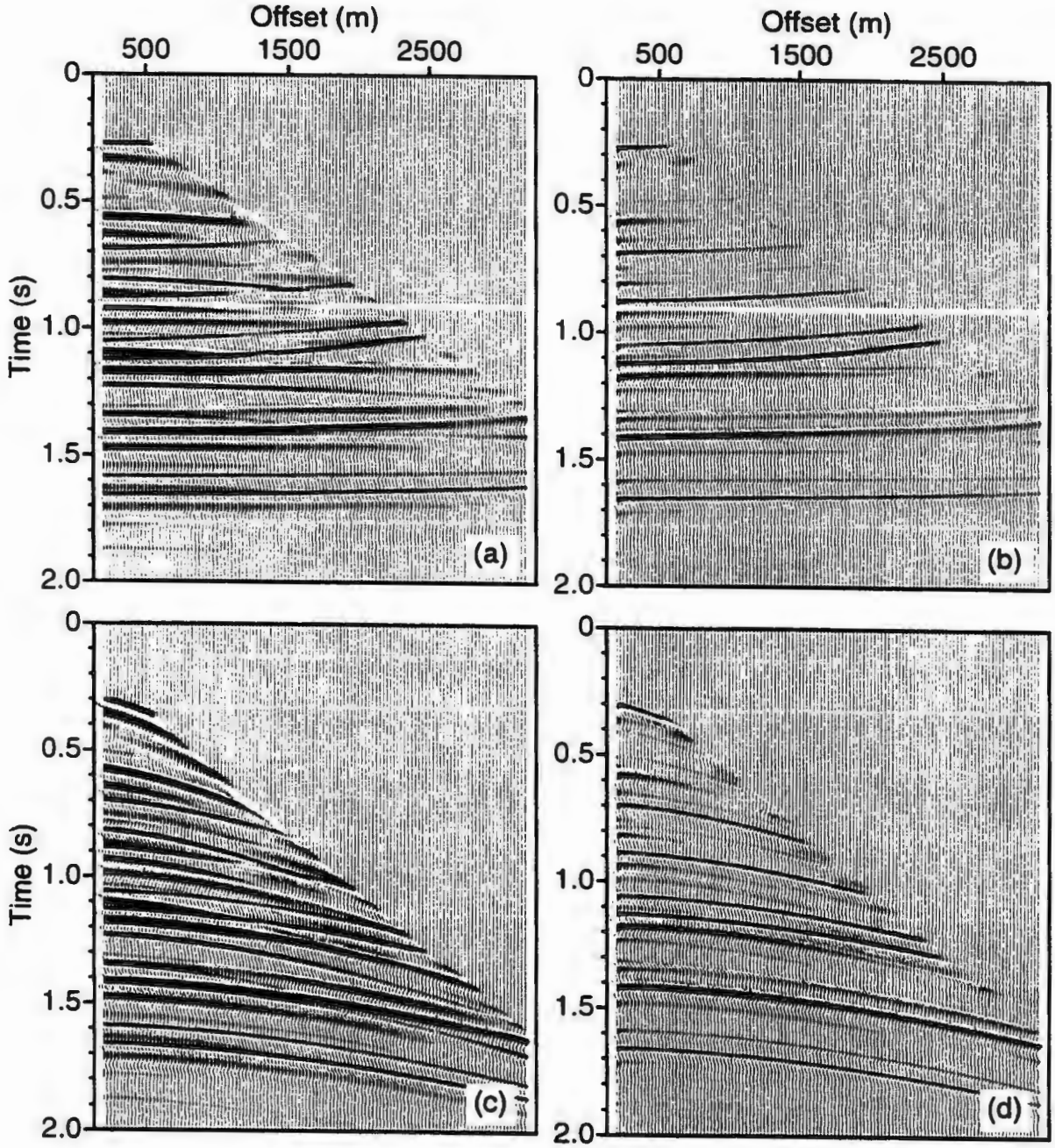

Figure 3.27. FK multiple attenuation. (a) shows the original gather with NMO applied using an intermediate velocity function; (b) shows the gather after FK filtering; (c) shows (a) after the NMO is removed; (d) shows (b) after the NMO is removed.

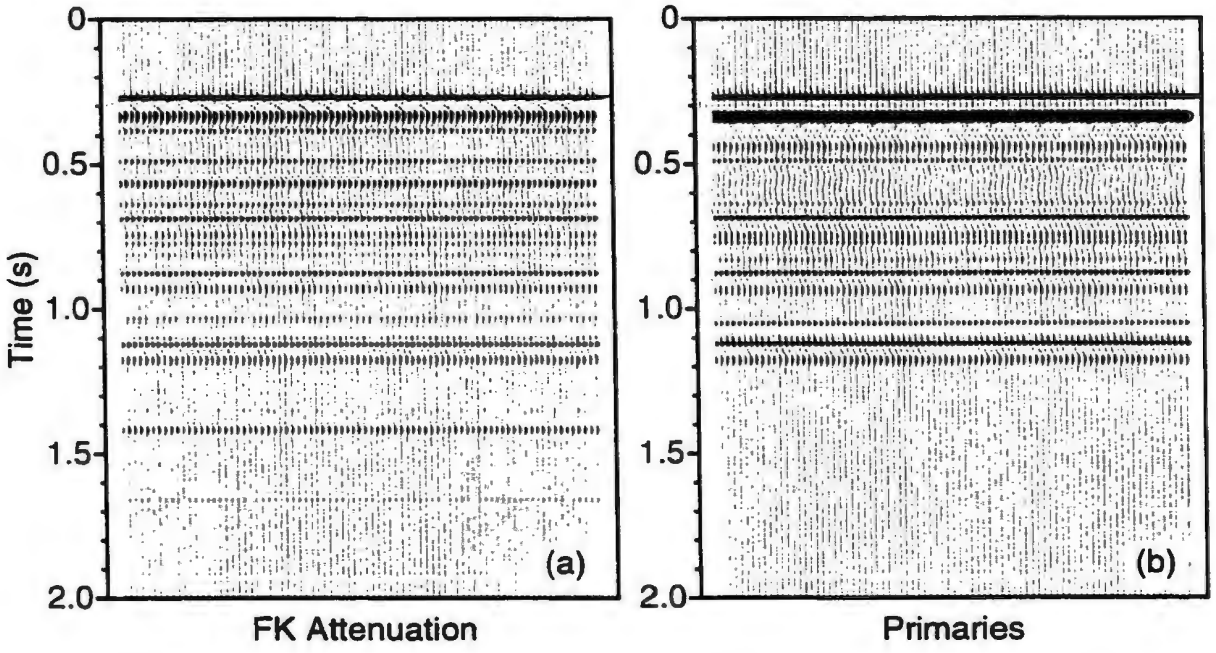

Figure 3.28. FK stack. (a) shows the stack of 3.27 (d); (b) shows the primaries-only stack. The excellent attenuation that was seen on the pre-stack gather at far offsets does not translate into much improvement of the stack.

There have also been a number of attempts to use τ-p space for velocity filtering. The standard τ-p transform does not separate multiple and primary energy very well, since the ellipses overlap as much as do the hyperbolae in x-t space. However, an alternate technique of calculating the τ-p transform, called 'hyperbolic velocity filtering', restricts the range of offsets which are included at each τ-p coordinate. By transforming each point into a line segment rather than a full line, it reduces the linear artifacts caused by the sampling (see Figure 3.29). In addition, since the line segments have a p range restricted by the primary velocity input, some of the multiple energy may not be transformed. However,

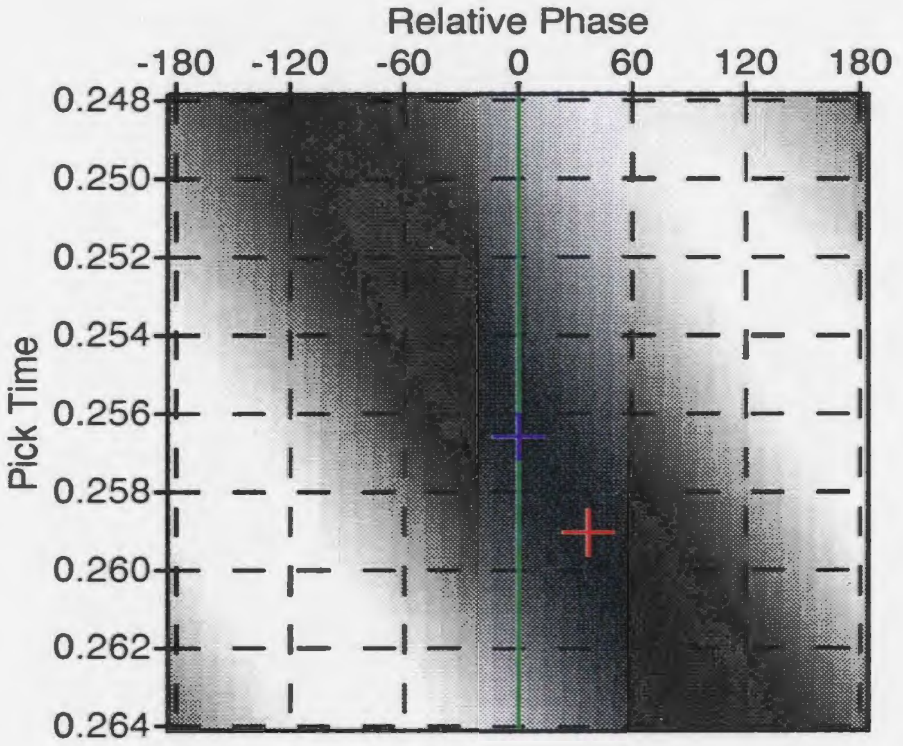

Figure 4.3. Cross-correlation of 30 Hz Ricker wavelet with a time and phase-shifted version of itself. The green line shows the correlation without a phase correction, with the blue + marking the position of the resulting pick. The red + shows the correct pick.

property that any phase rotation may be represented as a linear combination of the original trace and its Hilbert transform:

$$f_\phi(t) = f_0(t)\cos\phi + H[f_0(t)]\sin\phi \tag{4.4}$$

where ϕ is the phase shift, $f_0(t)$ is the original trace and $f_\phi(t)$ is the phase shifted version. We can use this to estimate the phase shift in the reference wavelet that best reproduces the pick trace.

The problem can be solved in a least-squares sense by defining an objective

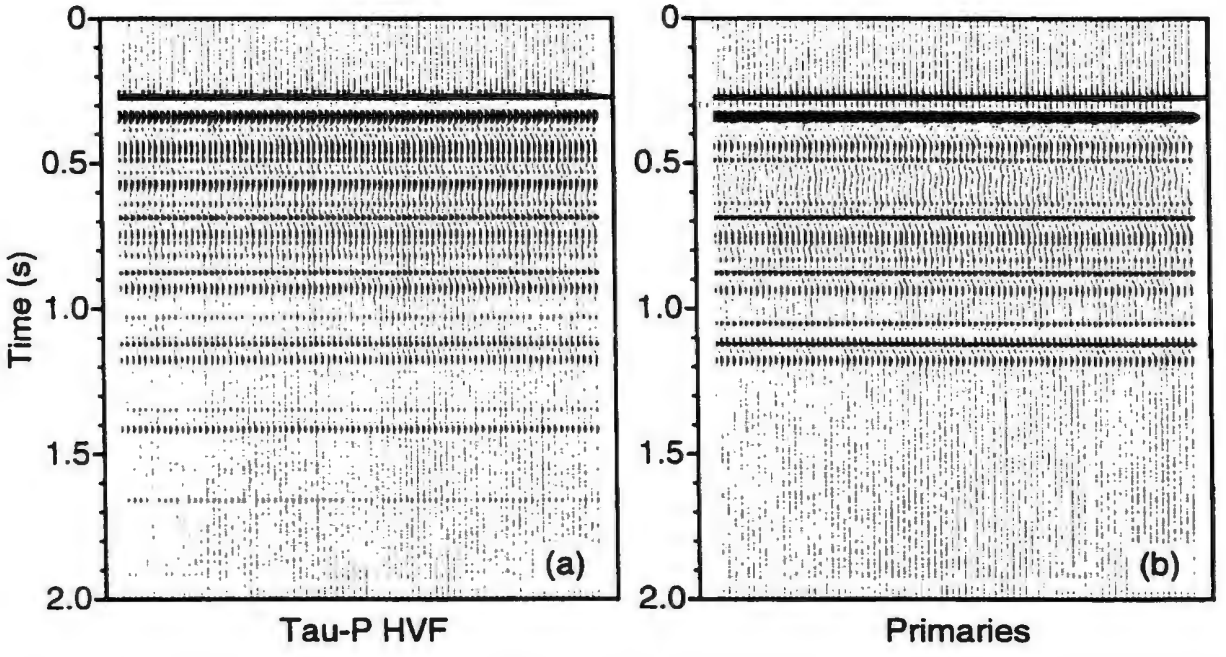

Figure 3.30. τ-p HVF stack. (a) shows the stack of 3.29d; (b) shows the primaries-only stack. Once again, the prestack improvements to not translate into post-stack improvements.

although it is more expensive to run than f-k attenuation, it is based on the same principle of moveout discrimination and hence has essentially the same performance and problems (see Figure 3.30).

Hampson (1986) used a radon transform, which is similar to τ-p but with parabolic rather than linear trajectories, to perform the velocity filtering:

$$v(q,\tau) = \int_{-\infty}^{\infty} u(x, \tau + qx^2)dx \qquad (3.12)$$

He showed that, after moving out the data at the primary velocities, the residual moveout of the multiples could be fairly accurately approximated with

parabolas. As a result, he was a able to use the radon transform to separate the multiple and primary events. The portion of transform space which contains the multiples is then muted (see Figure 3.31). Since the events are much better focused than in f-k or t-p space, the entire multiple event may be attenuated, at near offsets almost as well as at far offsets. The stacked traces therefore tend to show much better multiple attenuation (see Figure 3.32).

The improved focusing, unfortunately also reduces the ability of the inverse transform to retain the amplitude vs. offset information of the original data. In addition, the technique has problems in areas when the seafloor is very hard or has some topography, since the events do not focus as well. A similar approach was developed by Foster and Mosher (1992), who used a hyperbolic radon transform. However, while it is more expensive to run, it has the same basic problems as the parabolic transform.

Since all of these techniques require a prior knowledge of the primary velocities, they are not often practical in areas where the multiples completely overwhelm the primaries. A poor choice of primary velocities can cause serious attenuation of the primary energy, as well as reducing the effectiveness of the multiple suppression. In addition, because they all depend on the moveout difference between the multiples and the primaries, with the possible exception of the radon transform, they tend to work better at far offsets. Since stacking

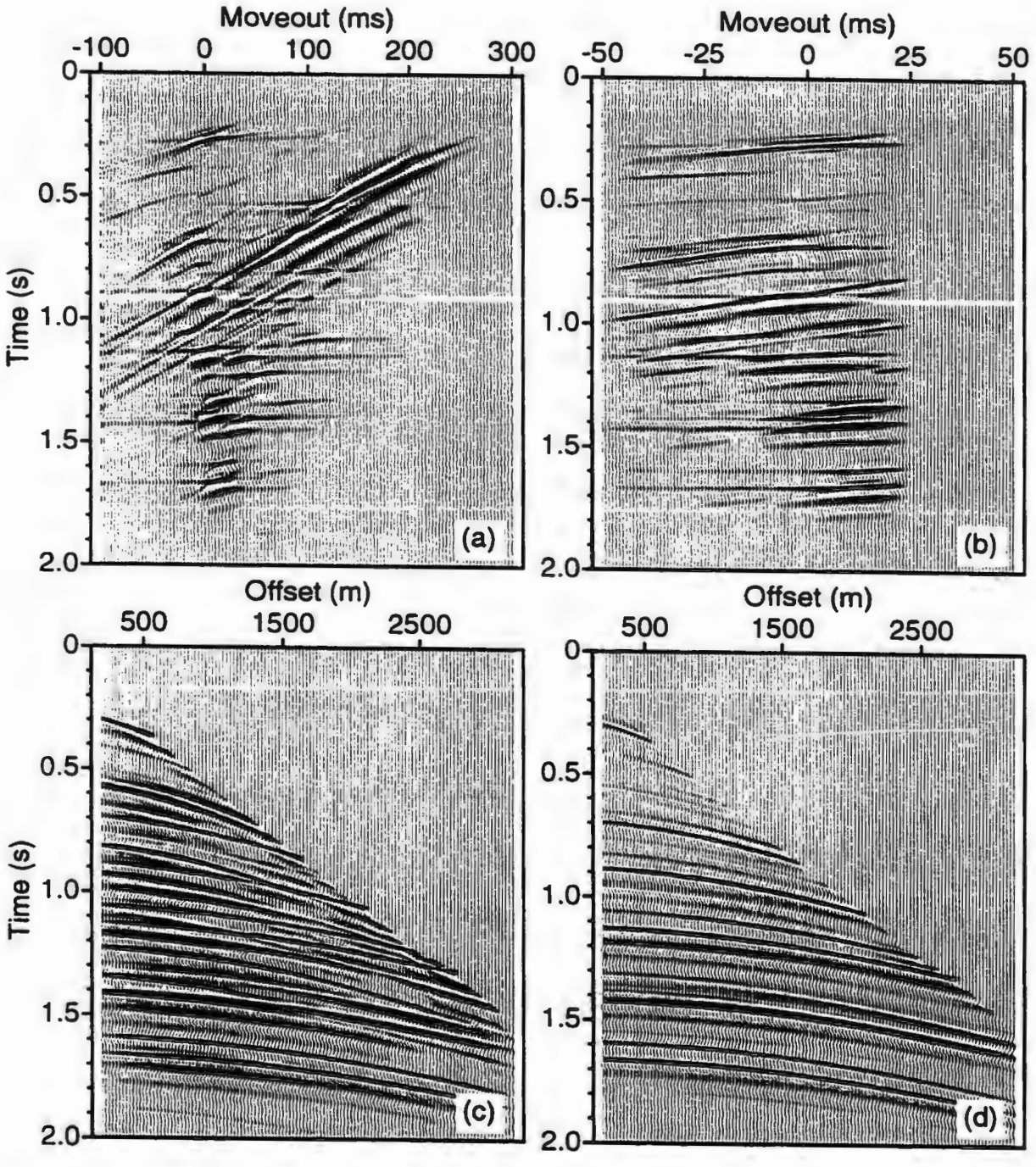

Figure 3.31. Parabolic radon transform. (a) shows the radon transform for a moveout range from -100 to +300 ms, which incorporates most of the gather's energy; (b) shows the filtered range between -50 and +25 ms; (c) shows the inverse transform of (a); (d) shows the inverse transform of (b).

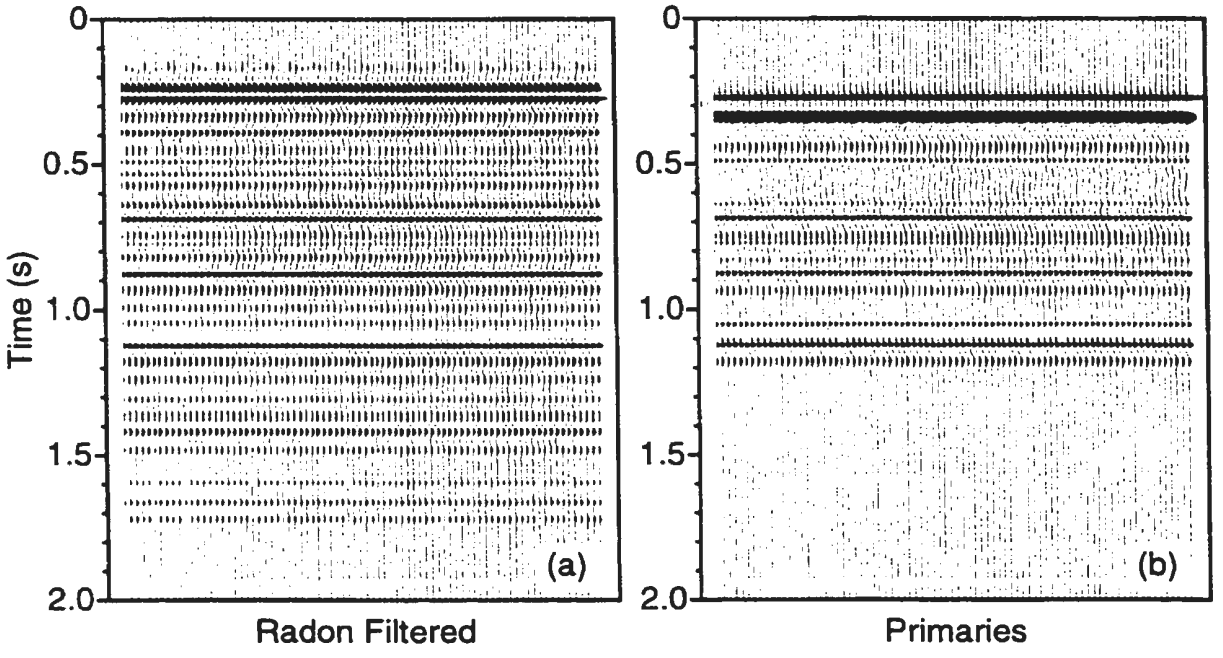

Figure 3.32. Parabolic radon stack. (a) shows the stack of 3.31 (d), while (b) shows the primaries-only stack. There is very good attenuation of events which have significant moveout difference for the primaries (for example, the first multiple at 0.6 seconds), but events which have similar moveout obviously are not affected (e.g., the pegleg at 1.4 seconds).

already does a good job at the far offsets, the improvements in the primary-to multiple ratio which are evident on the pre-stack gathers often do not translate into improvements in the stack.

3.4 Prediction / Subtraction

This group of attenuation methods is where most of the current research is being done, since it has the potential to handle sea floor irregularities as well as reflection coefficient variations and even a non-stationary wavelet. The basic

idea is that the problem can be solved in three steps: first determine what the actual sea-floor structure is, then model what the sea-floor multiples should look like, and finally subtract the modelled multiples from the data. They are an extension of predictive decon, but guided by a knowledge of the seafloor.

The simplest procedure which falls into this category can be called 'stack and subtract'. It is based on the idea that if a gather is moved out at water velocity and then stacked, the stacked trace should be an estimate of what the multiples look like at zero-offset. By choosing optimal scaling factors, to model amplitude variations, the scaled 'multiple' trace is subtracted from each trace in the gather (Brandsaeter and Ursin, 1979). Finally, NMO is removed and reapplied at primary velocities. The technique is related to the coherency weighting technique developed by Buttkus (1979). Since it assumes a flat sea-floor, and because it does not attempt to model phase variations, it has considerable difficulty with sea-floor irregularities and is unable to handle post-critical events.

A more sophisticated approach was suggested by Wiggins (1989 using the earlier research of Morley (1982). He showed that wavefield extrapolation can be used to produce wavefields which differ by one reverberation (see Figure 3.33). The multiples can then be eliminated by subtracting one wavefield from the other. This method has the advantage that, in addition to eliminating normal sea-floor multiples, it also eliminates all of the water layer pegleg multiples.

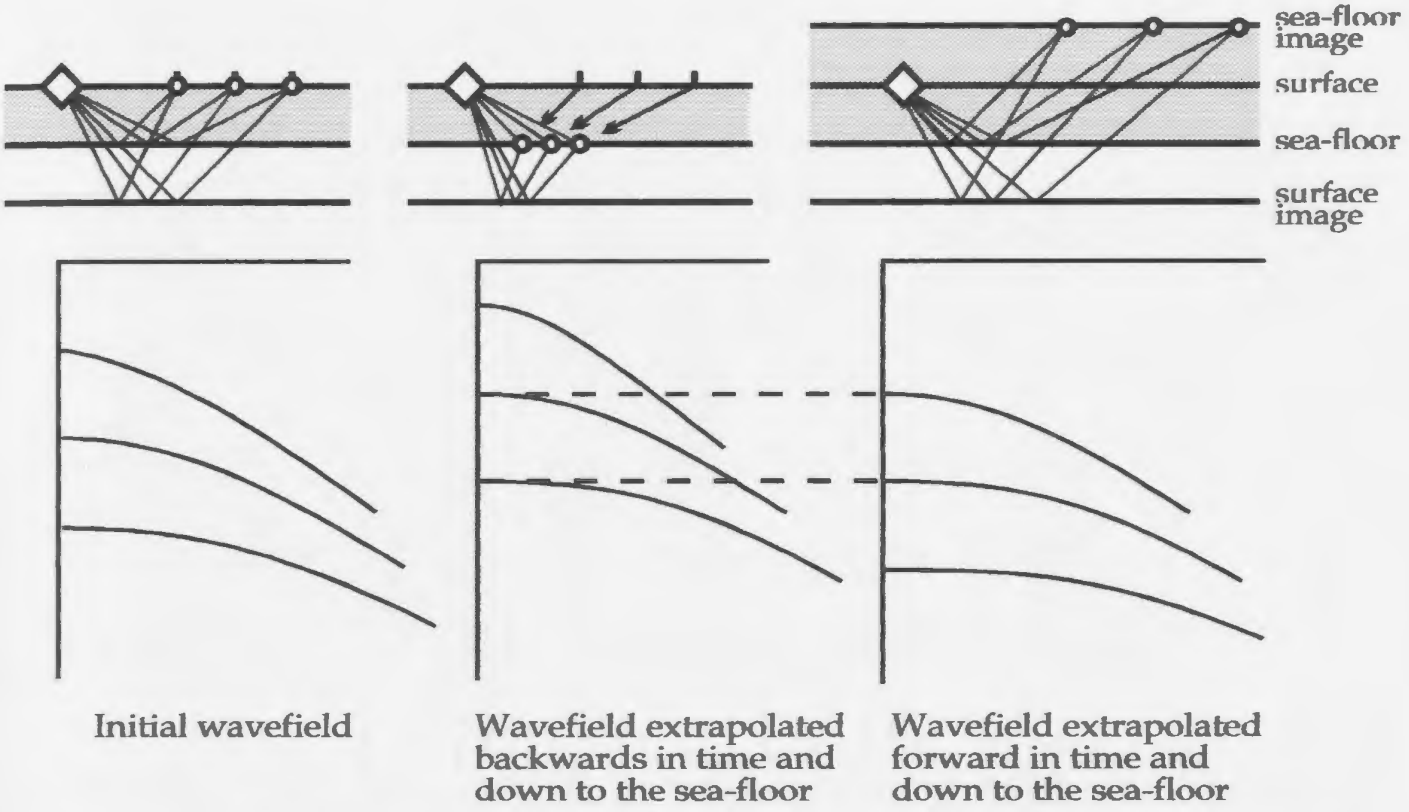

Figure 3.33. The extrapolation based prediction/subtraction method of Wiggins (1988). The forward extrapolated wavefield differs from the backward extrapolated wavefield by one reverberation. Multiples can be eliminated by multiplying the forward wavefield by the sea-floor reflection coefficient and then subtracting it from the backward wavefield.

Since the wavefield that has experienced the extra reverberation has had an extra reflection from the seafloor, it has to be scaled by the sea-floor reflection coefficient. However, since the reflection coefficient has been shown to be dependent on the angle of incidence, the scaling is time and offset dependent. In addition, there are many crossing events, for which the events have different angles of incidence at their intersection. This makes it impossible to determine a

theoretical scaling factor and requires the scale factor to be determined on the basis of optimal energy reduction. This means that phase corrections are impossible, and that the technique is restricted to pre-critical events.

Unfortunately, the extrapolation also tends to be a fairly noisy operation, due to boundary conditions, aliasing and problems dealing with amplitude anomalies (see Figure 3.34). In addition, it is very sensitive to the sea-floor model, and since the subtraction is dependent on the multiples being located correctly, model errors can greatly reduce the effectiveness of the multiple attenuation. However, if the model is good and the stacking is able to attenuate the extrapolation noise, this technique can give quite good results (see Figure 3.35).

A related technique, which has been getting considerable attention lately, is based on an inverse scattering approach (Carvalho et al, 1992; Verschur and Berkhout, 1992). It involves a series representation of the wavefield, of which the free-surface multiples are a subseries. In the f-k domain, the attenuation algorithm may be expressed as an infinite sum,

$$\begin{aligned} D' &= D^{(1)} + D^{(2)} + D^{(3)} + \ldots \\ &= D^{(1)} + D^{(1)}TD^{(1)} + D^{(1)}TD^{(1)}TD^{(1)} + \ldots \end{aligned} \qquad 3.13$$

where the n^{th} term of the series is responsible for the attenuation of the $(n-1)^{th}$ order multiples, $D^{(1)}$ is the input data and T represents the free-surface reflection coefficients (Matson and Weglein, 1996). Since the multiples are predicted

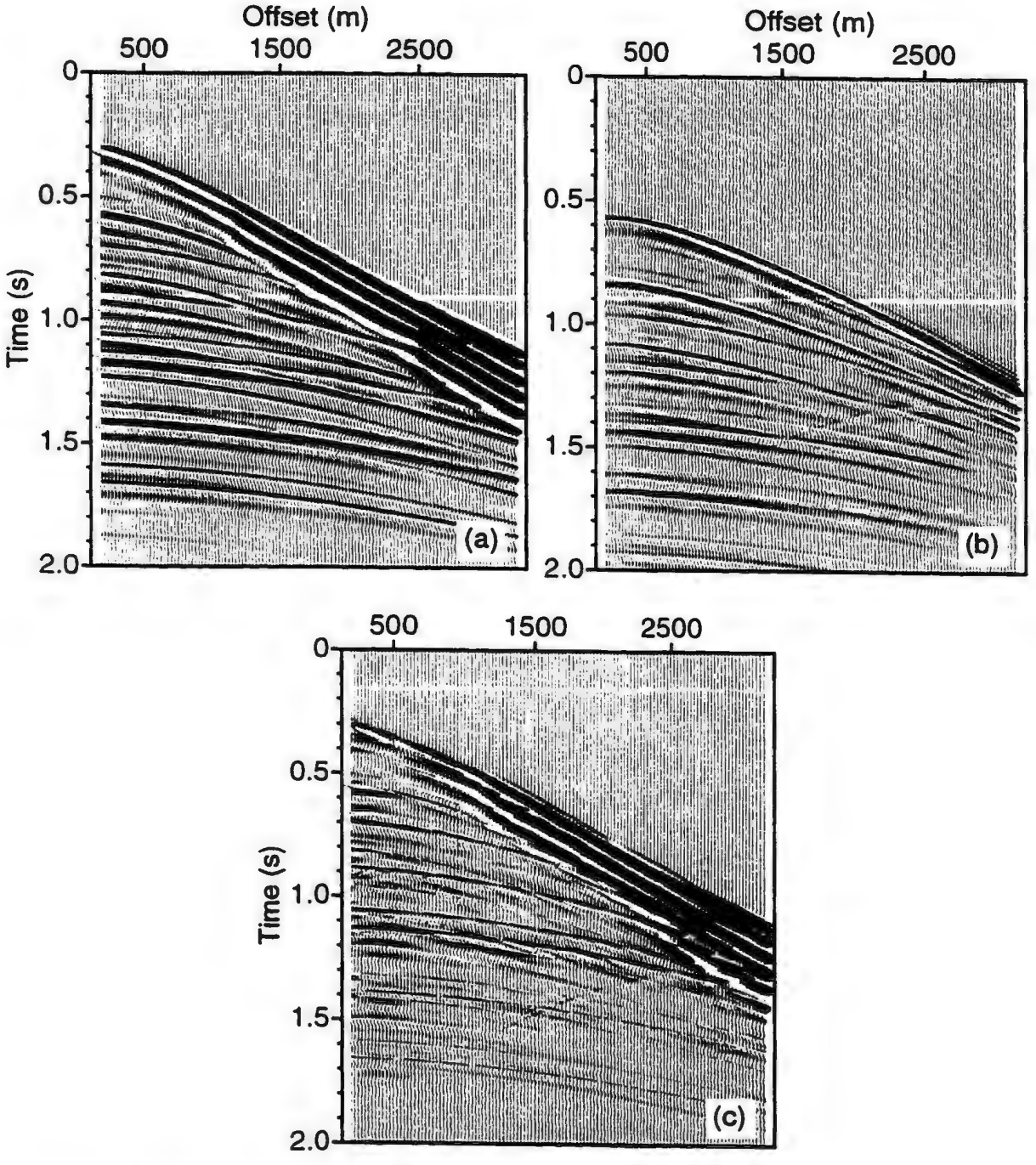

Figure 3.34. Wavefield extrapolation based attenuation of sea-floor multiples. (a) shows the original gather; (b) shows the result of forward extrapolation in time through the equivalent of two water layers, note the edge effects at 1.3 seconds despite the tapering of both near and far offsets; (c) shows the result of the optimized subtraction of (b) from (a).

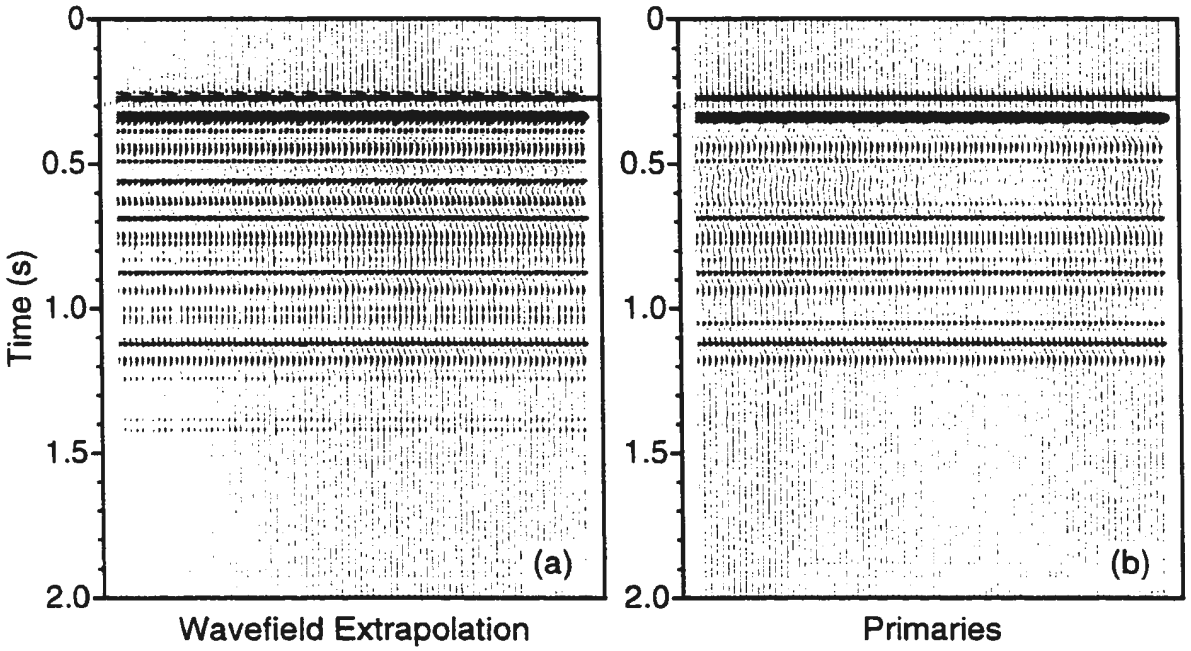

Figure 3.35. Wavefield extrapolation stack. (a) shows the stack of 3.34 (d), while (b) shows the primaries-only stack.

essentially by a convolving the dataset with itself, no velocity or structural information is required.

Unfortunately, the determination of which traces to use in the convolution is determined by the shape of the reflectors (see Figure 3.36), and can only be found by comparing the convolutions of a range of traces back to the original data. This is not only time consuming but also strongly subject to errors. In order to construct predicted multiples for the near traces, data must be collected to zero offset. Since this is very rarely done, data extrapolation to zero offset is necessary. In addition, the convolution itself results in a predicted wavefield

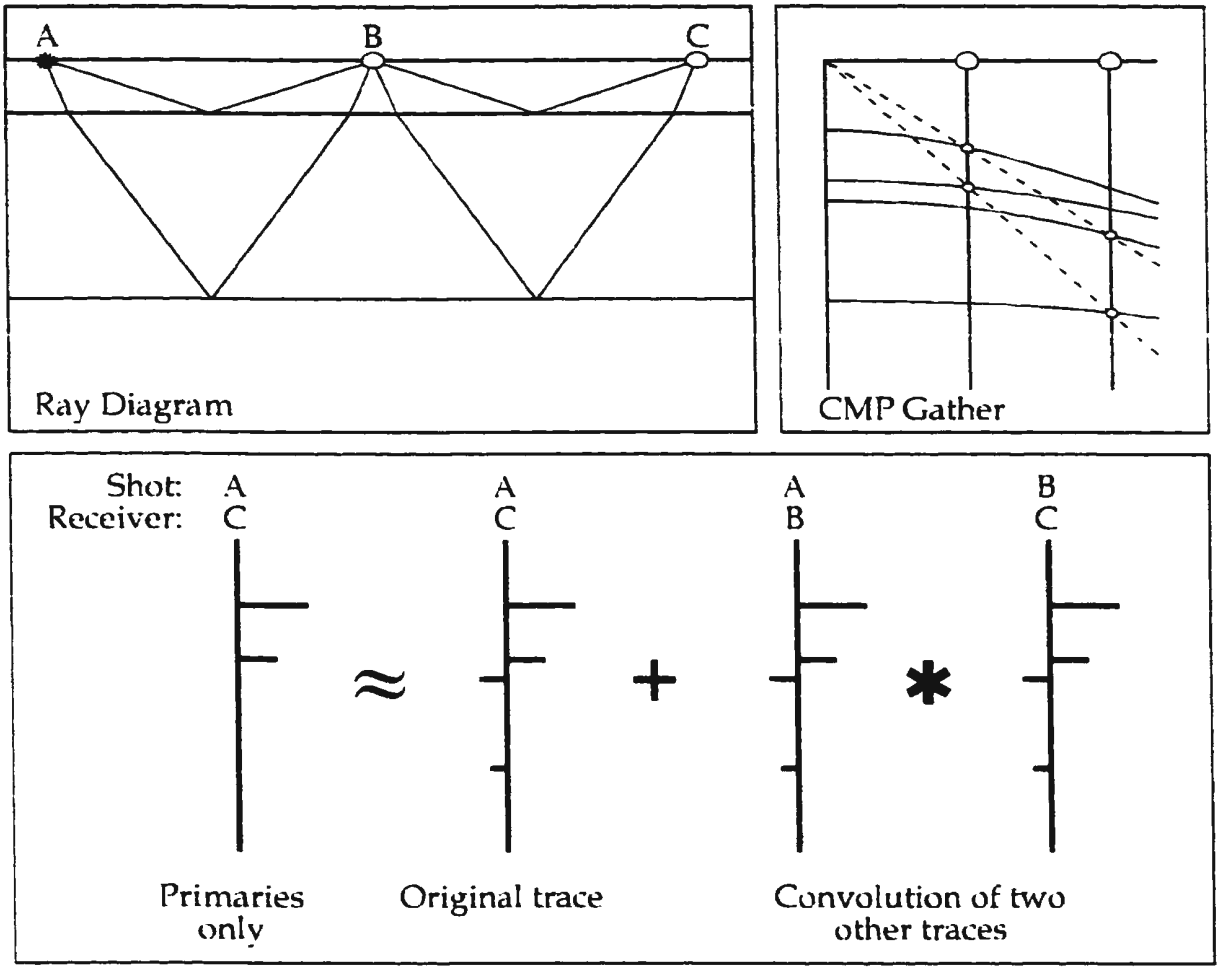

Figure 3.36. Inverse scattering approach to multiple suppression. The bottom diagram illustrates how the technique uses the convolution of two traces to predict the multiples on a third, which can then subtracted from the original data. For flat reflectors, the convolution projects the multiples along radial traces to the next multiple order, as illustrated in the upper right diagram.

which has had an extra convolution with the source wavelet. As a result, a deconvolution is required before the subtraction can be performed. These factors combine to produce an extremely time consuming technique which tends

to work quite well on synthetics but not so well on real data.

Calvert (1990) suggested using raytracing to model the multiple arrival times, and then applying a stack and subtract approach to attenuate the multiples. However, in order to provide much improvement over the simple stack and subtract, a very good knowledge of the sea-floor is required, since model errors are exaggerated by each successive order of multiple. Since phase corrections were not applied, it was also unable to handle post-critical reflections. The approach that I will be using in this study is essentially an extension of Calvert's technique which is able to adjust the raytracing predictions so that they better fit the data. Its adaptive nature makes it less sensitive to model errors and better able to handle amplitude and phase variations.

4. SEA-FLOOR ESTIMATION

4.1 Approach

The difference between the raytracing results and the data is obviously highly dependent upon the actual water bottom model. It is critical to this method that the model be consistent with the data. It is important to recognize that this does not require that the model be accurate, only that the combination of water velocity, water depths and static time shifts produce travel time estimates that closely agree with what is observed in the data. Although the data may be inverted to produce a very accurate model of the sea-floor, this is both time consuming and unnecessary, since a small perturbation in any one of these three parameters can be fairly well accommodated by adjusting the other two. I have therefore chosen to fix the water velocity, which is usually quite well known, and to use the data to estimate the water depths and the necessary time shifts.

Since the water velocity is assumed, the arrival time of the water bottom reflection at each source-receiver offset can be converted into an estimate of the water depth at some point between the source and receiver. This point is most accurately located when the offset is small. Therefore, I have chosen to perform the modelling using only the nearest trace on each shot gather. This is accomplished by picking the arrival time of the water-bottom reflection on each

trace and then correcting the time to estimate the water depth at the source-receiver midpoint. This correction is composed of two parts: normal moveout, which removes the horizontal component of the traveltime; and migration, which takes into account the topography of the sea-floor. In order to ensure that the picks are accurate and that the timing corrections have been applied properly, the model is then used to predict the arrival times of a number of multiples. The predictions are compared to the actual data and the model is automatically adjusted to produce a good fit.

Since the modelling does not attempt to invert the data itself, but rather several of its important characteristics, the process is extremely efficient, while still being able to produce a model which is sufficiently accurate for the raytracing.

4.2 Picking the Sea-bottom Arrival

As the subsequent timing analysis and migration should correct most errors, the initial picking does not have to be particularly accurate. However, in order to increase the likelihood of obtaining a good statics solution, as well as to improve the stability of migration, the picks at least should be close to the real arrivals. Very poor picking results could require manual editing of the resulting model.

Numerous techniques have been developed to perform automatic first break picking. These use everything from energy onset (Hatherly, 1982; Coppens, 1985) to cross correlation (Gelchinsky and Shtivelman, 1983) to more exotic techniques involving trainable neural networks (Murat et al., 1992) and even fractals (Boschetti and Dentith, 1996). I chose to use a combination of energy and correlation-based techniques which emphasize the consistent picking of the same point on the wavelet.

The first part of the picking routine involves the picking of the first break on the first trace of the near-trace gather. This uses an energy-based picking function which enhances the first break of the event. The function is given by,

$$F_k = \sum_{n=k}^{k+w} d_n^2 \Big/ \sum_{n=k-w}^{k} d_n^2 \qquad (4.1)$$

where w is the width of the picking window and d is the data. The numerator measures the energy in a window following the pick, while the denominator measures the energy in the window preceding the pick. In the absence of any signal, the picking function remains fairly constant. However as the lead window comes in contact with a seismic event, the function increases rapidly. When the trailing window also starts to sample the event, the function decreases. As a result, the function should peak exactly at the first break of the event, regardless of how the energy is distributed within the wavelet.

a)

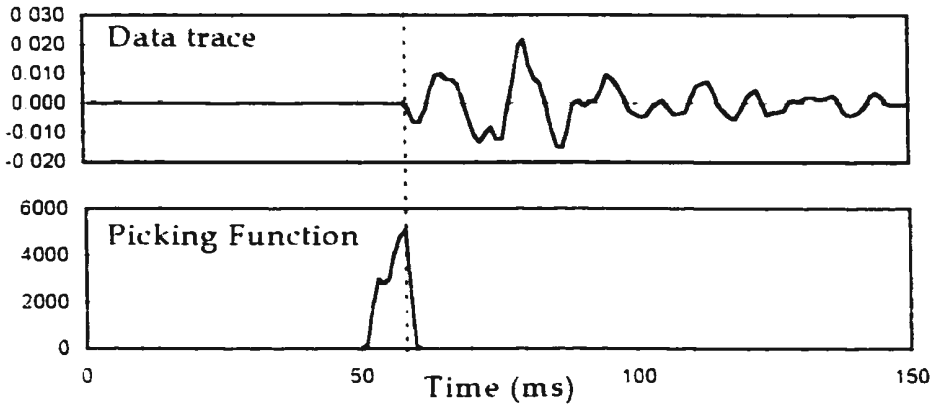

b)

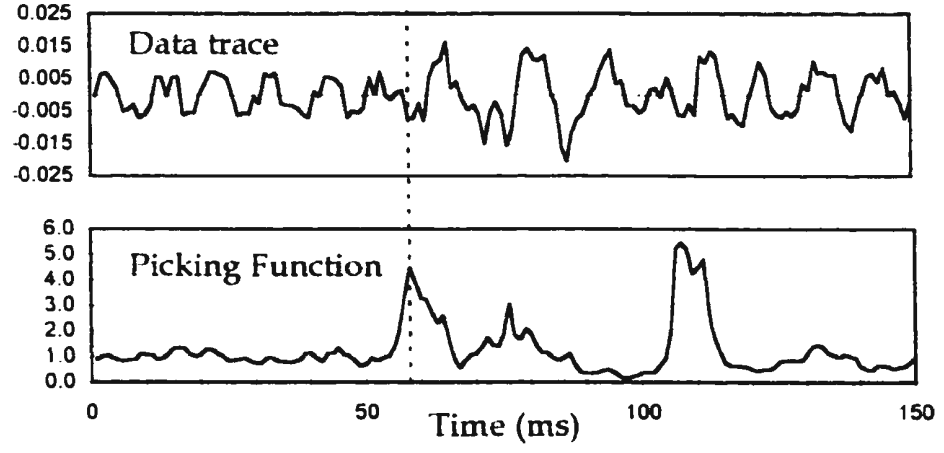

Figure 4.1. Illustration of automatic picking of the first break. a) shows the data and the picking function for clean data, with the actual pick shown by a dashed line. b) shows the picking of noisy data. Although the picking function has a major peak in the correct location, there is an even larger peak at 110 ms.

Figure 4.1a shows that the function is very effective in picking clean data. However when noise is added (Figure 4.1b), the function can have a number of false peaks, which can make the picking somewhat unreliable. In order to reduce this effect, the picking routine first searches for the window which contains the maximum energy, making the assumption that the first water

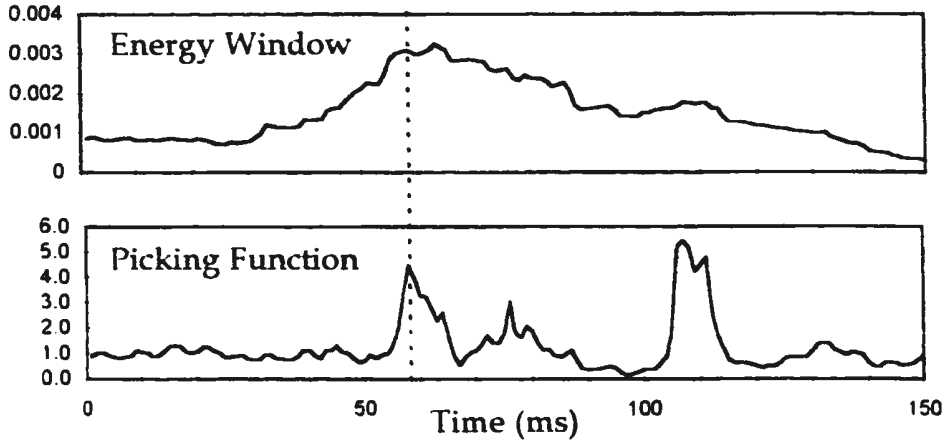

Figure 4.2. Choosing the correct peak of the picking function based on the energy window. The correct peak should be the one which precedes the maximum in the energy window.

bottom reflection will be the loudest event on the trace. It then looks for the split filter peak which immediately precedes it (Figure 4.2). This has proven to be very effective at picking the sea-floor arrival.

4.3 Automatic Picking of Near Traces

Once a pick has been made on the first trace, the remaining traces must be picked. In order to insure that the wavelet picks are consistent on all traces, I chose to use a cross-correlation-based approach. Cross-correlation is defined as the summed product of two data series:

$$Xcor(t) = \sum_k f_k * d(t)_k \qquad (4.2)$$

where, in our case, f is the reference wavelet, defined to be the data window on

the first trace beginning at the pick time determined above, and $d(t)$ is the trace to be picked (subsequently to be called the pick trace) which has been shifted by a time t. The relevant pick is at the value of t which maximizes the cross-correlation. However, cross-correlation is extremely phase dependent and is unable to differentiate between phase shifts and time shifts (see Figure 4.3). Since the reflections from a hard sea-floor are often post-critical, even at near offsets, it is important to the sea-floor modelling that the phase shifted wavelets be properly picked.

A simple solution is to compute additional correlations for phase shifted versions of the reference wavelet. This in effect samples the entire grid shown in Figure 4.3, rather than just the zero phase line. While this produces a much better estimate of the pick, it is dependent on how well the grid is sampled. Since we often would like to know the pick times to within a fraction of a sample, this can become quite time consuming.

A more elegant solution takes advantage of the properties of the Hilbert transform. An integral version of this transform is given by,

$$H[f(t)] = \frac{1}{\pi}\int\int f(t)\sin[\omega(t-\tau)]d\omega d\tau \qquad (4.3)$$

(Aki and Richards, 1980) but it is essentially just a filter which applies a 90° phase rotation to the data. Arons and Yennie (1950) showed that it has the very useful

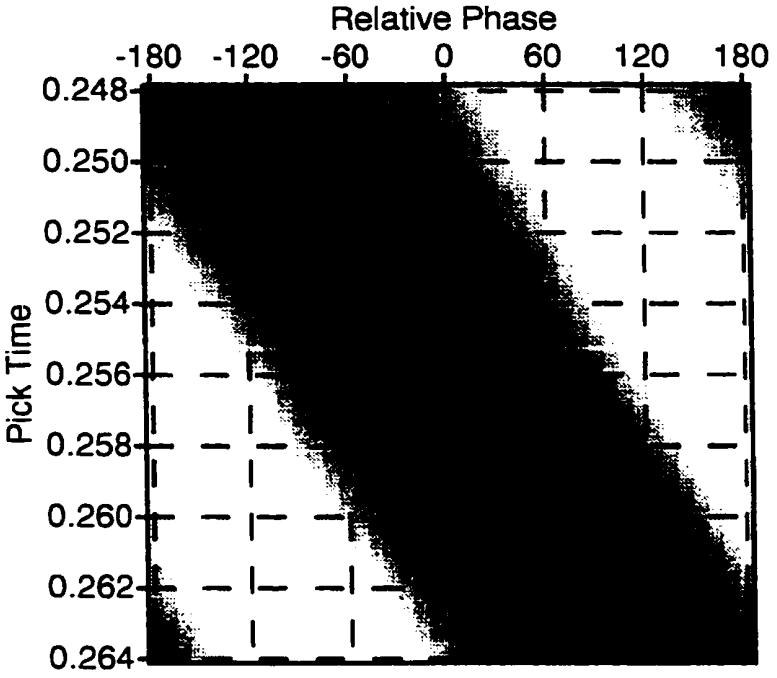

Figure 4.3. Cross-correlation of 30 Hz Ricker wavelet with a time and phase-shifted version of itself. The green line shows the correlation without a phase correction, with the blue + marking the position of the resulting pick. The red + shows the correct pick.

property that any phase rotation may be represented as a linear combination of the original trace and its Hilbert transform:

$$f_\phi(t) = f_0(t)\cos\phi + H[f_0(t)]\sin\phi \tag{4.4}$$

where ϕ is the phase shift, $f_0(t)$ is the original trace and $f_\phi(t)$ is the phase shifted version. We can use this to estimate the phase shift in the reference wavelet that best reproduces the pick trace.

The problem can be solved in a least-squares sense by defining an objective

function to be the squared difference between the pick trace and some linear combination of the reference and its Hilbert transform,

$$\Omega = \sum_k (\alpha f_k + \beta H[f]_k - d_k)^2 \tag{4.5}$$

where $\alpha = A\cos\phi$ and $\beta = A\sin\phi$ are the linear constants to be solved for. A is the relative amplitude and ϕ is the relative phase of the pick trace compared to the reference trace. The least-squares solution is obtained by differentiating Ω with respect to α and β and setting the results equal to zero:

$$\begin{aligned} \frac{\partial \Omega}{\partial \alpha} &= \alpha \sum_k f_k^2 + \beta \sum_k f_k H[f]_k - \sum_k f_k d_k = 0 \\ \frac{\partial \Omega}{\partial \beta} &= \alpha \sum_k f_k H[f]_k + \beta \sum_k H[f]_k^2 - \sum_k H[f]_k d_k = 0 \end{aligned} \tag{4.6}$$

This gives a solution of:

$$\beta = \frac{\sum_k f_k H[f]_k \sum_k f_k d_k - \sum_k f_k^2 \sum_k H[f]_k d_k}{(\sum_k f_k H[f]_k)^2 - \sum_k f_k^2 \sum_k H[f]_k^2} \quad , \quad \alpha = \frac{\sum_k f_k d_k - \beta \sum_k f_k H[f]_k}{\sum_k f_k^2} \tag{4.7}$$

The cross-correlation is then performed using the adjusted version of the reference wavelet and a time shifted pick trace:

$$Xcor(t) = \sum_k (\alpha f_k + \beta H[f]_k) * d_{k+t} \tag{4.8}$$

In effect, this technique allows us to move along the axis of the maximum cross-correlation and hence provides a very efficient solution. It is interesting to

note that only the pick trace is adjusted for the correlation time and as a result only two of the summations in Equation 4.7, i.e. those involving d_k, require updating. The rest can be calculated in advance, providing further improvement in run time.

In order to pick to within a fraction of a sample, interpolation of the pick trace is required. This is performed by convolving the trace with a sinc function, defined by:

$$sinc(t)_k = \frac{\sin 2\pi(t - k\Delta t)}{2\pi(t - k\Delta t)} \tag{4.9}$$

where t is the interpolated time and Δt is the sample rate. The number of points included in the actual convolution is dependent upon the length of the wavelet. In order to make the correlations of different time steps truly comparable, the sinc function should be twice as long as the wavelet. Shorter sincs can be used, but the results may be inaccurate. The actual times for which the interpolation is performed are determined using a standard binary search technique, wherein the time for each step is halfway between the times of the top two correlations from the previous step. This assumes that the correlation function varies smoothly between samples; a valid assumption for well sampled data. Four time steps are used, giving a precision of $1/16$ of a sample.

Figure 4.4 illustrates the correlation and phase curves involved in picking a

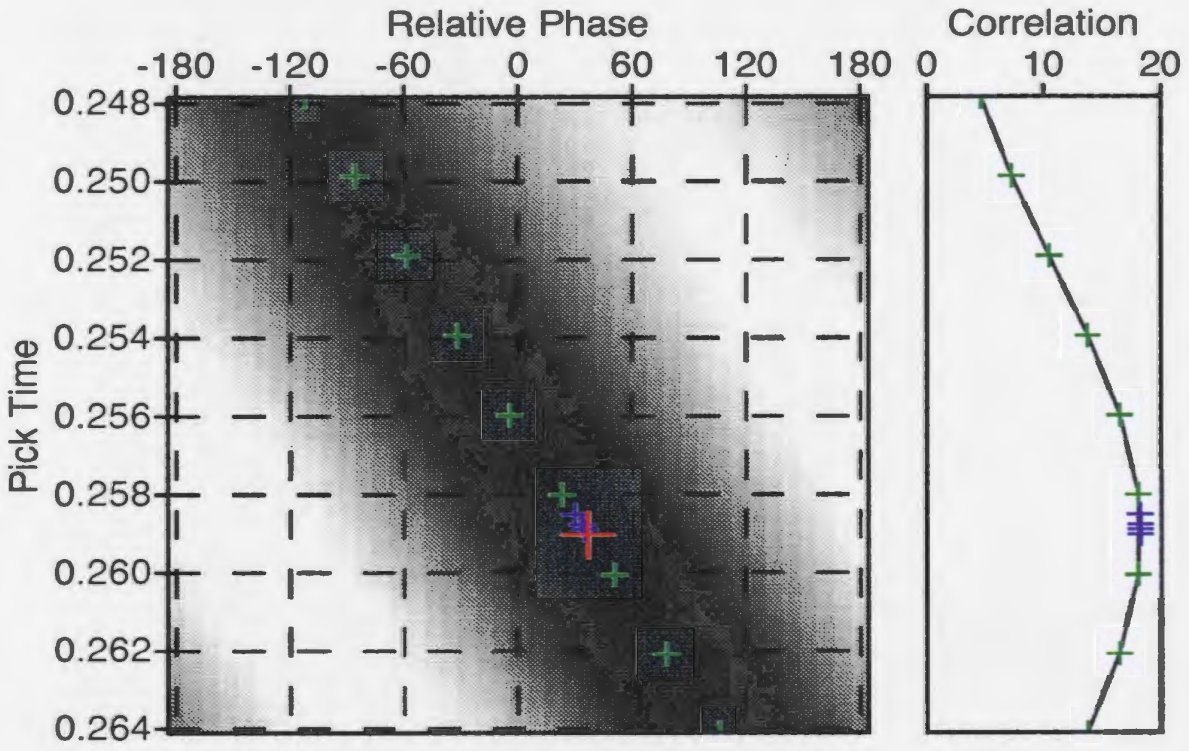

Figure 4.4. Cross-correlation of 30 Hz Ricker wavelet with a time and phase-shifted version of itself. The green +'s show the initial exhaustive search for the maximum correlation, the blue +'s show the subsequent binary search and the red + shows the final pick, exactly at the peak. The curve on the right shows the actual correlation values.

time and phase shifted wavelet, for the noise-free case. To illustrate the convergence path, the phase curve is plotted over the original correlation grid from Figure 4.3. There are two sets of points; one from the original exhaustive search at the sample rate and one from the binary search of the interpolated times. Although the correlation is a very broad peaked function, the location of the peak is very stable, and the pick converges to the correct time and phase.

Figure 4.5 shows the same example as Figure 4.4, but with 10% noise applied to both the reference wavelet and the pick trace. Again, the technique is

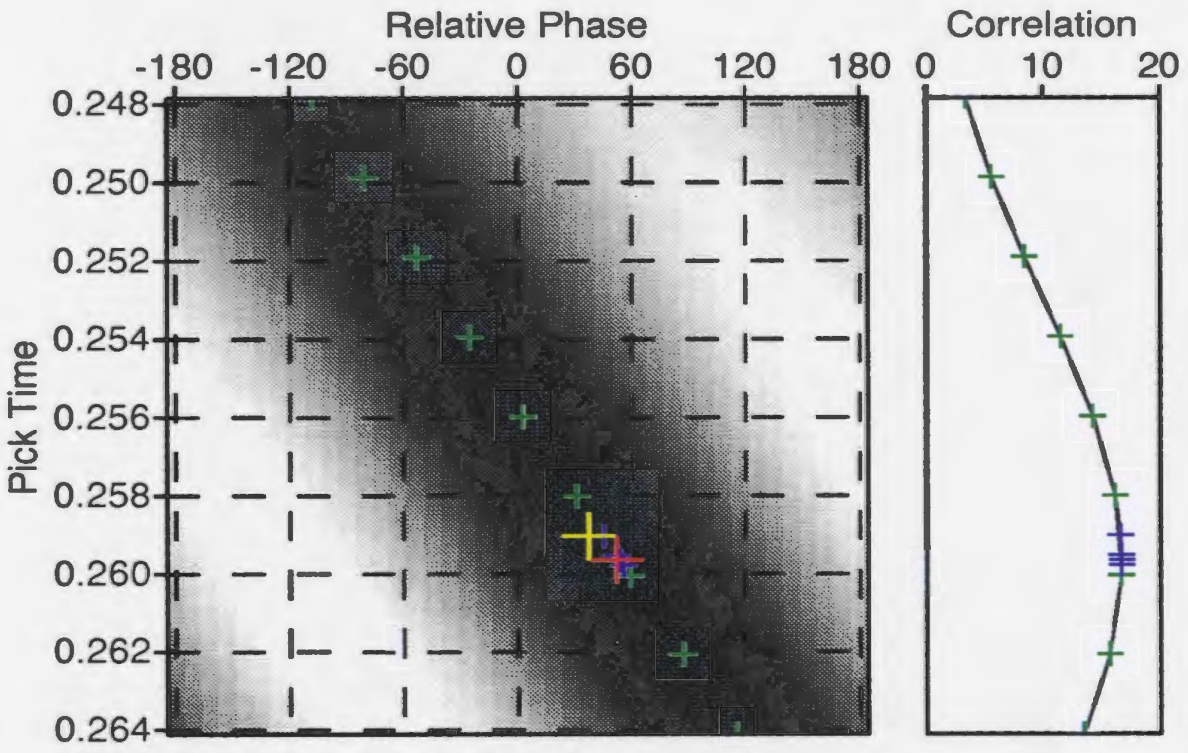

Figure 4.5. Same as Figure 4.4, but with 10% noise added to the time and phase-shifted wavelet. The yellow + shows the correct pick, while the red + shows the final pick, which has an error of 0.6 ms.

successful in finding the time and phase of maximum correlation, but the noise has introduced phase errors in the reference wavelet (see Figure 4.6) which have been translated into a picking error of about 1/3 of a sample. Since the reflection amplitudes from the sea-bottoms are generally well above any random background noise, the picking accuracy is typically between $^1/_4$ and $^1/_8$ of a sample. If the sea-floor is not overly rough, smoothing can help to reduce random picking errors, while the subsequent statics analysis can help to point out locations where the picks are particularly bad.

One potential problem is the assumption of a constant wavelet. Although

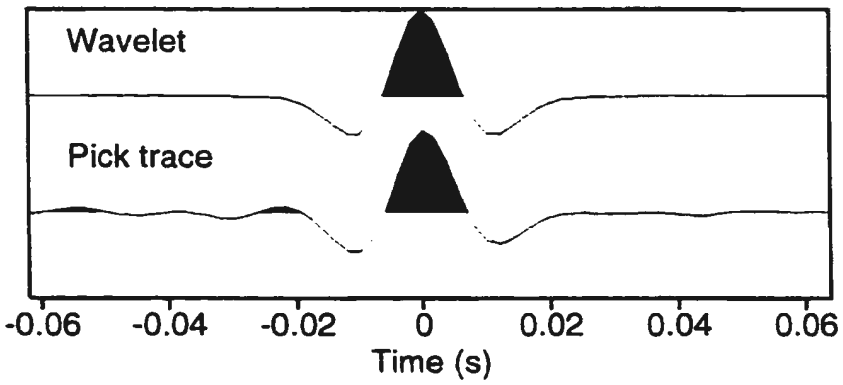

Figure 4.6. A comparison of the initial 30 Hz Ricker wavelet with the noisy pick trace that was used Figure 4.5. For easier comparison, the pick trace has been time and phase corrected. Note that the addition of random noise has produced an apparent phase shift.

marine seismic surveys tend to have a fairly consistent source signature, any variation in the wavelet could lead to picking errors. In order to reduce the likelihood of this happening, the routine includes a 'wavelet update' parameter, in which the reference wavelet is updated by combining it with some proportion (typically 5-10%) of the wavelet on the trace which is being picked. This should take into account smooth variations in the source signature.

4.4 Picking Routine Testing

In order to test the picking routine, synthetic seismograms were generated using a sea-floor model which has a fairly gentle undulation of twenty metres amplitude and 1000 metres wavelength. Initial velocities were chosen so that all of the near trace arrivals were pre-critical (constant phase). Figure 4.7a shows the picking of the noise-free case, which produced picking errors well within the

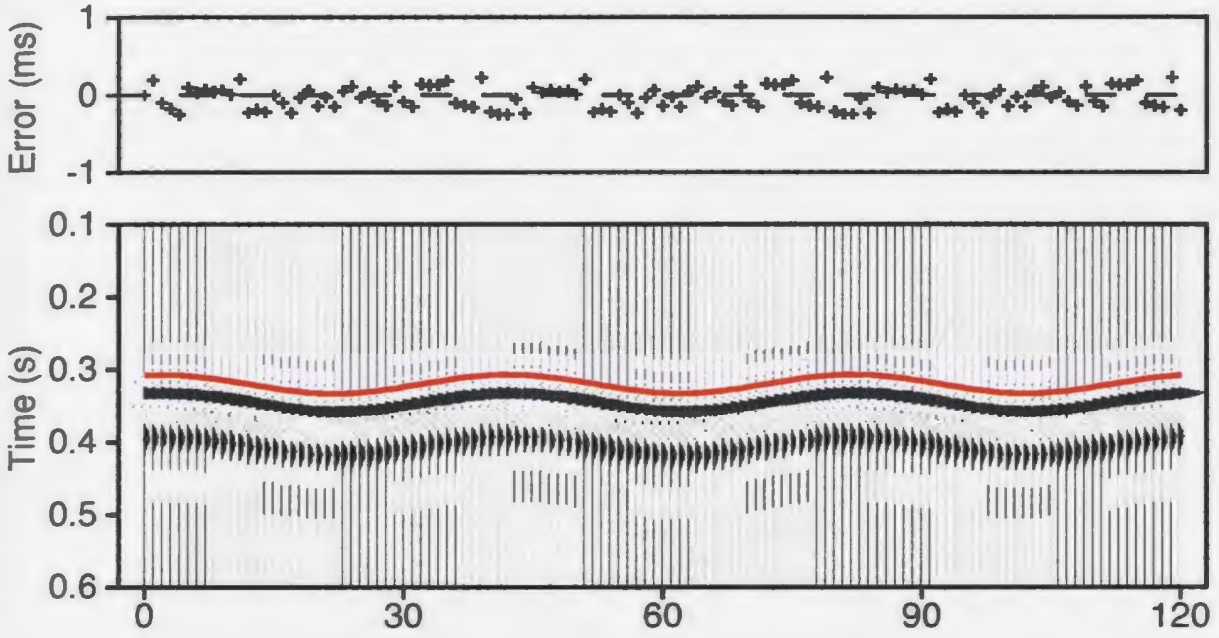

Figure 4.7(a) The automatic picking of undulating synthetics. Picking errors are within 0.25 ms, equal to 1/16th of a sample, the actual precision of the routine.

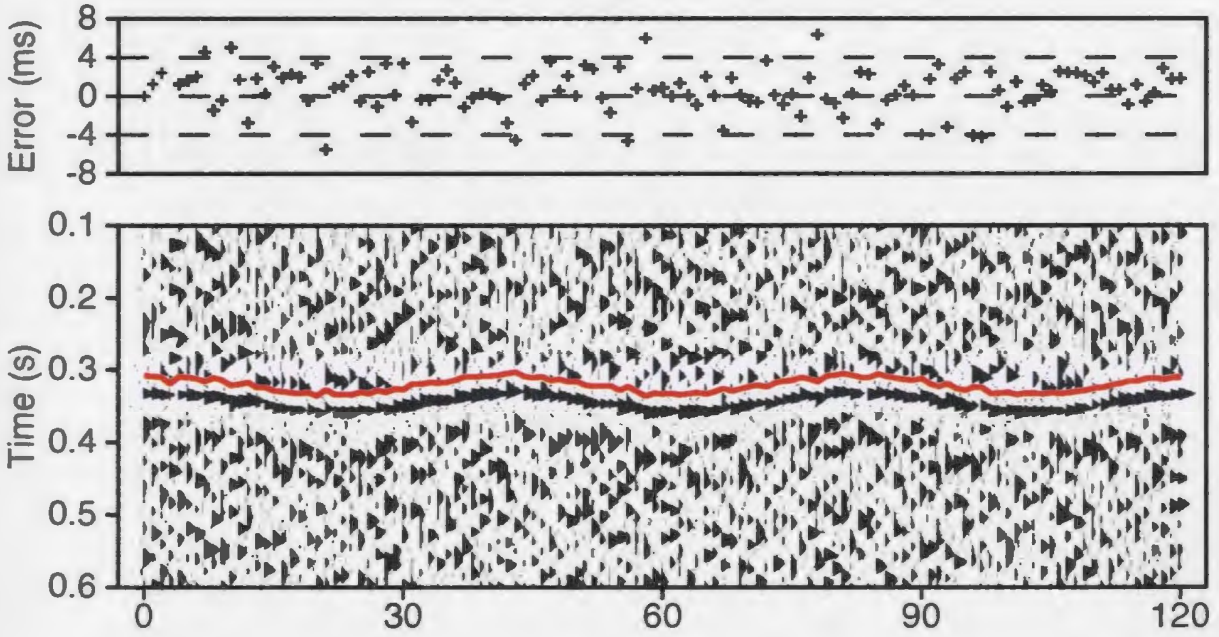

Figure 4.7(b) The picking of undulating synthetics after the addition of random noise. The maximum error has increased to over 4 ms.

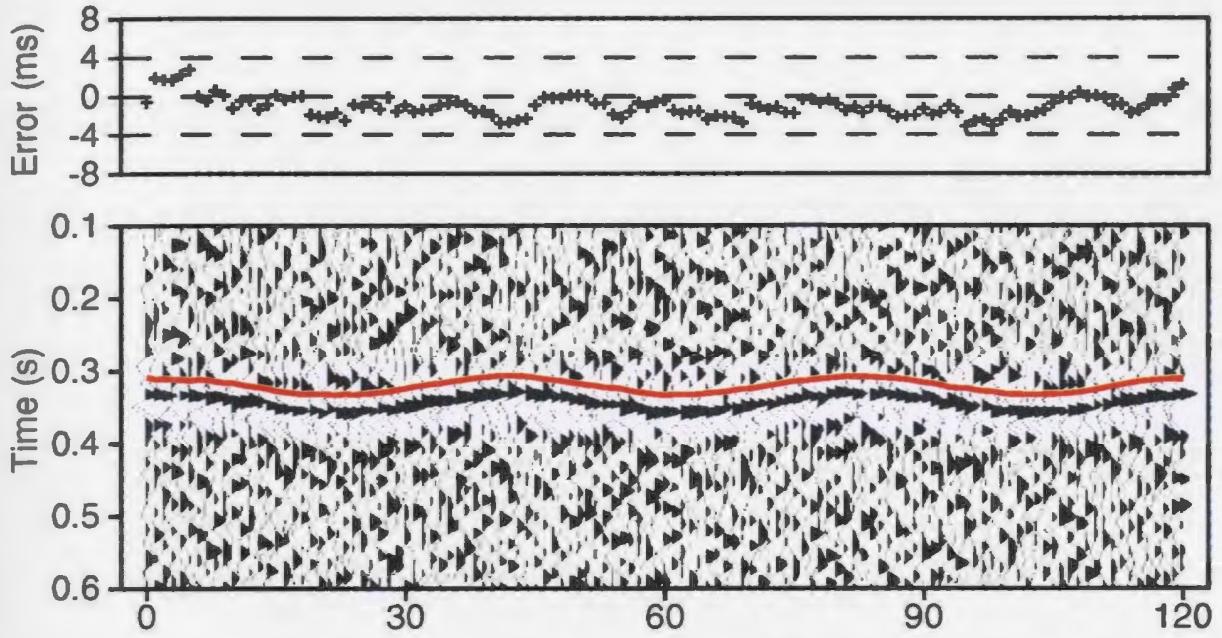

Figure 4.8. Results of picking noisy data after smoothing using a five point smoothing filter.

precision of the picking routine. Although hard sea-floors generally produce such strong reflections that background noise is not a problem, random noise is a simple way to test the stability of the picking routine. Figure 4.7b shows the picking results for noisy synthetics with a noise amplitude equal to the actual signal. As expected, the picks show considerable variation, with picking errors up to 4 ms. However, since the sea-floor topography was relatively mild, smoothing was very effective in reducing this type of random picking error (see Figure 4.8).

In order to test the phase prediction component of the picking routine, synthetics were generated using a dipping sea-floor model which contains a

major phase rotation (see Figure 4.9). The extreme phase variation was dealt with very successfully and again the picking errors were within the precision of the routine. Noise was added to the model to test the stability of the phase prediction (see Figure 4.10). Again, the phase variation was dealt with very well, with the noise introducing random picking errors of up to 4 ms.

For comparison, the model was also picked without the phase prediction (see Figure 4.11). Although the wavelet update was able to partially compensate for the phase variation, the picks are still pulled down off the true first breaks. This type of picking error clearly would produce significant errors in the sea-floor model.

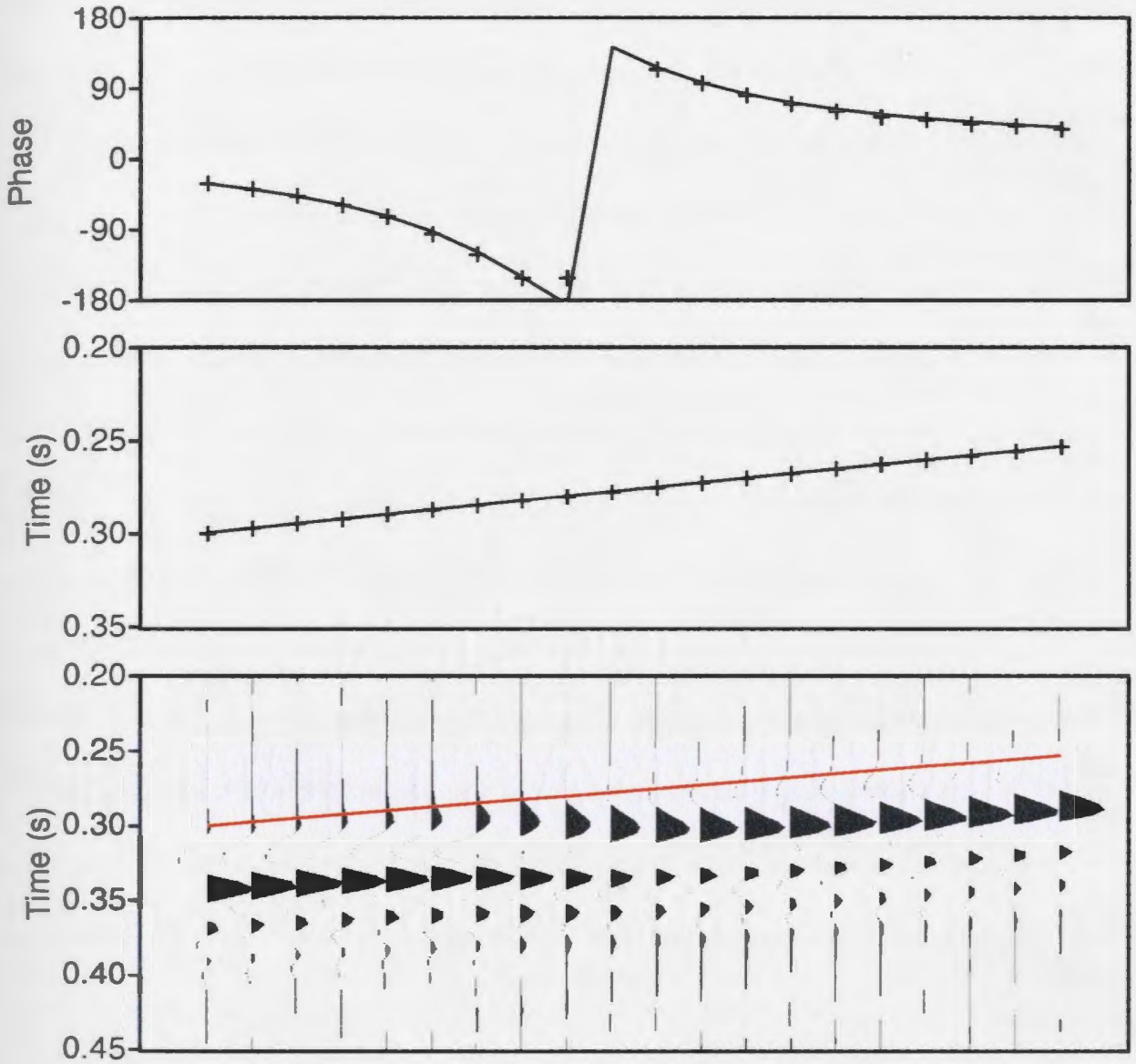

Figure 4.9. Picking results across a major phase rotation for noise-free data. The solid lines in the top two plots show the actual phase and time of the event, while the +s show the picked estimates. The bottom plot shows the picks on top of the data.

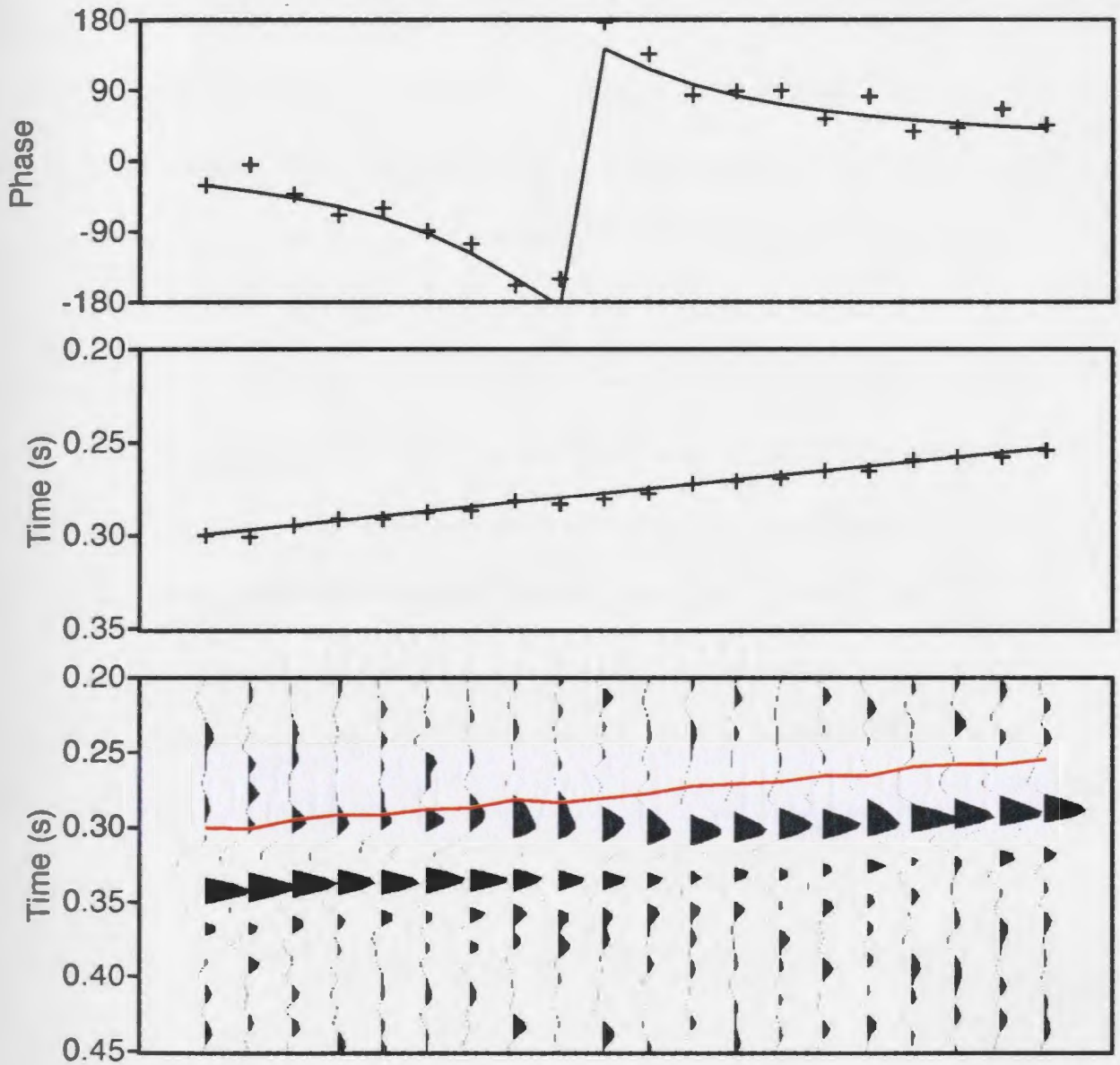

Figure 4.10. Picking results across a major phase rotation for noisy data (compare to Figure 4.9).

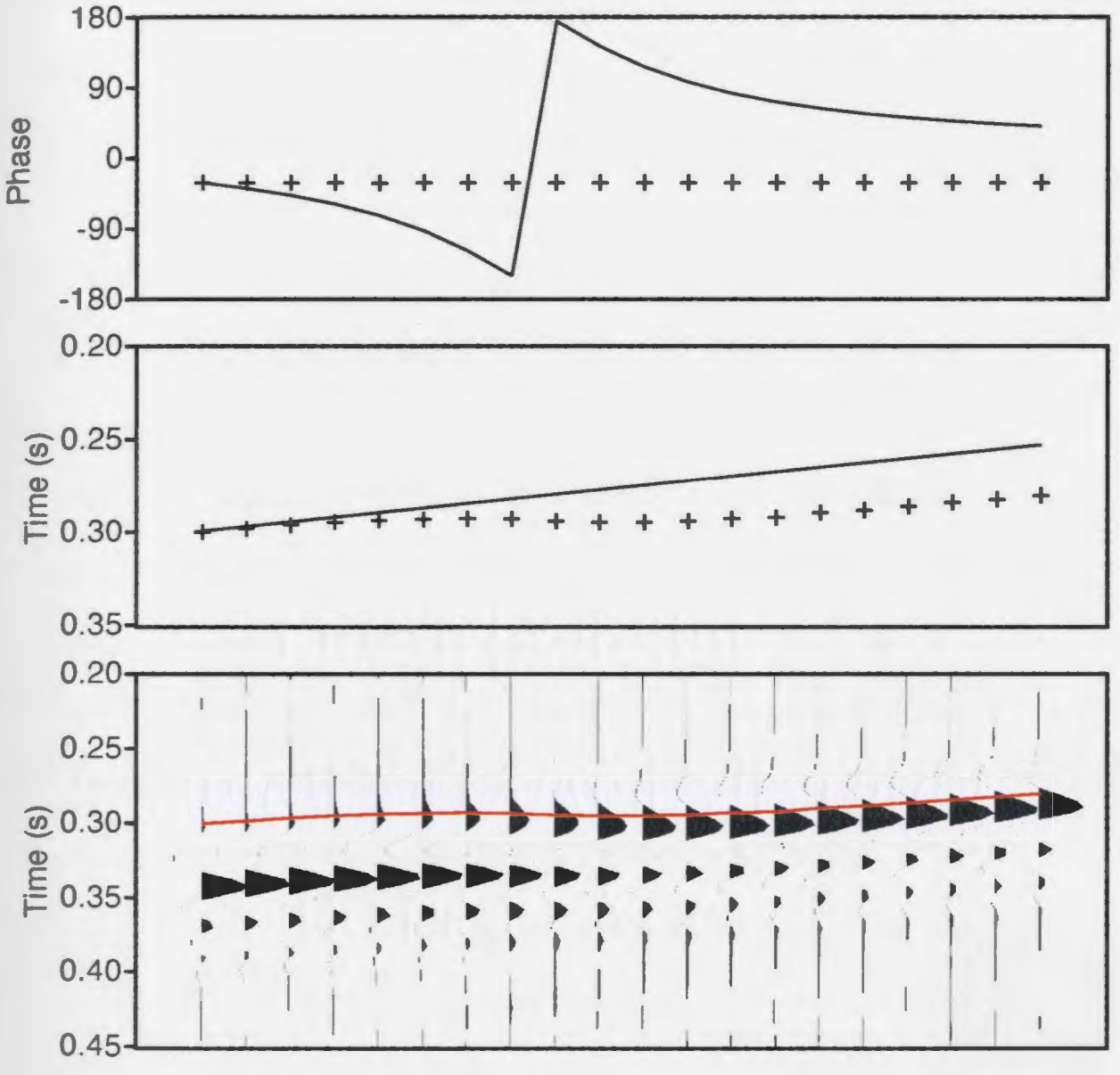

Figure 4.11. Picking results across a major phase rotation for noise-free data, without the phase estimation. The picking routine follows the initial peak of the wavelet, and hence is pulled off the true first break.

4.5 Pick Migration

If we were to assume that the sea-floor is relatively horizontal, then the water depth would simply be equal to half the product of the water velocity and the NMO corrected pick time. Unfortunately, this would lead to very large timing errors whenever the sea-floor is not horizontal. However, if we assume that the sea-floor is a locally planar reflector with constant dip between the source and receiver, the timing errors are significantly reduced, and even large topographic variations can be accommodated. Since we are considering here only the near traces, this is rarely a problematic assumption. In this case, the geometry can be described by the cosine law (see Figure 4.12):

$$\begin{aligned} r^2 &= 4h_0^2 + x^2 - 4h_0 x \cos(\tfrac{\pi}{2} - \theta) \\ &= 4h_0^2 + x^2 - 4h_0 x \sin\theta \end{aligned} \tag{4.10}$$

where r is the distance traveled by the ray, h_0 is the distance from the source to the sea-floor, x is the source-receiver offset and θ is the dip of the sea-floor. Therefore, the total travel-time, corresponding to our pick times, is given by

$$t_0 = (4h_0^2 + x^2 - 4h_0 x \sin\theta)^{\frac{1}{2}} / v \tag{4.11}$$

where v is the water velocity. This equation is easily solved for h_0:

$$\begin{aligned} h_0 &= \left(x\sin\theta + \sqrt{x^2\sin^2\theta - (x^2 - v^2 t_0^2)}\right) / 2 \\ &= \left(x\sin\theta + \sqrt{v^2 t_0^2 - x^2\cos^2\theta}\right) / 2 \end{aligned} \tag{4.12}$$

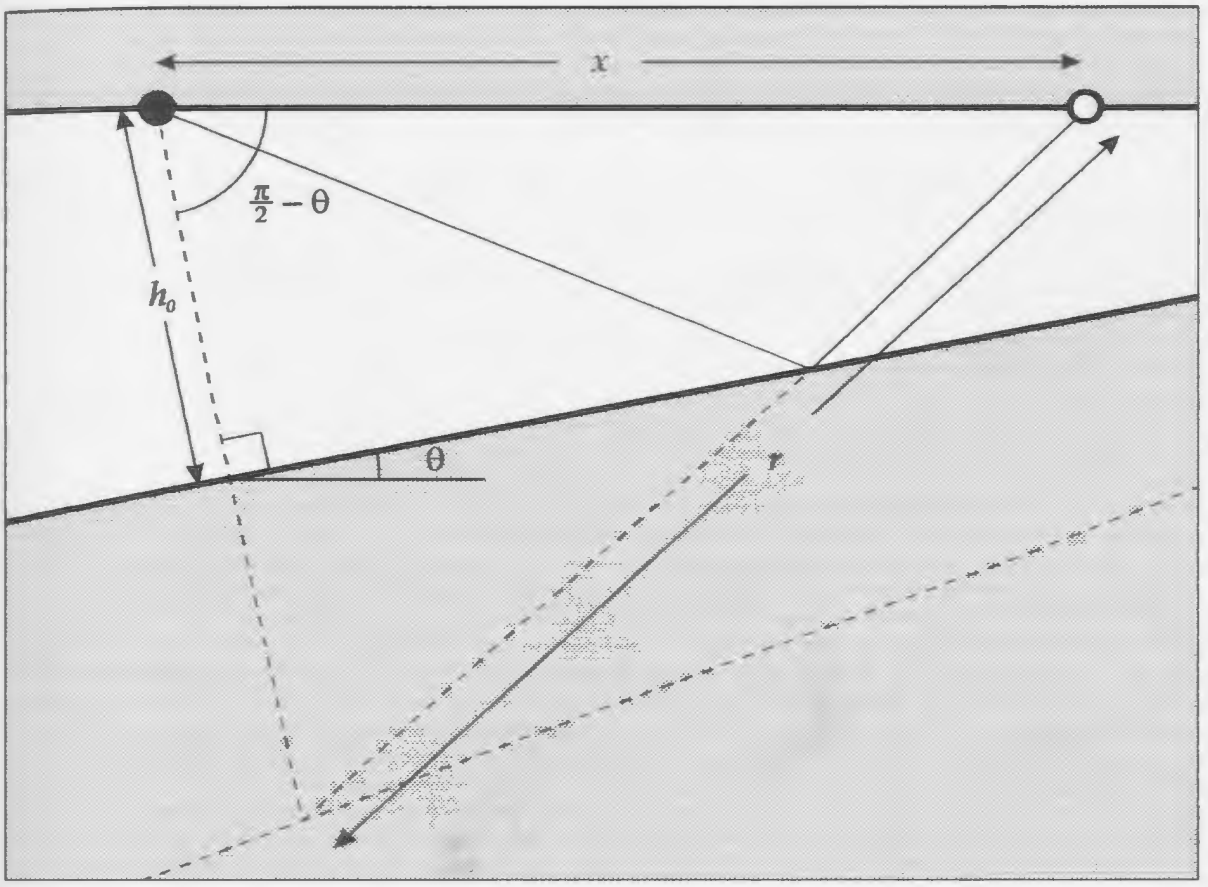

Figure 4.12. Illustration of the basic geometry for a primary arrival from a dipping sea-bottom. By imaging the source below the reflector, the calculation of ray length becomes a simple application of the cosine law.

Once h_0 has been determined, the actual water depth is calculated by moving along the plane to the midpoint (see Figure 4.13). The actual relationship is:

$$\begin{aligned} d &= \frac{h_0}{\cos\theta} - \frac{x}{2}\tan\theta \\ &= \left(h_0 - \frac{x}{2}\sin\theta\right) / \cos\theta \\ &= \frac{1}{2}\sqrt{\frac{v^2 t_0^{\,2}}{\cos^2\theta} - x^2} \end{aligned} \tag{4.13}$$

This is very dependent upon the sea-floor dip, θ, which is the only term that is

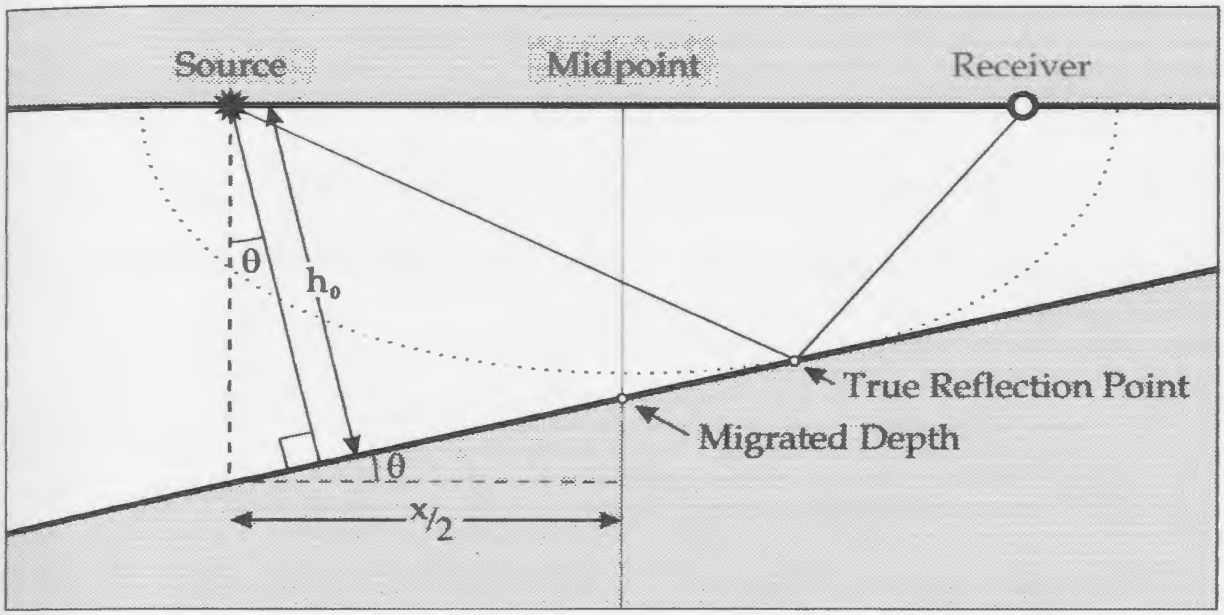

Figure 4.13. Constant dip migration of travel time picks. The true location of the pick is known to lie on the dotted ellipse. If we assume that the reflector has a constant dip between the source and the receiver and that the dip is known, we can determine the location of the true reflection point. We can then calculate the depth at the source-receiver midpoint.

not predetermined. As a result, the accuracy of our model is based to a large extent on our ability to determine θ.

I chose to predict θ using an iterative approach in which the NMO corrected picks of adjacent source-receiver pairs provide a starting estimate of the water depths at the source and receiver. The sea-floor dip is determined using

$$\theta_{BD} = \tan^{-1}\left(\frac{v(t_{nmo}^{CE} - t_{nmo}^{AC})}{2x}\right) \tag{4.14}$$

where θ_{BD} is the dip for the source-receiver pair BD and t_{nmo}^{CE} is the NMO corrected pick from source-receiver pair CE in Figure 4.14. Once we have a

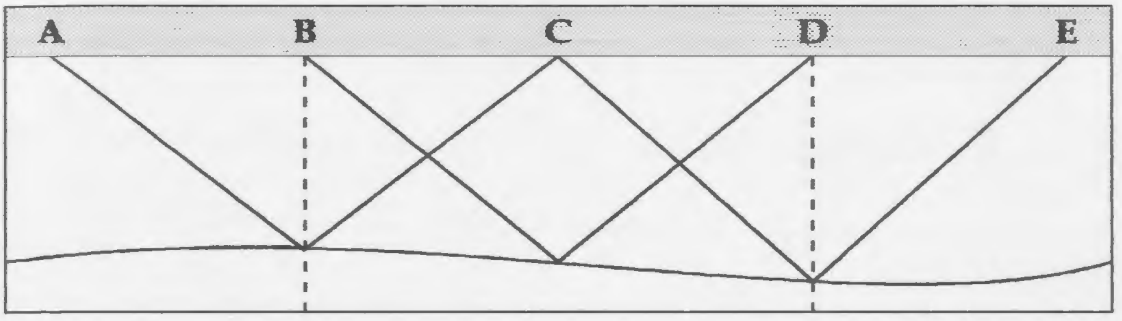

Figure 4.14. Schematic illustration of the experiment locations described in Equations 4.14 and 4.15. The source-receiver pairs AC and CE are used to estimate the dip and subsequently the depth at the midpoint of BD.

starting value for θ, we can use Equation 4.13 to calculate initial depth estimates, which can then be used to improve the dip accuracy. The dip calculation then becomes:

$$\theta_{BD} = \tan^{-1}\left(\frac{d^{CE} - d^{AC}}{x}\right) \tag{4.15}$$

We can iterate between Equations 4.13 and 4.15 until θ converges. This occurs very quickly; even steep dips require only 3 iterations. Figure 4.15 shows the convergence and associated timing errors for a reflector which has a depth starting at 100 metres and a dip of 45°.

Seafloor variations having wavelengths less than the near offset will not be properly modelled by this technique. However, the errors that this introduces in the raytracing results will be corrected in the adaptive part of the multiple attenuation routine. Furthermore, the raytracing routine is able to find the correct rays more easily if the seafloor topography is not complicated. Since the

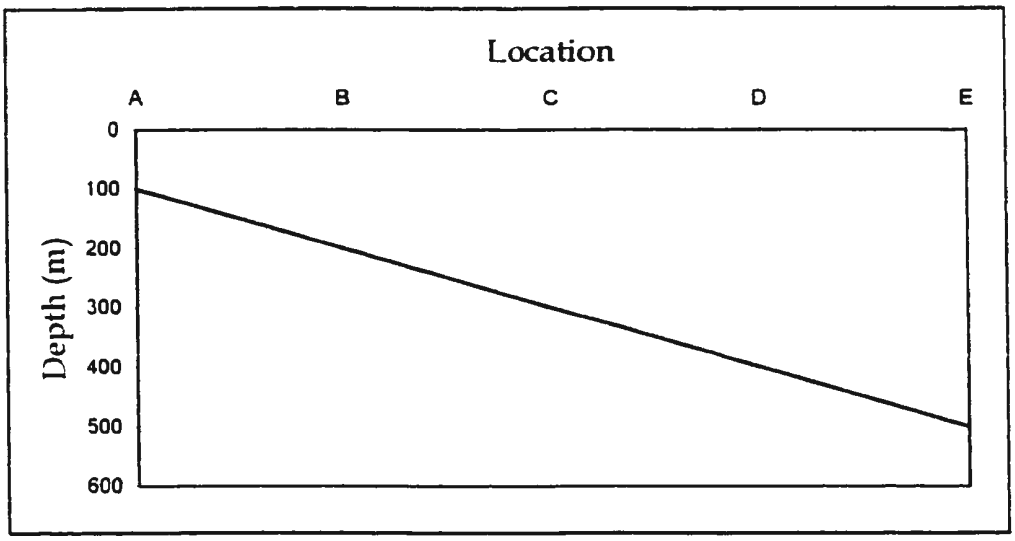

Iteration	Θ	Timing Errors (s)	
		Primary	Multiple 4
0	37.12	-0.0090	-0.0449
1	46.01	0.0011	0.0053
2	44.87	-0.0001	-0.0007
3	45.02	0.0000	0.0001
4	45.00	0.0000	0.0000

Figure 4.15. The convergence of the dip calculation. The model has a dip of 45°, a source-receiver offset of 200 m and a source interval of 100 m. Iteration 0 refers to the initial dip estimate which is based on NMO corrected times for AC and CE. Subsequent calculations iterate between Equations 4.13 and 4.15.

modelling effectively ignores the short wavelength features, it forces the seafloor model to be relatively smooth and improves the convergence of the raytracing.

4.6 Timing Considerations

Before using the picks to generate a sea-floor model, we must be sure that the picks are truly indicative of the water depth. Source and receiver statics must be

accurate and the picks must be exactly at the first break of the wavelet. Any errors can produce model errors which can in turn reduce the effectiveness of the multiple suppression. Fortunately, the time interval between the multiples is independent of these timing considerations and therefore can be used to determine any necessary corrections.

If we recall that the multiples can be considered reflections from an image of the sea-surface mirrored across the sea-floor (see Figure 4.16a), the multiple travel-times are given by

$$t_k = (4h_k^2 + x^2 - 4h_k x \sin[(k+1)\theta])^{\frac{1}{2}} / v \qquad (4.16)$$

where k is the multiple order.

Since the imaged reflectors for all multiple orders intersect the sea surface at the same point (see Figure 4.16b), there is a simple relationship between the source-image distances:

$$h_k = \frac{h_0 \sin[(k+1)\theta]}{\sin\theta} \qquad (4.17)$$

By combining equation 4.17 with equation 4.16, we are able to calculate the travel times for any multiple order based on the dip estimate generated during the initial migration.

In order to calculate the optimal timing correction for each trace, a time shift is applied to the pick time before the migration. Once the position of the reflector is calculated, times are generated for a given number of sea-floor

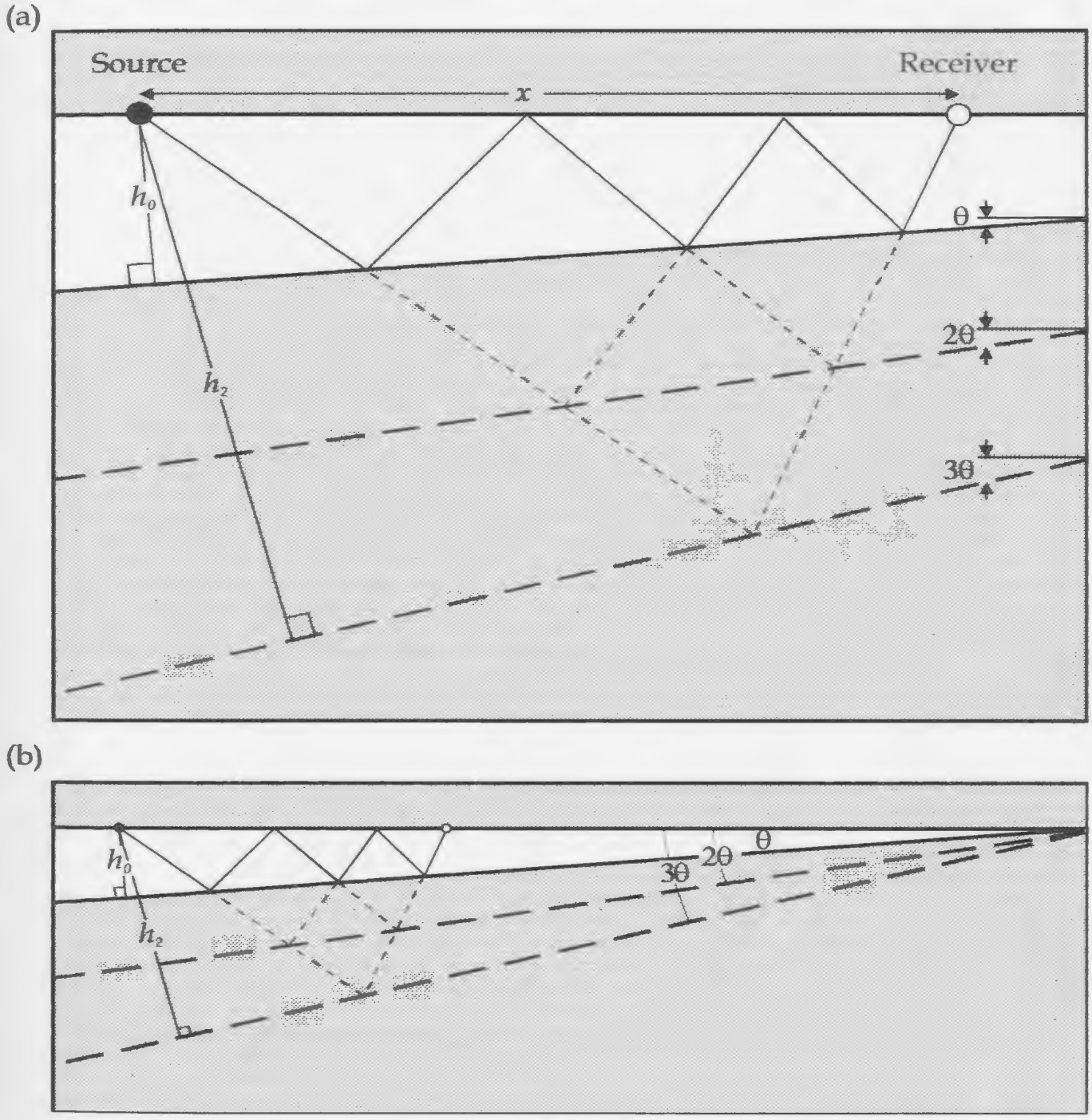

Figure 4.16. Geometry of the ray path for a second order multiple. (a) illustrates how the multiple can be imaged as if it were a primary from an event with depth h_2 and a dip of 3θ. (b) shows the relationship between h_2 and h_0.

multiples. The data windows immediately following those times are then stacked, and the total stacked energy is recorded. A range of time shifts are tested, and the shift which produces the highest stacked energy is chosen as the best shift for that trace. The procedure is then repeated for each trace independently.

If the correct statics have been applied to the data, the optimal time shift should be equal to the difference between the pick time and the actual first break time of the water-bottom reflection. If the picking has consistently picked the same part of the wavelet, the time shift should be the same for all traces. As a result, one bulk time shift is chosen by using a multi-pass averaging algorithm in which outliers are excluded from the average. This shift is then applied to all traces, and the picks are again migrated in order to produce the optimal depth model. If the shifts are not relatively constant, the anomalies can be used to identify problem areas and the model can be fine tuned, either by smoothing or by manual picking.

4.7 Modelling Examples - Sloping Data

Since the modelling routine is based on a constant dip assumption between each source and receiver pair, the obvious choice for the initial testing is one in which the sea-floor has a constant dip over the entire section. Figure 4.17 shows

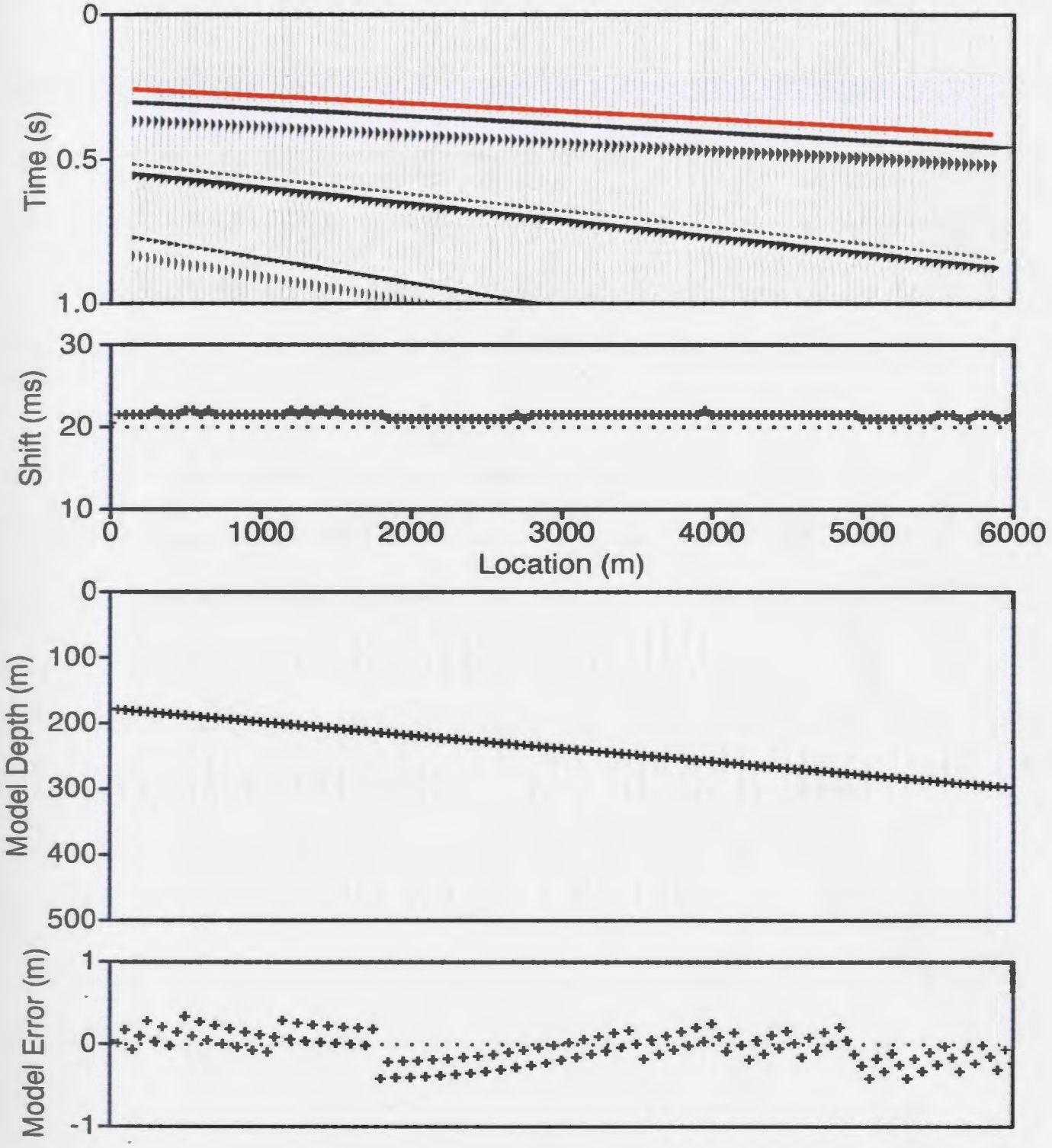

Figure 4.17. Overlay of automatic picks on the sloping data, the results of the static estimates on each trace, the resulting model and the model errors. Four orders of multiples were used in stacking the statics estimate.

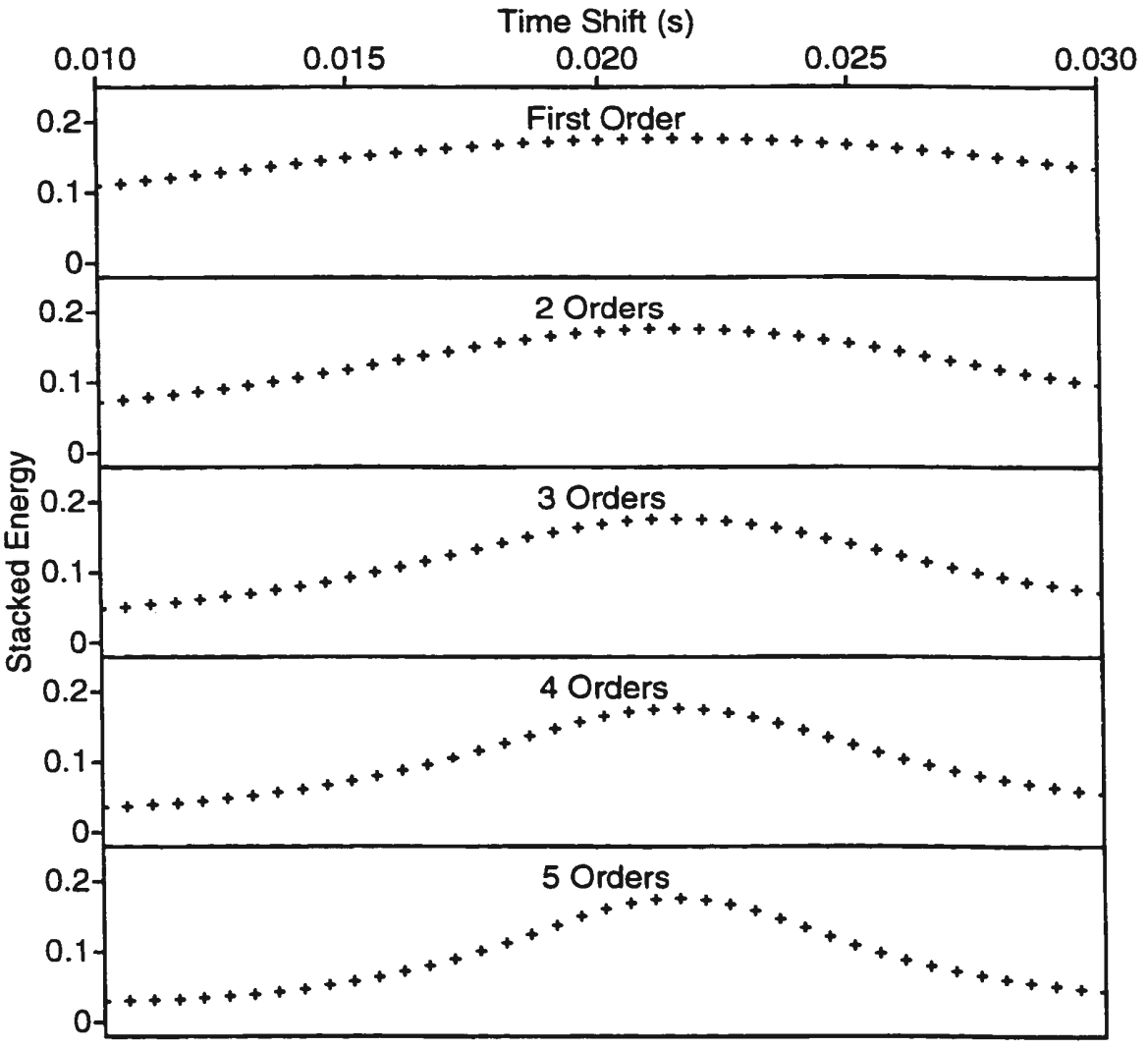

Figure 4.18. Resolution of the statics solution. As higher order multiples are included in the stack, the peak becomes narrower, improving the resolution.

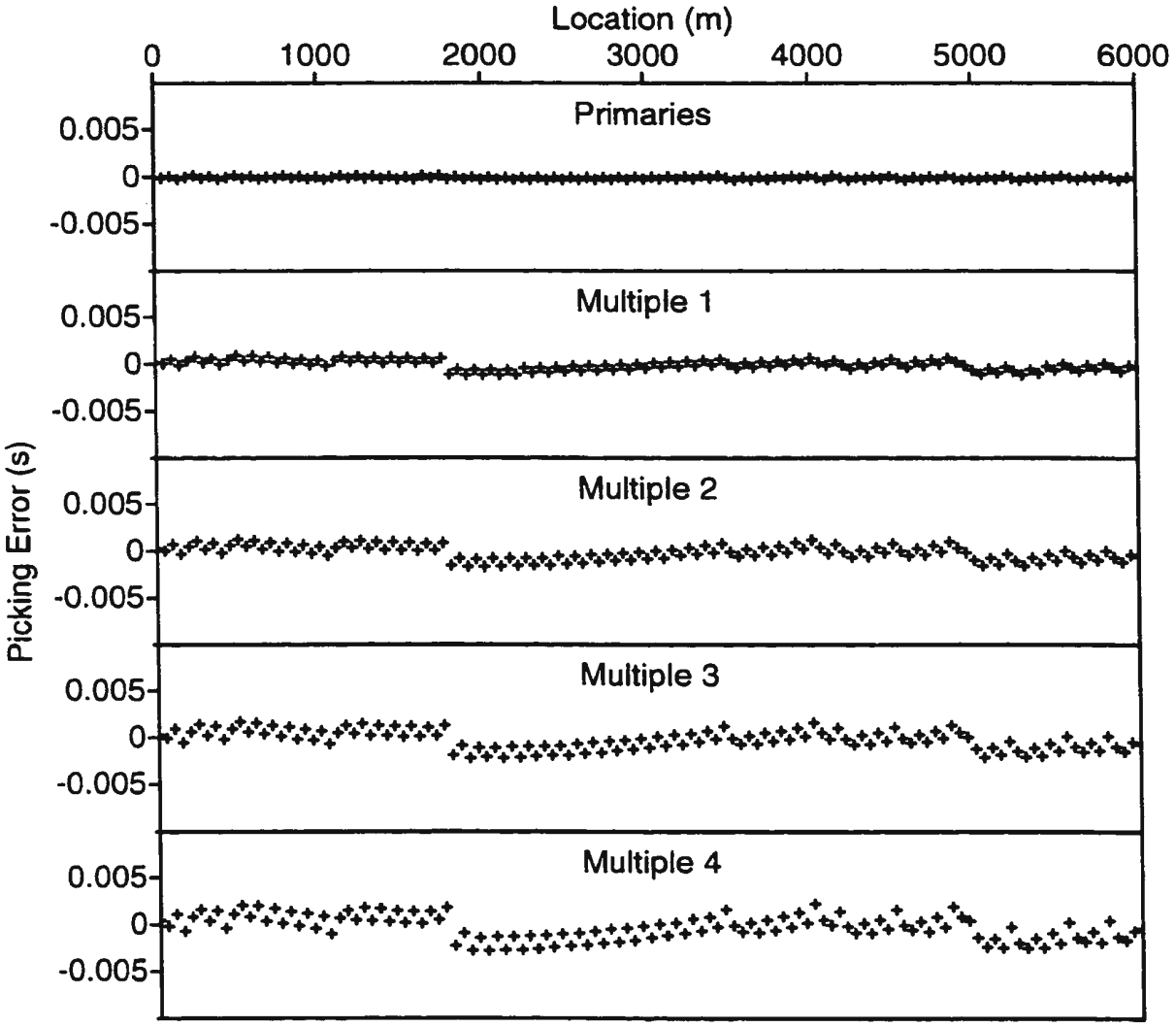

Figure 4.19. Errors in the timing estimates which have been caused by errors in the pick times. The initial picking errors on the primaries are exaggerated by each successive order of multiple.

the test data with the automatic picks as well as the modelling results. The time shift estimates converge to within a millisecond and the resulting depth model has errors of less than a metre.

Figure 4.18 illustrates how stacking more multiples improves the resolution of the statics estimate, since higher order multiples are more sensitive to the actual water depth. However, this sensitivity can also be a problem since it also amplifies picking errors. The timing errors for the first four orders of multiples are shown in Figure 4.19. As expected, the picking errors are exaggerated by each successive multiple order, so that the error of less than one millisecond on the primary is translated into almost four milliseconds on the fourth order multiple. This implies that there are limits to how many multiples should be used to generate the statics estimates, since the amplification of the picking errors reduces the likelihood of subsequent multiples stacking constructively. In general, the inclusion of four to six orders of multiples seems to produce good results.

In order to look at the effect of choosing an incorrect water velocity, the data were also modelled using a velocity of 1500 ms^{-1}. The solution appears to be very good (see Figure 4.20). The estimated arrival times for the multiples do coincide with actual events. However, when the predicted model is raytraced, there is a very obvious problem on the far traces, where the arrival estimates are

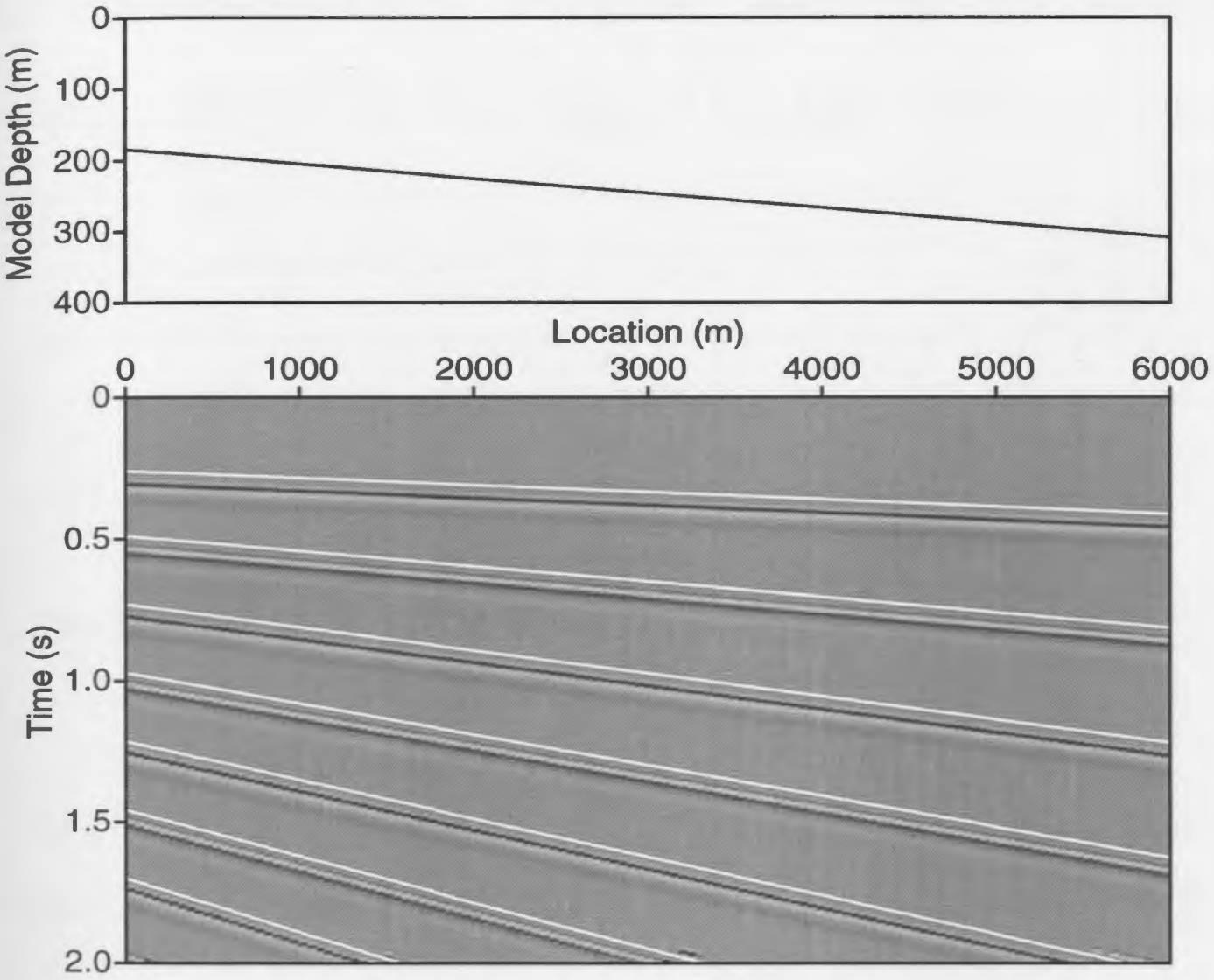

Figure 4.20. The results of modelling the multiples with the wrong water velocity. The picks (solid white lines) look very good on the near trace gather, following the events almost perfectly.

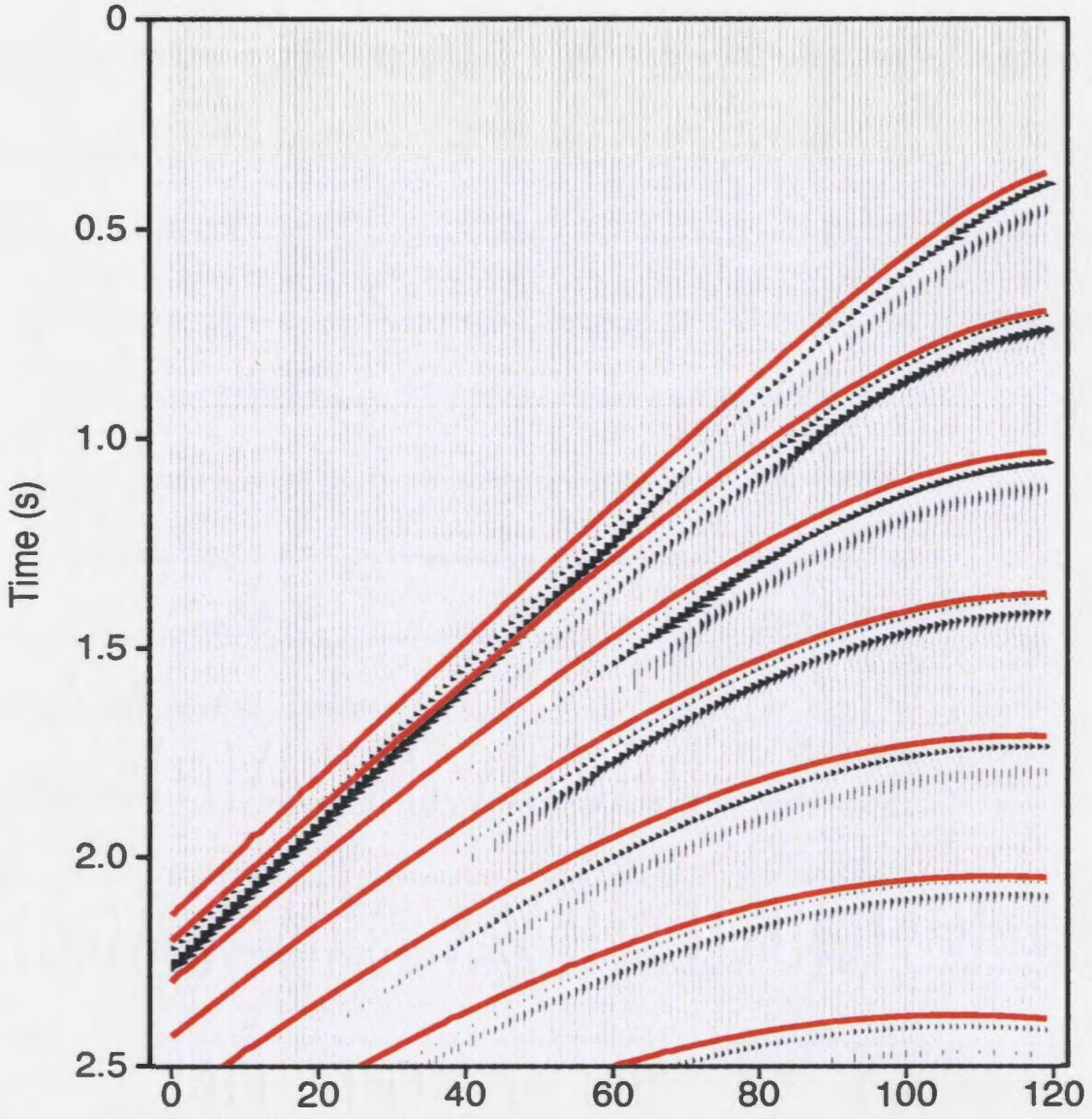

Figure 4.21. The raytracing results for a shot gather at location 6000 m. The model was generated with the wrong velocity, consequently the picks do not follow the events at the far offsets.

early (see Figure 4.21). This clearly illustrates the need for water velocity testing before the model is used for raytracing-based multiple suppression.

4.8 Modelling Examples - Undulating Data

The next series of examples use the same undulating data that was used for testing the picking routine. Figure 4.22 shows the synthetic near-trace gather from the undulating sea-floor model, with the automatic picks and the modelling results. Again, the statics solution is excellent as is the resulting model estimate. The constant-dip approximation does not cause significant reduction in the effectiveness of the modelling. The model error is still less than a metre.

The final test uses the same data, but with 20% noise added. The picks are good (see Figure 4.23), but the scatter increases the model error to more than two metres in some places. Application of a three point smoothing filter before the modelling is able to reduce that error to less than a metre (see Figure 4.24). While this type of filtering clearly reduces the lateral resolution of the water bottom, it does generate a smoother model which is more likely to produce reasonable raytracing results. Although the resulting model is not necessarily 'correct', it is sufficient for our purposes.

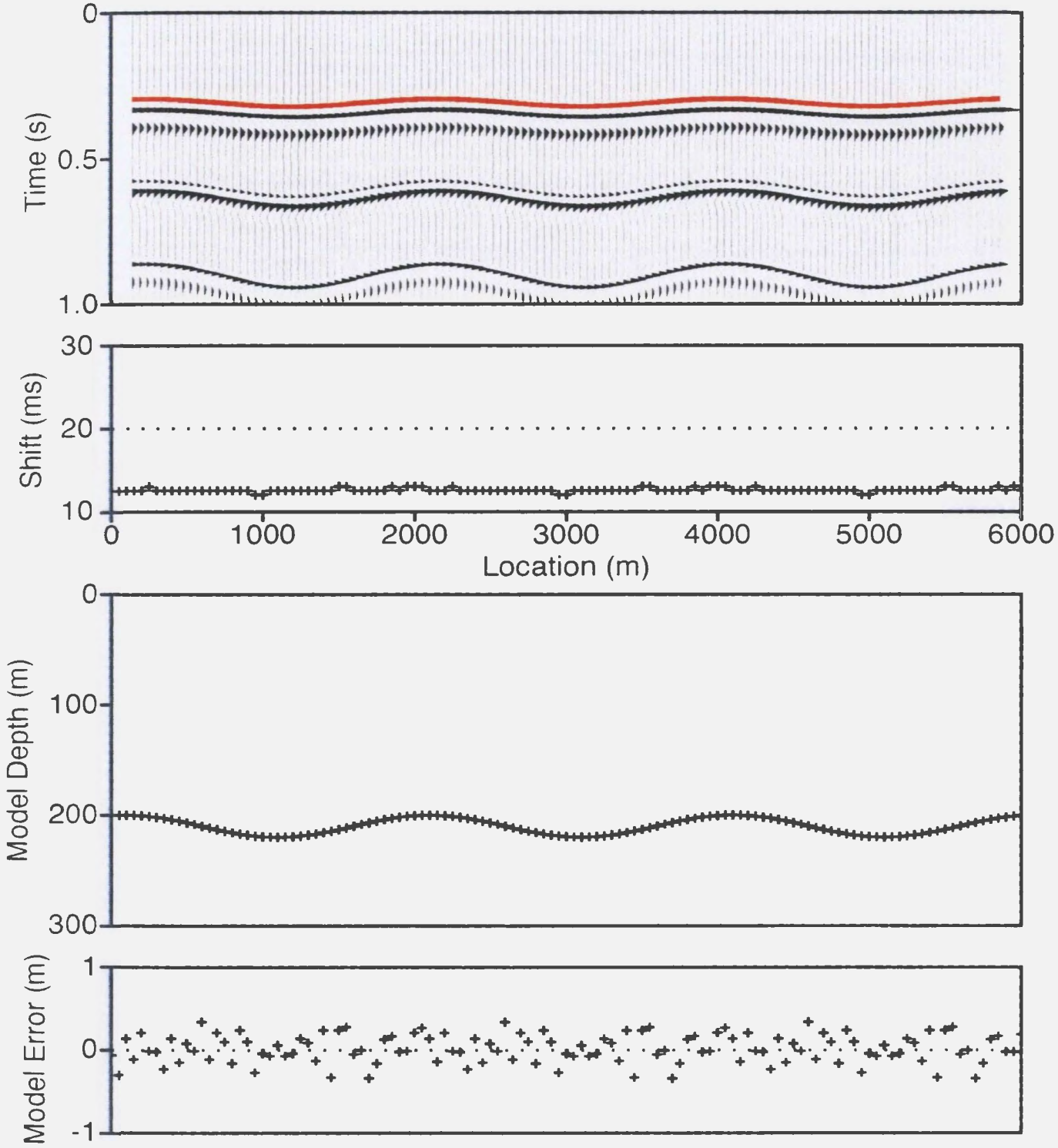

Figure 4.22. The modelling results for the undulating synthetics. The model has been reproduced to within 0.5 metres.

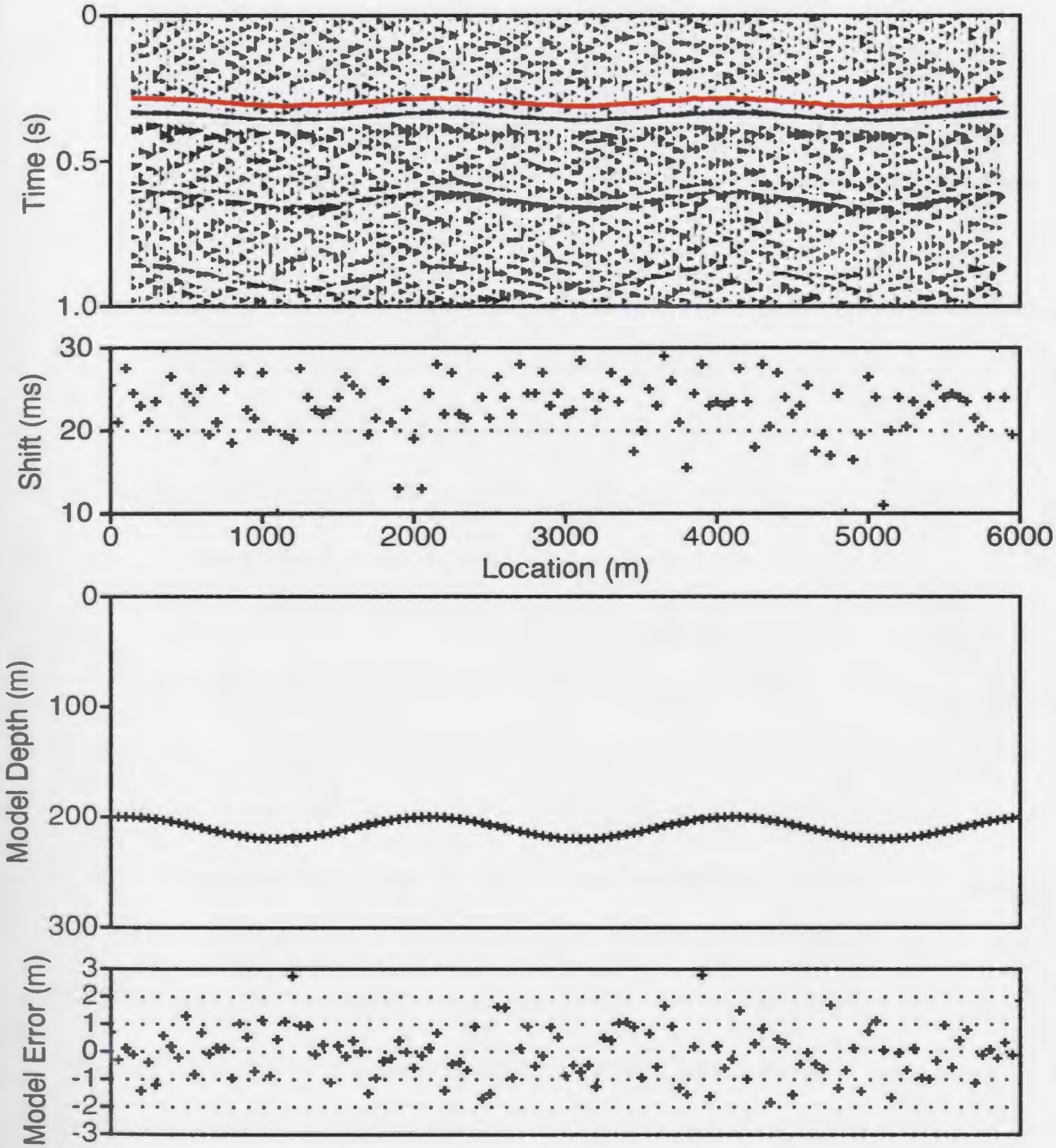

Figure 4.23. The modelling results for noisy data. Model errors exceed two metres at some locations, but overall the model is good.

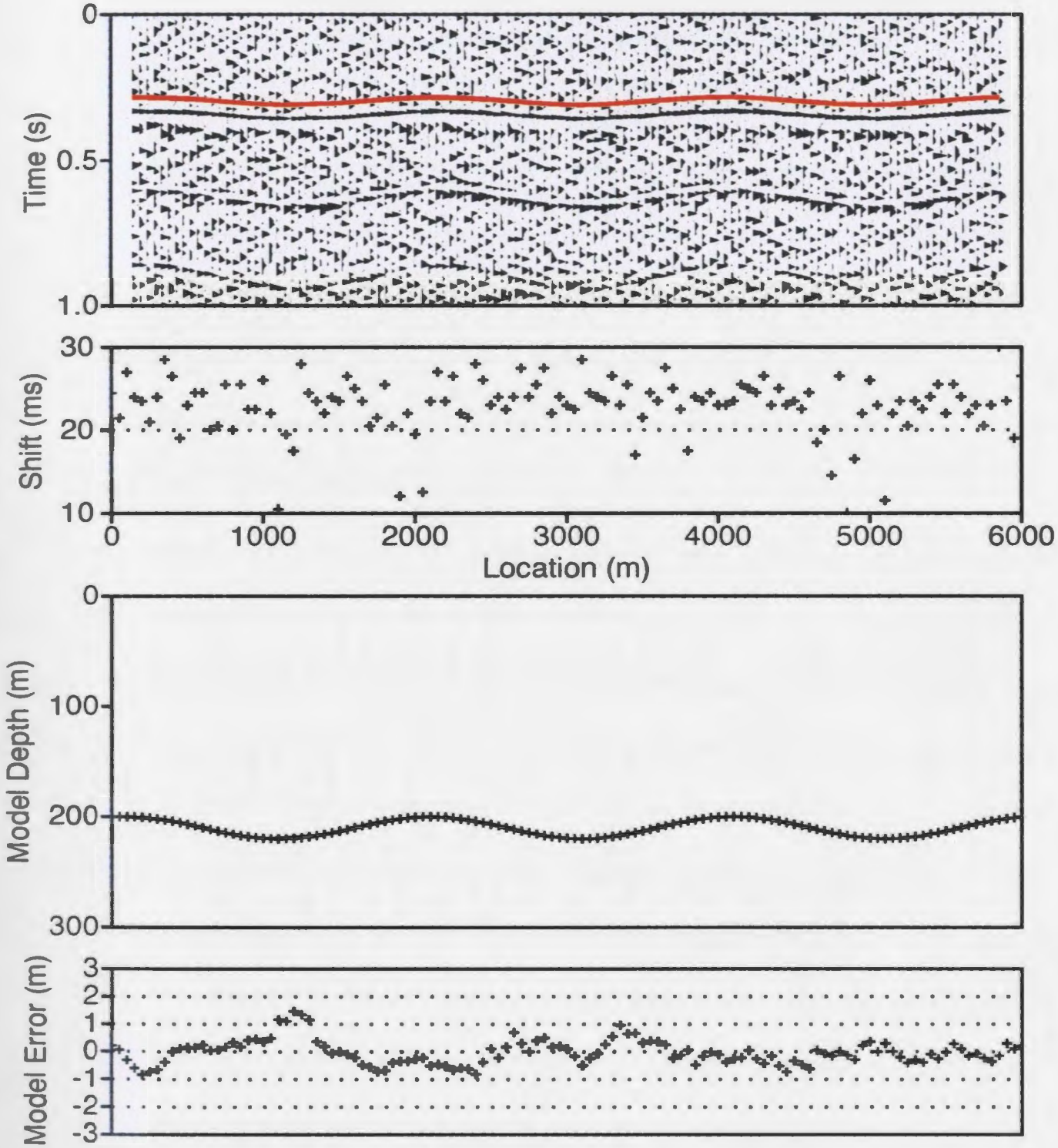

Figure 4.24. The modelling results produced by applying a five point smoothing filter to the initial picks. Since the original model was very smooth, smoothing the picks has reduced the error in the estimated model.

5. RAYMULT

5.1 Introduction

The combination of a very high velocity sea-floor and severe topography greatly reduces the effectiveness of most attenuation techniques. Raymult is a multiple attenuation technique which was developed to handle these conditions, which are prevalent off the coast of Newfoundland. Raymult models the arrival times, amplitudes and phases of the water bottom multiples on each shot gather, and then adapts the predictions to better fit the data. It generates an estimate of the seismic wavelet for each multiple and then subtracts the predicted multiples from the data.

5.2 Model interpolation

The model which is output by the near-trace pick migration gives the water bottom depths at a series of regularly spaced points corresponding to the near-trace midpoints. Since the raytracing requires a continuous surface, model interpolation is required. In order to guarantee a smooth surface, I chose to use a modified version of cubic splines,

$$f(x) = ax^3 + bx^2 + cx + d \tag{5.1}$$

where the spline parameters, a, b, c, and d, are determined using the depths and

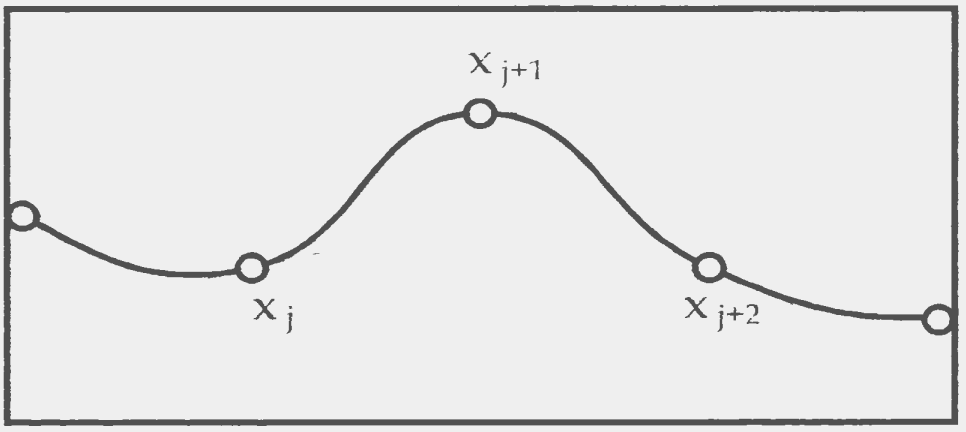

Figure 5.1. Illustration of modified cubic spline interpolation. The points between x_j and x_{j+1} are calculated using a cubic function which is determined by the depth and slope at those endpoints. The slope at x_{j+1} is approximated by the finite difference between the depths at x_j and x_{j+2}.

slopes of the adjacent points (see Figure 5.1). The boundary conditions are therefore:

$$\begin{aligned} f(0) &= x_j = d \\ f(\Delta x) &= x_{j+1} = a\Delta x^3 + b\Delta x^2 + c\Delta x + d \end{aligned} \tag{5.2}$$

as well as the finite difference derived slopes:

$$\begin{aligned} f'(0) &= (x_{j+1} - x_{j-1}) / 2\Delta x = c \\ f'(\Delta x) &= (x_{j+2} - x_j) / 2\Delta x = 3a\Delta x^2 + 2b\Delta x + c \end{aligned} \tag{5.3}$$

The spline is locally defined for each interval, with an x range of 0 to Δx. Since two of the cubic parameters, c and d, are set by the boundary conditions, only a and b actually need to be calculated, resulting in much faster computation than standard splines. The water bottom depth is calculated by first finding the correct interval for the desired location, and then using the appropriate spline

parameters to find the depth.

5.3 Raytracing

Numerous techniques have been developed for modelling seismic arrivals, but they can generally be classified into one of two categories: raytracing techniques, in which each event is modelled individually (e.g. asymptotic ray theory, WKBJ) and finite difference techniques in which the wave equation is used to propagate the entire wavefield through the model. Since Raymult requires information about specific events, raytracing was the obvious choice for modelling the multiples.

The raytracing routine used in Raymult is based on zero-order asymptotic ray theory (ART), in which the wave field is approximated by an infinite series of rays propagating at all angles away from the source (Cerveny et al., 1977). Since each ray has an infinitesimal width, ART is essentially a very high (i.e. infinite) frequency approximation of full wave theory. As a result, it is very sensitive to high frequencies in the model. The spline interpolation, which produces a smooth model, helps to minimize these effects.

The raytracing for each shot gather is performed using a 'shooting' approach, in which a range of start angles are used to project the ray from the source down to the sea-bottom and back to the surface until the ray arrives close to the desired

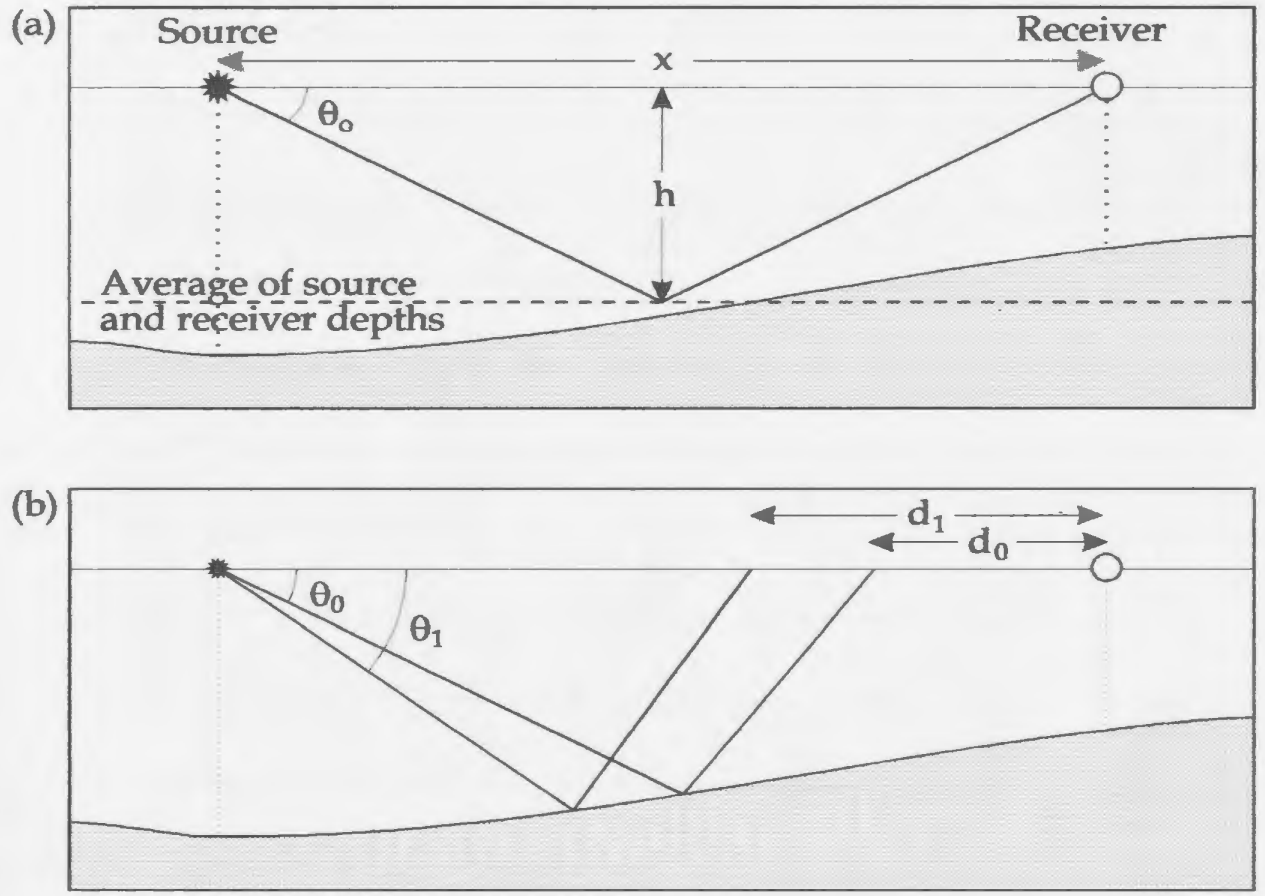

Figure 5.2. Illustration of raytracing parameters. (a) shows how the initial angle is determined using the average depth, while (b) shows the results of tracing the first two rays.

receiver. The initial angle estimate is based on a flat sea-floor approximation with a depth equal to the average of the depths below the source and the receiver (see Figure 5.2):

$$\theta_0 = \text{atan}(2h / x) \tag{5.4}$$

Two rays are then reflected off the sea-floor and back to the surface, one with a start angle equal to the initial estimate and the second with a start angle equal to the initial estimate plus a small increment (see Figure 5.2b). The angle

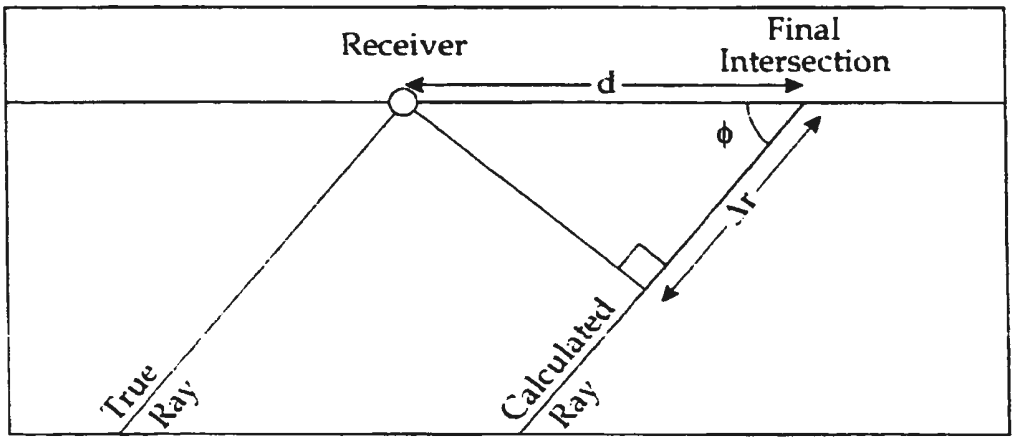

Figure 5.3. The final adjustment of the arrival time to account for the raytracing error.

increment for subsequent iterations is determined using the Newton-Raphson method (Press et al., 1986) and is based on the results of the previous two iterations:

$$\Delta\theta_{new} = -\frac{f(\theta)}{f'(\theta)} \qquad \text{where } f(\theta) = d_i$$
$$= -\frac{d_i}{d_i - d_{i-1}}\Delta\theta_{old} \tag{5.5}$$

The iterations are performed until the ray arrives within an acceptable distance of the receiver (usually 1-5 metres).

If convergence has not occurred within a given number of iterations (typically 10-20), the best result of all the iterations is used as a new starting point with a small initial increment. If convergence still does not occur, the closest result is taken and a warning is issued.

To minimize the timing errors, a small correction is made to the arrival times to account for the distance from the point of arrival to the actual receiver (see Figure 5.3):

$$\Delta t = \frac{\Delta r}{v_{\cdot\cdot}} = \frac{d\cos(\phi)}{v_{\cdot\cdot}} \tag{5.6}$$

Multiples are modelled in the same way, but obviously with multiple reflections from the sea-surface and sea-floor. Although this usually requires more iterations, all of the models I have tested have been raytraced successfully.

Figure 5.4 shows the arrival times, for the seafloor reflection and the first five orders of multiples, produced by raytracing a sloping model which has a water depth of 300 metres below the source and a constant slope of 0.1. A maximum arrival error of 10 m was allowed. This was chosen purposely to be greater than the allowable error that would ever be actually used, in order to illustrate the maximum timing errors that are likely. Without the timing correction, the errors are generally within 5 ms (see Figure 5.4b). With the timing correction, the maximum error is only 0.4 ms, with most events within 0.05 ms (see Figure 5.4c). This is more than sufficient for the attenuation routine.

5.4 Amplitude and Phase Modelling

Once the optimal ray has found, the amplitude and phase of the event has to be determined. These are calculated using the Tooley et al. (1965) solution of

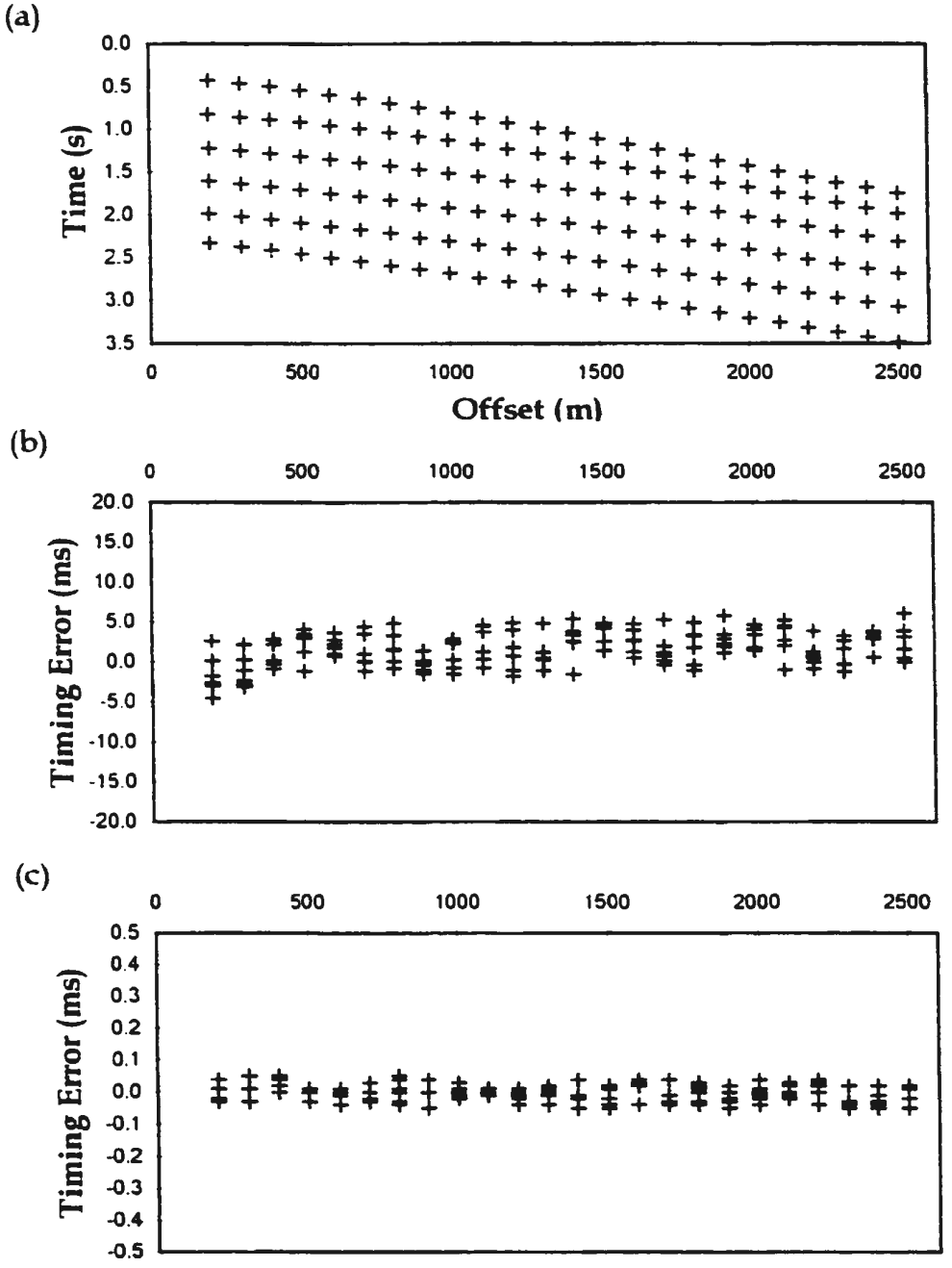

Figure 5.4. (a) Illustration of the arrival times of the seafloor reflection and the first five orders of multiples produced by raytracing a sloping model. (b) The actual timing errors after using a maximum arrival error of 10m. (c) The corrected timing errors produced by application of Equation 5.6.

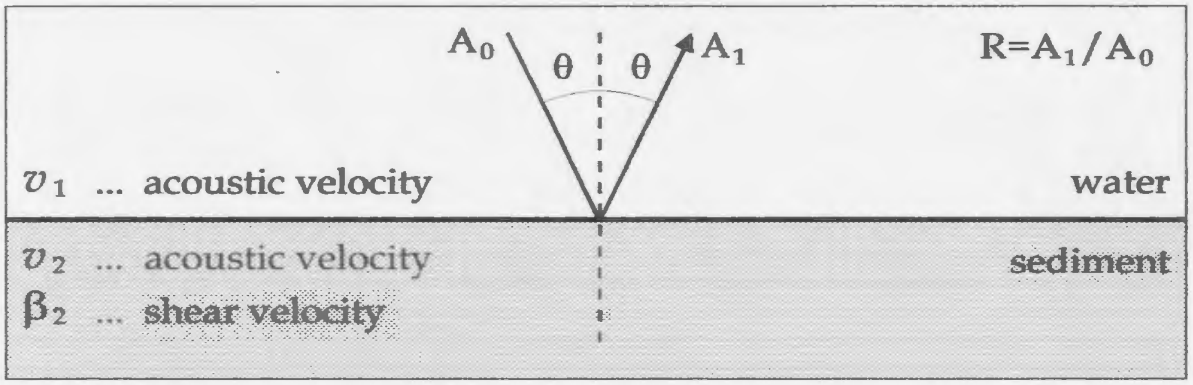

Figure 5.5. Reflection of a ray at the water-bottom, illustrating the parameters used in Equations 5.7-5.9.

Zoeppritz's equations for the reflection coefficient for the compressional wave:

$$R = -\frac{\frac{\rho_s^{\,2}\beta_s^{\,3}}{\rho_w^{\,2}v_w^{\,3}}\sin^2\theta\cdot a_1b_1a_2b_2 + \frac{v_s}{v_w}a_1q^2 - \frac{\rho_s}{4\rho_w}a_2}{\frac{\rho_s^{\,2}\beta_s^{\,3}}{\rho_w^{\,2}v_w^{\,3}}\sin^2\theta\cdot a_1b_1a_2b_2 + \frac{v_s}{v_w}a_1q^2 + \frac{\rho_s}{4\rho_w}a_2} \tag{5.7}$$

where,

$$a_1 = \cos\theta\,; \quad a_2 = (1-\frac{\alpha_s^{\,2}}{\alpha_w^{\,2}}\sin^2\theta)^{\frac{1}{2}}\,; \quad b_2 = (1-\frac{\beta_s^{\,2}}{\alpha_w^{\,2}}\sin^2\theta)^{\frac{1}{2}} \tag{5.8}$$

and

$$q = \frac{\rho_s}{\rho_w}\left(\frac{1}{2} - \frac{\beta_s^{\,2}}{\alpha_w^{\,2}}\sin^2\theta\right). \tag{5.9}$$

The variables α and β are the acoustic and shear velocities, while ρ is the density and θ is the angle of incidence (see Figure 5.5). The subscript w refers to water properties while the s refers to sea-floor properties. Clearly, as θ increases past the P-wave critical angle, a_2 becomes complex, and when θ passes the PS-wave critical angle, b_2 becomes complex. These two terms therefore control the phase of the event.

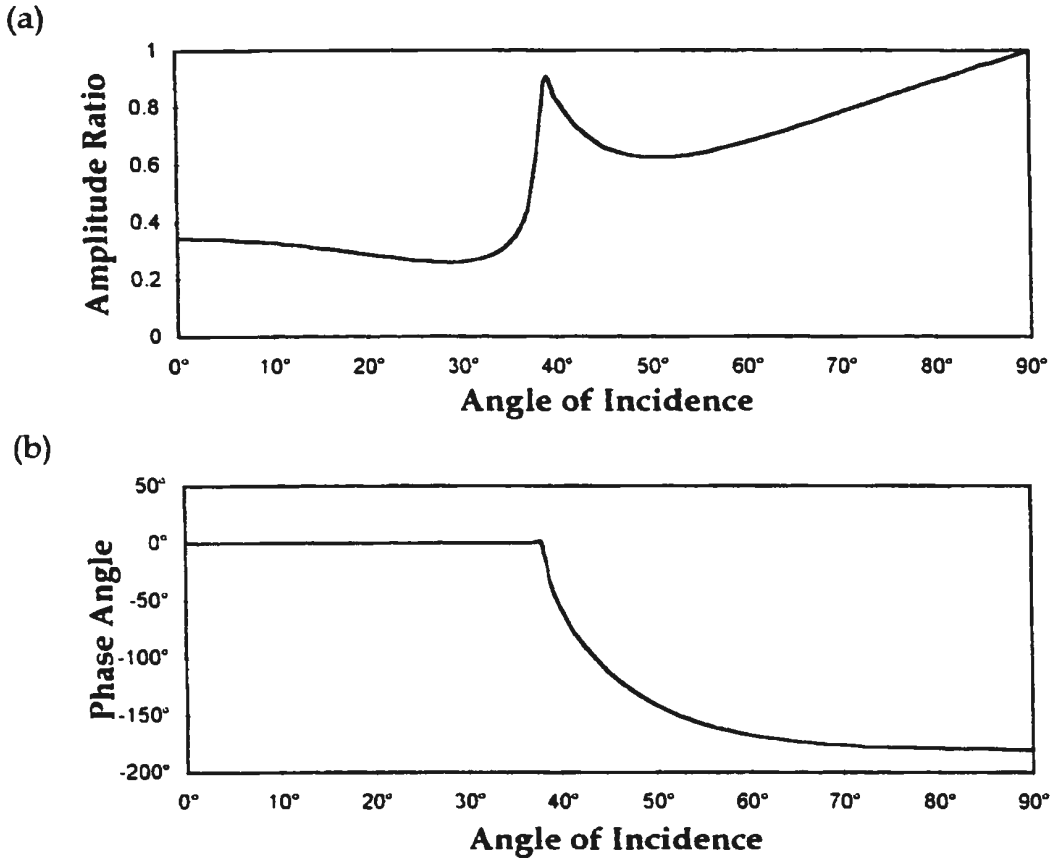

Figure 5.6. (a) Amplitude and (b) phase as a function of the incident angle for Young and Braille's (1976) model.

The reflection coefficients were tested against the results of modelling by Young and Braille (1976). Their model used the following parameters:

$\alpha_w = 2000$ ms^{-1} $\beta_w = 1155$ ms^{-1} $\rho_w = 2600$ kgm^{-3} (incident medium)

$\alpha_s = 3225$ ms^{-1} $\beta_s = 1865$ ms^{-1} $\rho_s = 3291$ kgm^{-3} (refracted medium)

The amplitude and phase results calculated by this routine are shown in Figure 5.6. The energy ratios calculated here exactly match the results of Young and

Braille. Since they did not publish phase results, the phase values were compared to those of Pilant (1979), who ran the same model, and again the match is exact.

5.5 Initial wavelet estimation

Once the raytracing has been performed, the predicted travel-times are used as the starting points for extracting windows of data from the shot gathers. Sinc functions are used for the data interpolation required to extract a wavelet starting at the predicted arrival time. However, in order to remove the phase effects predicted by the modelling, a phase shifted sinc function is used:

$$f(t,\phi) = \frac{\cos\phi \sin t - \sin\phi(1-\cos t)}{t} \qquad (5.10)$$

where ϕ is the phase and t is the normalized time (=time$\cdot\pi/\Delta$t). By convolving this function with each trace of the shot gather, we obtain phase and time-corrected estimates of the wavelet. However, these estimates are obviously contaminated by random noise as well as the coherent 'noise' which is due to the presence of both primaries and pegleg multiples. In order to improve the signal to noise ratio, the trace windows are stacked. This provides an initial estimate of the wavelet which will be used for the multiple subtraction.

Although the amplitudes can also be corrected based on the raytracing results, the sensitivity of seismic amplitudes to small scale velocity and structural

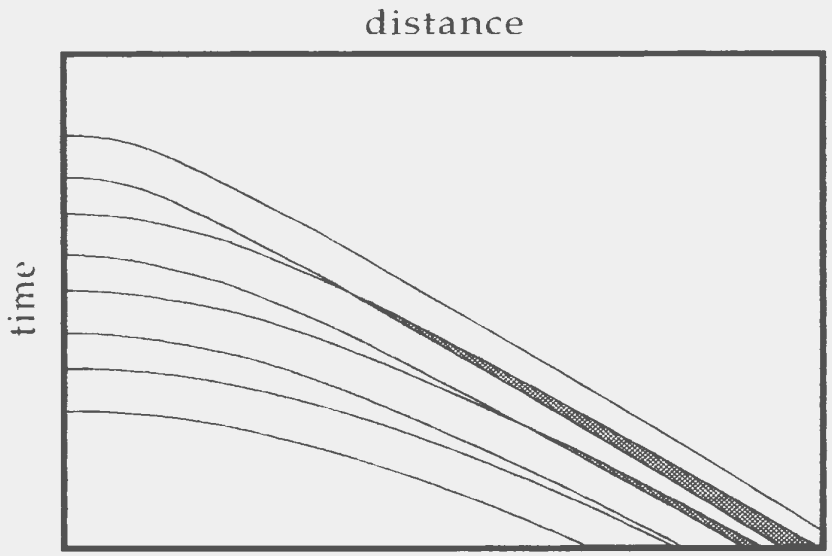

Figure 5.7. Schematic illustration of the data windows for a primary water bottom arrival and three orders of multiples. The windows are shaded light gray, while the overlapping portions are shown in dark gray.

anomalies can produce a wide range of window amplitudes across the gather. This can greatly reduce the effectiveness of the stacking, since the resulting wavelet could be dominated by only one or two windows. As a result, the windows are normalized by their RMS amplitudes before stacking.

One potential problem is the convergence of arrival times for the multiples at wide offsets (see Figure 5.7). This causes the windows for different orders of multiples to overlap. The overlapping portions are therefore excluded from the stack, and the resulting wavelet is adjusted for the variation in fold at each sample. Ideally, therefore, the wavelet should be chosen to include as much of the source pulse as possible, without causing serious overlap problems. For most data sets, this is typically between 80 and 160 ms.

Once an initial stacked wavelet has been obtained, it is used as a reference wavelet against which the original data windows are compared. The times and phases predicted by the raytracing are then adjusted using the techniques described in Section 4.2. The adjusted time is at the peak of the correlation function:

$$Xcor(t) = \sum_{k} (\alpha f_k + \beta H[f]_k) * d_{k+t} . \tag{5.11}$$

where f is the reference wavelet, $H[f]$ is its Hilbert transform and d is the original window. The coefficients, α and β, are calculated using the inversion described in Equation 4.7. The phase of the original data with respect to the reference wavelet is then:

$$\phi_{new} = \phi_{old} - \text{atan}(\beta/\alpha) \tag{5.12}$$

where ϕ_{old} is the phase that was used for the data extraction.

New data windows are extracted using the improved time and phase estimates. They are then compared to the wavelet estimate in order to generate a weighting function which can be used to stack an improved estimate of the wavelet. The function is inversely related to the difference between the wavelet and the data window:

$$= 1 - \left(\sum (d_i - w_i)^2 / \sum w_i^2 \right)^{\frac{1}{2}} \tag{5.13}$$

where d is the data window and w is the wavelet. The function has a maximum

of 1 when there is a perfect match, and is restricted to a minimum of 0.1.

The procedure is repeated until the change in the wavelet between iterations is relatively small (typically 1-5%). Since the weighting function causes the stack to emphasize those windows which look like the wavelet, convergence is inevitable, usually within 5-10 iterations. The wavelet amplitude on each trace is then calculated, a byproduct of the phase determination:

$$A = (\alpha^2 + \beta^2)^{\frac{1}{2}} \tag{5.14}$$

where A is the scale factor and α and β are the coefficients from Equation 5.11. After the wavelet is time-, amplitude- and phase-corrected for each trace, it is subtracted from the trace. The routine then moves on to the next multiple.

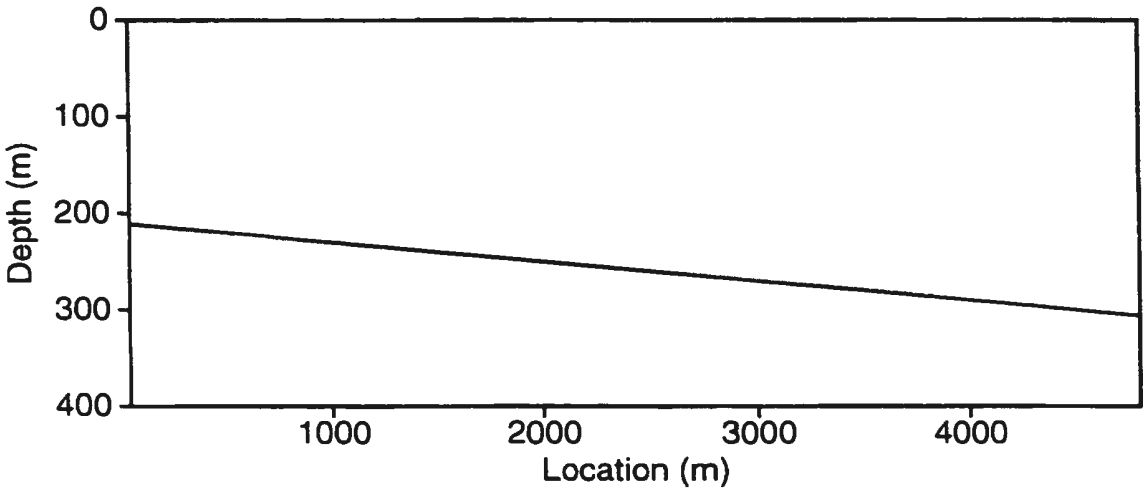

Figure 5.8. The dipping sea-floor model for the initial testing of Raymult.

5.6 Routine testing

The first test is of a completely noise-free case, which only contains the water-bottom primary and subsequent multiples. Since the synthetics were generated using the raytracing routine, we expect perfect attenuation of the multiples if the correct model is used. Figure 5.8 shows the original model. The source was located at 4000 m while 100 receivers were located with a minimum offset of 200 m and a group interval of 25 m. Figure 5.9 shows the original shot gather, constructed using a water velocity of 1500 ms^{-1}, a sea-floor velocity of 2500 ms^{-1}, and a sea-floor density of 2400 kgm^{-3}. The arrival times have been plotted over the data to show the start of the attenuation windows. The window length of 32 samples was chosen for all the synthetic tests. Figure 5.10 shows the gather after

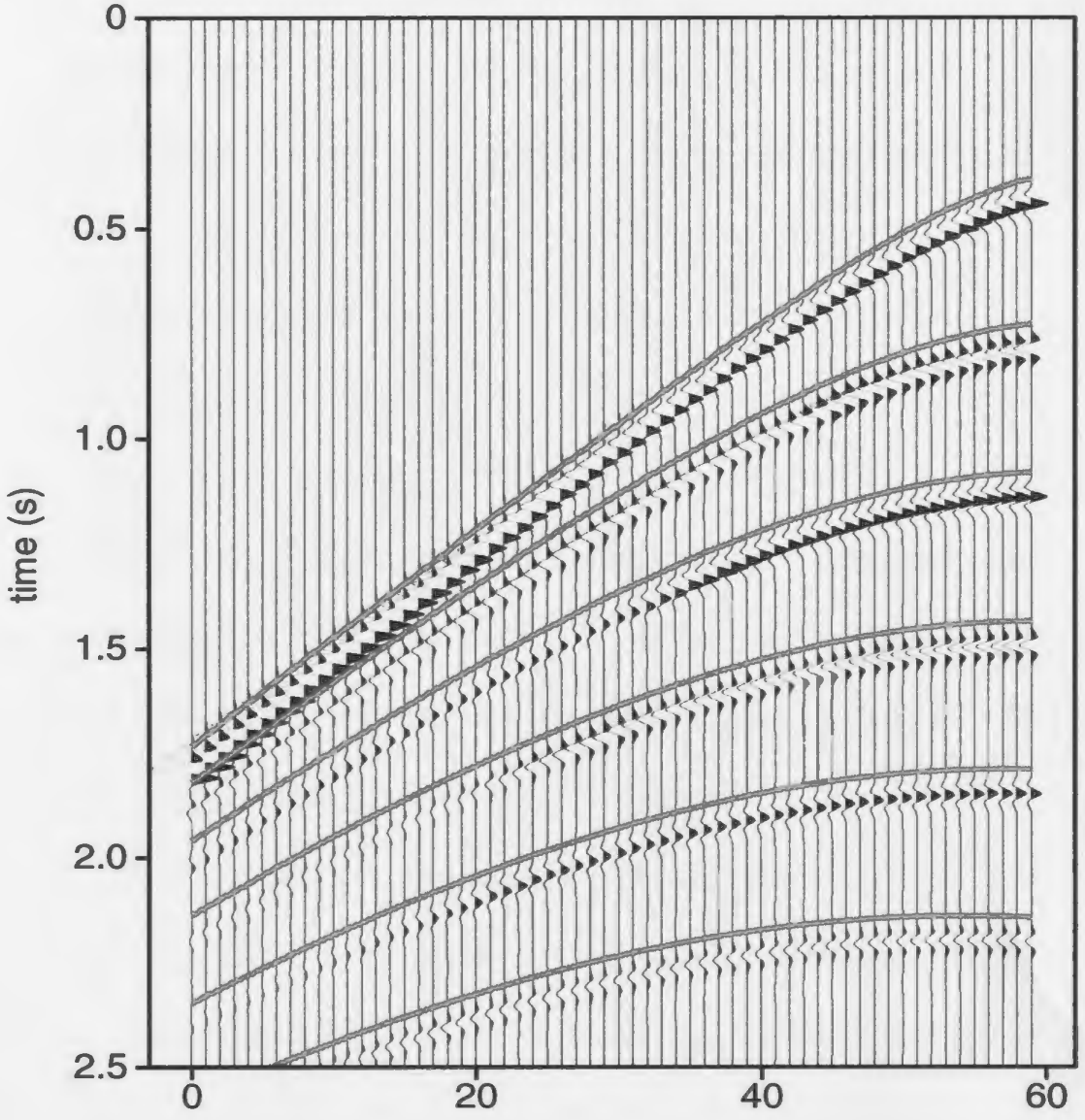

Figure 5.9. The shot gather used for initial testing of Raymult, including an overlay of the arrival times. The source location was at 3000 m, with receivers located at 40 m intervals from 2800 m back to 440 m. It contains only the water bottom primary and five orders of sea-bottom multiples. A time-dependent scale factor (T^2) has been applied to the data to enhance the later events.

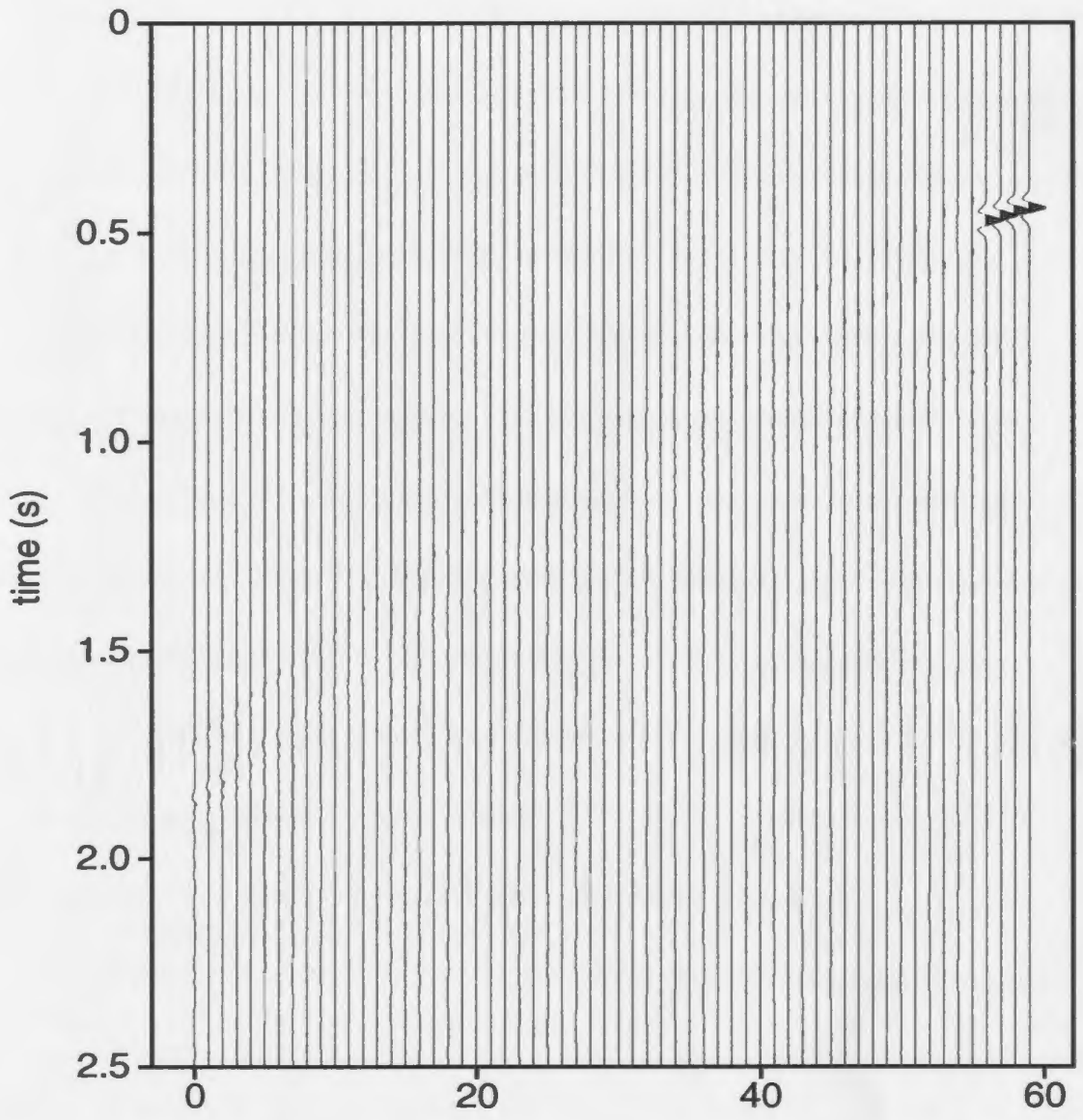

Figure 5.10. The shot gather of Figure 5.9 after application of Raymult. The water bottom primary has been left on the four traces nearest the source so that the final stack will have a water bottom event.

multiple attenuation. Clearly, the multiples have been almost completely removed, the average attenuation is 125 dB.

Since the water bottom primaries could interfere with the multiple attenuation of subsequent windows, they have been attenuated on all but the nearest four traces. A standard stretch mute would remove these events before stacking, so this technique should not damage the final stack. In fact, since the very slow water-bottom events are no longer a concern, it can potentially allow for a much milder final mute, and this in turn could produce better stacking of the primaries.

The second test uses the same data, to which random noise has been added (see Figure 5.11). Since the higher order multiples have much lower amplitudes, the noise obviously interferes with these events most severely, with the fifth order multiples having amplitude levels comparable to the noise. Figure 5.12 shows the gather after attenuation. Although there are some remnants of the water-bottom primary at far offsets, likely due to small errors in the phase estimate, the multiples have been virtually eliminated, with an average attenuation of 40 dB.

I should point out that since the 'attenuation' is determined by simply calculating the ratio of the energy in the windows before and after the wavelet subtraction, the addition of noise to the windows reduces how meaningful this

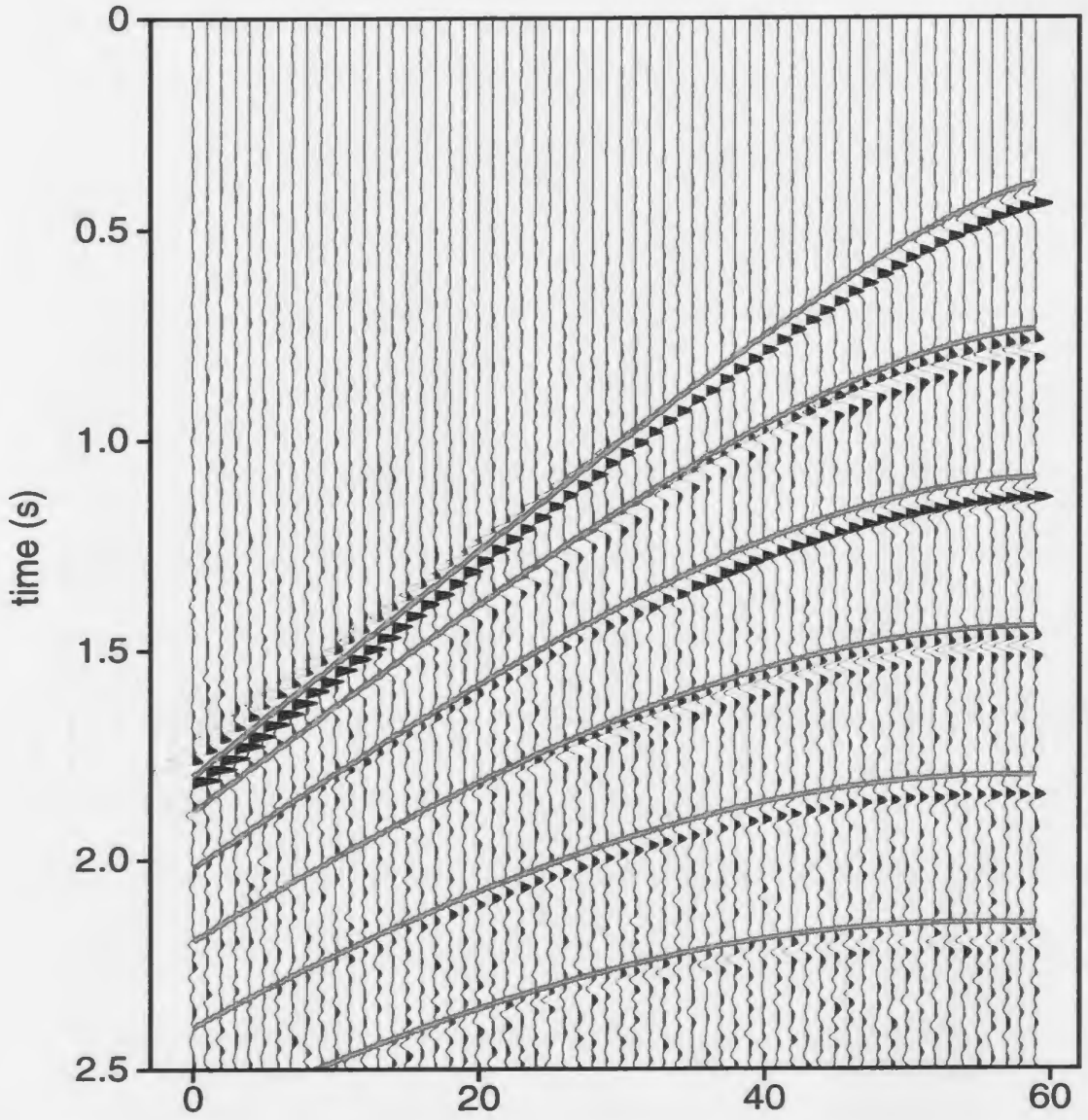

Figure 5.11. The shot gather of Figure 5.9 after the addition of random noise. The time-dependent scaling has boosted the noise level at later times.

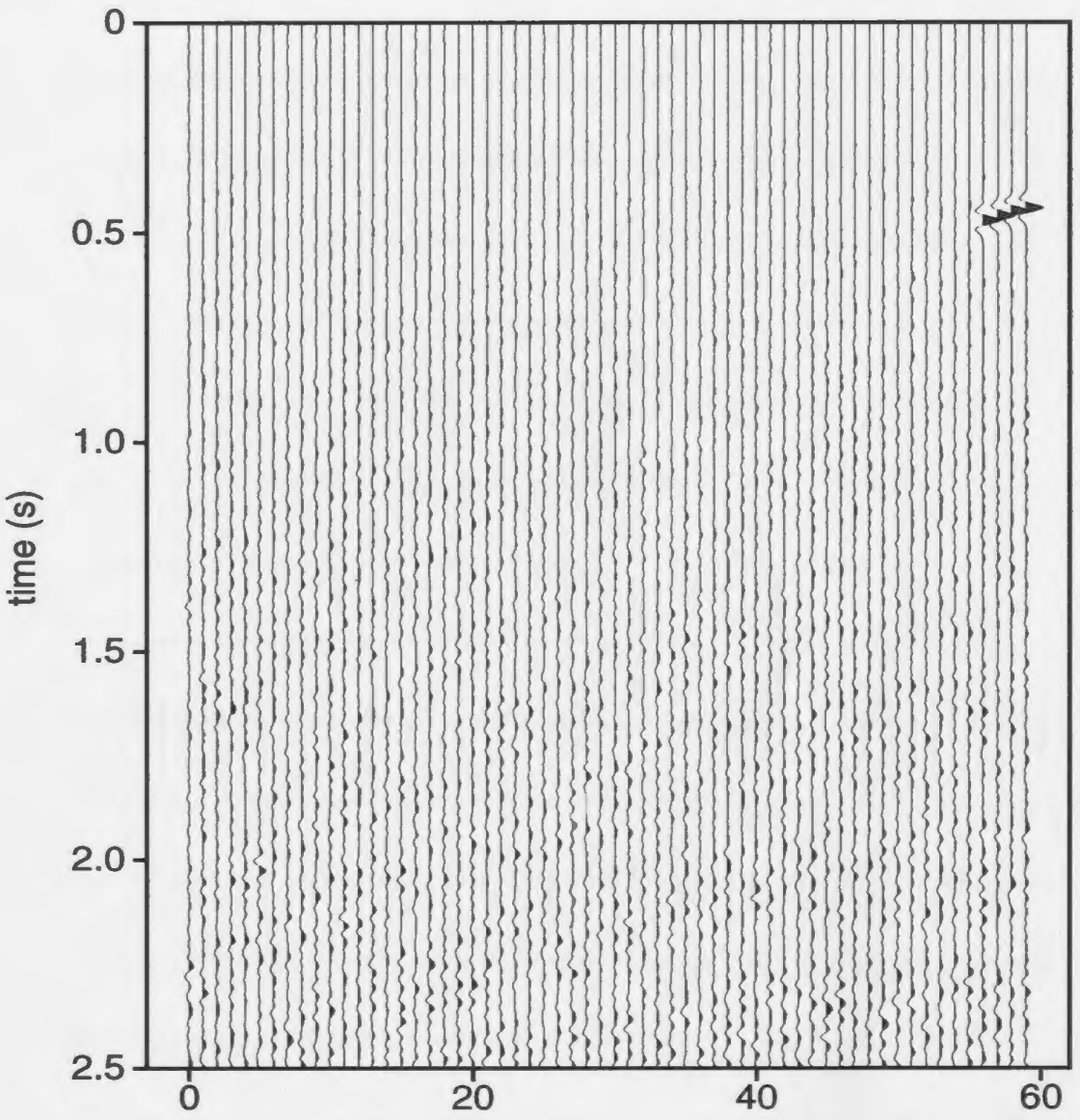

Figure 5.12. The shot gather of Figure 5.11 after the application of Raymult.

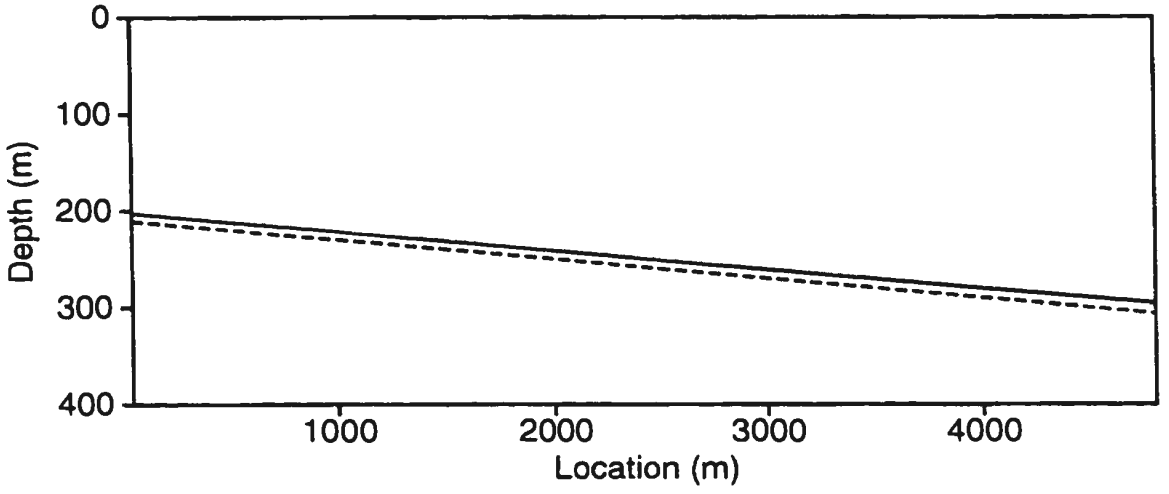

Figure 5.13. The model constructed using a water velocity of 1450 ms^{-1} instead of the correct velocity of 1500 ms^{-1}. The dashed line shows the location of the true water bottom.

number actually is. Complete elimination of the multiple may only require an attenuation of 5 or 10 dB if the noise has an amplitude comparable to the multiples. However, when used in conjunction with visual inspection, the 'attenuation' does give a fairly good idea of how successful the routine was in removing the multiples.

The next set of tests uses the same data, but uses the wrong velocities for the modelling and attenuation routines. The water velocity was 1450 m/s, while the sea-floor velocity was 2000 m/s. This introduces several potential problems. The modelling routine estimates the water depth to be more than 10 m shallower than it actually is (see Figure 5.13), producing significant timing errors at the far

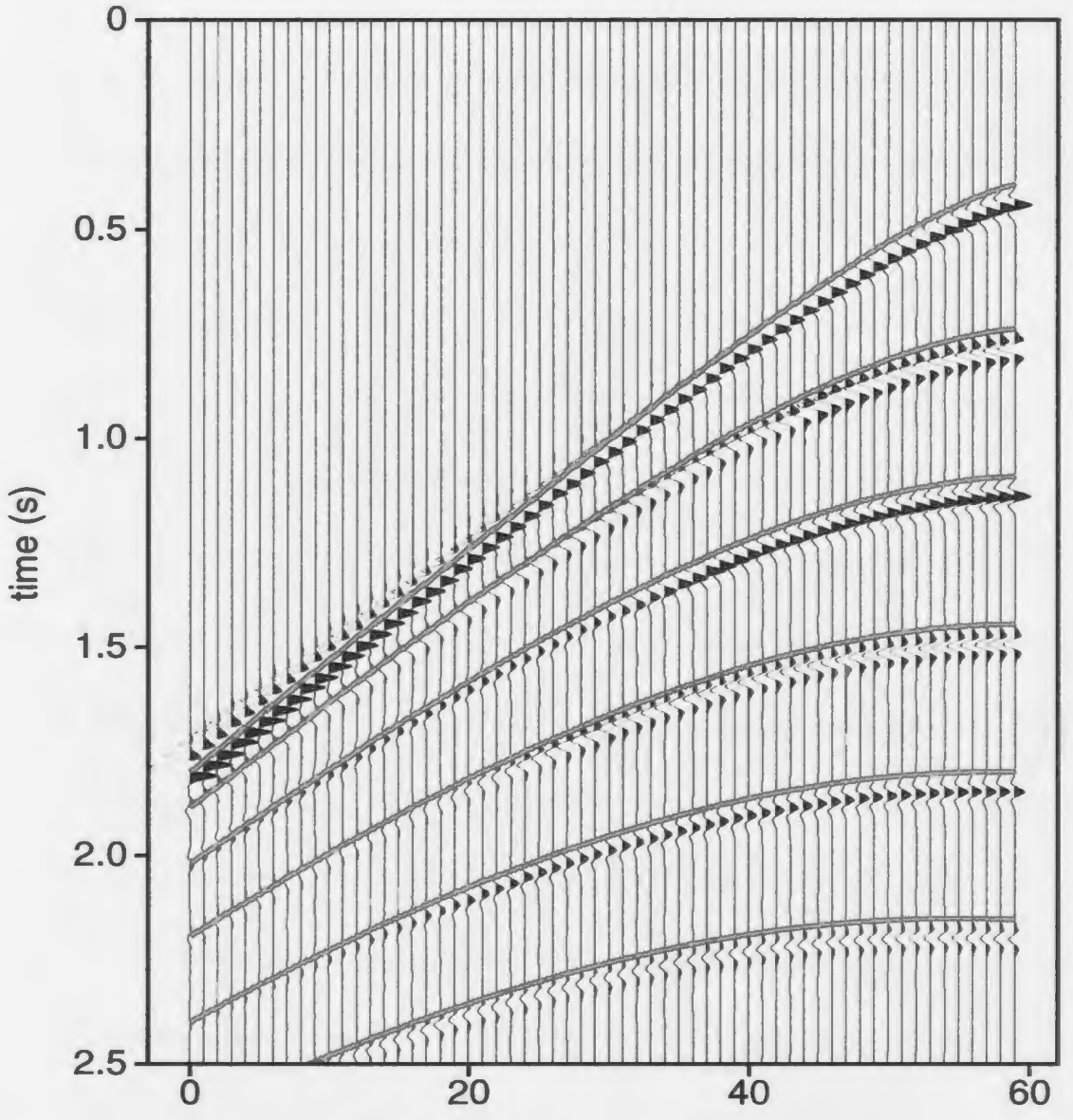

Figure 5.14. The shot gather of Figure 5.9 with an overlay of the arrival times determined using a water velocity of 1450 ms^{-1}. The model perfectly reproduces the arrivals on the near trace, but there is considerable error on the far traces.

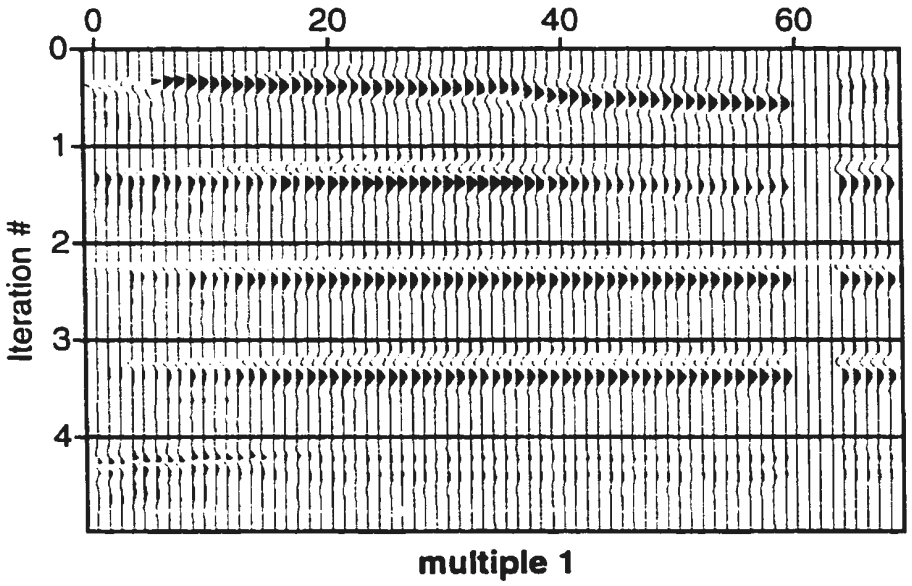

Figure 5.15. Illustration of the wavelet iterations for the first order multiples. The top window shows the initial data window after the time and phase corrections predicted by the raytracing of the 1450 ms^{-1} model. Clearly, the wavelet has not been properly corrected. The five traces on the right show the wavelet estimated by stacking the window. Subsequent windows show the data after each iteration of the wavelet prediction algorithm, scaled by the weighting function. By the third iteration, the wavelet estimate is good, and the appropriate phase corrections have been applied. The final window shows the data after subtraction of the multiples.

offsets (see Figure 5.14). In addition, the error in the velocity ratio causes significant error in the estimated critical distance, which in turn causes major phase differences between the data and the raytracing results, making it more difficult to obtain a good initial wavelet estimate. In practice, model testing would alert the processor to such a poor choice of velocities, so it is unlikely that model-related errors would ever be this severe. To partially compensate for the

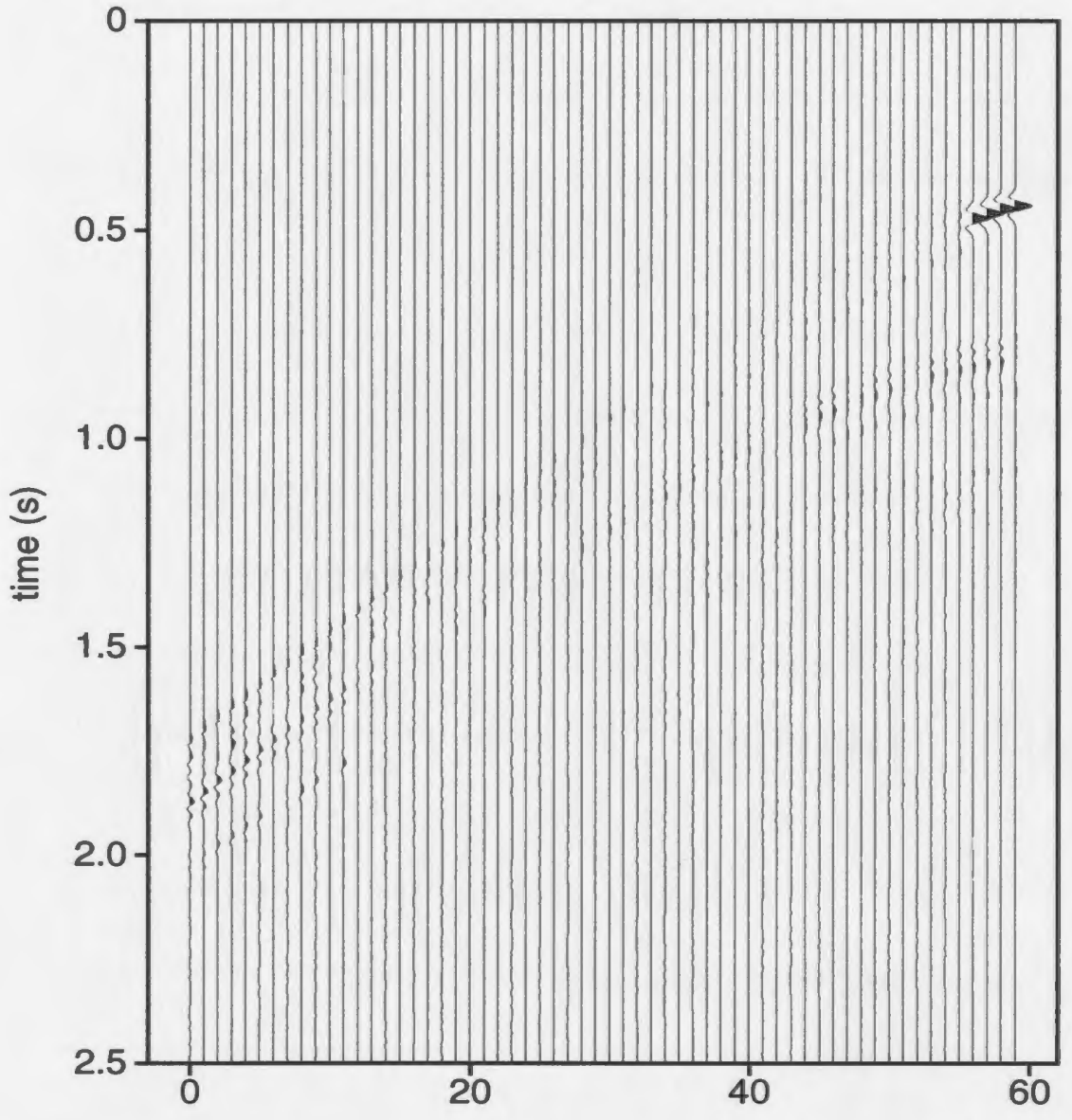

Figure 5.16. The shot gather of Figure 5.9 after Raymult attenuation using the 1450 ms^{-1} model.

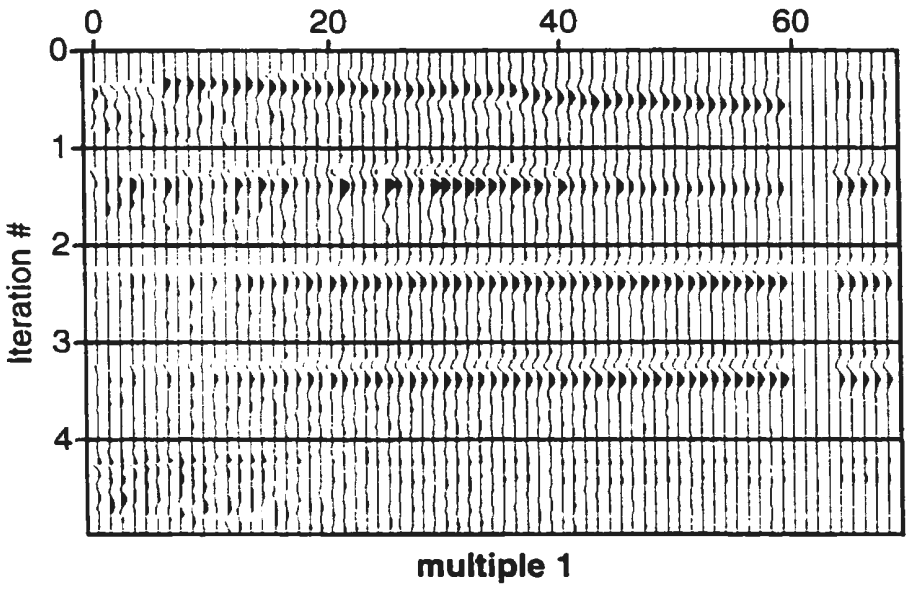

Figure 5.17. Illustration of the wavelet iterations for the first order multiples of the noisy data shown in Figure 5.11. See Figure 5.15 for full explanation.

timing errors, the window length was increased to include an additional 4 samples at the beginning and the end. The wavelet iterations are able to correct the timing and phase errors (see Figure 5.15) to produce excellent attenuation, which averages almost 100 dB. For comparison to Figure 5.10, Figure 5.16 shows the multiple-attenuated shot gather. The slight deterioration in the performance at the far offsets appears to be caused by the overlap mute. The wider windows cause an increase in the length of the mute zone in each window, which reduces the reliability of the phase calculation at those locations.

When noise is added, the wavelet iterations are still able to find appropriate

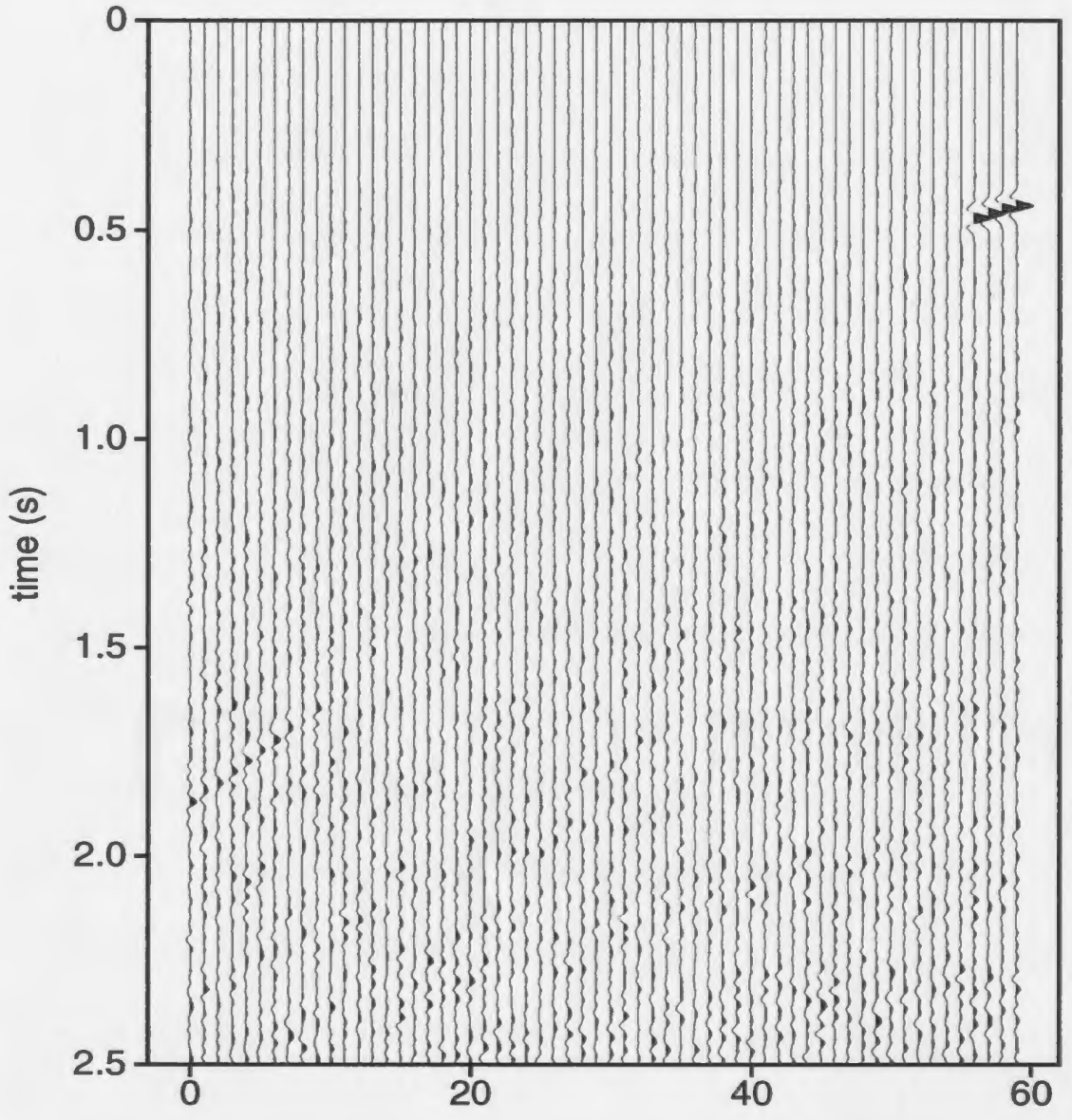

Figure 5.18 The shot gather of Figure 5.11 after Raymult attenuation using the 1450 ms^{-1} model.

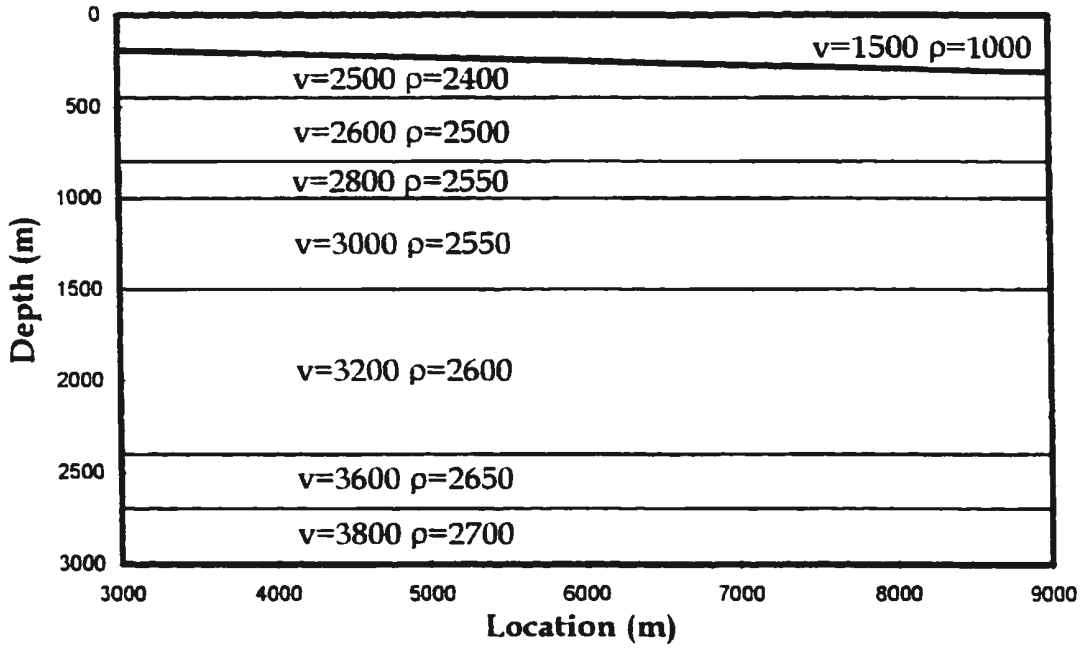

Figure 5.19. The model used for generating synthetic primaries for Raymult testing. The units for velocity, v, are ms^{-1}; the units for density, ρ, are kgm^{-3}.

phase and time shifts (see Figure 5.17) and the attenuated gather (see Figure 5.18) is comparable to the correct model example (Figure 5.12). The average attenuation was calculated to be 34 dB.

The final set of examples uses the original shot gather but adds a series of primary reflections. Figure 5.19 shows the model used for generating the primaries. Figure 5.20 shows the modelled primary events which will be the desired output for the attenuation tests, while Figure 5.21 shows the multiple-contaminated gather which is to be tested.

The first test uses the correct model, once again with excellent results (see

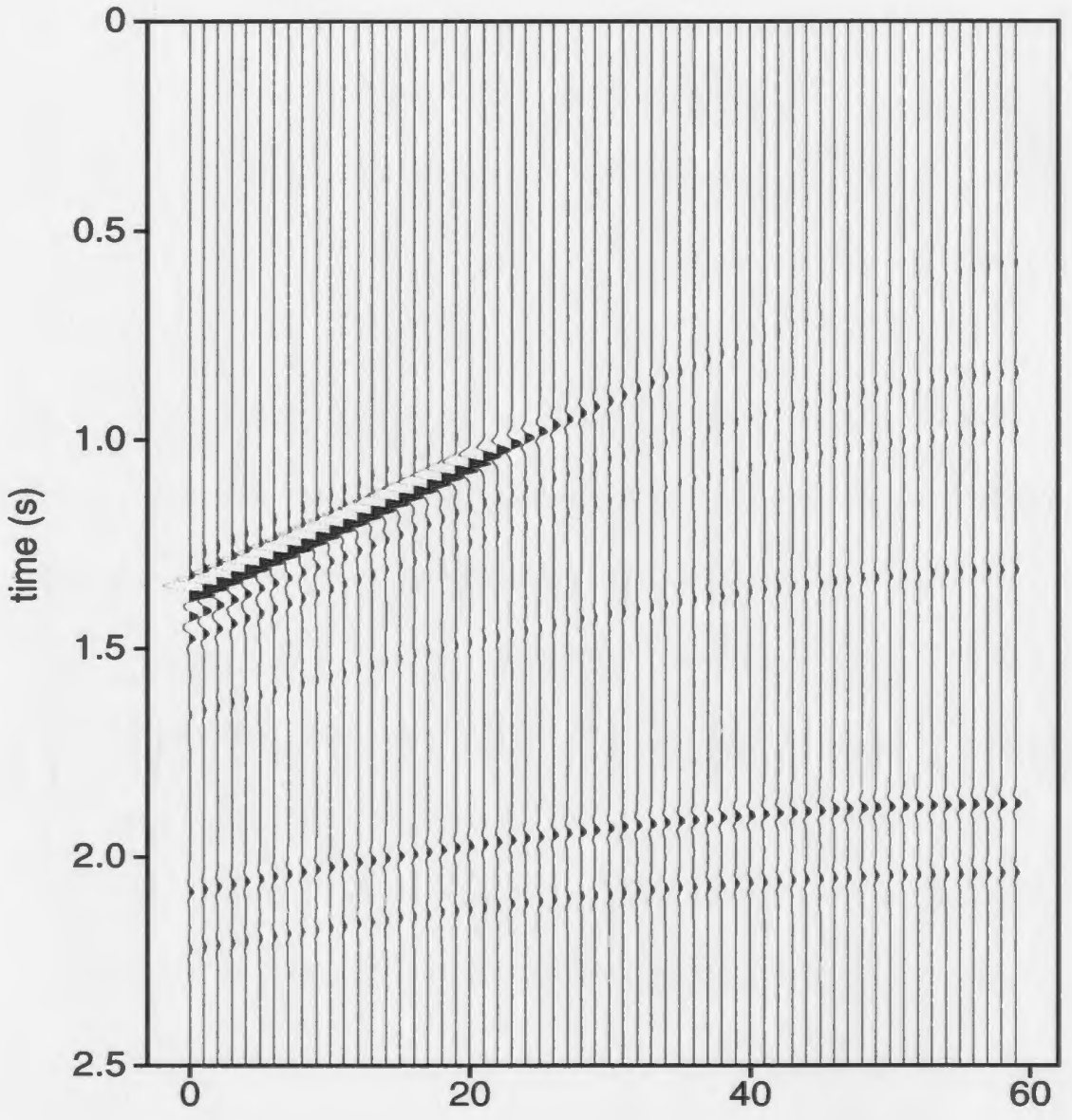

Figure 5.20. The synthetics primaries generated using the model in Figure 4.19. The same shooting geometry was used as in Figure 5.19, with a source at 3000 m, a 200 m near offset and a 40 m receiver interval. The water bottom primary has not been modelled. This is the 'desired output' for the Raymult tests to follow.

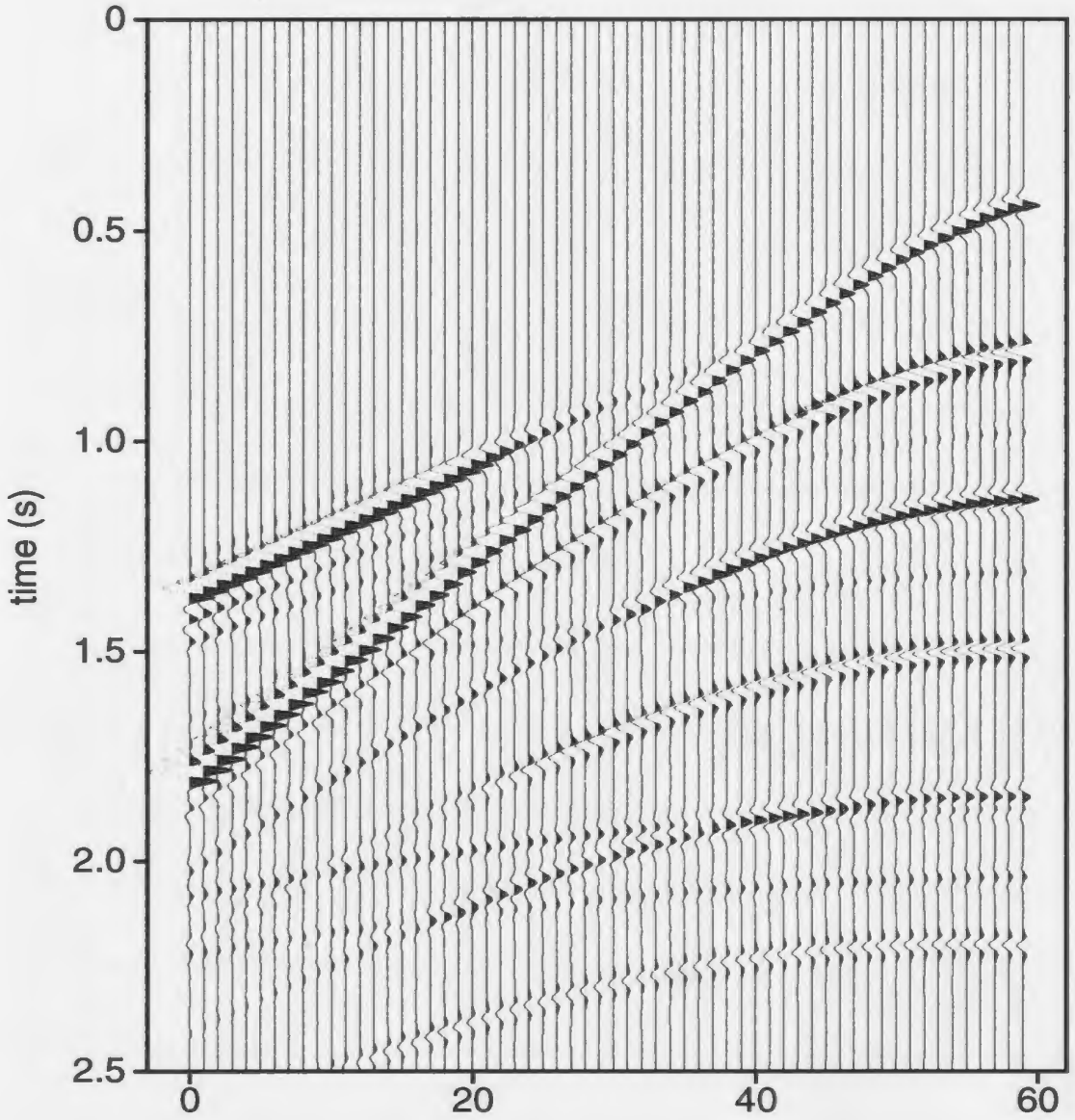

Figure 5.21. The test gather, generated by combining Figures 5.9 and 5.20, which is to be used for Raymult testing.

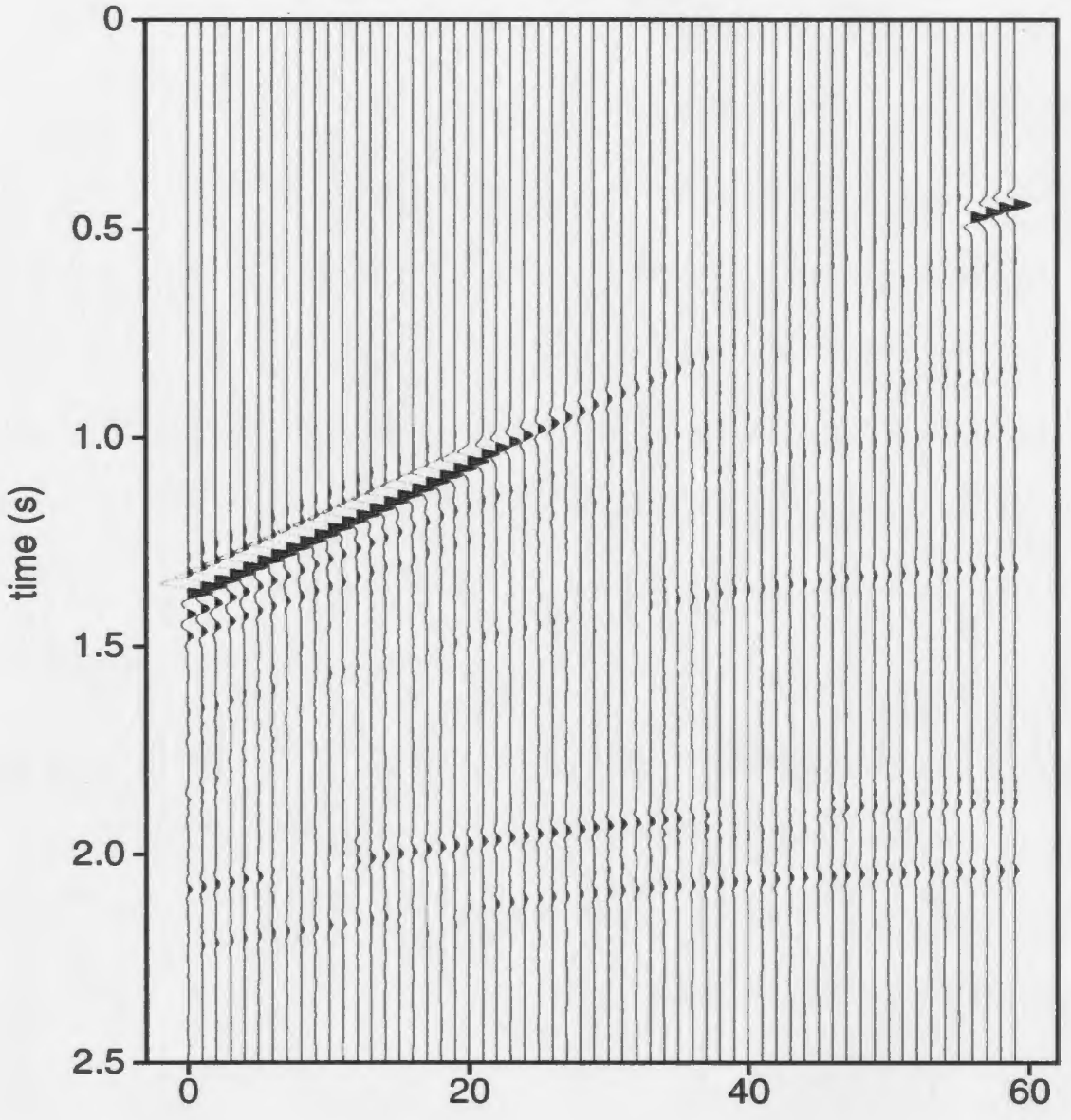

Figure 5.22. The test gather of Figure 5.21, after Raymult attenuation. The multiples have been completely removed, but there is some damage to the primaries.

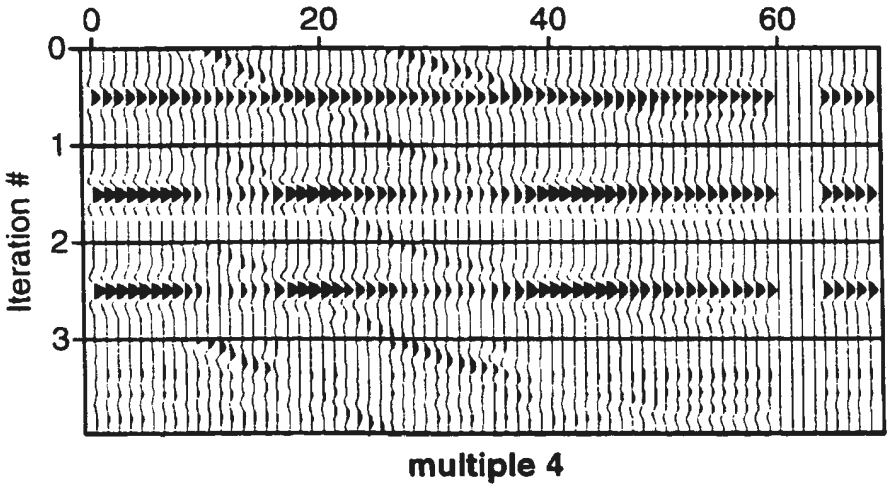

Figure 5.23. Illustration of the wavelet iterations for the fourth order multiples of the data shown in Figure 5.21. See Figure 5.15 for full explanation. The weighting function has reduced the contribution to the stack of those traces which contain crossing events.

Figure 5.22. The average attenuation was 78 dB. Unfortunately, there is some damage to the primaries. This is to be expected since, at the points of intersection between multiples and primaries, the routine is unable to distinguish which part of the combined wavelet is multiple and which part is primary. As a result, it removes the entire wavelet, including the primary component. However, this effect is only significant at relatively small zones around the intersection points. The combined wavelet does not damage the wavelet estimate because the weighting function reduces the contribution of the cross-over windows to the stack (see Figure 5.23).

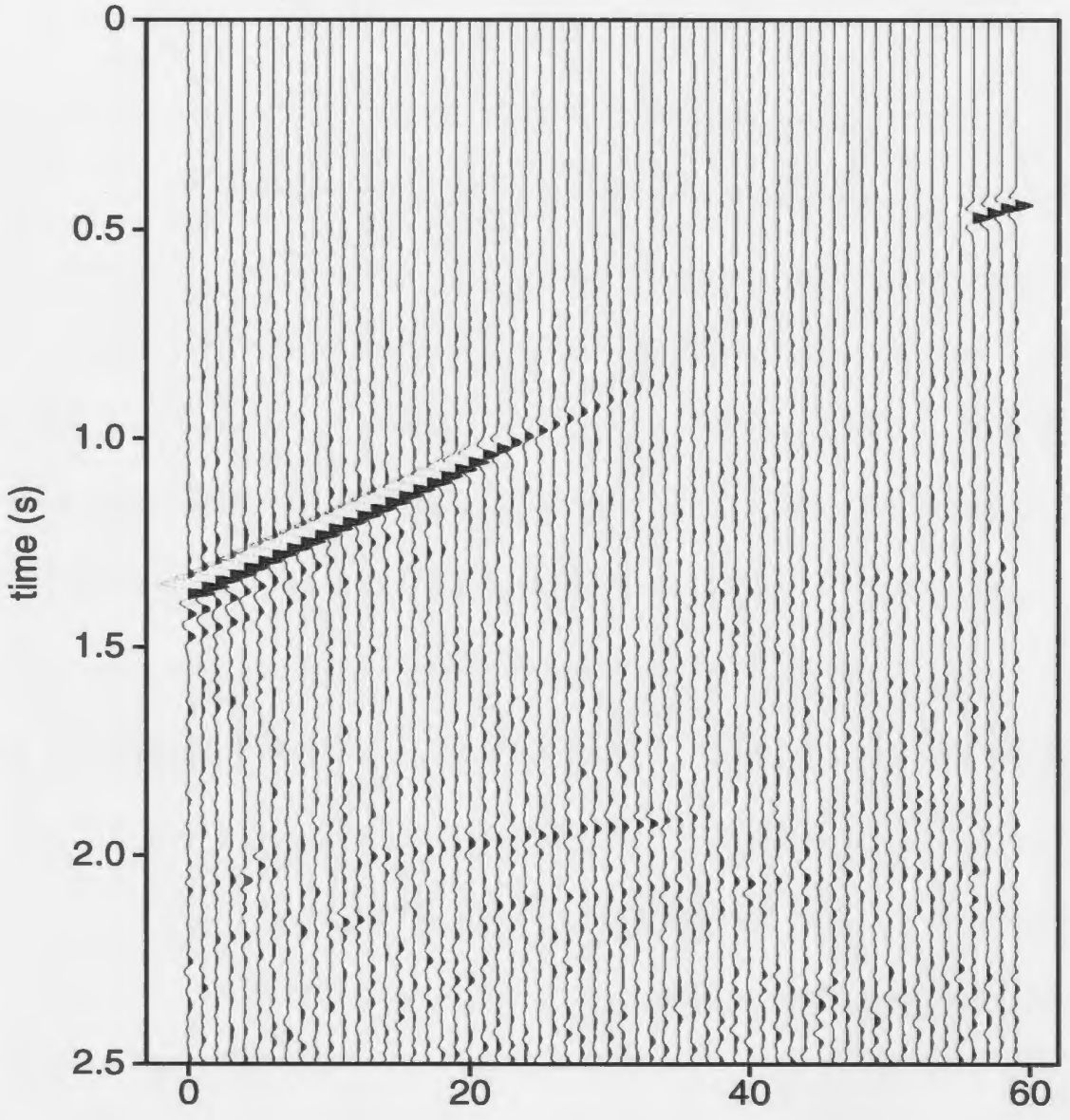

Figure 5.24. The data of Figure 5.21 after the addition of random noise and the subsequent application of Raymult.

The addition of random noise (see Figure 5.24) does not appear to seriously affect the actual attenuation, although the routine does require several additional iterations for each order of multiple. The average attenuation of 33 dB is comparable to that produced on the primary-free data. Once again there is some damage to the primaries at the intersections with the multiples.

Finally, the use of the inaccurate model parameters causes very little reduction in attenuation. The noise-free case shows an average attenuation of 75 dB (Figure 5.25), while the noise-added data shows an attenuation of 32 dB (Figure 5.26). Once again, the wavelet iterations had very little problem adjusting the predicted times and phases to fit the data (see Figure 5.27). It is important to emphasize however, that parameters this much in error would not typically be used, since raytracing tests of one or more shot gathers (as illustrated in Figure 5.14) would clearly show that the model needs adjustment.

Overall, the routine performed very well through all of the testing, even in the most difficult situations. Although there was some attenuation of the primaries, the effects were generally limited to a few traces, so stacking should significantly reduce this problem. In addition, since the attenuation was particularly strong on the near traces, stacking should provide further multiple attenuation.

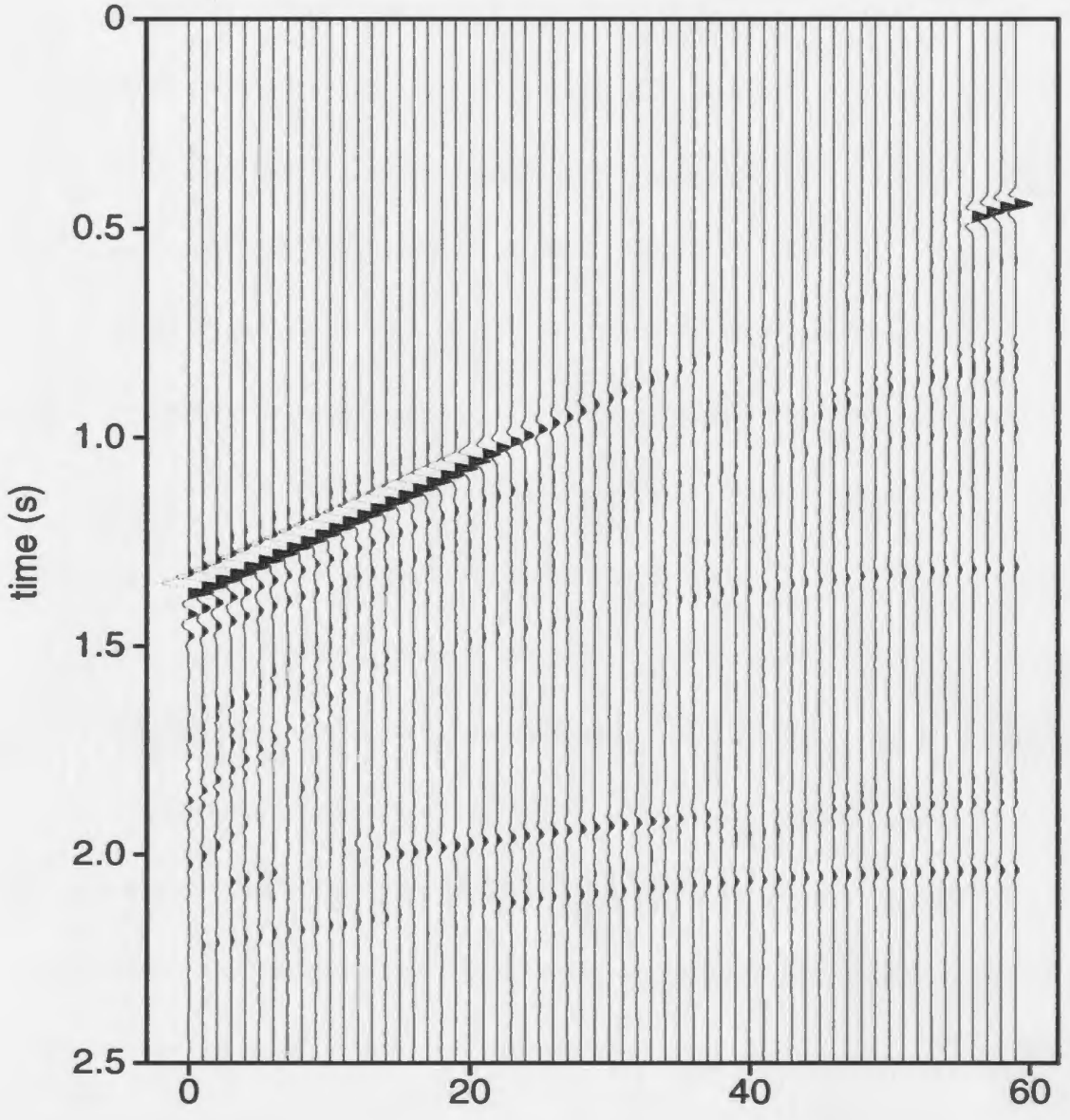

Figure 5.25. The data of Figure 5.21 after the application of Raymult using the 1450 ms^{-1} model.

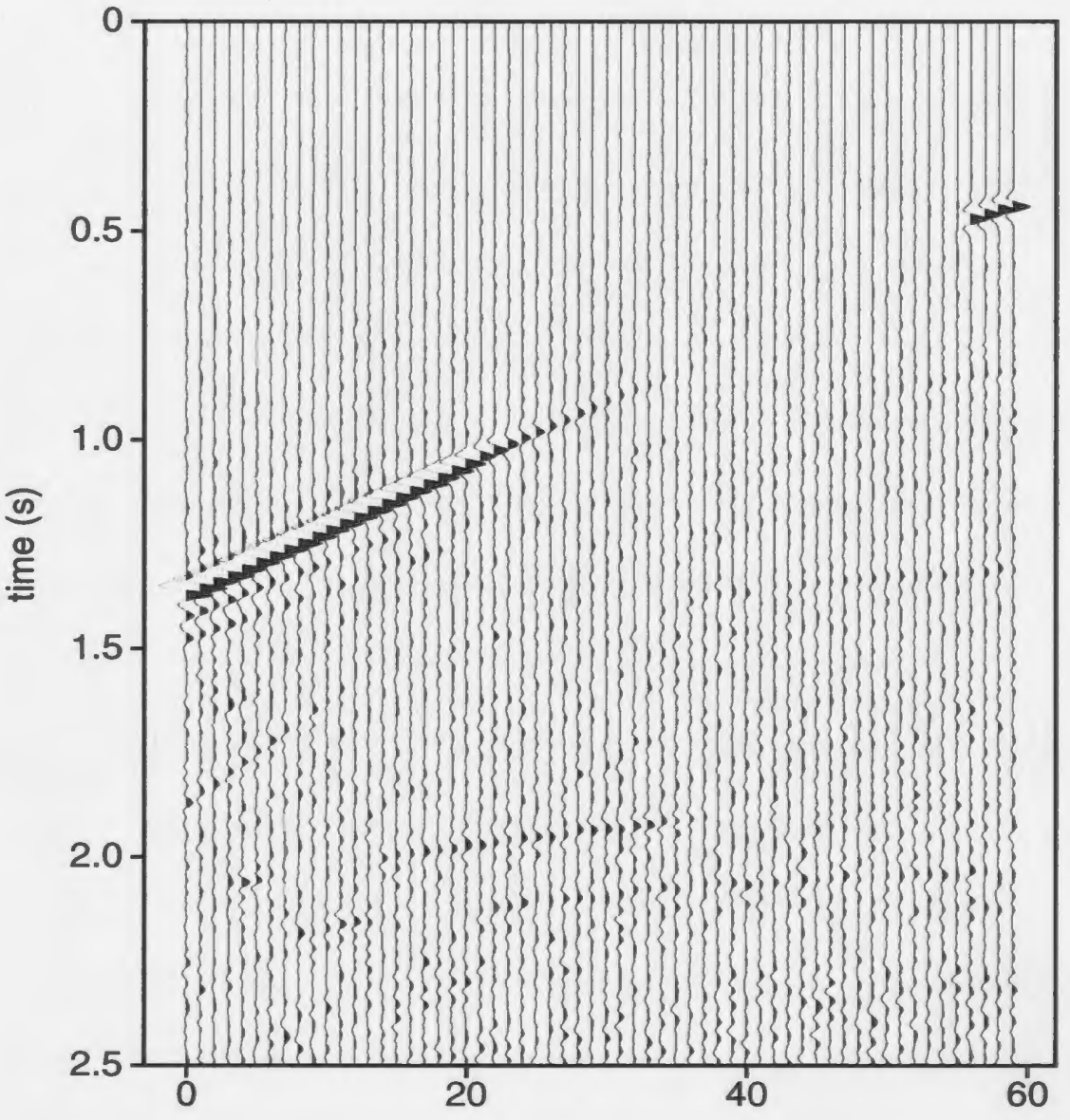

Figure 5.26. The data of Figure 5.21 after the addition of random noise and the subsequent application of Raymult using the 1450 ms^{-1} model.

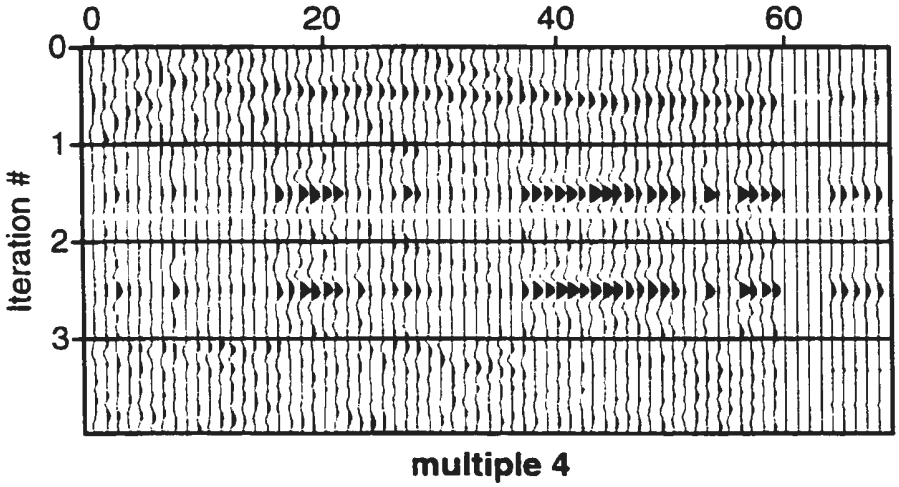

Figure 5.27. Wavelet iterations for the fourth order multiple of the gather in Figure 5.21 after the addition of random noise. See Figure 5.15 for full explanation.

6. PROCESSING EXAMPLES

6.1 Introduction

This chapter illustrates the use of Raymult in the processing of marine seismic data from a number of different settings. Four data sets will be processed, two synthetic and two real. The synthetics include the data used for the pre-stack testing in Chapter 5. The real data examples are from two very different seismic surveys. The first is a high frequency line that contains a number of coherent primaries under a smoothly varying, shallow water bottom, while the second is a lower frequency line over a very hard, very rough sea-bottom, without obvious primaries.

Raymult is applied in the shot domain, before deconvolution, in order to improve the likelihood of wavelet consistency. Although this generally helps the subsequent processing, it does present a minor problem with respect to predictive deconvolution, which can be used for the subsequent attenuation of pegleg multiples. Since the water bottom primary is usually the highest amplitude arrival, it tends to dominate the autocorrelation that is used for designing the prediction filter. However, since the multiples associated with this event have been removed, the amplitude of the prediction filter will be a very poor estimate. Therefore, the deconvolution is only effective if the design

window starts below the actual water bottom arrival. It is then able to focus all of its attention on the pegleg problem. As a result, the deconvolution routine was set up to use the model generated by the Raymult processing. It sets the start of the design window to just below the end of the water bottom event and the prediction lag to slightly less than the water layer travel time.

The velocity functions for the synthetic seismograms and for the first real data set were determined using semblance analyses for a range of velocities from 1400 ms^{-1} to 4400 ms^{-1}, with a 25 ms^{-1} increment. The lack of good coherent primaries on the second real data set reduced the effectiveness of the semblance and as a result, constant velocity stacks were used.

6.1 Synthetic Example: Sloping sea-floor

The first synthetic example was generated by raytracing the sloping sea-floor model that was shown in Figure 5.19. A total of 120 shot gathers were produced, with 60 traces per gather. The first shot was at location 4000 m and the shot spacing was 40 m. The minimum offset was 200 m, with a trace spacing of 40 m, giving a maximum offset of 2560 m. This resulted in a CMP spacing of 20 m, with 30 fold coverage from 3880 m to 7500 m. The source used a zero-phase Ricker wavelet with a centre frequency of 30 Hz. Only the primary reflections and the water bottom multiples were modelled. Figure 6.1a shows the complete near trace gather, while Figure 6.1b shows a near trace-gather which contains

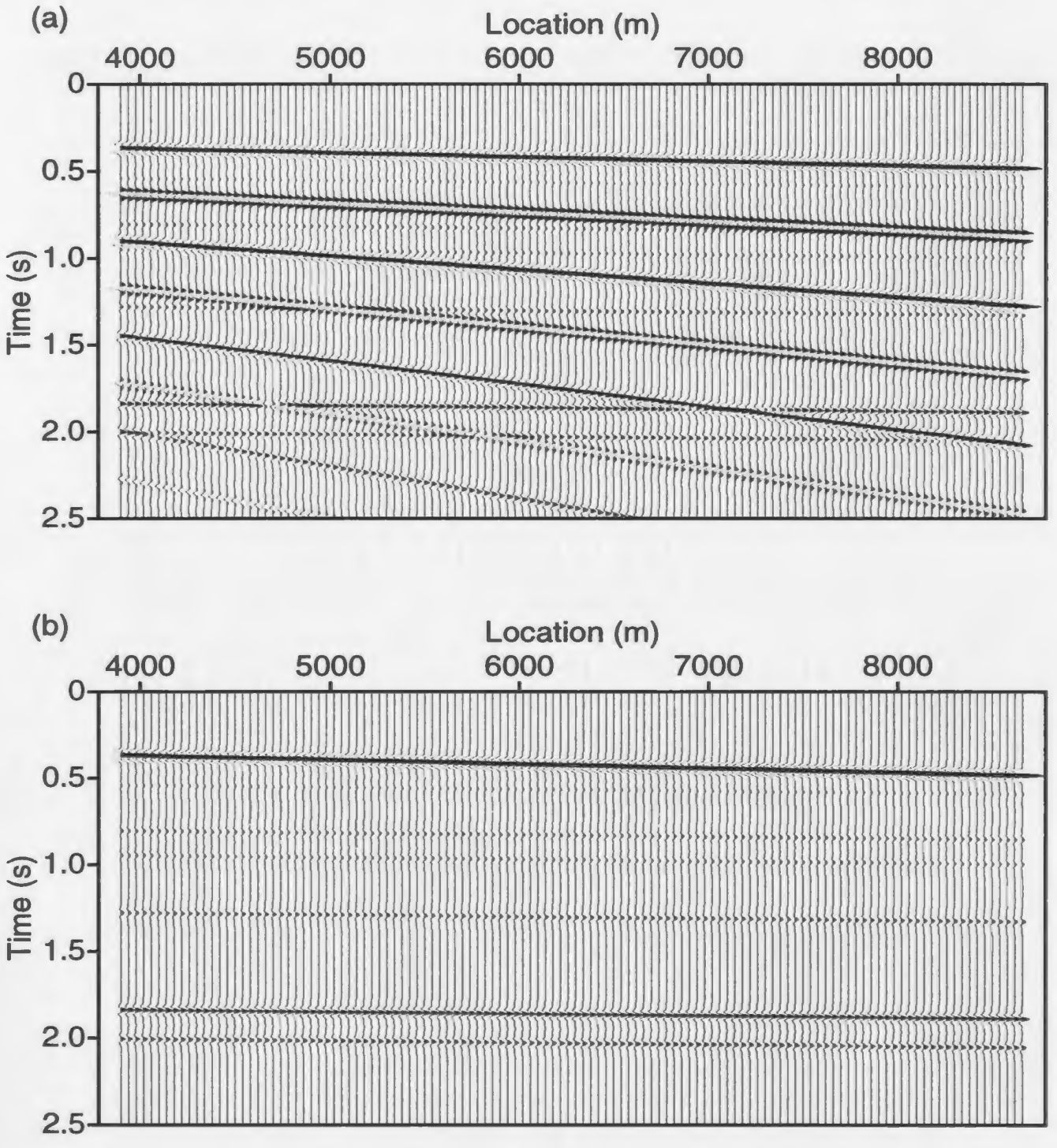

Figure 6.1. Near trace gathers for dipping sea-floor synthetics: (a) shows the complete data set, including water-bottom multiples, while (b) shows only the primaries.

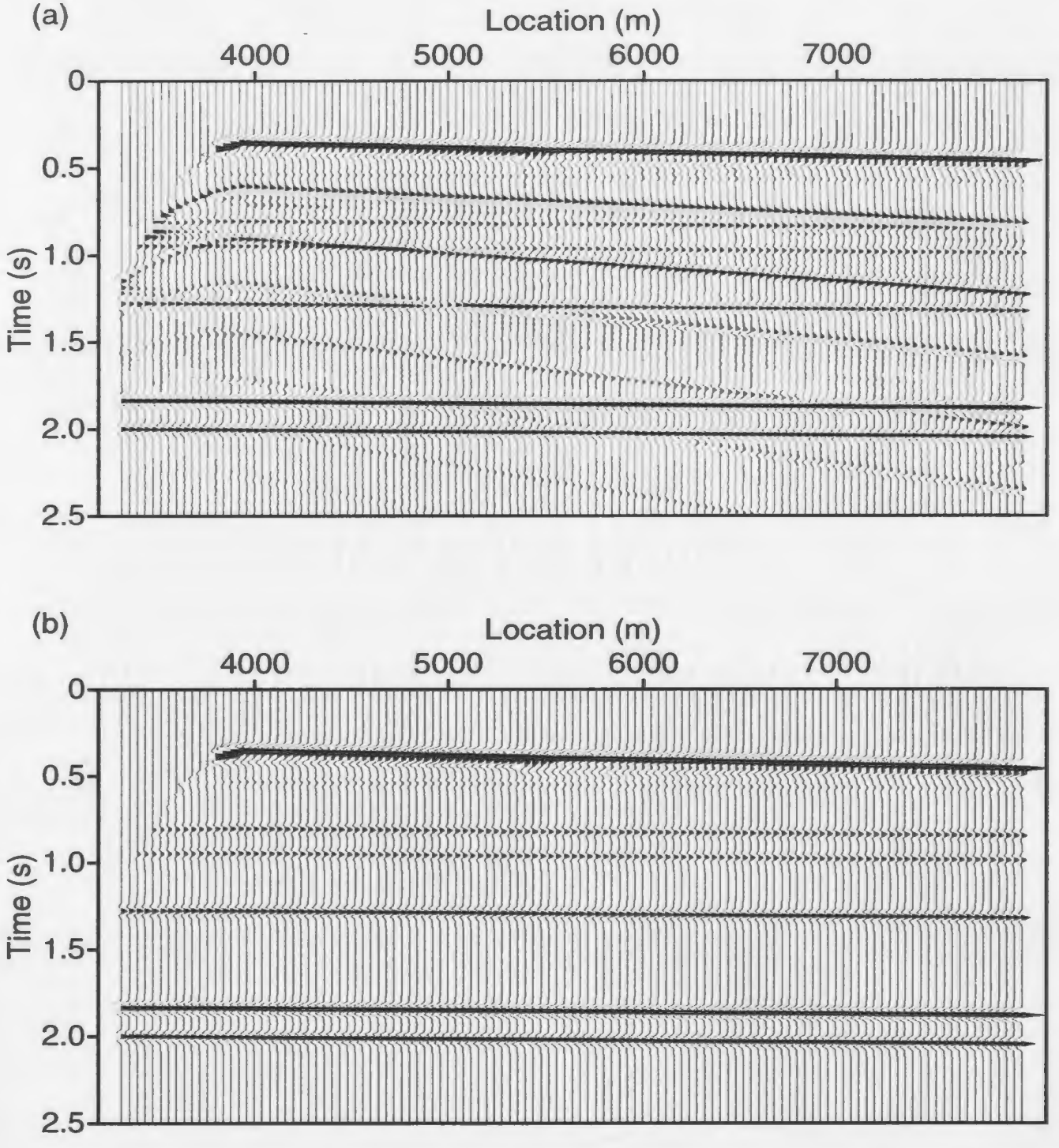

Figure 6.2. Brute stacks for dipping sea-floor synthetics: (a) shows the stack of the complete data set, including water-bottom multiples, while (b) shows the primary-only stack.

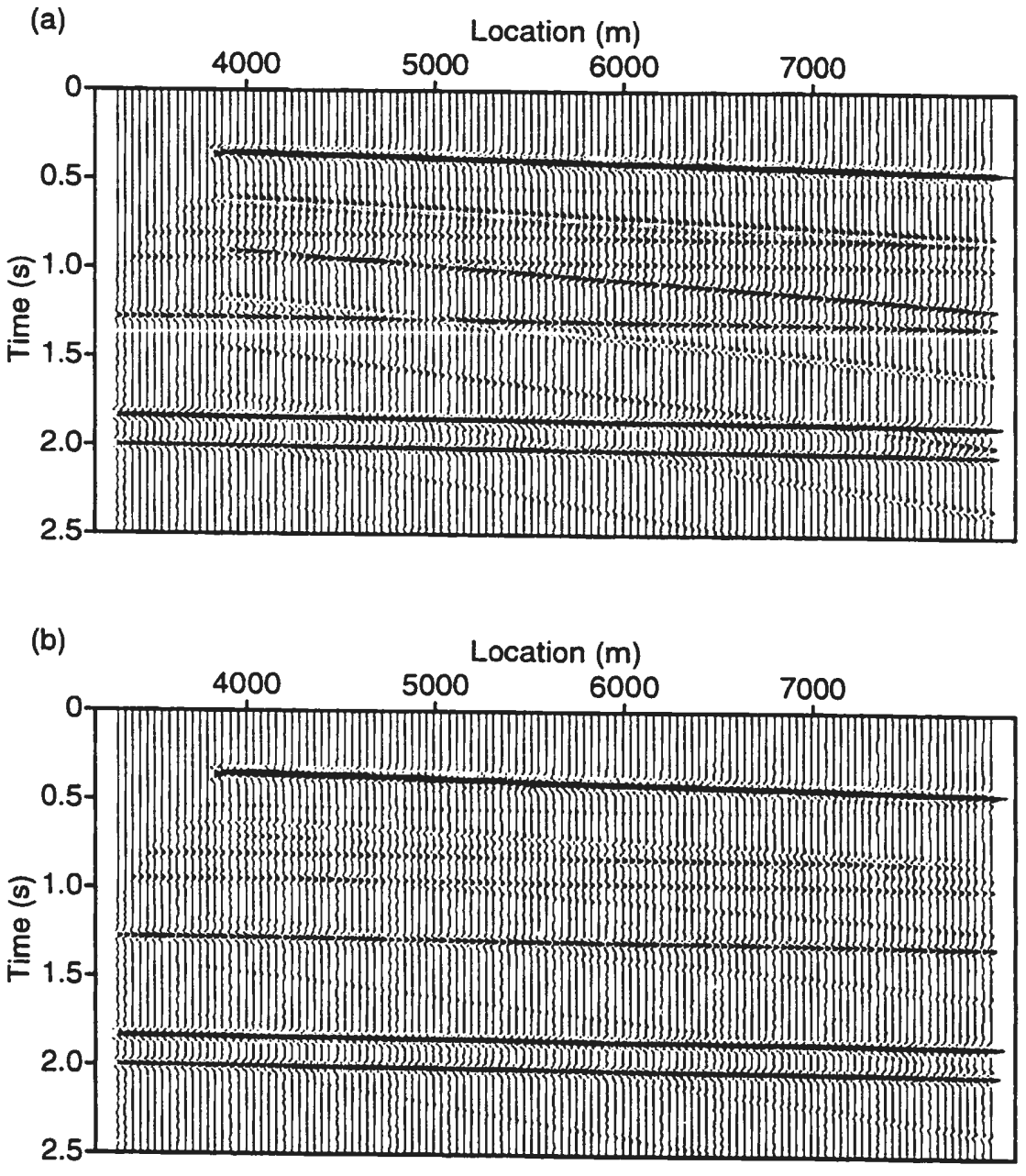

Figure 6.3. FK multiple attenuation for dipping sea-floor synthetics: (a) shows the stack of the complete data set after applying an FK filter to the shot gathers, while (b) shows the stack produced by a combination of FK filtering and a near trace mute.

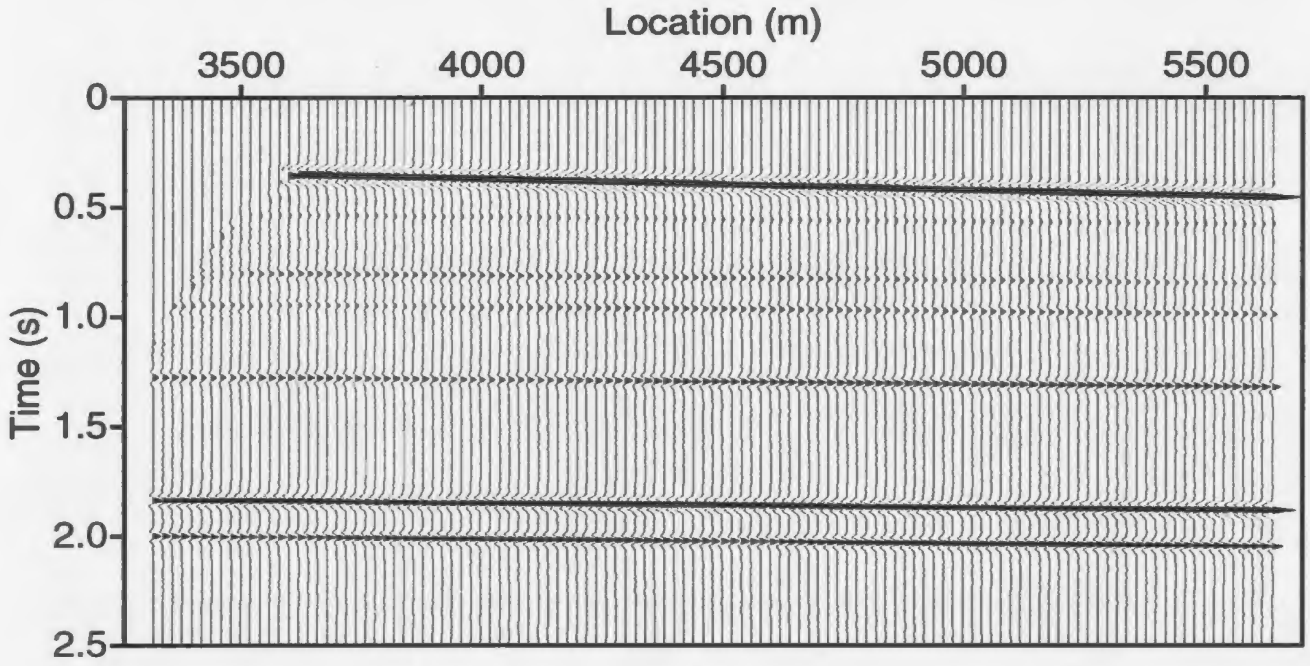

Figure 6.4. The stack of the complete dataset after applying Raymult to the original shot gathers.

only the primaries. Clearly, the multiples make it difficult to see the primaries, particularly in the first second of data. The power of CDP stacking is illustrated in Figure 6.2, which shows the stacked data, for the full dataset (Figure 6.2a) and the primaries-only dataset (Figure 6.2b). There is a significant improvement in the primary-to-multiple amplitude ratio compared with the near-trace gather, and all of the primaries at least can be seen. However, there is a considerable amount of multiple energy still present in the data.

Figure 6.3a illustrates the improvement provided by FK filtering in the shot domain after NMO using intermediate velocities. Since this technique was applied with a prior knowledge of the true velocity function, it has been optimally applied. The technique is only marginally successful in providing

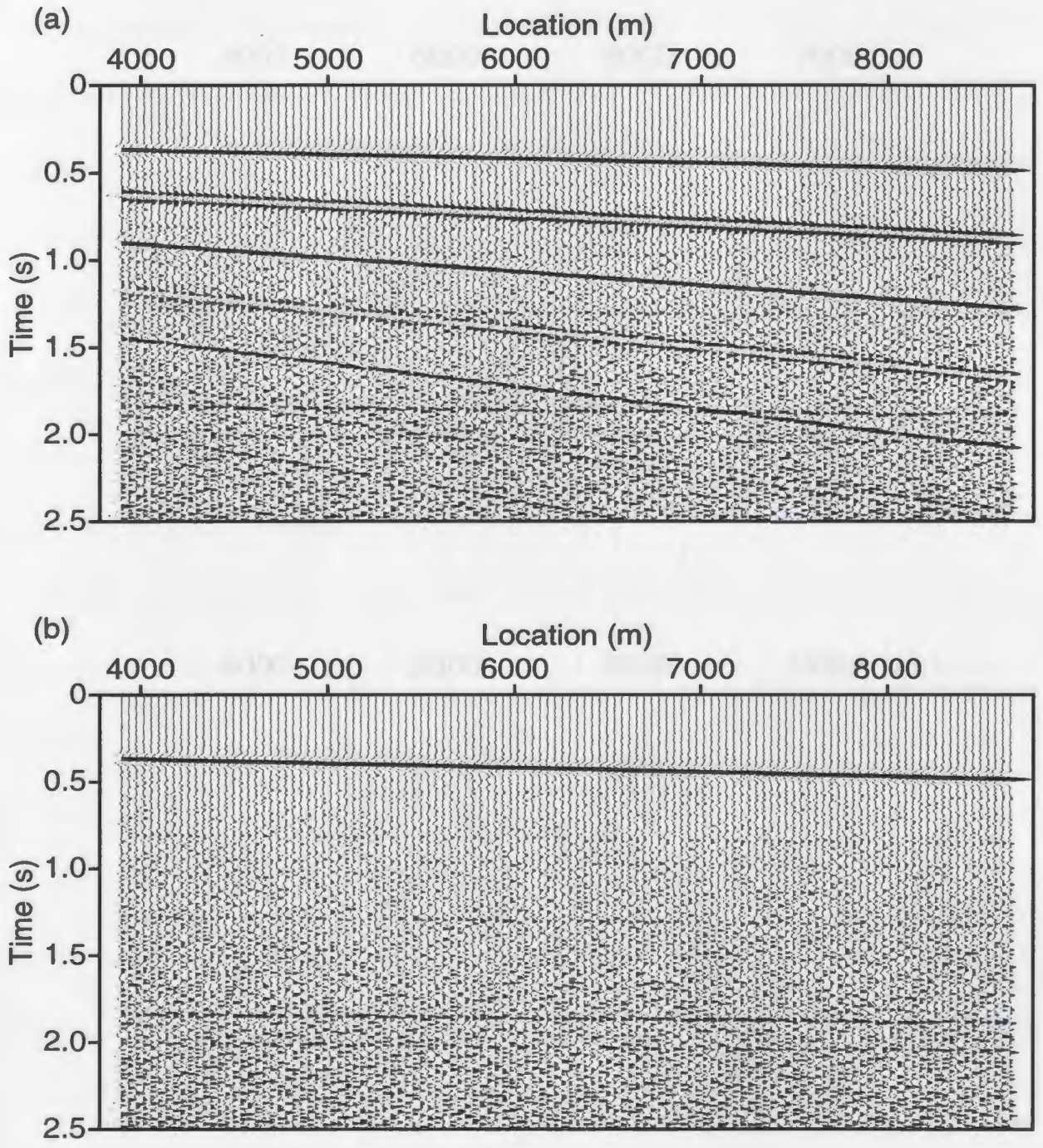

Figure 6.5. Near trace gathers for dipping sea-floor synthetics including noise: (a) shows the complete data set, including water-bottom multiples, while (b) shows only the primaries.

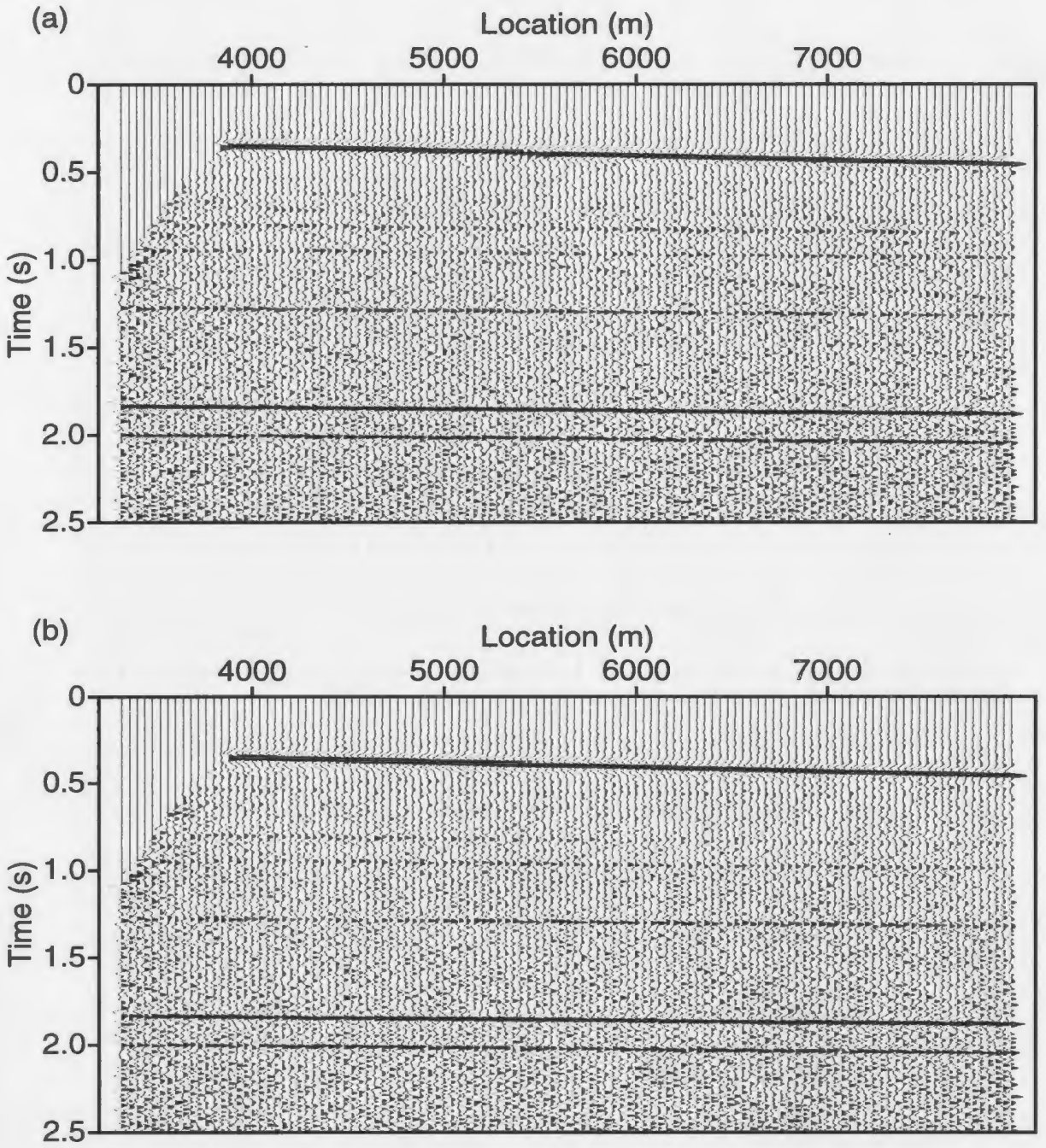

Figure 6.6. Comparison of FK filtering and Raymult for dipping sea-floor synthetics with noise: (a) shows the results of processing with FK filtering of shot gathers and a subsequent near trace mute, while (b) shows the results of Raymult processing.

further multiple attenuation. However, since the FK filtering is ineffective at small offsets, the attenuation is significantly enhanced by applying the filter in combination with an inside mute (Figure 6.3b).

Figure 6.4 shows the performance of Raymult on the same dataset. There is very little multiple energy remaining, while the primaries are well preserved. As seen in the pre-stack gathers, there is a slight dimming of the primary amplitudes in a few locations, however stacking has reduced this effect. Clearly, the overall performance is excellent.

Figure 6.5 shows the near trace gather after the addition of random noise. The noise caused picking errors of up to 1.5 ms, which were enhanced by choosing an incorrect water velocity of 1475 ms^{-1}, producing model errors between 4.5 and 6.5 metres. However, Raymult was still able to adapt the raytracing results to fit the data, and the final attenuation was very good (see Figure 6.6). Once again, the Raymult stack is superior to the FK filtered stack, in which second order multiples, in particular, are clearly visible just below one second.

6.2 Synthetic Example: Undulating sea-floor.

The second synthetic dataset used the same basic velocity structure as the first, but with an undulating water bottom, rather than a sloping one. It was generated using the same acquisition geometry as the first; a 200 m near offset

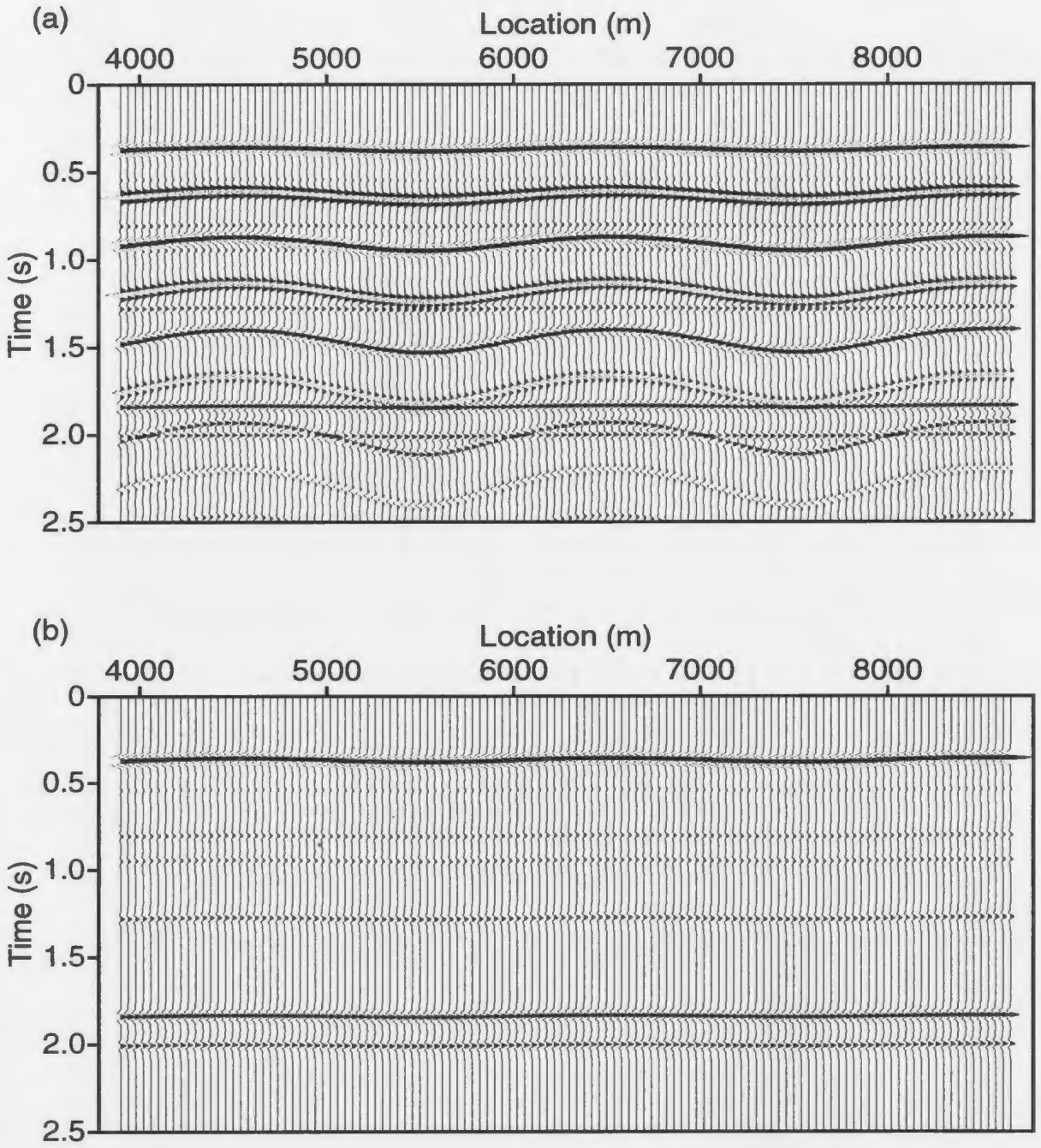

Figure 6.7. Near trace gathers for undulating sea-floor synthetics: (a) shows the complete data set, including water-bottom multiples, while (b) shows only the primaries.

and 40 m receiver spacing. Figure 6.7 shows the near trace gathers with and without the water bottom multiples. As expected, the multiples exaggerate the water-bottom undulations, making it very difficult to see the primaries.

Figure 6.8 shows the brute stacks. While there is a significant improvement in the primary-to multiple energy ratio, the multiples are still a problem, with at least the first four orders still having amplitudes comparable to the primaries. FK filtering provides additional attenuation (see Figure 6.9), especially when used in combination with a near trace mute, but its effectiveness is dip dependent. This is because FK attenuation depends on the moveout difference between the primaries and the multiples. When the sea-floor is dipping away from the source, there is an apparent decrease in the velocity of the reflection. This increases the moveout difference and, as a result, improves the ability of the FK filtering to remove the event. Conversely, when the dip is towards the source, there is an increase in the apparent velocity and a corresponding decrease in the effectiveness of the filtering. The net result is dip-dependent multiple attenuation, which can be a major problem. Although the filtered data looks relatively clean, the multiple energy which remains is not continuous and hence is not immediately identifiable as multiple. As a result, this can produce misinterpretation of multiples as primaries.

Figure 6.10 shows the result of Raymult processing. The multiple attenuation

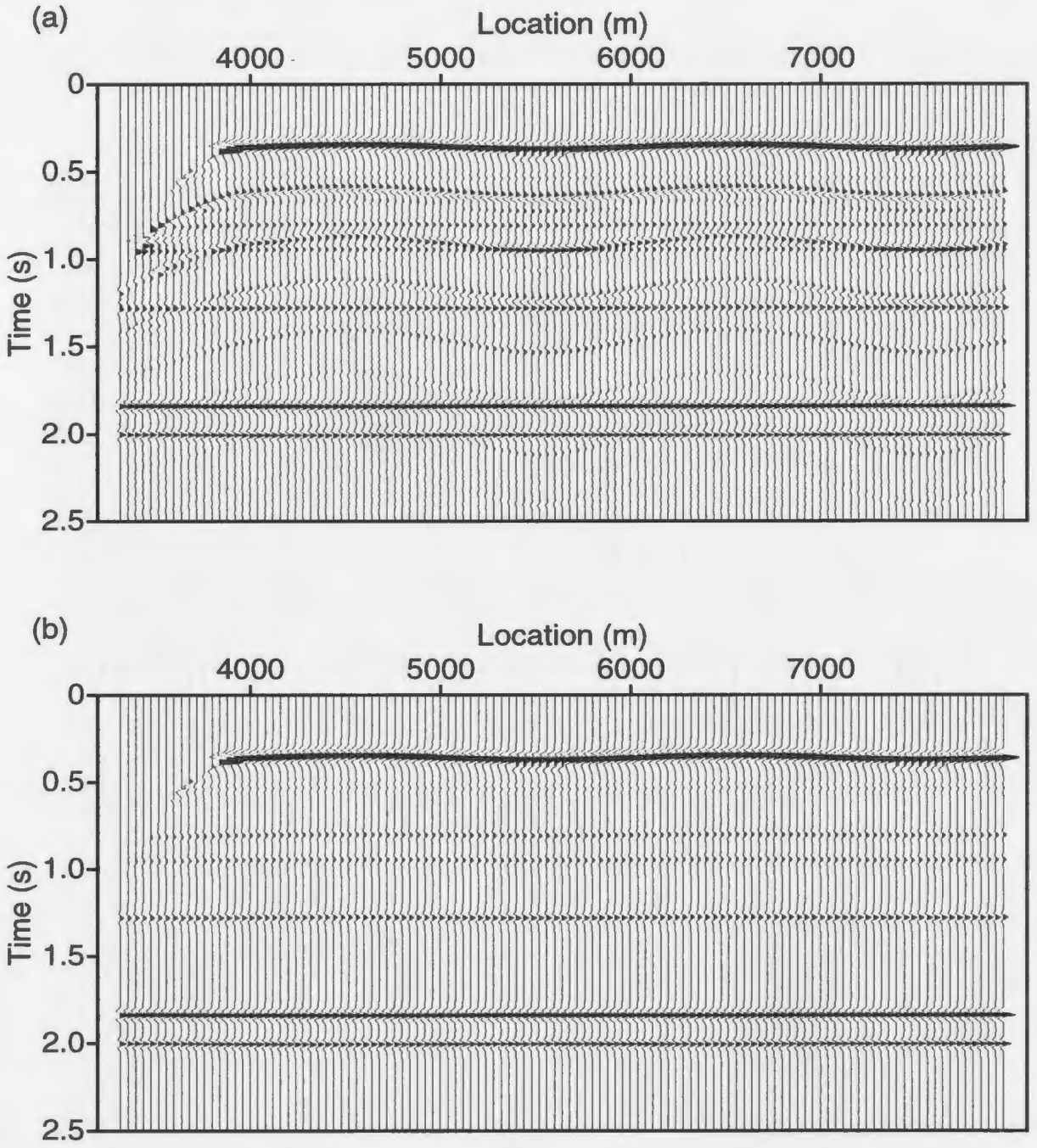

Figure 6.8. Brute stacks for undulating sea-floor synthetics: (a) shows the stack of the complete data set, including water-bottom multiples, while (b) shows the primary-only stack.

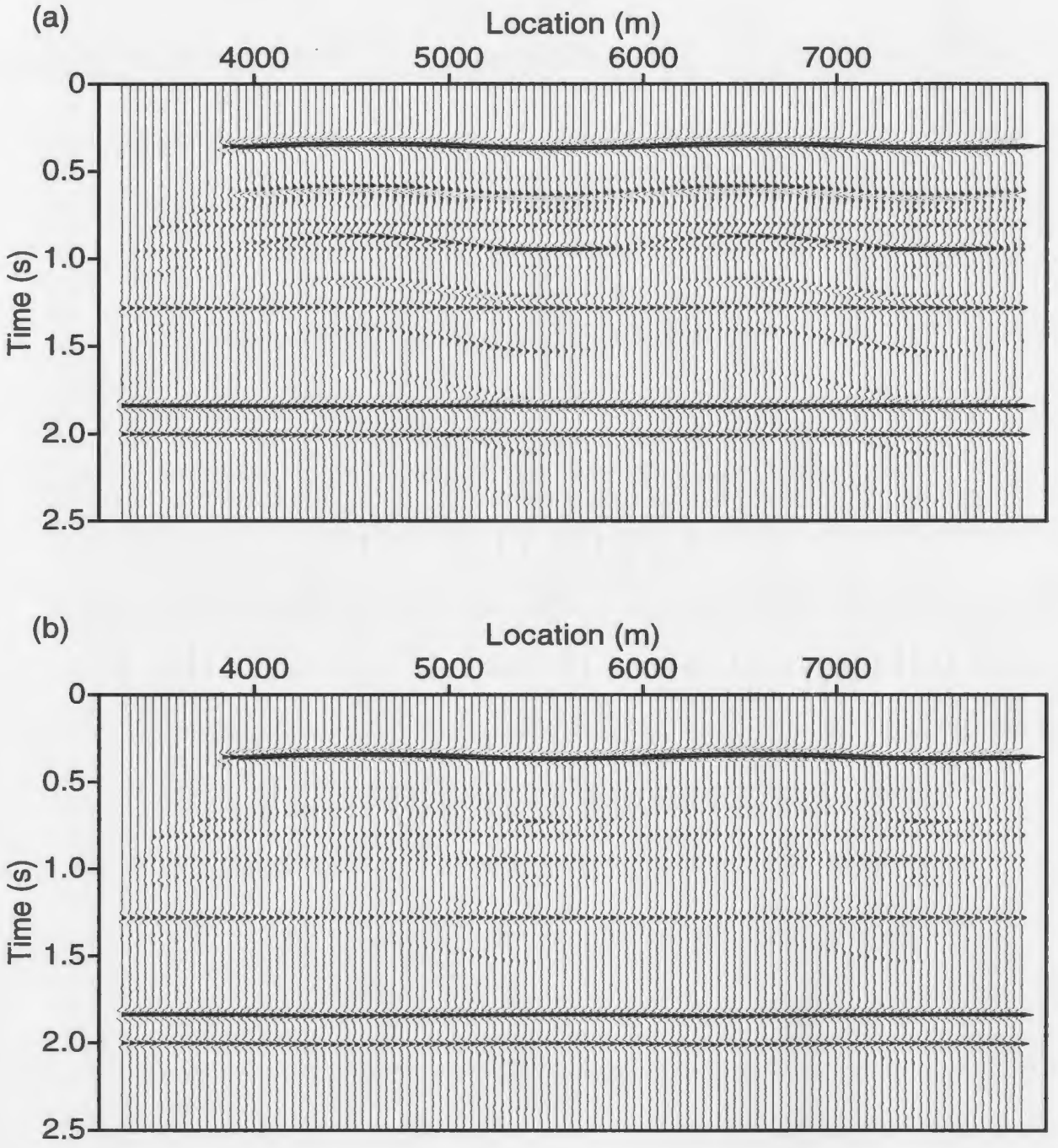

Figure 6.9. FK multiple attenuation for undulating sea-floor synthetics: (a) shows the stack of the complete data set after applying an FK filter to the shot gathers, while (b) shows the stack produced by a combination of FK filtering and a near trace mute.

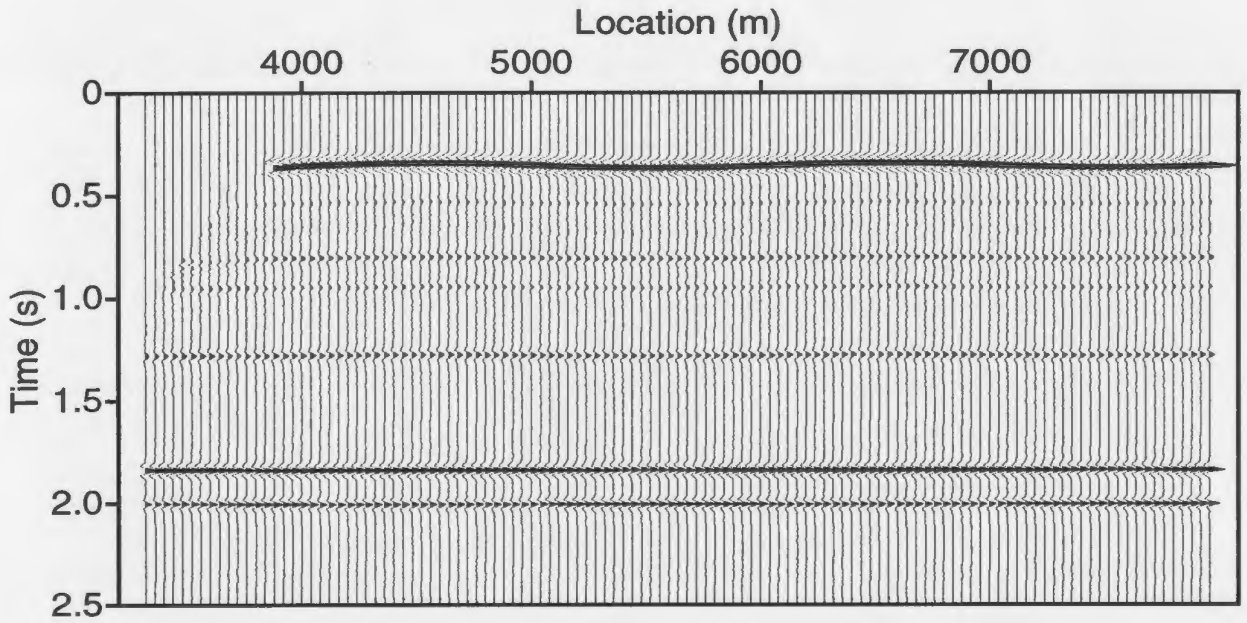

Figure 6.10. The stack of the complete dataset after applying Raymult to the original shot gathers.

is excellent and unaffected by changes in dip. While there is a slight decrease in primary amplitudes at those locations where multiples and primaries cross, the effect is minor.

6.3 Real Example: Hunt '95 dataset.

The first real dataset examined was shot by Memorial University in 1995, off the west coast of Newfoundland as part of a survey for Hunt Oil. The data were collected over a relatively hard sea-floor using a high frequency source and a short 48 channel streamer. The near offset was 53.5 m and the group interval was 12.5 m, producing a far offset of only 641 m. A total of 421 shots were collected with a 12.5 m shot spacing. The data were generally very good, but in

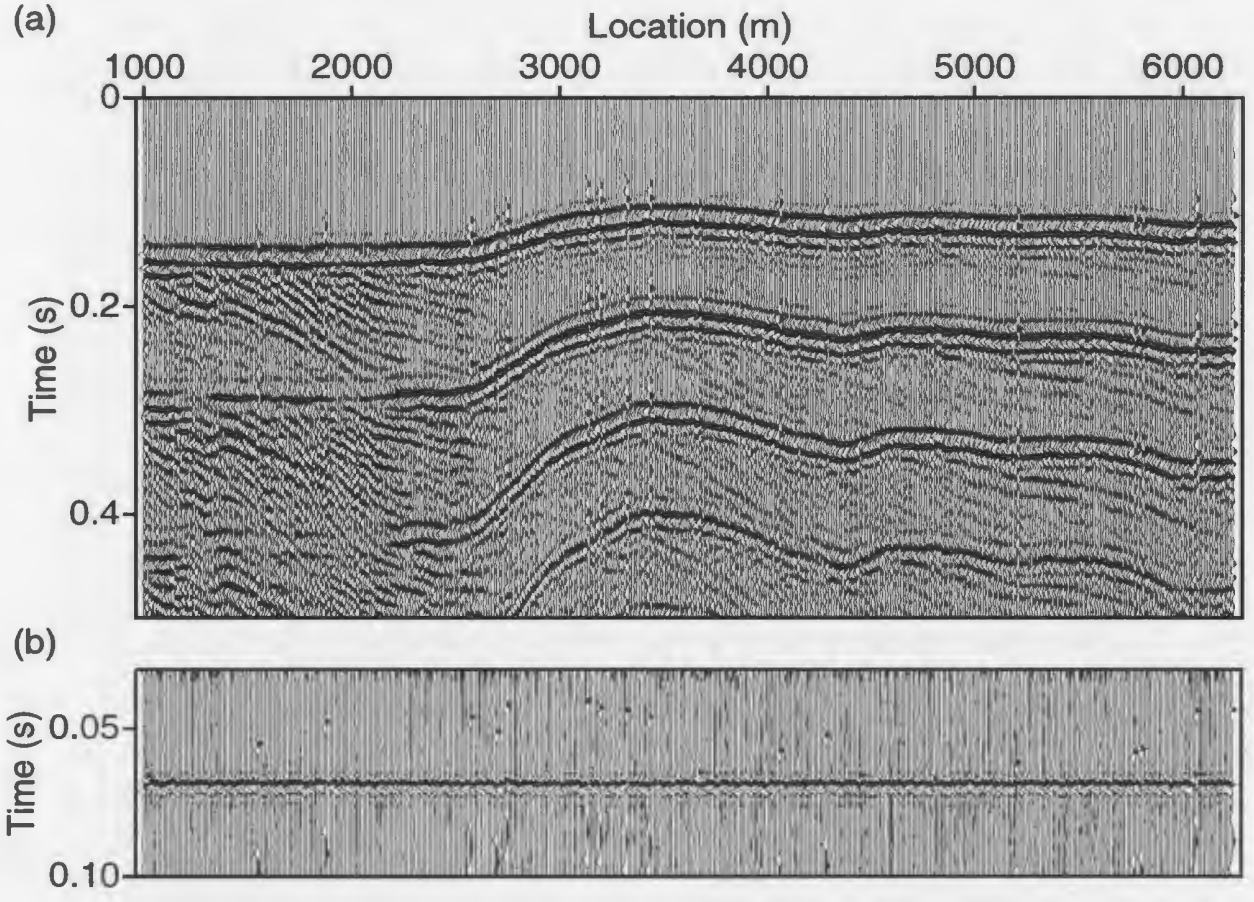

Figure 6.11. (a) Near trace gather for the Hunt '95 dataset. (b) A close-up image of the direct arrivals at approximately 70 ms. Note the event's apparent scattering, which can only be caused by a timing problem.

addition to the obvious multiple problem, there was a serious problem with the source timing. The near trace gather clearly shows that several traces (see Figure 6.11) have major timing errors. This was corrected by picking the direct arrivals on the near trace gather, and using the picks to determine the necessary static shift for each shot gather. The results of the statics application are shown in Figure 6.12 (a). The corrected gather was then used for modelling the sea-floor.

Figure 6.12 (a) also shows the initial picking results. The routine appears to

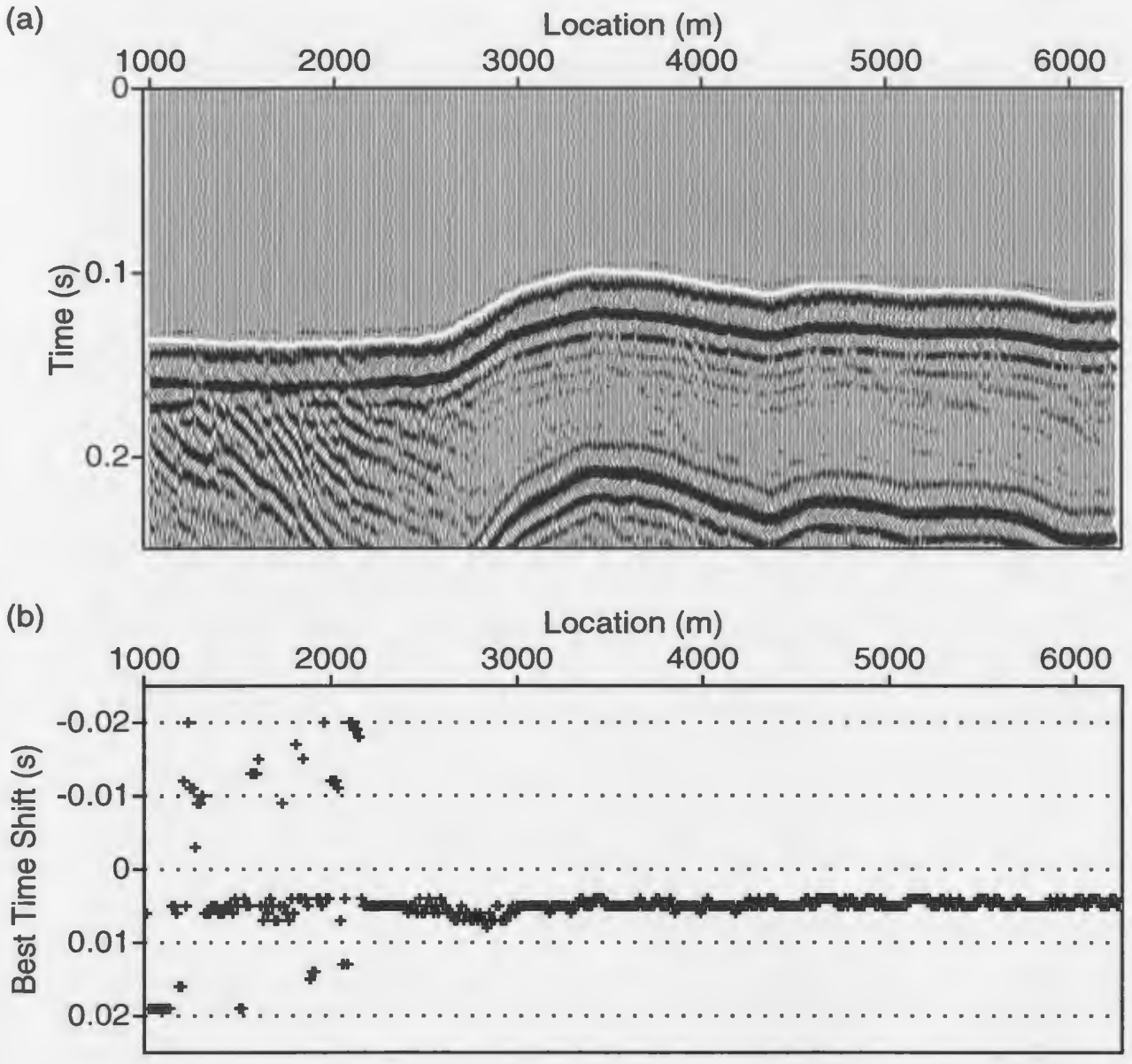

Figure 6.12. (a) The near trace gather after application of shot statics. The white line shows the automatic picking of the sea-floor reflection. (b) The multiple-based statics solution - indicates that the picks require a 4 ms shift.

have done a good job, despite the wavelet inconsistencies around location 2000 caused by the intersection of numerous primary reflectors with the sea-floor. A three point smoothing filter was applied to the picks before the statics

calculations in order to reduce the slight scatter produced by these inconsistencies. The resulting statics estimate for each trace is shown in Figure 6.12 (b). There is excellent consistency in the statics estimate, except at the beginning of the line, where the primaries have caused some problems. After applying the estimated 4 ms shift, the picks were migrated to generate the sea-floor model (see Figure 6.13). The timing estimates for the first seven orders of water-bottom multiples show very good agreement with the observed events.

In order to ensure that the water velocity of 1470 ms^{-1} was accurate, a shot gather was raytraced. Figure 6.14 shows an overlay of the raytraced times on the actual gather, confirming that the water velocity was reasonable. The shot gathers were then processed using Raymult. Figure 6.15 shows the same shot gather after the multiple attenuation. The strong reflection at 0.25 s appears to be a pegleg multiple caused by a reflector just below the sea-floor. This could explain the fact that the strong 'sea-floor' refraction does not appear continuous with the actual sea-floor reflection. The refractions may actually be from the strong reflector just below the sea-floor. Since the event is very close to the actual water bottom reflection, its moveout is sufficiently similar that a second pass of Raymult was able to eliminate its water-bottom pegleg multiples as well (see Figure 6.16). The data were stacked using the velocities shown in Figure 6.17. A comparison of the brute stack and the Raymult stack is shown in Figure 6.18.

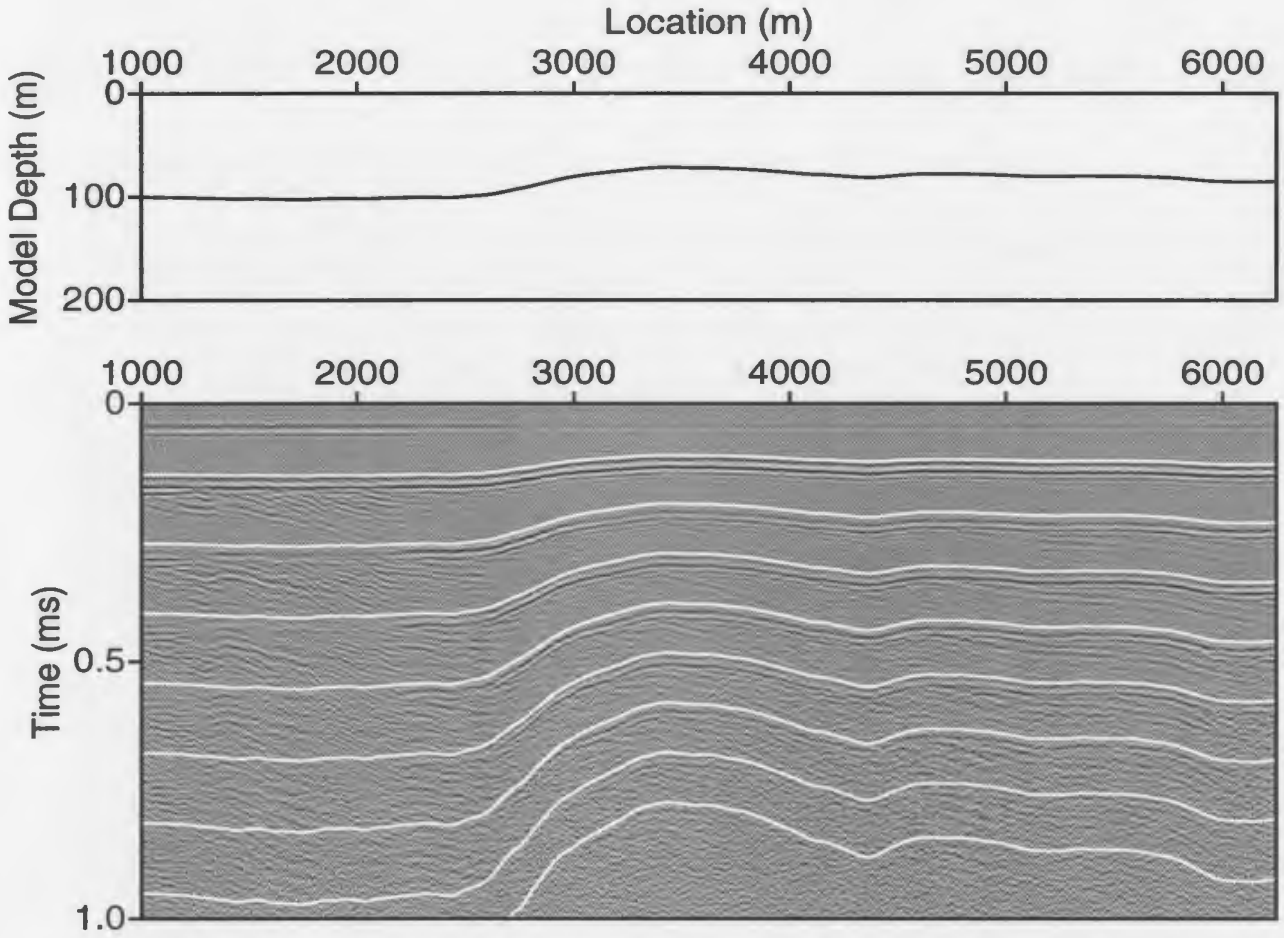

Figure 6.13. The estimated model and resulting multiple arrival-time predictions (white lines) for the high frequency dataset. A five point smoothing filter was applied to the picks before migration. The model does a very good job of predicting the arrivals times of the first seven orders of water-bottom multiples.

The water-bottom multiples have been attenuated extremely well, but there is still a significant pegleg problem. This should be helped by applying predictive deconvolution, with a design window starting just below the sea-floor. While the combination of dipping reflectors and inconsistent amplitudes reduces the effectiveness of the deconvolution, there is still a fair amount of pegleg attenuation (see Figure 6.19). Clearly the results are a significant improvement

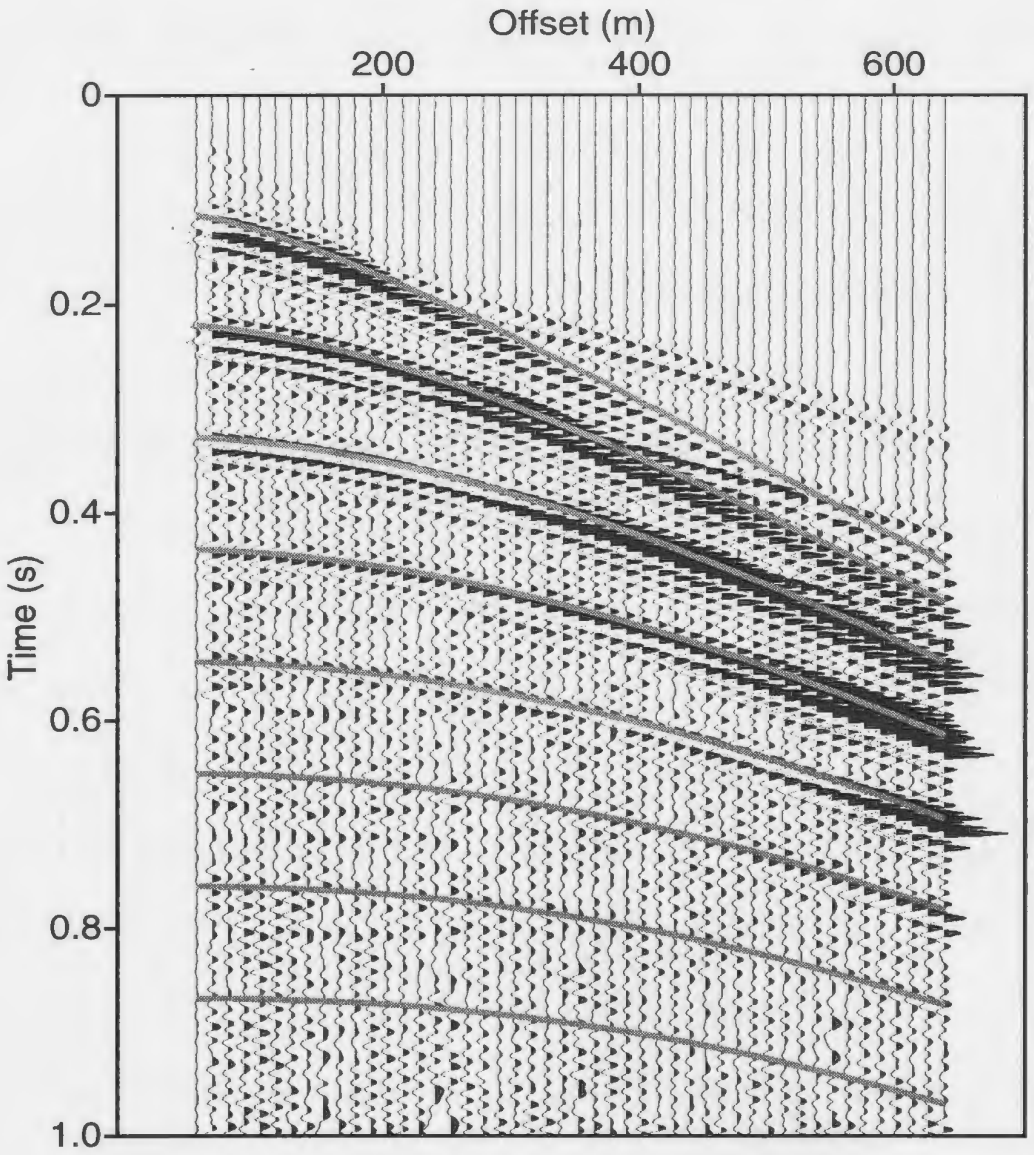

Figure 6.14. Overlay of arrival-time estimates on an original shot gather using a water velocity of 1470 ms^{-1}. The good fit at the far offsets indicates that the water velocity was estimated accurately.

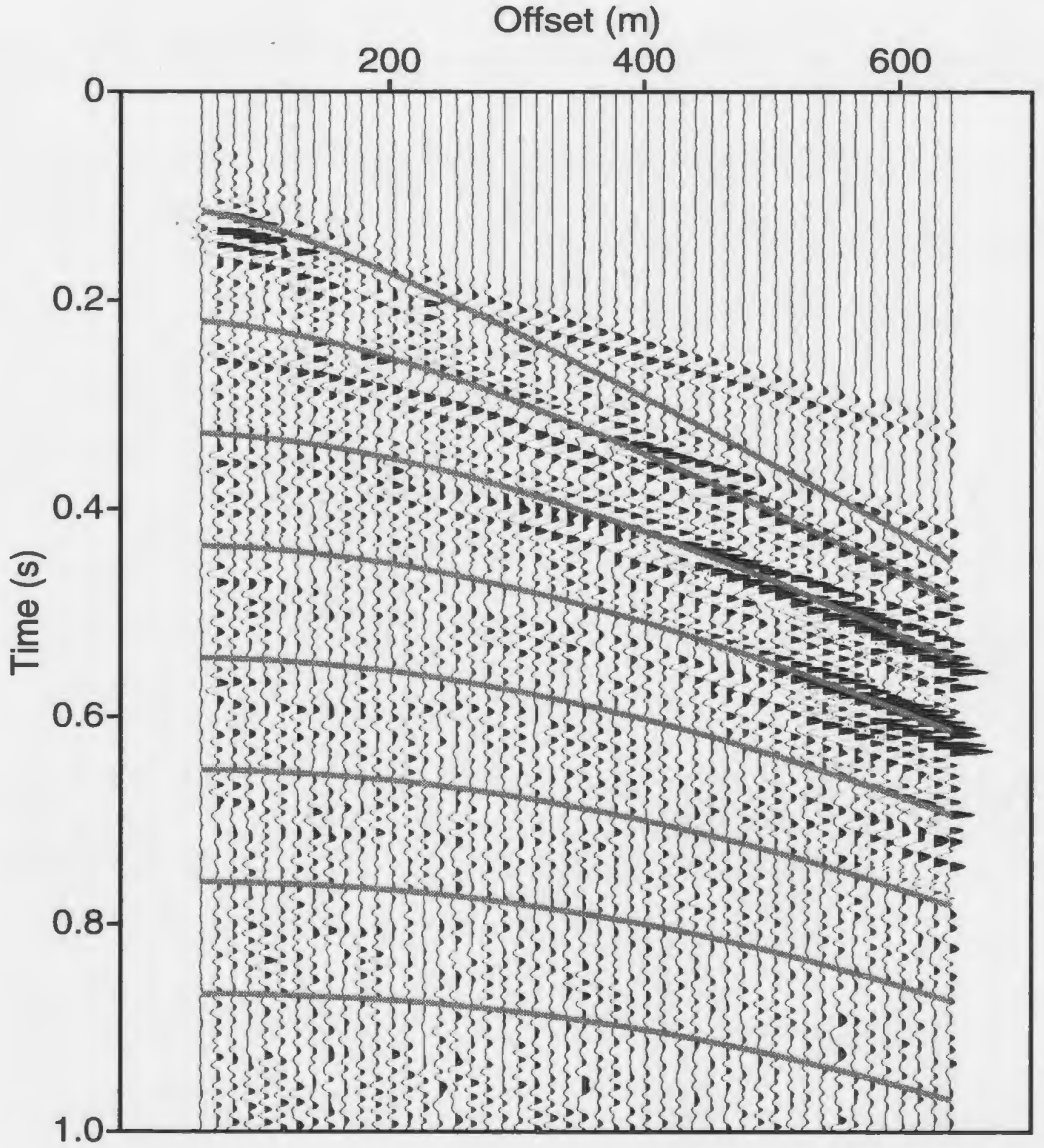

Figure 6.15. The same shot gather as in Figure 6.14 after application of Raymult. The multiple attenuation was very good, but there appears to be a reflector just below the sea-floor which has generated significant pegleg energy, particularly between 0.2 and 0.4 seconds.

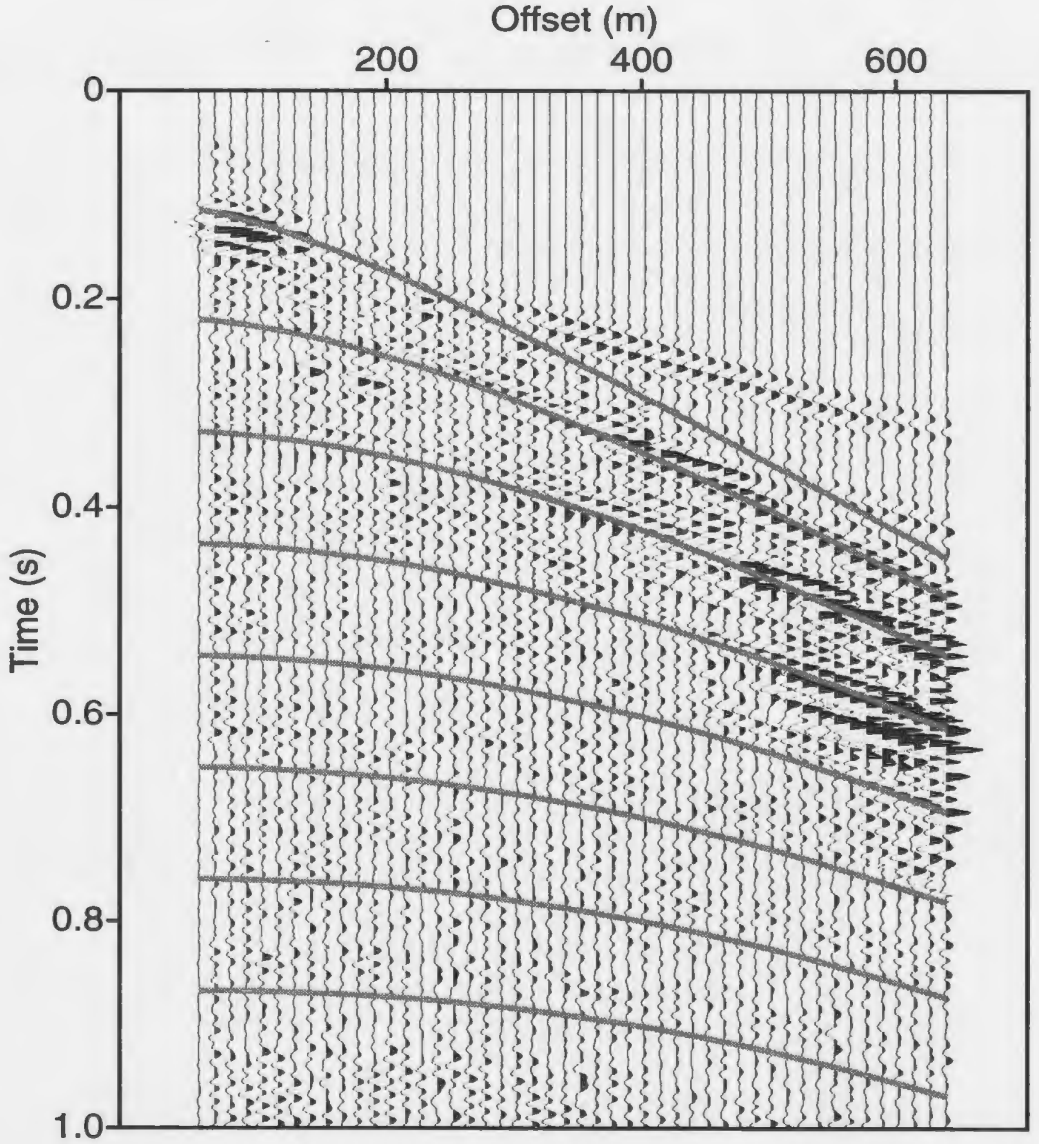

Figure 6.16. The same shot gather as in Figure 6.14 after the second pass of Raymult. The peglegs produced by the reflector just below the sea-floor have been attenuated along with the water-bottom multiples.

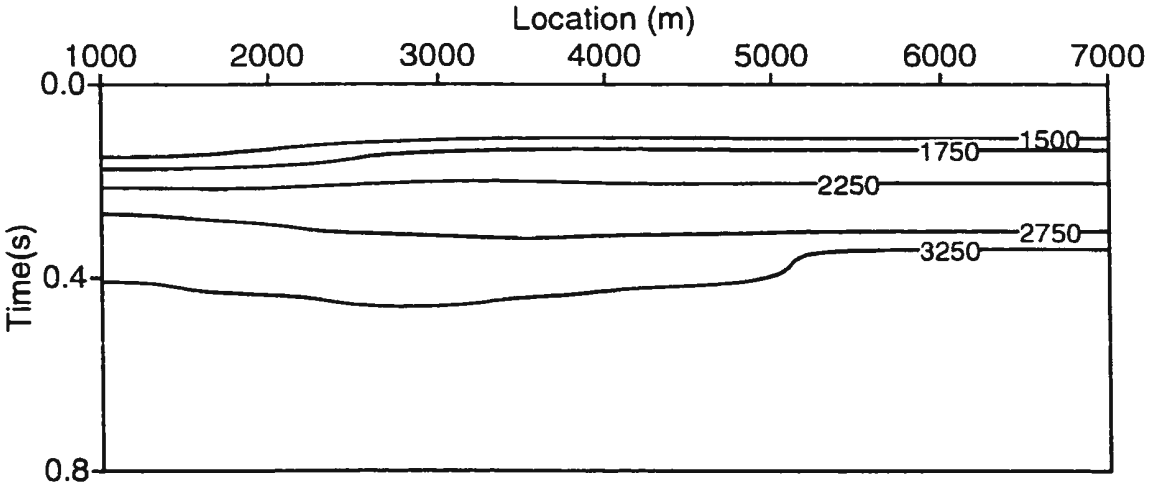

Figure 6.17. The NMO velocity model used for stacking the Hunt '95 dataset.

over deconvolution used alone. However, any interpretation must account for the possibility that apparent primaries may be peglegs of earlier events.

For comparison, the data were also processed using parabolic radon filtering as the main multiple attenuation technique. While the filtering reduced the amount of random noise, it did not remove much of the water-bottom multiple energy (see Figure 6.20a). This is undoubtedly due to the restricted offset range, which reduces the ability of the technique to discriminate between primary and multiple moveouts.

The combination of the radon transform and the subsequent stack is unlikely to have preserved the amplitude relationships between the multiples, even if the amplitudes had been perfectly geometric in the first place. As a result, predictive deconvolution is unable to attack all of the multiples simultaneously. (see Figure

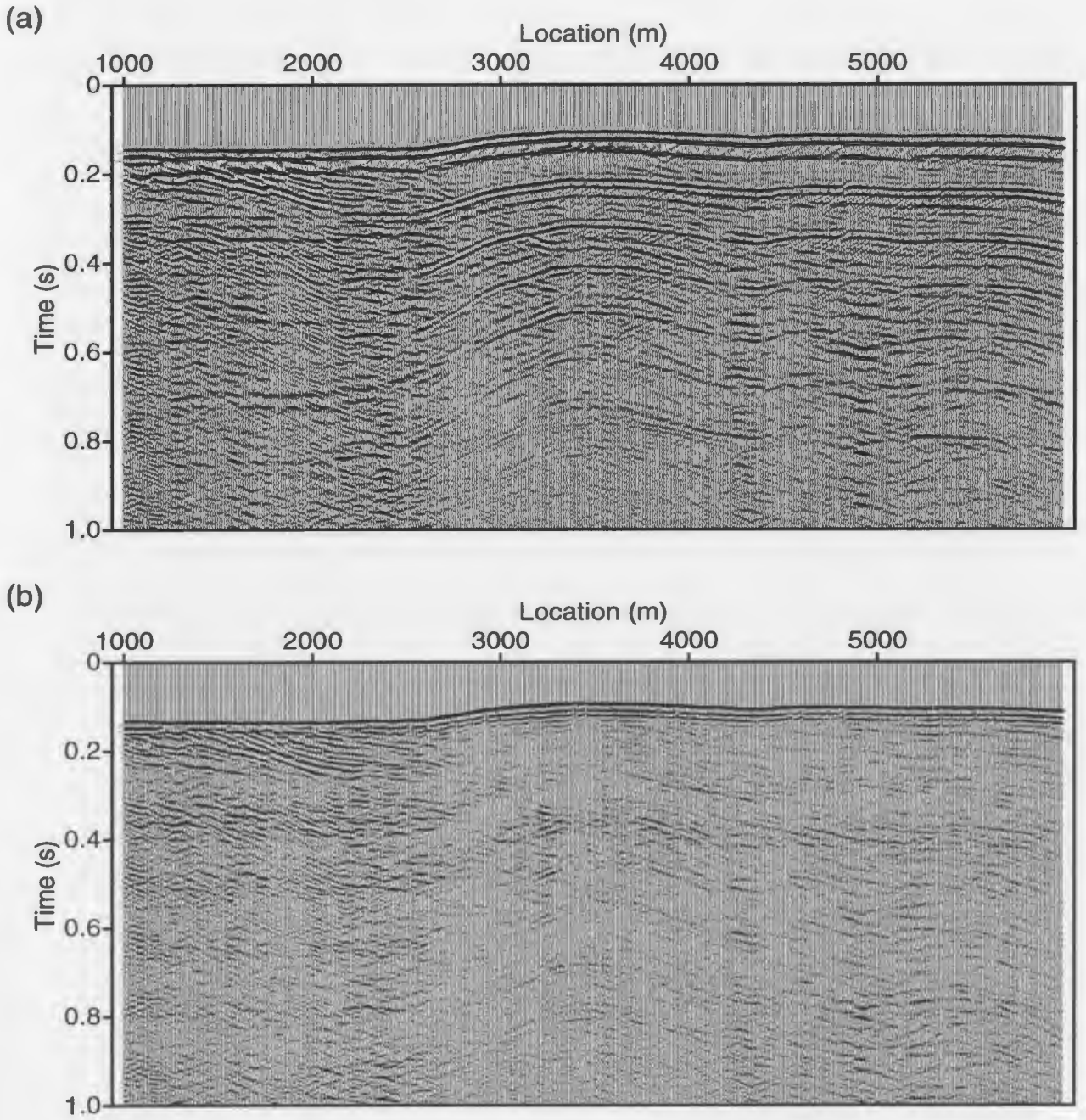

Figure 6.18. (a) Brute stack of Hunt '95 dataset. (b) Stack using identical processing stream except for the application of Raymult to the original shot gathers.

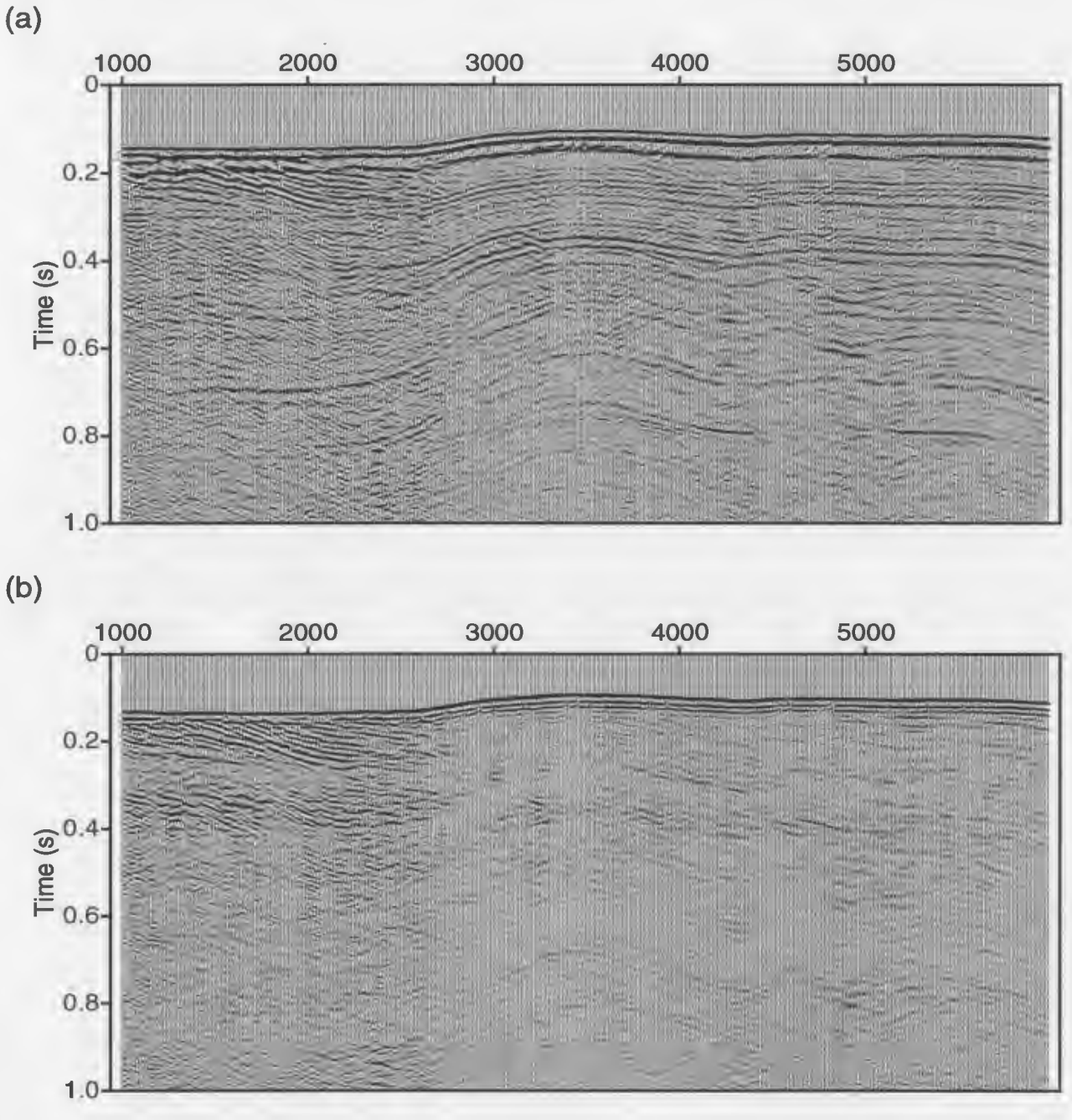

Figure 6.19. (a) Stack of Hunt '95 dataset after the application of post-stack predictive deconvolution. (b) Raymult stack after post-stack deconvolution.

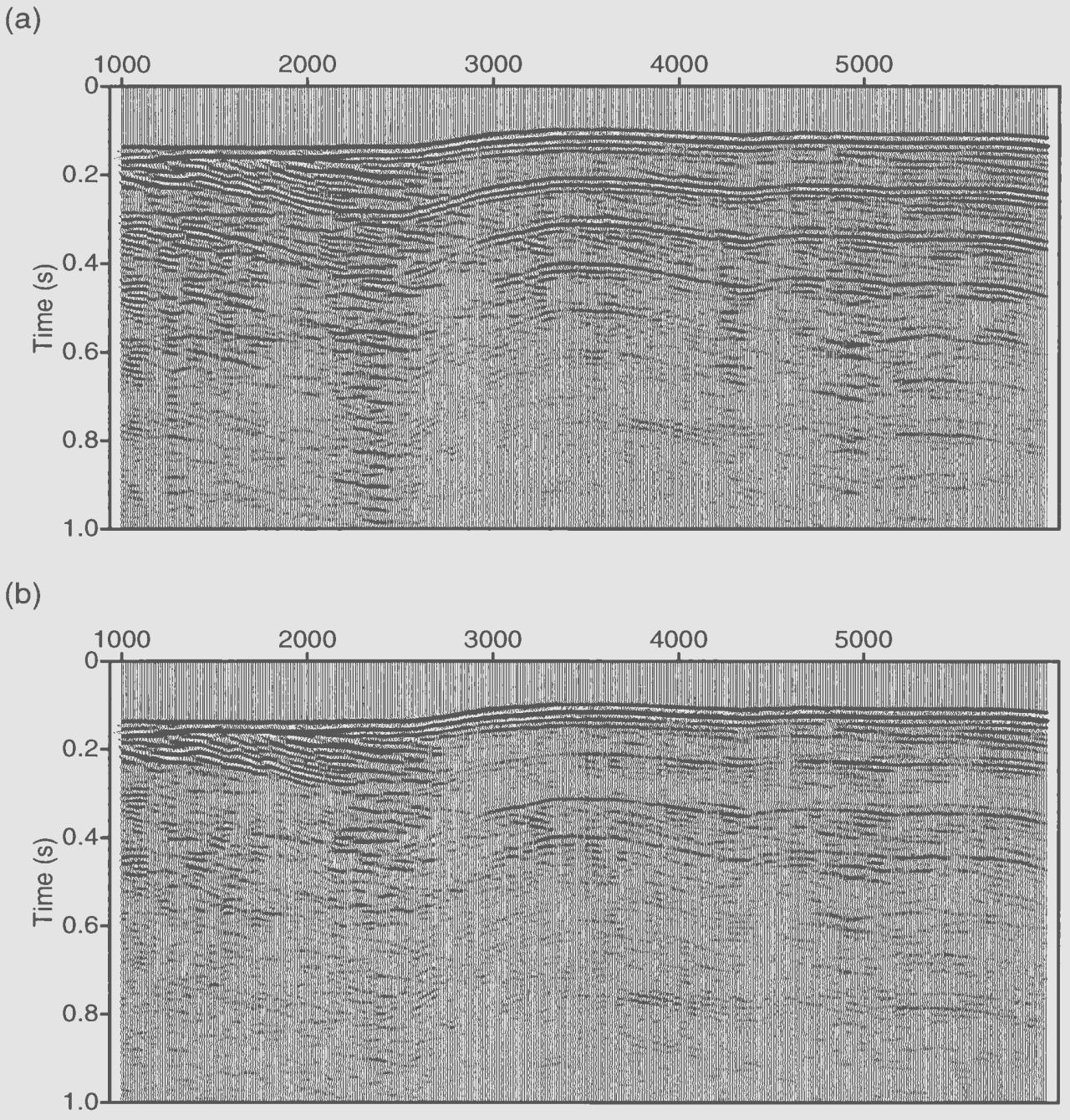

Figure 6.20. (a) Stack of the Hunt '95 dataset, using radon filtering of the shot gathers as the main multiple attenuation technique. (b) The same dataset after predictive deconvolution using the sea-floor model for determining the prediction lag.

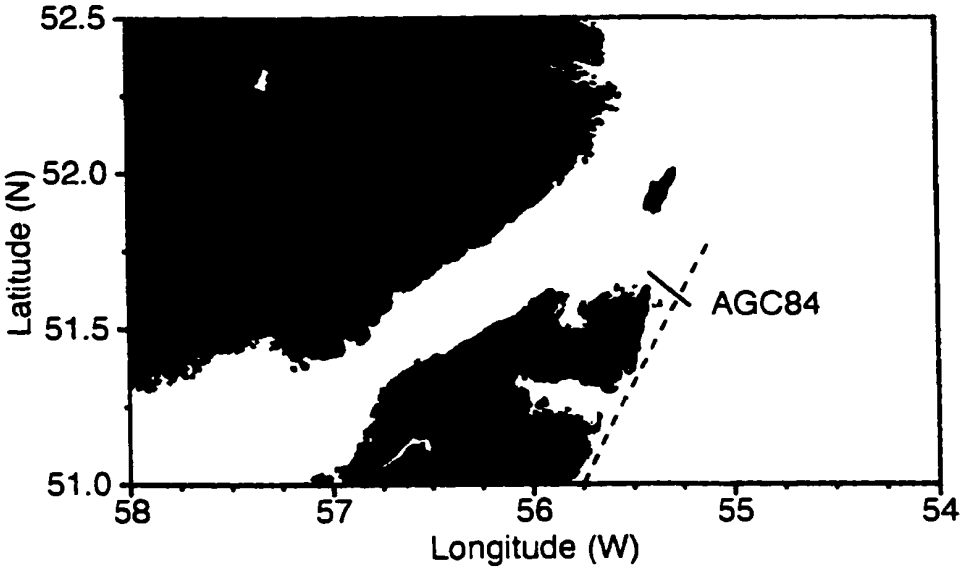

Figure 6.21. Location map for the second real dataset, which was collected by the AGC as part of a deep crustal experiment in 1984. The dashed line marks the approximate location of a major fault thought to intersect the line (Langdon, 1996).

6.20b). While deconvolution does produce additional multiple attenuation, the performance is not consistent. Some multiples have been virtually eradicated while others have been hardly touched. The net result is a stack which would be very difficult to interpret.

6.4 Real Example: AGC '84 data

The second real data example is very different from the first. The data were collected by the Atlantic Geoscience Centre in 1984, off the northern tip of the island of Newfoundland (see Figure 6.21), as part of a deep crustal seismic

experiment. The near offset was 291 metres, the group spacing was 25 metres and the shot interval was 50 metres, thereby producing a CDP spacing of 12.5 metres. The streamer contained 120 receiver groups, generating an average fold of 30.

The sea-floor in this area is extremely hard, with very little soft sediment cover. As a result, the water bottom multiples completely dominate the data. To further complicate matters, the sea-floor is very rough, so that water bottom diffractions and their multiples are also a significant problem. The net result is a data set which was essentially discarded without interpretation. Both the original publication of the data (Keen et al., 1986) and the later compilation of several related data sets (Marillier et al., 1989) leave the first 4 to 6 seconds without interpreted primaries. However a deep reflection experiment on land in 1989 produced numerous reflectors throughout the crust (Quinlan et al., 1992). Since it is unlikely that these reflectors would end at the coastline, the lack of reflectors offshore is apparently due to the inability of the processing to image them. Undoubtedly, this is a result of the extreme water-bottom multiple problem.

Processing the data using Raymult was not straightforward. Since the critical offset is well inside the near trace, the phase variations in the water-bottom reflection are so severe that it is hardly recognizable as a coherent event on the

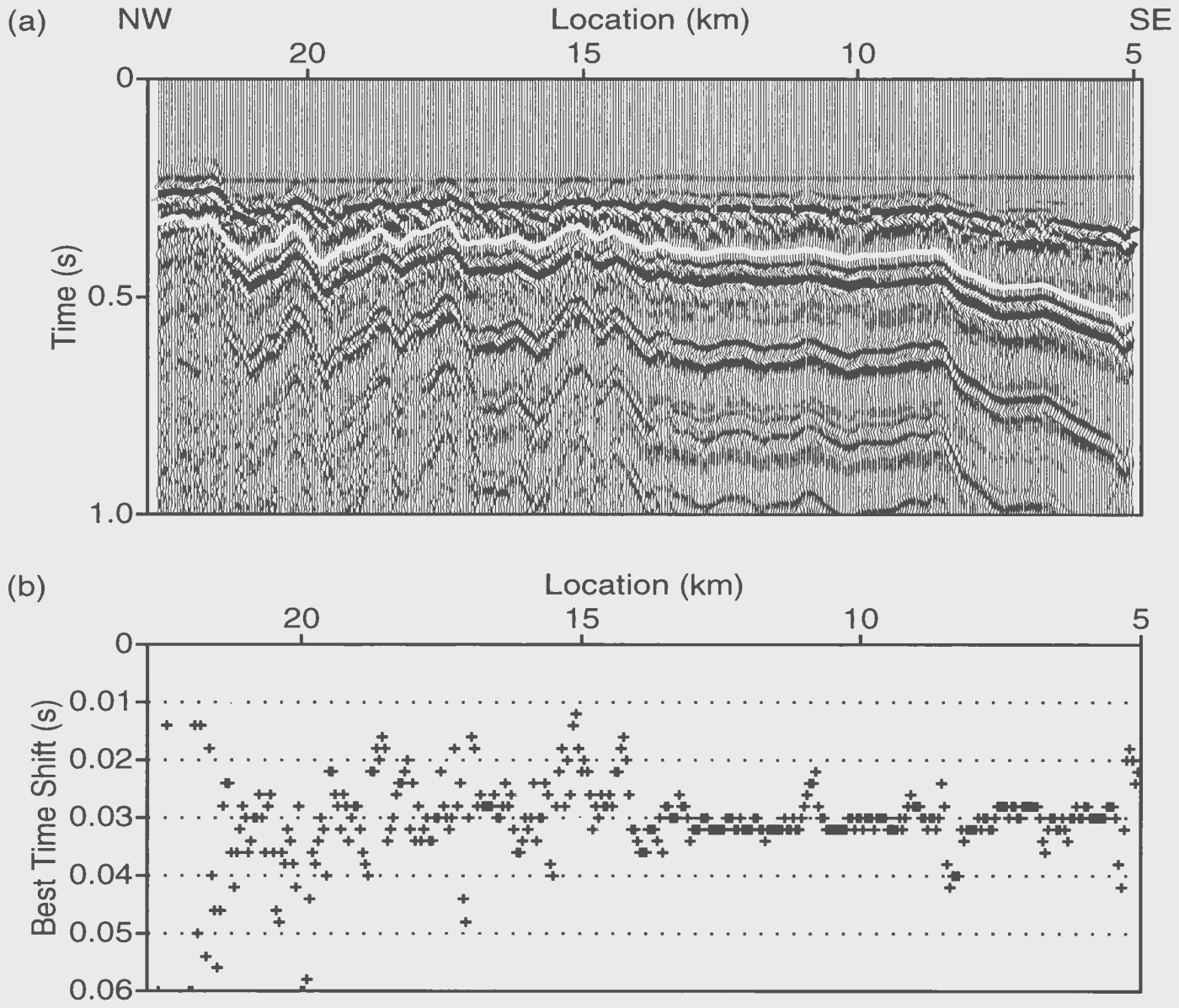

Figure 6.22. (a) The near trace gather for AGC '84. The white line shows the automatic picking of the first order multiple. (b) The multiple-based statics solution - indicates that the picks require a 32 ms shift.

near trace gather (see Figure 6.22). Since the event is also disrupted by numerous diffractions, reliable picking is virtually impossible. The first order multiple, on the other hand, is just pre-critical so that the phase variations are relatively

minor. As a result, I chose to pick the multiple event, and I adapted the modelling routine to take that into account. Figure 6.22 (a) shows the picking results, while Figure 6.22 (b) shows the results of the statics calculations. The complexity of water bottom and the severe diffractions produced quite a lot of scatter in the statics estimate, but the model estimate appears to be good (see Figure 6.23). The timing predictions for the first six orders of multiples are in very good agreement with the data.

Since Raymult is able to remove only multiple energy from the reflected event, it is unable to attenuate diffracted energy. This is clearly a major problem with this data set, since the diffractions are almost as severe as the multiple reflections. As a result, I chose to run a prestack migration using the water velocity before applying Raymult. It was performed on common offset gathers using Stolt's algorithm in FK space (Yilmaz, 1987).

In theory, this should collapse the water-bottom related diffractions, without doing too much damage to subhorizontal primary reflections. Figure 6.24 shows the results of migrating the near trace gather. The diffractions have been collapsed into the reflected events, leading to a marked improvement in the coherence of the multiples. The benefits of the migration are even more obvious on the shot gathers. Figure 6.25 shows shot 1510, which had a source location near location 8 km. The diffractions centered at 1400 m offset are clearly visible,

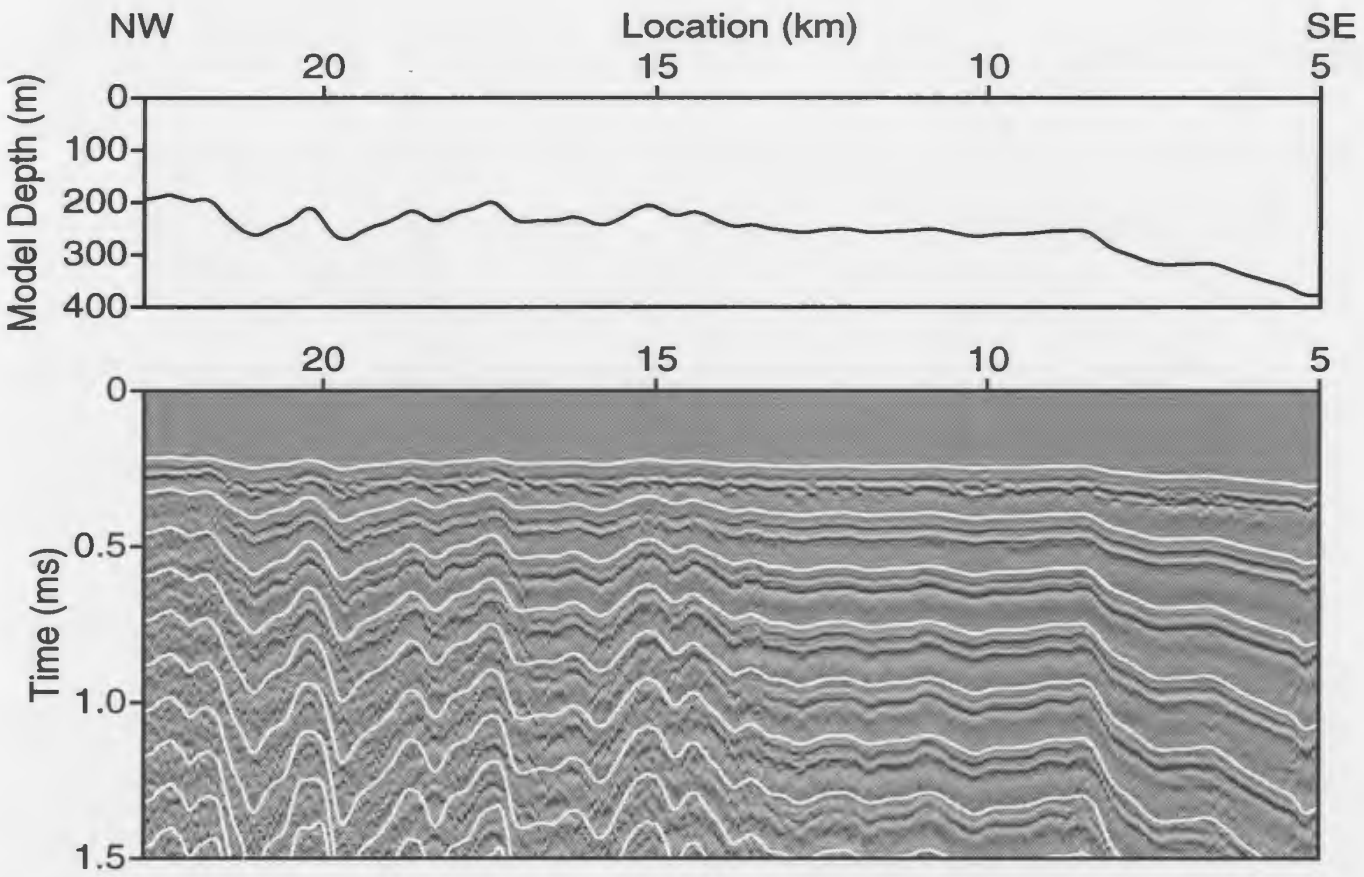

Figure 6.23. The estimated model and resulting multiple arrival-time predictions (white lines) for the AGC '84 dataset. A five point smoothing filter was applied to the picks before migration. The model does a very good job of predicting the arrivals times of the first six orders of water-bottom multiples.

while the diffractions approximately parallel to the multiples below 1.5 seconds are less obvious. The migration does an excellent job of collapsing these events into the multiple reflections themselves (see Figure 6.26). Raymult is then very effective at removing most of the energy from those events (see Figure 6.27). The attenuation generally averaged between 20 and 24 dB.

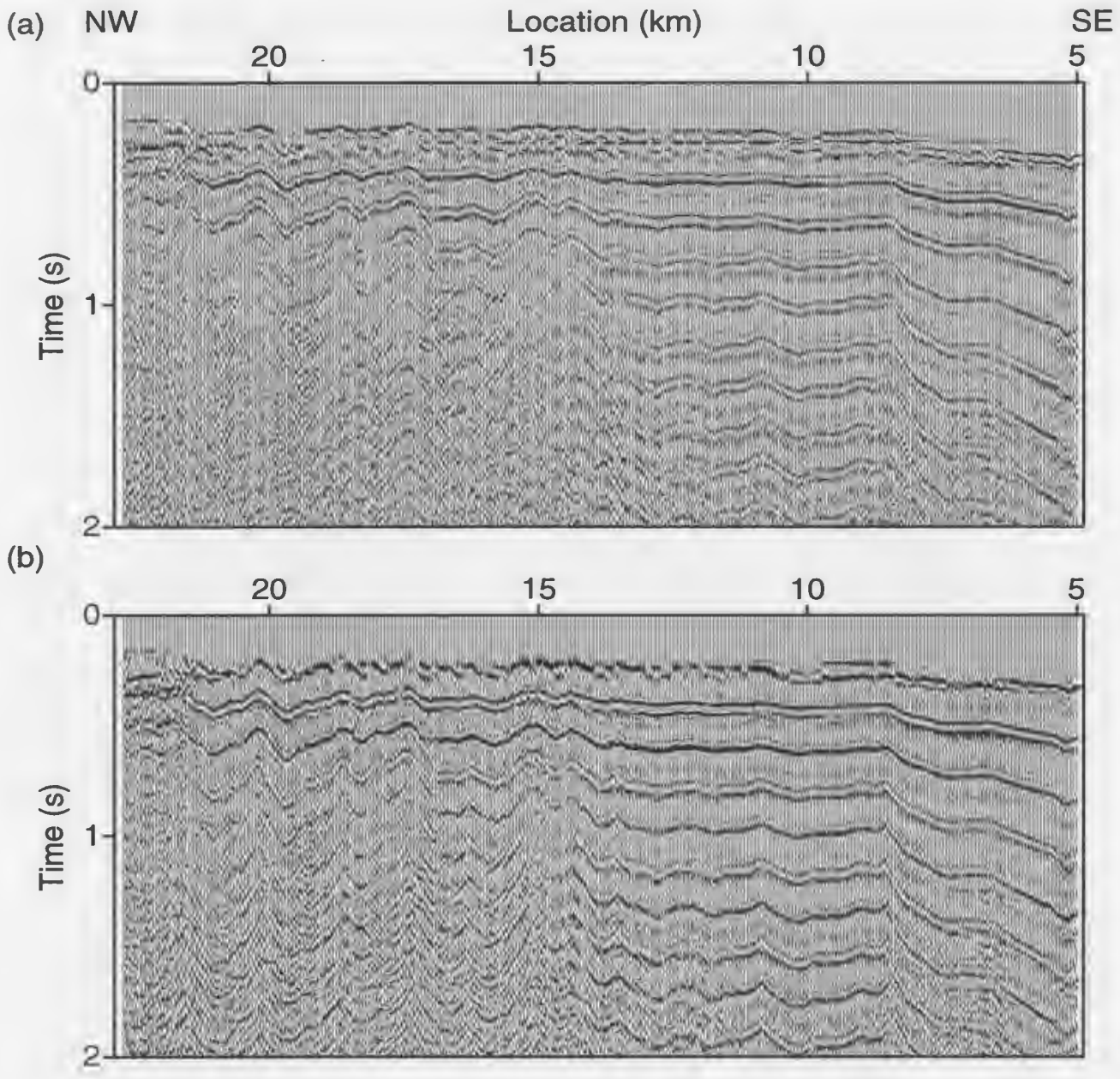

Figure 6.24. The effect of constant velocity migration on the near trace gather. (a) shows the original gather, (b) shows the gather after FK migration using the water velocity (1450 ms^{-1}).

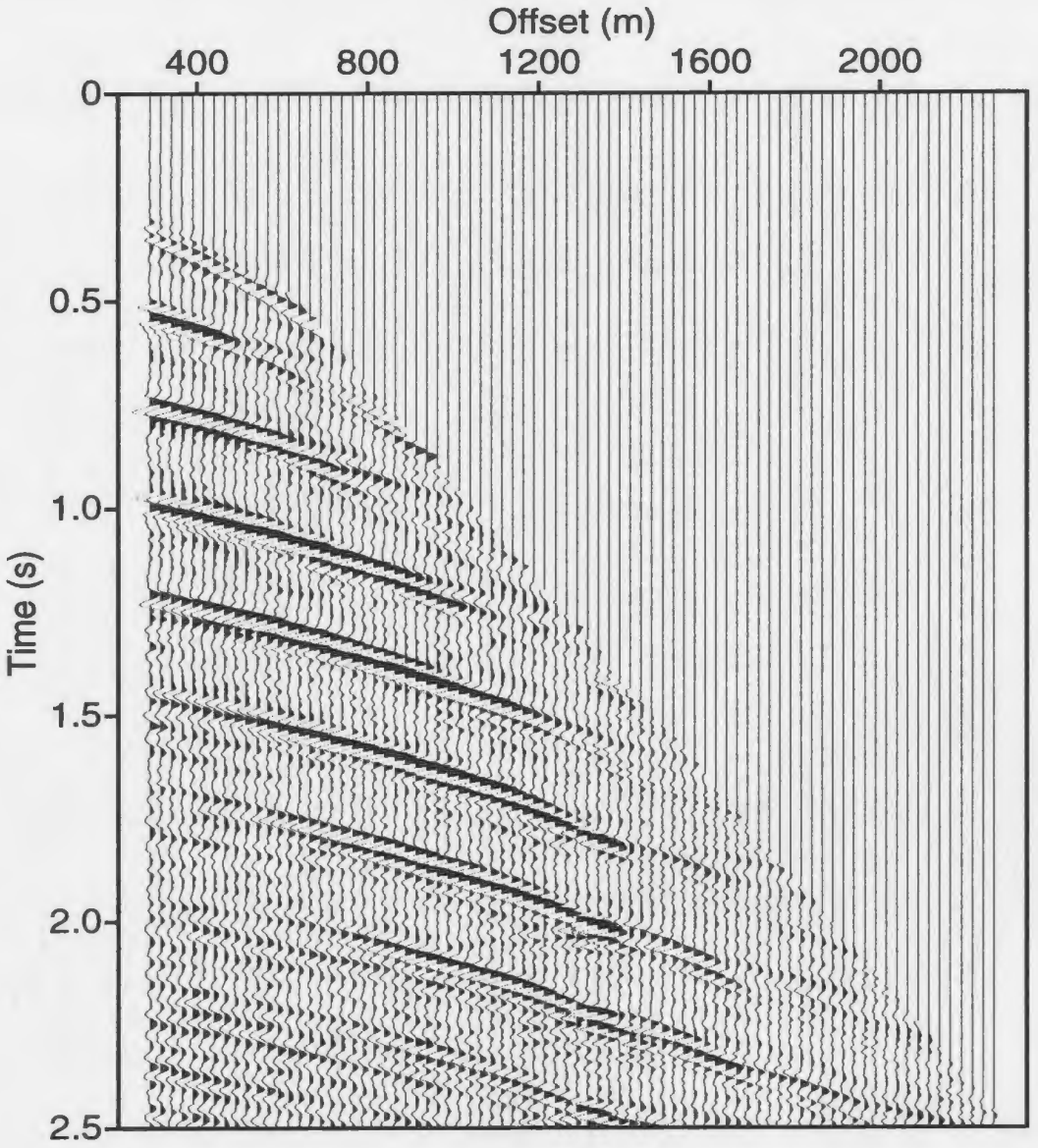

Figure 6.25. The original data gather for shot 1510, at location 8 km.

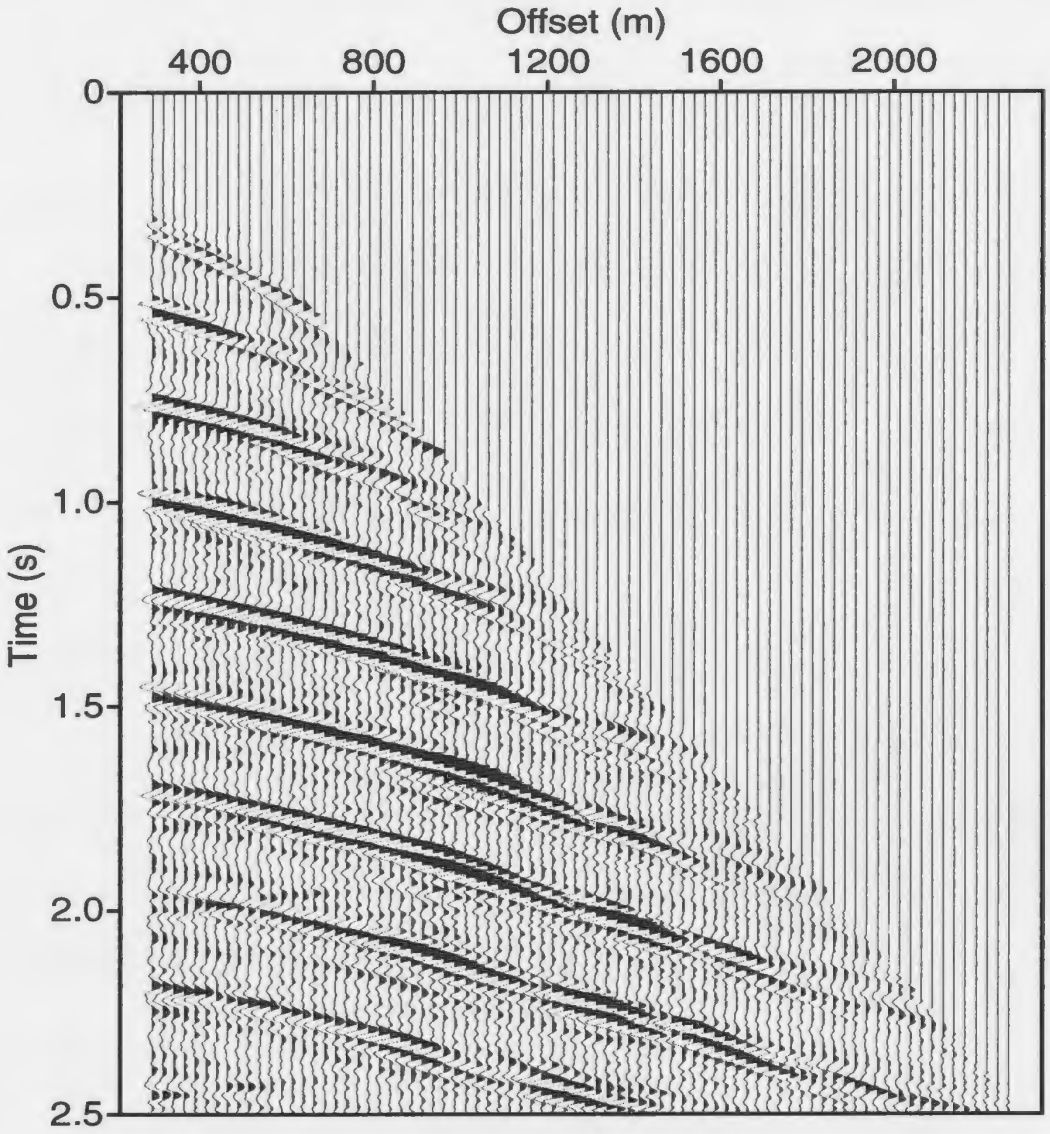

Figure 6.26. The data gather for shot 1510 resorted after migration in the common-offset domain. There is obvious decrease in diffracted energy, which makes the multiples stand out as discrete events.

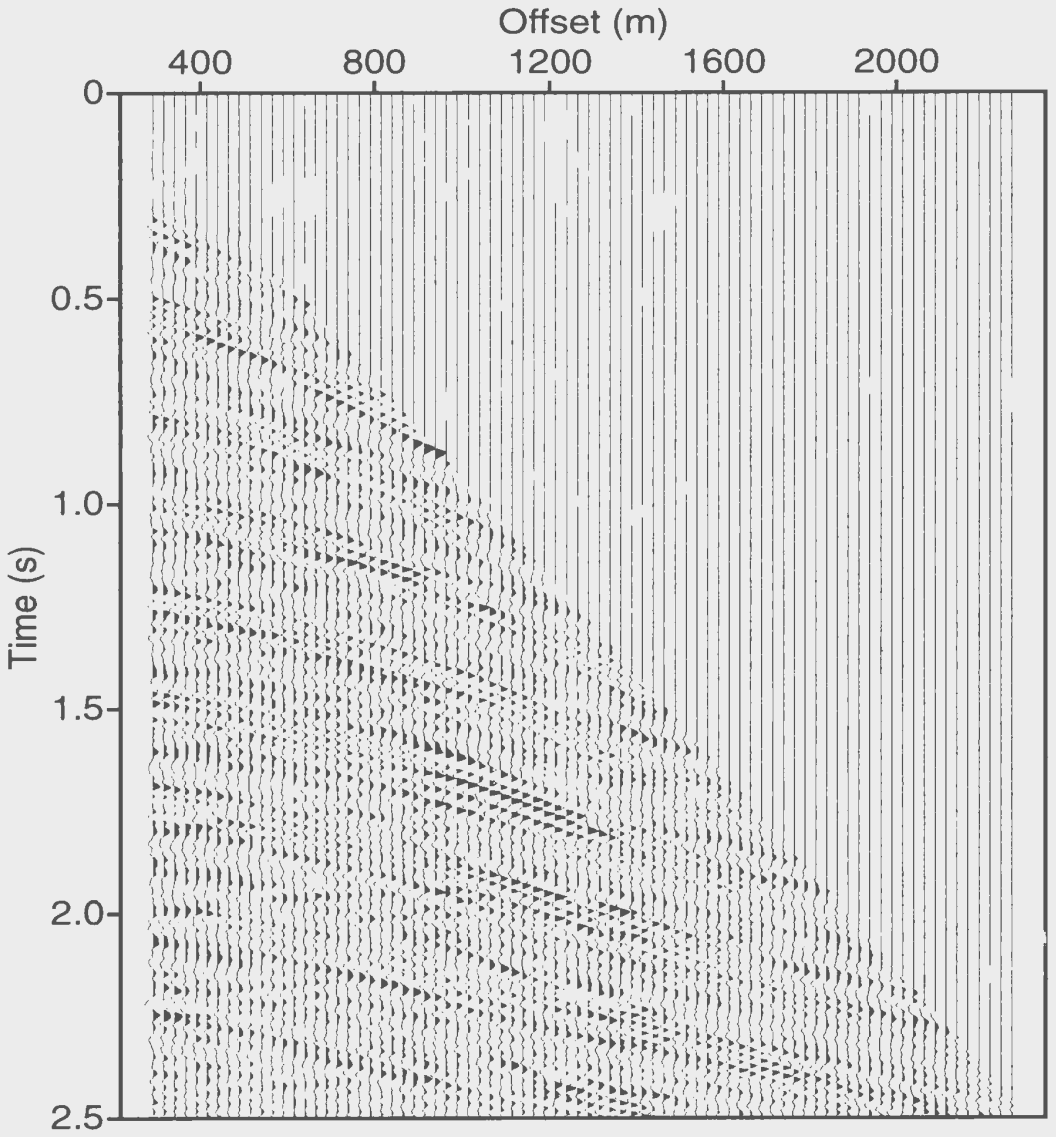

Figure 6.27. The migrated data gather for shot 1510 after application of Raymult. There clearly is a significant reduction in the multiple energy.

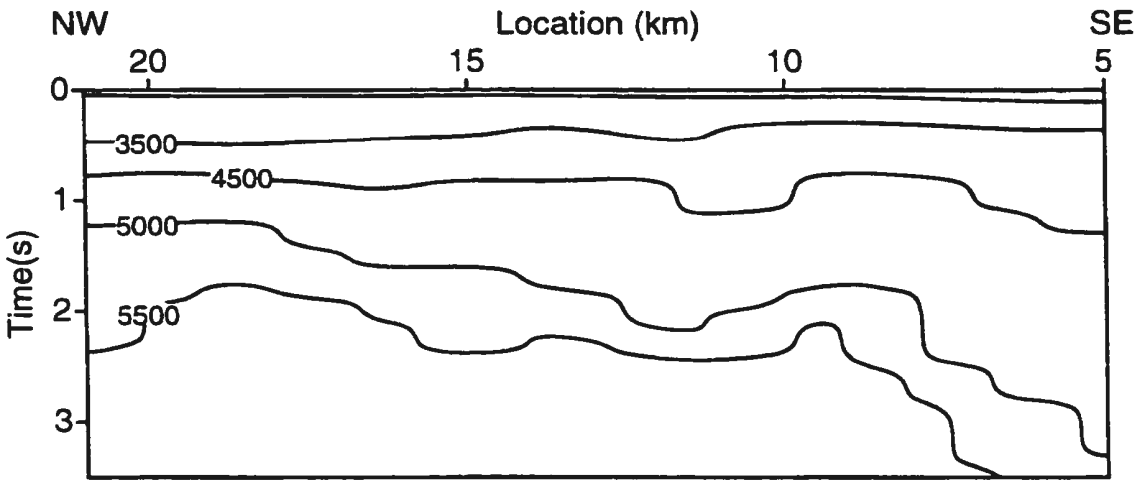

Figure 6.28. The NMO velocity model used for stacking the AGC '84 dataset.

After Raymult, a mild FK attenuation was applied in order to remove some of the residual multiple energy. This produced sufficient attenuation that an estimate of the primary velocities could be developed (see Figure 6.28). Adjacent CDP gathers were combined to increase the fold to between 20 and 25. The data were then stacked to produce Figure 6.29. In order to reduce the importance of high amplitude events to the stack, diversity stacking was used. This technique normalizes the energy within a window on each trace before stacking and then scales the result by the sum of the normalizing factors. This effectively balances the contribution of each trace to the final stack.

There are a number of reflections at the eastern end of the line that appear to be primaries. The low frequency content is consistent with the sub-optimal

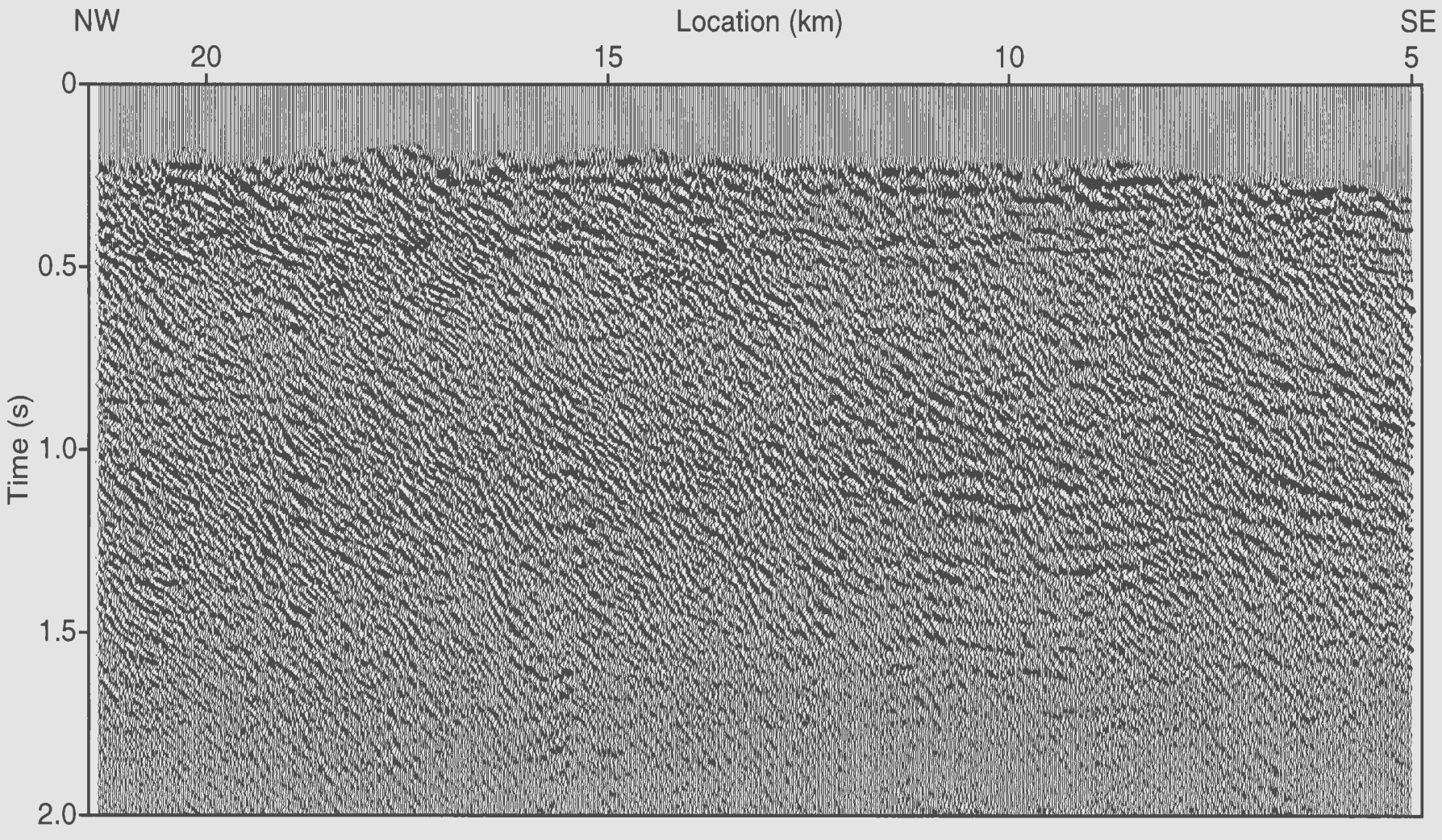

Figure 6.29. Stack of AGC '84 data after applying Raymult to the original shot gathers. Adjacent CDP gathers were combined to increase the fold to between 20 and 25. Diversity stacking was used to reduce the effect on the final stack of high amplitude events on some traces.

stacking of events whose moveout is non-hyperbolic. Since the timing of primary events should be distorted by the sea-floor topography, these low frequencies are expected. Figure 6.30 shows these events in a little more detail. There are several arguments for these events to be primaries:

1. The location and dip of the events are different from those expected of the water-bottom multiples.
2. The events show sufficient dip variability that it is unlikely that they are caused by processing artifacts.
3. Most importantly, there is some evidence of primaries on the CMP gathers (see Figure 6.31).
4. Finally, the local geology is thought to consist of a number of eastward dipping faults (Langdon, 1996), which is consistent with the general trend of the observed reflectors.

While these events may not be completely convincing, they are considerably more convincing than anything on the standard stack. Figure 6.32 shows the data processed in exactly the same manner as Figure 6.29, but without Raymult. The strong westward dipping events are produced by the stacking of multiple energy which has not been attenuated (refer back to Figure 3.7), while the sub-horizontal events are the result of FK smearing of the multiples on the near traces. Hence, virtually all of the energy is due to water bottom related

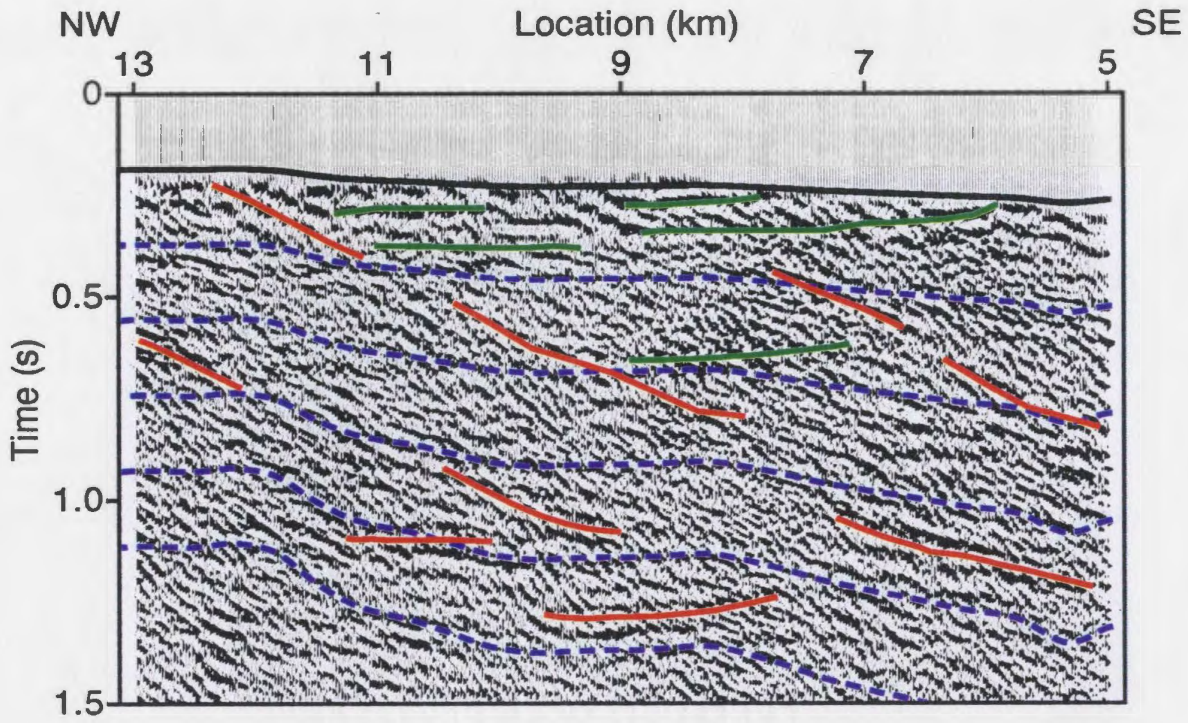

Figure 6.30. A close up view of the eastern end of the line, showing possible events. The dashed blue lines show the approximate locations of the original water bottom multiples. The solid red lines mark a number of events which could be primaries, possibly produced by eastward dipping faults. The sub-horizontal green lines are less reliable, but could be primaries of stratigraphic origin.

multiples. Very few, if any, of the potential primaries seen in Figure 6.30 are visible in this stack. This clearly emphasizes the importance of Raymult in the processing of these data.

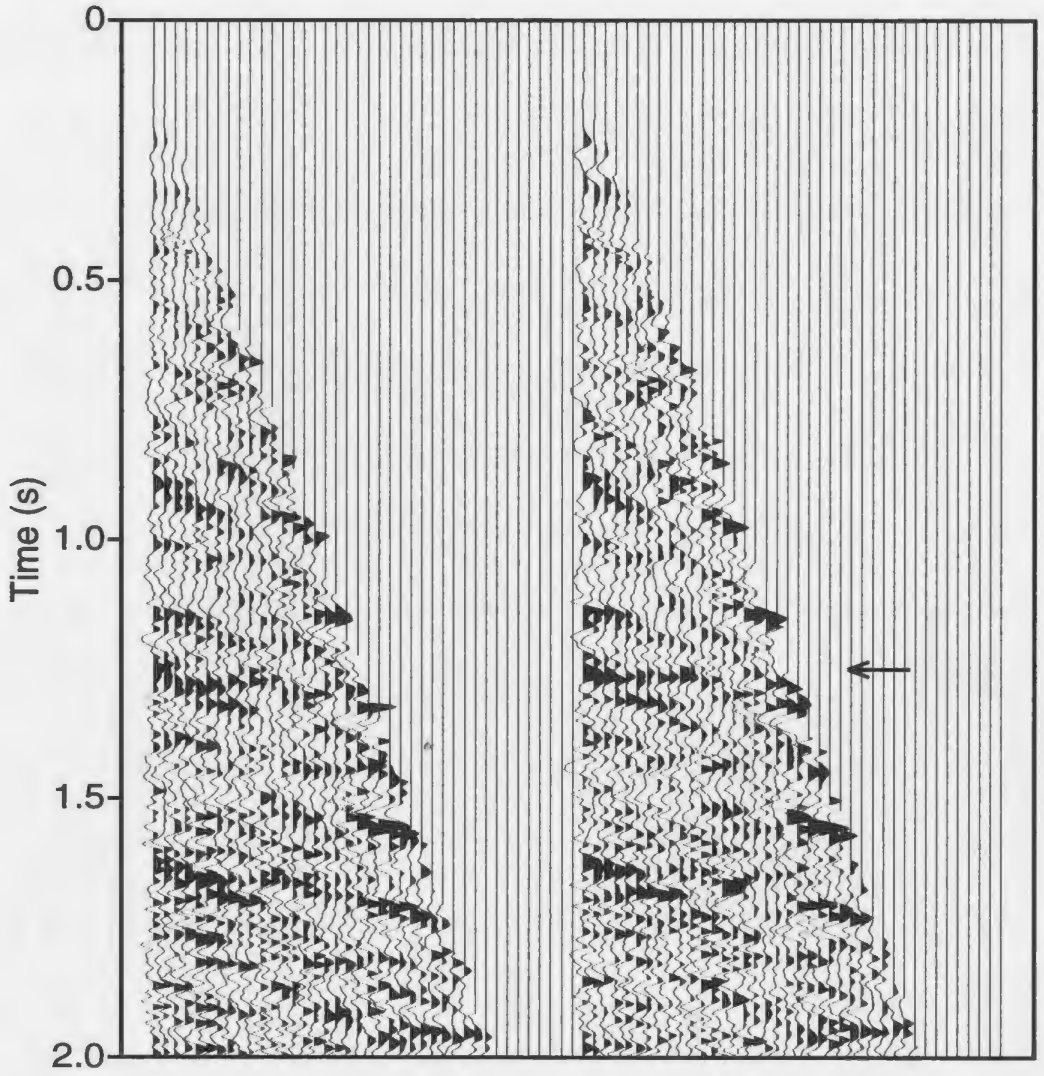

Figure 6.31. CMP 'super gather' from near location 9 km , produced by combining four standard CMP gathers. The data have been processed using Raymult and FK filtering, and NMO has been applied. The arrow marks an apparent primary reflection at approximately 1.25 seconds.

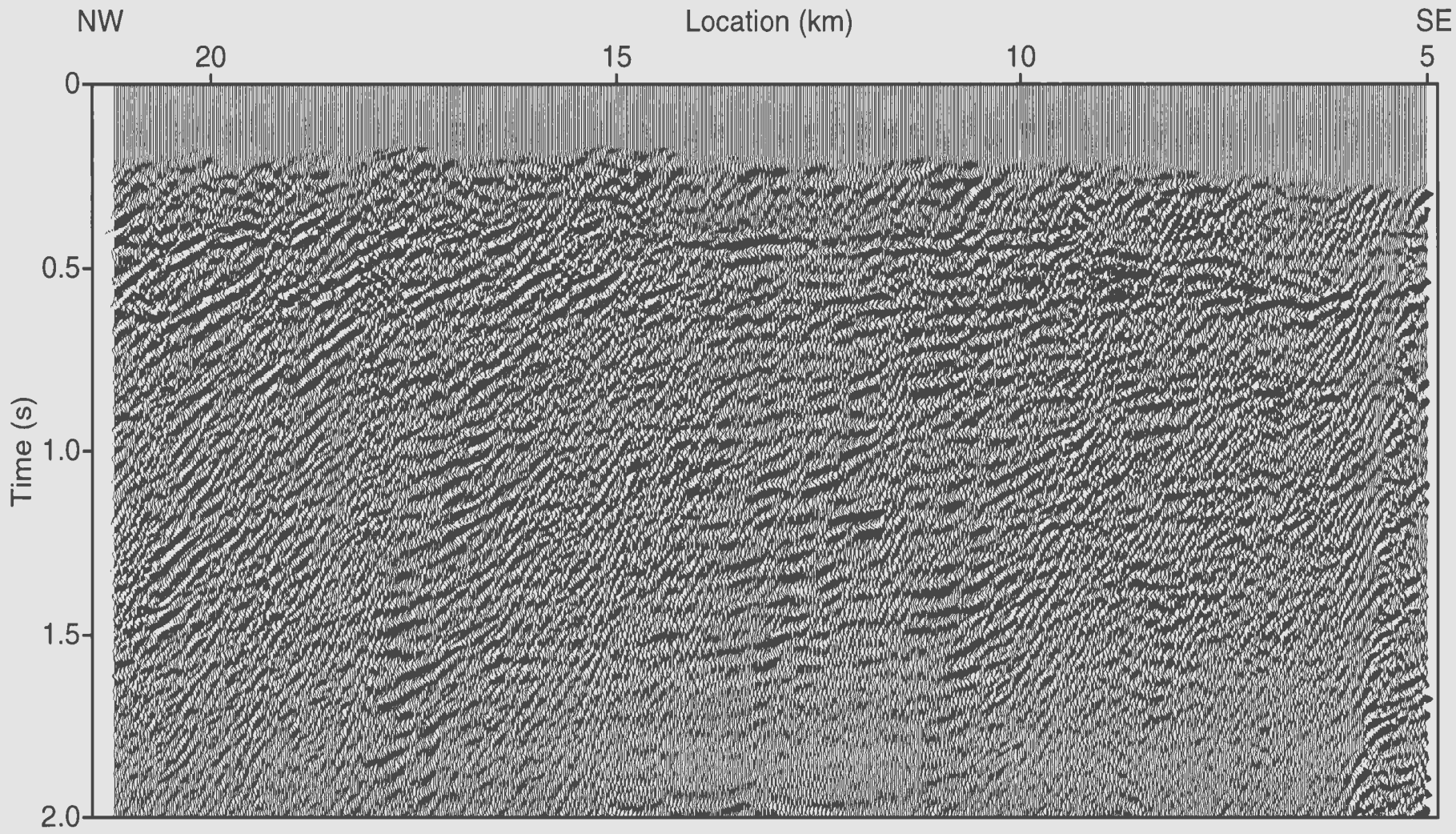

Figure 6.32. Stack of AGC '84 data without using Raymult. FK filtering was the primary technique used for multiple attenuation. Virtually all of the energy can be attributed to water-bottom multiples.

7. CONCLUSIONS

7.1 Water-bottom multiples

Water-bottom multiples are the most severe form of coherent noise found in marine seismic data. Since they are produced by the source energy reverberating within the water layer, they are dependent upon the particular features of the water-bottom itself. The arrival times are controlled by the water depth, while the amplitudes and phases are controlled by the topography of the water-bottom and the acoustic properties of the underlying sediments.

Many algorithms have been developed for multiple attenuation, ranging from velocity filtering techniques such as CMP stacking and FK attenuation to more predictive techniques such as deconvolution, wave-field extrapolation or inverse scattering. Generally, these are able to handle most water-bottom multiples. However, in situations where there is considerable sea-floor topography or very hard sea-floor sediments, their performance is less than satisfactory.

7.2 Raymult: adaptive ray-tracing based multiple suppression

Since rough sea-floor conditions produce multiples with arrival times, amplitudes and phases that are extremely variable, it was decided that the only

way to deal with them effectively was an approach which can adapt its assumptions to fit the actual data. As a result, Raymult was developed. It uses ART raytracing to calculate initial estimates of the multiples' properties for each shot gather. The estimates are used to extract an average wavelet for each order of multiple. The adaptive part of the routine then adjusts the estimates and the wavelet until the predicted multiples best fit the data. Finally, the predicted multiples are subtracted from the data. The only assumptions are that the wavelet has a constant amplitude spectrum for each multiple on each shot gather and that the multiple orders do not have significant overlap, which generally implies that the water depth is greater than 100 m.

The whole process is performed quite economically. The sea-floor model is developed automatically from the near traces, and a 500 trace model generally requires only 10-20 seconds of computation time. Even with extensive testing of different water velocities and smoothing parameters, a good model typically can be found within 15-30 minutes of actual user time. Raymult generally takes about 45 seconds of CPU time (on a SPARC 1000 server) for a 120 trace shot gather to attenuate 10 orders of multiples. The actual raytracing only accounts for roughly 2-5 seconds of this, with the adaptive part the of routine using the bulk of the remaining time. Since the adaptation is performed iteratively, the amount of time required clearly depends on the number of iterations, which in

turn depends on how good the model is, the severity of the multiples and the consistency of the wavelet. As a result, the shot gather mentioned above could take anywhere from 30 to 60 seconds, roughly equivalent to the time required for parabolic radon filtering.

The constant wavelet assumption deserves some discussion. Since marine seismic data is collected using receiver groups (arrays), the recorded response should be dependent upon the angle of incidence. As a result, it seems unlikely that the wavelet recorded at the far offsets, where the rays would be primarily horizontal, would be the same as the wavelet recorded at the near offsets, where the rays would be primarily vertical. This problem is most severe when the water is shallow or when the streamer is long. Clearly it affects low order multiples more than higher ones, since each successive multiple requires steeper ray angles. The problem is most easily dealt with by restricting the offset ranges, through the application of a linear front mute.

7.3 Processing Results

Since the sea-floor conditions around Newfoundland are exactly those described above - rough topography with hard sediments, there was an abundance of local data on which to test Raymult. Two very different data sets were chosen; a high frequency data set in relatively shallow water which

contained numerous strong primary reflectors, and lower frequency dataset over a very hard, very rough sea-floor which had only a few, very weak primary reflectors.

The high frequency dataset was collected for Hunt Oil off the west coast of Newfoundland using a short 48 channel streamer. Since the maximum offset was only 640 m, the traditional techniques, which use moveout-discrimination for multiple suppression, were ineffective. In addition, the combination of sea-floor topography and a hard water-bottom reflector made predictive deconvolution unreliable. Raymult, on the other hand was very successful. Virtually all of the water-bottom multiple energy was removed from the stack, while subsequent predictive deconvolution was able to remove a significant amount of the pegleg energy.

The AGC '84 dataset was much more difficult. It was collected off the tip of the Northern Peninsula as part of a deep crustal reflection experiment, and therefore used a lower frequency source and had much longer offsets. The sea-floor was extremely hard, with velocities in excess of 3000 ms^{-1}, and very rough. The topography not only made it difficult to model the multiples, it also produced severe diffractions which were as significant a noise problem as the multiples themselves. However, prestack migration using the water velocity was very successful at collapsing the diffractions into the reflections, resulting in a

major improvement in the amount of energy Raymult was able to remove from the data. Subsequent FK attenuation followed by post-stack predictive deconvolution was able to remove much of the remaining multiple energy. Consequently, the final stack was relatively multiple-free. Unfortunately, the primary reflectors were very weak, so although the stack does appear to contain a number of possible primary events, they are somewhat questionable and their exact timing is difficult to ascertain. They do, however, agree with the general prediction of eastward dipping geological structures.

7.4 Future Research

There are a number of areas on which future research could focus, both for improving the performance of Raymult and for extending its use into related noise suppression. First, Raymult does cause some attenuation of primary energy at those locations where the multiples and primaries intersect. It should be possible to separate the primary and multiple components at the cross-overs since the technique already produces a good estimate of the wavelet. Deconvolution may be able to do this.

It would also be good to use Raymult for attenuating pegleg multiples. This should be relatively easy to implement, since it only requires changes to the raytracing code. However, it does require a good model for the reflector which

is generating the peglegs. Wavelet iterations could be avoided by simply using the wavelet estimates from the water-bottom multiple attenuation. This could also reduce the potential damage to the primaries, since it would be difficult to construct a good wavelet estimate from the peglegs which would likely be more poorly estimated.

Finally, it would be relatively easy to adapt Raymult into a surgical event editor. Essentially, any coherent noise that can be picked in pre-stack gathers could be effectively attenuated using Raymult's adaptive approach. While this would not be recommended as part of a standard processing stream, there are times when events are clearly identifiable as noise, such as side scattering from off-line events or refractions, and are not easily attenuated by usual techniques. It might be a useful tool.

8. REFERENCES

Aki, K. and Richards, P.G. (1980) *Quantitative seismology; theory and methods.* W.H. Freeman and Co., San Francisco, United States.

Arons, A.B. and Yennie, D.R. (1950) Phase distortion of acoustic pulses obliquely reflected from a medium of higher sound velocity. *Journal of the Acoustic Society of America*, **22**, 231-237.

Backus, M. (1959) Water reverberations, their nature and elimination. *Geophysics*, **24**, 233-261.

Boschetti, F. and Dentith, M.D. (1996). A fractal-based algorithm for detecting first arrivals on seismic traces. *Geophysics* **61**, 1095-1102.

Brandsaeter, H. and Ursin, B. (1979) Adaptive long-period multiple attenuation. *Geophysical Prospecting*, **27**, 709-725.

Burg, K.E., Ewing, M., Press, F. and Stulken, E.J. (1951) A seismic wave guide phenomenon. *Geophysics*, **16**, 594.-612.

Buttkus, B. (1979) Coherency weighting - an effective approach to the suppression of long leg multiples. *Geophysical Prospecting*, **27**, 29-39.

Calvert, A.J. (1990) Raytracing based prediction and subtraction of water layer multiples. *Geophysics*, **55**, 443-455.

Carvalho, P.M., Weglein, A.B. and Stolt, R.H. (1992) Nonlinear inverse scattering for multiple suppression: application to real data.Part I. *62nd Annual Meeting of the SEG, Expanded Abstracts*, 1093-1095.

Cerveny, V., Molotkov, A. and Psencik, I. (1977) *Ray Method in Seismology*, University of Karlova, Prague, Czechoslovakia.

Clarke, G.K.C. (1968) Time-varying deconvolution filters. *Geophysics*, **33**, 936-944.

Coppens, F. (1985). First arrival picking on common-offset trace colections for automatic estimation of statics corrections. *Geophysical Prospecting* **33**, 1212-1231.

Dragoset, B. and Barr, F. (1994) Ocean-bottom cable dual-sensor scaling. *64th Annual Meeting of the SEG, Expanded Abstracts*, 857-860..

Ellsworth, T.P. (1948) Multiple reflections. *Geophysics*, **13**, 1-18.

Foster, D.J. and Mosher, C.C. (1992) Suppression of multiple reflections using the Radon transform. *Geophysics*, **57**, 386-395.

Gelchinsky, B. and Shtivelman, V. (1983). Automatic picking of first arrivals and parameterization of traveltime curves. *Geophysical Prospecting*, **31**, 915-928.

Griffiths, L.J., Smolka, F.R. and Trembly, L.D. (1977) Adaptive deconvolution: a new technique for processing time-varying seismic data. *Geophysics*, **42**, 742-759.

Hampson, D. (1986) Inverse velocity stacking for multiple elimination. *Journal of the Canadian Society of Exploration Geophysicists*, **22**, 44-55.

Hatherly, P.J. (1982). A computer method for determining seismic first arrival times. *Geophysics*, **47**, 1431-1436.

Keen, C.E., Keen, M.J.,Nichols, B., Reid, I., Stockmal, G.S., Colman-Sadd, S.P., O'Brien, S.J., Miller, H., Quinlan, G., Williams, H. and Wright, J. (1986) A deep seismic reflection profile across the northern Appalachians. *Geology*, **14**, 141-145.

Langdon, G. (1996) *Tectonics and Basin Deformation in the Cabot Strait Area and Implication for the Late Paleozoic Development of the Appalachians in the St. Lawrence Promontory*. Ph.D. Thesis, Memorial University of Nwefoundland.

Marillier, F., Keen, C.E., Stockmal, G.S. Quinlan, G.M., Williams, H., Colman-Sadd, S.P. and O'Brien, S.J. (1989) Crustal structure and surface zonation of the Canadian Appalachians: implications of deep seismic reflection data. *Canadian Journal of Earth Sciences*, **26**, 305-321.

Matson, K. and Weglein, A.B. (1996) Free surface elastic multiple removal using inverse scattering. *Annual Meeting of the CSEG, Expanded Abstracts*, 56-57.

Mayne, H.W. (1962) Common reflection point horizontal data stacking techniques. *Geophysics*, **28**, 927-938.

Morley, L.C. (1982) *Predictive Techniques for Marine Multiple Suppression.* Ph.D. Thesis, Stanford University.

Moldoveanu, N. and Chang, M. (1994) Multiple attenuation using buried vertical hydrophone arrays. *56th Meeting of the EAEG, Extended Abstracts*, B032.

Moldoveanu, N., Henman, R., Lang, J. and Chang, M. (1993) Undershooting using the vertical hydrophone array - The South Marsh Island experiment. *63rd Annual Meeting of the SEG, Expanded Abstracts*, 536-539.

Murat, M.E. and Rudman, A.J. (1992) Automatic first arrival picking, a neural network approach. *Geophysical Prospecting*, **40**, 587-604.

Officer, C.B (1951) Normal mode propagation in three layered liquid half-space by ray theory. *Geophysics*, **16**, 207-212.

Paffenholz, J. and Barr, F. (1995) An improved method for deriving water-bottom reflectivities for processing dual-sensor ocean-bottom cable data. . *65th Annual Meeting of the SEG, Expanded Abstracts*, 987-990.

Pilant, W.L. (1979) *Elastic Waves in the Earth.* Elsevier Sci. Publ. Co., Amsterdam, Netherlands.

Press, F. and Ewing, W.M. (1950) Propagation of explosive sound in a liquid layer overlying a semi-infinite elastic solid. *Geophysics*, **15**, 426–446.

Press, W.H., Flannery, B.P., Teukolsky, S.A. and Vetterling, W.T. (1986) *Numerical Recipes*. Cambridge University Press, Cambridge, UK.

Quinlan, G., Hall, J., Williams, H., Wright, J., Colman Sadd, S., O'Brien, S., Stockmal, G., and Marillier, M. (1992) Lithoprobe on-shore seismic reflection transects across the Newfoundland Appalachians. *Canadian Journal of Earth Sciences*, **29**, 1865-1877.

Robinson, E.A. and Treitel, S. (1980) *Geophysical Signal Analysis*, Prentice Hall Inc., Englewood Cliffs, United States.

Schneider, W.A., Prince, E.R. and Giles, B.F. (1965) A new data-processing technique for multiple attenuation exploiting differential normal moveout. *Geophysics*, **30**, 348-362.

Sloat, J. (1948) Identification of echo reflections. *Geophysics*, **13**, 27-35.

Taner, M.T. (1980) Long period sea-floor multiples and their suppression. *Geophysical Prospecting*, **28**, 30-48.

Tooley, R.D., Spencer, T.W. and Sagoci, H.F. (1965) Reflection and transmission of plane compressional waves. *Geophysics*, **30**, 552-570.

Treitel, S., Gutowski, P.R. and Wagner, D.E. (1982) Plane wave decomposition of seismograms. *Geophysics*, **47**, 1375-1401.

Tsai, C.J. (1985) Use of autocorrelation to suppress first-order, long-period multiples. *Geophysics*, **50**, 1410-1425.

Verschur, D.J. and Berkhout, A.J. (1992) Surface-related multiple elimination: practical aspects. *62nd Annual Meeting of the SEG, Expanded Abstracts*, 1100-1103.

Wiggins, J.W. (1989) Attenuation of complex water-bottom multiples by wave-equation-based prediction and subtraction. *Geophysics*, **53**, p. 1527-1539.

Yilmaz, O. (1987) *Seismic Data Processing*, Society of Exploration Geophysics, *Investigations in Geophysics No. 2*.

Young, G.B. and Braille, L.W. (1976) A computed program for the application of Zoeppritz's amplitude equations and Knott's energy equations. *Bulletin of the Seismological Society of America*, **66**, 1881-1885.